TEL AVIV UNIVERSITY

THE IBY AND ALADAR FLEISCHMAN FACULTY OF ENGINEERING

The Zandman-Slaner Graduate School of Engineering

EXTENSION OF THE VIRTUAL CRACK CLOSURE TECHNIQUE AND CLIFFORD FORMALISM

By

Elad Farkash

THESIS SUBMITTED TO THE SENATE OF TEL-AVIV UNIVERSITY

in partial fulfillment of the requirements for the degree of

"DOCTOR OF PHILOSOPHY"

May 2022 ISBN: 978-88-31482-52-3

THE IBY AND ALADAR FLEISCHMAN FACULTY OF ENGINEERING
The Zandman-Slaner Graduate School of Engineering

EXTENSION OF THE VIRTUAL CRACK CLOSURE TECHNIQUE AND CLIFFORD FORMALISM

By

Elad Farkash

THESIS SUBMITTED TO THE SENATE OF TEL-AVIV UNIVERSITY
in partial fulfillment of the requirements for the degree of
"DOCTOR OF PHILOSOPHY"

Under The Supervision of Prof. Leslie Banks-Sills

May 2022

THE IBY AND ALADAR FLEISCHMAN FACULTY OF ENGINEERING

The Zandman-Slaner Graduate School of Engineering

This work was carried out under the supervision of

Research Supervisor: Prof. Leslie Banks-Sills

To my loving family

To Michal my beloved and supporting wife

Abstract

The Virtual Crack Closure Technique (VCCT) was first presented in 1977 for calculating stress intensity factors of cracks in linear elastic, homogeneous and isotropic material. It makes use of the Irwin crack closure integral to obtain values of the modes I, II and III energy release rates from finite element data. Using the energy release rates, the stress intensity factors may be obtained. In the literature, failure criteria make use of the stress intensity factors. Thus, accurate values for the stress intensity factors are valuable. It was seen in the literature that it was difficult to obtain accurate results for interface cracks with VCCT. In Banks-Sills and Farkash (2016), a criterion was proposed to overcome this difficulty for this method allowing accurate calculation of stress intensity factors for two-dimensional problems of an interface crack between two dissimilar linear elastic, homogeneous and isotropic materials with fine meshes. For this criterion, new energy release rates were presented, namely, the dual energy release rates. The virtual crack extension (VCE) consists of a number of elements rather than one element as was used in previous studies. The new criterion indicates the optimal number of elements to be used as the VCE.

It is found that although quarter-point elements are recommended for calculations of the stress intensity factors using the J and M-integrals, it is not recommended for the VCCT (Farkash and Banks-Sills, 2020). The VCCT is extended to two-dimensional interface cracks between two anisotropic materials (Farkash and Banks-Sills, 2017). The criterion using the dual energy release rates is extended for these interfaces. It is used to determine the optimal number of elements for the numerical calculations which is presented here and shown to provide accurate results. In addition, the VCCT is extended to three-dimensional problems containing a straight through finite length interface crack and a penny-shaped interface crack in which many elements are used to represent the VCE. Materials chosen for study include homogeneous and isotropic, as well as bimaterial isotropic and anisotropic. In order to use conservative integrals, obtaining the auxiliary solution is required. This task requires extensive mathematical developments, as well as

great care to avoid errors. For VCCT, some of this work must be carried out to obtain the relation between the interface energy release rate and the stress intensity factors, as well as the oscillatory singularity. But this is much simpler than obtaining the first term of the displacement fields for the auxiliary solution for the interaction energy integral. Excellent results are obtained for the two and three-dimensional problems when compared to analytical solutions, as well as with comparison to results obtained with conservative integrals. Hence, the VCCT may be used for new interfaces instead of conservative integrals. New results are obtained for several problems.

In Liu and Hong (2015), a Clifford algebra (Clifford, 1873) was considered for solving three-dimensional problems of anisotropic materials which is presented here. The eigenvalues and eigenvectors are found for specific anisotropic materials. New stress functions and stress vectors for this formalism are developed. In addition, a general solution, using the Clifford formalism, for uniform stress problems is presented. Several problems are solved using it. The results obtained by means of the Clifford formalism are validated by results obtained by the finite element method. The initial hope was to use this formalism for solving crack problems. This does not appear to be possible. This formalism may be extended for other three-dimensional problems such as an ellipsoidal cavity subjected to a uniform loading.

Contents

Abstract **i**

List of Symbols **vi**

List of Figures **vi**

List of Tables **xi**

1 Introduction **1**

1.1 Crack in a linear elastic, homogeneous and isotropic material 2

1.2 Interface crack between two isotropic materials 6

1.3 J- and M-integrals 9

1.4 Stroh and Lekhnitskii Formalisms 13

1.5 Clifford algebra 15

1.6 Virtual crack closure technique (VCCT) 20

1.6.1 Calculation of the energy release rates using the virtual crack closure technique 20

1.6.2 Extraction of the stress intensity factors from the energy release rates 39

1.7 Research objectives 46

2 VCCT for two-dimensional problems **49**

2.1 Derivations of equations for calculating the energy release rates 49

2.2 Numerical results for different types of elements 53

2.3 A new equation for calculation of the phase angle 60

2.4 The coupled energy release rate and the dual energy release rates 68

2.5 VCCT for an interface crack between two transversely isotropic materials . 76

2.5.1 Interpenetration zone 78

2.5.2 An interface crack in an infinite body 79

2.5.3 Interface cracks in a CCT and a DCB specimens 88

2.5.4 Summary 91

3 VCCT for three-dimensional problems **92**

3.1 Derivations of equations for calculating the energy release rates in three-dimensional problems 92

3.2 Numerical results for a straight through finite length crack and a penny-shaped crack in an infinite body of isotropic, homogeneous material 98

3.3 Numerical results for an interface crack between two dissimilar linear elastic, homogeneous and isotropic materials 106

3.4 Numerical results for an interface crack between two dissimilar transversely isotropic materials 113

4 A Clifford formalism **122**

4.1 The eigenvalue problem for various anisotropic materials 122

4.1.1 Eigenvalue solution for orthotropic materials 125

4.1.2 Equations for various material symmetries 128

4.2 The eigenvector for various anisotropic materials 135

4.3 A three-dimensional Clifford formalism 143

4.4 Analytical and numerical results of the three-dimensional Clifford formalisms 153

4.4.1 A solution for a pure shear problem 154

4.4.2 A general solution for a uniform stress field 157

4.4.3 Combined tensile stress problem for $P_{12} = 1$ 158

4.4.4 Combined tensile stress problem for $P_{13} = 1$ 160

5 Summary and conclusions **164**

Bibliography **172**

A Maintaining displacement continuity across the interface of a penny-shaped interface crack **179**

B Equations of parameters for a $+45°//-45°$ interface **182**

List of Figures

1.1 Mode deformation: (a) Mode I, (b) Mode II and (c) Mode III. 3

1.2 Cartesian and polar coordinates systems emanating from the crack tip. . . 3

1.3 Interface crack between two dissimilar materials. 6

1.4 (a) A contour for the line J-integral and (b) an integration area for the area J-integral. 9

1.5 Virtual crack extension along the crack front denoted on the finite element mesh (from Banks-Sills, 2010). 11

1.6 Cross-sectional view of the first and second domains for the M-integral. . . 11

1.7 An interface crack between two dissimilar linear elastic, transversely isotropic and homogeneous materials. 13

1.8 Bivectors of (a) $\mathbf{u} \wedge \mathbf{v}$ and (b) $\mathbf{v} \wedge \mathbf{u}$ and (c) a trivector $\mathbf{u} \wedge \mathbf{v} \wedge \mathbf{w}$. 16

1.9 (a) Crack of length a and (b) crack of length $a + \Delta a$. 20

1.10 Nodal point forces and displacement jumps for (a) four-noded elements and (b) eight-noded elements for VCCT following Ramamurthy et al. (1986) and Raju (1987). 22

1.11 (a) Quarter-point element and (b) schematic description of the singularity area of it. 22

1.12 Quarter-point twenty-noded element. 23

1.13 The nodal point forces and displacement jumps for VCCT using QP-elements. 24

1.14 The forces obtained at nodes 1 and 3 from the finite elements analysis. . . 25

1.15 The elements used for calculation of the energy release rates when using two elements ahead and four elements behind the crack tip (the two lower elements not shown) for (a) four-noded and (b) eight-noded elements, using the approach of Beuth (1996). 26

1.16 (a) The elements used for calculation of the energy release rates when using three elements ahead of the crack tip. (b) The ($i'^{\,th}$) element located below the (i^{th}) element for $i = 1, 2, 3$. 27

1.17 Upper view of the nodal point forces and displacement jumps for eight-noded brick elements following Shivakumar et al. (1988). 28

1.18 Upper view of the nodal point forces and displacement jumps for twenty-noded brick elements following Shivakumar et al. (1988). 30

1.19 (a) Specimen configuration and loading for $a/t = 0.2, a/c = 1.0, t/b = 0.09$ and $R/t = 2.78$ and (b) comparison of normalized K calculated from three-dimensional VCCT, force and COD methods for a semicircular surface crack in a single edge notched tension specimen from Shivakumar et al. (1988). 30

1.20 (a) DCB specimen dimensions and loading and (b) comparison of $\mathcal{G}/\mathcal{G}_{p\bar{\varepsilon}}$ calculated from three-dimensional VCCT, COD method and two-dimensional finite element model from Raju, Shivakumar and Crews (1988). 31

1.21 Upper view of the nodal point forces and displacement jumps for corner nodes of twenty-noded brick elements along the crack front using the approach of Whitcomb (1988). 32

1.22 (a) Skin-stiffener debonded configuration and (b) comparison between Raju, Shivakumar and Crews (1988) and Whitcomb (1988) approaches presented in Raju et al. (1996). 34

1.23 Original and transformed coordinate systems. 34

1.24 Mesh of a quarter of a penny-shaped crack and ΔA following Smith and Raju (1998). 36

1.25 (a) A body with an embedded elliptic crack and (b) the embedded crack parameters. 36

1.26 A mesh of a quarter of an elliptical crack and ΔA following Okada et al. (2005) 37

1.27 The oscillatory behaviour of $\mathcal{G}_I$ and $\mathcal{G}_{II}$ for (a) $\varepsilon = 0.01$ and (b) $\varepsilon = 0.1$ (adapted from Toya, 1992). 40

1.28 Interface crack in an infinite body subjected to remote tensile and shear stresses. 43

2.1 (a) The lower edge of an eight-noded isoparametric element using its natural coordinate ξ. For eight-noded regular elements: (b) the crack before and (c) after the VCE in Cartesian coordinates. 50

2.2 For a QP-element: (a) the crack before and (b) after the VCE. (c) IQP-element containing node $2'$ and QP-element containing node 2. 52

2.3 Geometry for (a) a CCT specimen, (b) a DCB specimen and (c) a pure mode II beam specimen. 53

2.4 Schematic view of (a) the mesh and (b) focused mesh in the crack tip region that is used to carry out the FEA of the CCT specimen for a VCE of 0.5 μm. 54

2.5 The normalized stress intensity factors obtained by the different approaches divided by the analytical solution for the CCT specimen. Solid black line is the exact solution. 55

2.6 The mode I energy release rates $\mathcal{G}_I$ obtained by the different approaches normalized by $\mathcal{G}_{SBT}$ for the DCB specimen in eq. (2.14). Solid black line is the comparison solution. 58

2.7 The mode II energy release rates $\mathcal{G}_{II}$ obtained by the different approaches normalized by $\mathcal{G}_{II(SBT)}$ for the pure mode II beam specimen. Solid black line is the solution in eq. (2.20). 59

2.8 An interface crack of length $2a$ between two dissimilar linear elastic, isotropic and homogeneous materials in an infinite body subjected to tension σ_{22} and shear σ_{12} stresses. The width and height of the body $2w/2a = 2h/2a = 40$, respectively, are used in the finite element analysis. 65

2.9 A schematic view of the mesh that was used to carry out the finite element analysis for the body in Fig. 2.8. 66

2.10 An illustration of the energy release rates and the phase angles obtained numerically. 67

2.11 A crack of length $2a$ in a linear elastic, homogeneous and isotropic infinite body subjected to remote tensile and shear tractions. The width and height $w/a = h/a = 40$, respectively, are used in the finite element analysis. . . . 71

2.12 Numerical results of the energy release rates for the problem in Fig. 2.11. . 72

2.13 Numerical results and analytical values of the (a) normalized nodal point forces and (b) normalized crack face displacement jumps. 74

2.14 An interface crack between two dissimilar transversely isotropic materials in an infinite body subjected to remote tensile and shear stresses. 80

2.15 Schematic view of part of mesh A presented in Table 2.11. This mesh contains 1,037,444 eight noded isoparametric elements and 3,117,284 nodal points. 82

2.16 Schematic view of (a) the crack region and (b) the crack tip region of meshes B and C presented in Table 2.11. 83

2.17 For case 3 in Table 2.10 using mesh B, a schematic view of the deformed configuration of the crack faces using data obtained from the finite element analysis. 87

2.18 Geometry for (a) a CCT specimen and (b) a DCB specimen with an interface crack. 88

3.1 View from above of the nodes that are used for calculating the energy release rates in rows 4 and 7, using twenty-noded brick elements. 93

3.2 View from above of the nodes that are used for calculating the energy release rates in row 6 for a penny-shaped crack. 96

3.3 A straight through crack in an infinite body. 98

3.4 A schematic view of (a) the x_1x_2-plane of the mesh that was used for a straight through crack in an infinite body and (b) a close up of the vicinity of the crack tip for this mesh. 99

3.5 Numerical results for a straight through finite length crack in an infinite body. 101

3.6 A penny-shaped crack in an infinite body. 102

3.7 A view of (a) the mesh that was used for a penny-shaped crack in an infinite body and (b) a close up of the vicinity of the crack tip for this mesh. . . . 102

3.8 Upper view of the virtual crack extension of a penny-shaped crack for an axisymmetric problem. 103

3.9 (a) Isoparametric and (b) upper views of the mesh used for the penny-shaped crack. 105

3.10 An infinite, bimaterial body subjected to tension σ_{22} and tractions $\sigma_{11}^{(1)}$, $\sigma_{11}^{(2)}$, $\sigma_{33}^{(1)}$ and $\sigma_{33}^{(2)}$ parallel to the interface plane. The width, height and thickness are $2w$, $2h$ and $2b$, respectively. 106

3.11 Numerical results of a straight through interface crack, shown in Fig. 3.10, where the mechanical properties are $E_1 = 1$ GPa, $\nu_1 = 0.3$, $E_2/E_1 = 0.1$ and $\nu_2/\nu_1 = 1$. 109

3.12 Numerical results of a straight through interface crack, shown in Fig. 3.10, for $2b = 15$ mm, for (a) K_1, (b) K_2 and (c) K_{III}. 111

3.13 A penny-shaped interface crack problem. 112

3.14 (a) Isoparametric and (b) upper views of the mesh used for the penny-shaped crack. 115

3.15 Numerical results for an interface penny-shaped crack using mesh B3D in Table 3.11. 120

B.1 (a) An interface crack between two unidirectional composites and (b) an upper view of the crack. 182

List of Tables

1.1 Effective mechanical properties of graphite/epoxy AS4/3501-6 (Banks-Sills and Boniface, 2000). 14

1.2 Multiplication table of quaternions. 16

1.3 Multiplication table of reduced biquaternions. 17

1.4 Data for an interface crack in an infinite body analysis carried out with the finer mesh in Banks-Sills and Farkash (2016). 46

2.1 Errors of the normalized stress intensity factors obtained by the different approaches for the CCT specimen. 56

2.2 Errors of $\mathcal{G}_I$ obtained by the different approaches for the DCB specimen. . 58

2.3 Errors of $\mathcal{G}_{II}$ obtained by the different approaches for the pure mode II beam specimen in Fig. 2.3c as compared to eq. (2.20); errors in parenthesis obtained as compared to the J-integral result in eq. (2.21). 60

2.4 Data for the solved problem in Fig. 2.8. 66

2.5 Numerical values for the energy release rates and ψ_D using the inverse trigonometric functions in eqs. (2.56) to (2.58). 67

2.6 The analytic expressions for the normalized nodal point forces at nodes $i = 1$ to 10 ahead of the crack tip in the x_p-direction ($p = 1, 2$). 70

2.7 Percent errors of the normalized energy release rates obtained with eight-noded isoparametric elements. 72

2.8 Percent errors of the normalized nodal point forces and normalized crack face displacement jumps. 74

2.9 Parameters used to calculate the stress intensity factors. 80

2.10 Applied tractions and the analytic solutions for the cases investigated in this study. 81

2.11 The size ℓ of the elements near the crack tip and the number of elements and nodes for each mesh. 82

2.12 Data for case 1 in Table 2.10, solved with mesh A ($\ell = 5$ μm) in Table 2.11. 83

2.13 Data for case 1 in Table 2.10, solved with mesh B ($\ell = 0.05$ μm) in Table 2.11. 84

2.14 Data for case 1 in Table 2.10, solved with mesh C ($\ell = 0.5$ μm) in Table 2.11. 85

2.15 Data for case 2 in Table 2.10, solved with mesh A ($\ell = 5$ μm) in Table 2.11. 86

2.16 Data for case 2 in Table 2.10, solved with mesh B ($\ell = 0.05$ μm) in Table 2.11. 87

2.17 Data for case 2 in Table 2.10, solved with mesh C ($\ell = 0.5$ μm) in Table 2.11. 87

2.18 Data for case 3 in Table 2.10, solved with mesh B ($\ell = 0.05$ μm) in Table 2.11. 88

2.19 Data for the CCT specimen. 89

2.20 Data for the DCB specimen using the first mesh. 90

2.21 Data for the DCB specimen using the second mesh. 91

3.1 The number of elements and nodes for each three-dimensional mesh for a straight through finite length crack in Fig. 3.3. 100

3.2 Numerical results for a straight through finite length crack using two-dimensional meshes from Table 3.1. 100

3.3 The size ℓ of the elements near the crack tip and the total number of elements and nodes for each mesh for the penny-shaped crack and axisymmetric mesh. 103

3.4 Data for mesh A in Table 3.3 ($\ell = 50$ μm). 104

3.5 Data for mesh B in Table 3.3 ($\ell = 10$ μm). 104

3.6 Numerical results for a penny-shaped crack using a three-dimensional mesh ($\ell_r \times \ell_2 \times \ell_\theta = 10 \times 10 \times 157 \mu\text{m}^3$). 105

3.7 Numerical results of $\mathcal{G}_i^{(n)}$, $\mathcal{G}_I^{(n)}$, $\mathcal{G}_{II}^{(n)}$, $\mathcal{G}_{III}^{(n)}$, $\mathcal{I}_I^{(n)}$, $\mathcal{I}_{II}^{(n)}$ and $\mathcal{I}^{(n)}$ for $2b = 15$ mm in rows $n = 1$ and $n = 145$ using mesh C in Table 3.1 for an interface crack in Fig. 3.10. 108

3.8 Numerical results of the stress intensity factors for $2b = 15$ mm in rows $n = 1$ and $n = 145$ using mesh C in Table 3.1 for an interface crack in Fig. 3.10. 110

3.9 Data for an interface penny-shaped crack in Fig. 3.13 using the axisymmetric mesh A in Table 3.3 ($\ell = 50$ μm). 113

3.10 Numerical results for a penny-shaped interface crack in Fig. 3.13 using the axisymmetric mesh B in Table 3.3 ($\ell = 10$ μm) and using three-dimensional mesh ($\ell_r \times \ell_2 \times \ell_\theta = 10 \times 10 \times 157 \mu\text{m}^3$). 114

3.11 The size ℓ_r of the elements near the crack tip and the total number of elements and nodes for each mesh for the penny-shaped interface crack and three-dimensional meshes. 114

3.12 Parameters used to calculate the stress intensity factors for the $+45°//-45°$ interface. 119

3.13 Numerical results for a penny-shaped interface crack in Fig. 3.14 using meshes A3D and B3D in Table 3.11 ($\ell_r = 50$ μm). 119

4.1 Effective mechanical properties of SC-Si. 130

4.2 Effective mechanical properties of a graphite/epoxy plain weave with yarn in the 0° and 90° directions. 132

4.3 Elastic constants of Single-Crystal Forsterite. The units are GPa. 134

5.1 A comparison between the two-dimensional Stroh and Lekhnitskii formalism and the three-dimensional Clifford formalism. 168

List of Symbols

Lower Case Latin letters

a	half or full crack length
Δa	virtual crack extension
a_i $(i = 0, 1, 2, 3)$	real scalars
a_{ij} $(i, j = 1, 2)$	functions of ε and Δa
$\mathbf{a}$	vector
	eigenvector of Stroh and Clifford formalism
$\mathbf{a}\ \mathbf{b}$	bivector
b	specimen width or thickness
$\mathbf{b}$	vector
	eigenvector of Stroh and Clifford formalism related to $\mathbf{a}$
$c^{(n)}$	ratio for $F_p^{(n)}$
$c^{(m,n)}$	ratio for $F_p^{(m,n)}$
$\mathbf{d}, \mathbf{d}^*, \mathbf{d}^{**}$	eigenvector of Clifford formalism
ds	differential arc length
e_{ij} $(i, j = 1, 2, 3)$	bivector
e_{123}	trivector
$\mathbf{e}_i$ $(i = 1, 2, 3)$	unit vector
$f(y)$	arbitrary function
$f(y_i)$ $(i = 1, 2, 3)$	arbitrary function of y_i
$[\mathbf{f}(y)]$	vector composed of $f(y_i)$
$[\tilde{\mathbf{f}}(y)]$	vector composed of $f(y_{i+3})$
$\langle f(y_*)\rangle$	diagonal matrix composed of $f(y_i)$
$f(z)$	arbitrary function
g	the ratio between $\mathcal{G}_{II}$ and $\mathcal{G}_I$
$\mathbf{g}$	eigenvector of Clifford formalism

$\mathbf{g}^{(\gamma)}$	eigenvector of Clifford formalism related to $P_{13}^{(\gamma)}$
h	half-height of specimen
k_i $(i = 1, 2, 3)$	normalization factors in Clifford formalism
l_i $(i = 1, 2)$	length in specimen
ℓ_i $(i = 1, 2, 3, r, s, \theta)$	length of element in the x_i-direction
$\ell_i^{(N)}$ $(i = 1, 2)$	length of element in the x_i-direction in row N
m	element or node or column or arc number
n	element or node or row or ray number
n_1	component of outward vector
n_i $(i = 1, 2, 3)$	components of the normal vector
p_{11}, p_{12}	eigenvalues obtained by Stroh formalisms
q	arbitrary complex constants
	quaternion
q_1	normalized virtual crack extension function
$\mathbf{q}$	arbitrary 3×1 constant vector
r	radius in polar coordinate system
r_c	estimated small scale interpenetration length
s	contact length
	tangent coordinate
s_{ij}	components of the compliance matrix
$s_{ij}^{(k)}$	components of the compliance matrix of material k
s'_{ij}	components of the reduced compliance matrix
$s_{ij}^{\prime(k)}$	components of the reduced compliance matrix of material k
t	specimen thickness
t_{nm}	weights
$\mathbf{t}_i$ $(i = 1, 2, 3)$	stress vector
u_i $(i = 1, 2, 3)$	components of displacement field
$u_i^{(k)}$ $(\alpha = 1, 2, 3)$	displacement components for material k
$u_i^{(2\alpha)}$ $(i = 1, 2, 3;\ \alpha = a, b, c)$	components of displacement field of the auxiliary solution
${}_k u_i$ $(i = 1, 2, 3)$	components of displacement field
${}_k u_i^{(1)}$ $(i = 1, 2, 3)$	components of displacement field of the problem sought for material k
$\mathbf{u}$	vector form of the displacement field
	vector

$\mathbf{u}^{(k)}$ $(k = 1, 2)$	displacement vector for material k
Δu_p $(p = 1, 2, 3)$	displacement jumps in the x_p-direction
$\Delta u_p^{(m')}$ $(p = 1, 2, 3, r, \theta)$	displacement jumps in the x_p-direction at node number (m')
$\Delta u_p^{(m',n)}$ $(p = 1, 2, 3, r, \theta)$	displacement jumps in the x_p-direction at node number (m', n)
$\mathbf{v}$	vector
w	width of body
$\mathbf{w}$	vector
x_i $(i = 1, 2, 3)$, or x, y, z	axes in cartesian coordinate system
y	arbitrary argument
z	complex variable

Upper Case Latin letters

A	auxiliary integral
A_1	integration area
A_E	auxiliary integral for a $+45°//-45°$ interface
A_T	auxiliary integral for a $0°//90°$ interface
$\mathbf{A}$	complex 3×3 matrix composed of eigenvectors
$\tilde{\mathbf{A}}$	complex 3×3 matrix composed of eigenvectors
$\bar{\mathbf{A}}$	complex 3×3 matrix composed of conjugate eigenvectors
$\mathbf{A}_k$ $(k = 1, 2)$	complex 3×3 matrix composed of eigenvectors for material k
B	thickness of a specimen
$\mathbf{B}$	complex 3×3 matrix composed of eigenvectors
$\tilde{\mathbf{B}}$	complex 3×3 matrix composed of eigenvectors
$\bar{\mathbf{B}}$	complex 3×3 matrix composed of complex conjugate eigenvectors
$\mathbf{B}_k$ $(k = 1, 2)$	complex 3×3 matrix composed of eigenvectors for material k
C	a constant
$\tilde{C}$	constant related to the first two diagonal members of matrix $\mathbf{D}$
C_i $(i = 1, 2)$	integration path
C_{ij}	components of the stiffness matrix

C_{ijkl}	components of the stiffness tensor
$C_{\alpha\beta}$	stiffness tensor under contracted notation
$\mathbf{C}$	stiffness matrix
$\mathbf{C}_{ij}$	matrix composed from components of the stiffness matrix
$C\ell$	Clifford algebra
$C\ell_3(\mathbb{R})$	grade 3 of Clifford algebra
D	auxiliary integral
D_{ij}	components of the matrix $\mathbf{D}$
D_E	auxiliary integral for a $+45°//-45°$ interface
D_T	auxiliary integral for a $0°//90°$ interface
$\mathbf{D}$	3×3 matrix related to $\mathbf{L}_k$
E	Young's modulus
$\bar{E}$	generalized Young's modulus
E_i $(i = 1, 2)$	Young's moduli of material k in the bimaterial interface
E_{ij} $(i = 1, 2, 3)$	constant related to the members of matrices $\mathbf{D}$ and $\mathbf{W}$
E_{kk} $(k = 1, 2, 3)$	Young's moduli in the x_1, x_2 and x_3-directions
E_A	Young's modulus in the axial direction of the fiber
E_T	Young's modulus in the transverse direction of the fiber
F_p $(p = 1, 2, 3)$	the nodal point force in the x_p-direction
$F_p^{(m)}$ $(p = 1, 2, 3, r, \theta)$	the nodal point force in the x_p-direction at node number (m)
$F_p^{(m,n)}$ $(p = 1, 2, 3, r, \theta)$	the nodal point force in the x_p-direction at node number (m, n)
G_{ij} $(i, j = 1, 2, 3)$	shear moduli
G_A	shear modulus in the axial direction of the fiber
G_T	shear modulus in the transverse direction of the fiber
$\mathbf{G}$	complex 3×3 matrix composed of eigenvectors
$\tilde{\mathbf{G}}$	complex 3×3 matrix composed of eigenvectors
$\bar{\mathbf{G}}$	complex 3×3 matrix composed of conjugate eigenvectors
$\mathcal{G}$	energy release rate
$\mathcal{G}_i$	interface energy release rate

$\mathcal{G}_m$ $(m = I, II, III)$	energy release rate corresponding to deformation mode m
$\mathcal{G}_m$ $(m = I-II, I-III)$	coupled energy release rates
$\hat{\mathcal{G}}_m$ $(m = I, II, I-II)$	normalized energy release rates
H_1, H_2	mechanical property
I_m $(m = c, s, 0)$	integrals
$\mathbf{I}$	the identity matrix
$\hat{\mathbf{I}}$	6×6 matrix
$\mathcal{I}$	difference between $\mathcal{I}_I$ and $\mathcal{I}_{II}$
$\mathcal{I}_m$ $(m = E, T)$	difference between $\mathcal{I}_I^{(m)}$ and $\mathcal{I}_{II}^{(m)}$
$\mathcal{I}_m$ $(m = I, II, III)$	dual energy release rates
$\hat{\mathcal{I}}_m$ $(m = I, II)$	normalized dual energy release rates
$\Im$	imaginary part of a complex expression
J	J-integral
K	complex stress intensity factor,
K_m $(m = 1, 2, 3, I, I, II, III)$	stress intensity factors
$\hat{K}_m$ $(m = I, II)$	normalized stress intensity factors
$K_{m_N}^{(1)}$ $(m = 1, 2, III)$	stress intensity factors for the N^{th} element
$K_m^{(1)}$ $(m = 1, 2, III)$	stress intensity factors of the problem sought
$K_m^{(2\alpha)}$ $(m = 1, 2, III;\ \alpha = a, b, c)$	stress intensity factors of the auxiliary solution
L	arbitrary length parameter
$\hat{L}$	arbitrary length parameter
$\mathbf{L}_k$ $(k = 1, 2)$	real matrix for material k
M	number of nodes or elements ahead of the crack tip
M, $M^{(1,2\alpha)}$ $(\alpha = a, b, c)$	M-integral
N	number of rows or rays
N_i	shape function at node i
$\mathbf{N}_m$ $(m = 1, 2, 3)$	matrices of the eigenvalue problem
$\mathbf{N}_m^*$ $(m = 1, 2, 3)$	matrices of modified eigenvalue problem
P	applied load
	function of the special function Gamma
P_I	imaginary part of P
P_R	real part of P
Q	applied load
Q_{1m} $(m = 2, 3)$	parameter used for the eigenvalue problem
$Q(\beta_i)$ $(i = 1, 2, 3)$	function of β_i

R	radius of a body
$R(\theta)$	the crack radius as a function of θ
$\Re$	real part of a complex expression
$S_{\alpha\beta}$	components of the compliance matrix
$\mathbf{S}_k$ $(k = 1, 2)$	real matrix for material k
$\mathbf{S}$	compliance matrix
T	denotes transversely isotropic material
T_i	traction in the x_i-direction
${}_kU_\alpha^{(1)}(\theta)$, ${}_kU_\alpha^{(2)}(\theta)$ $(k = 1, 2)$	in-plane displacement functions for material k
${}_kU_3^{(III)}(\theta)$ $(k = 1, 2)$	out-of-plane displacement function for material k
V	integration volume
W	specimen width
$W^{(1,2\alpha)}$ $(k = 1, 2)$	interaction or mutual strain energy
W_{12}	component of $\mathbf{W}$
$W^{(m,p)}$	shape function at node (m, p)

Lower Case Greek letters

α_i $(i = 1, 2, 3)$	real constant related to real part of P_{12}
β	related to ε
β_i $(i = 1, 2, 3)$	real constant related to imaginary part of P_{12}
δ	stress singularity
δ_{ij}	Kronecker delta
ε	oscillatory parameter
$\boldsymbol{\eta}$	left eigenvector
θ	angle in polar coordinate system; angle of a ray perpendicular to the crack front in respect to the crack plane
κ	Kosolov parameter in a homogeneous, linear elastic, isotropic material
κ_k $(k = 1, 2)$	Kosolov parameter for material k
λ	Lamé constant parameter which depends on the mechanical properties
μ	shear modulus
μ_k $(k = 1, 2)$	shear modulus for material k

ν	Poisson's ratio
ν_{ij} $(i,j=1,2,3)$	Poisson's ratios
ν_k $(k=1,2)$	Poisson's ratio for material k
ν_A	Poisson's ratio in the axial direction of the fiber
ν_T	Poisson's ratio in the transverse direction of the fiber
ξ, η, ζ	natural coordinates
$\boldsymbol{\xi}$	right eigenvector
σ	applied remote stress
σ_{21}	remote shear stress
σ_{22}	remote tensile stress
σ_{ij}	components of the stress tensor
$\sigma_{ij}^{(k)}$	components of the stress tensor for material k
${}_k\sigma_{ij}^{(1)}$	stress components of the problem sought
${}_k\sigma_{ij}^{(2\alpha)}$ $(\alpha=a,b,c)$	stress components of the auxiliary solution
σ_α	stress components under contracted notation
ϕ	phase angle
ϕ_i	components of stress function
$\boldsymbol{\phi}$	stress function vector
$\boldsymbol{\phi}^{\mathbf{b}}, \boldsymbol{\phi}^{\mathbf{b}}$	stress function vectors
ψ	phase angle of the complex stress intensity factor
$\hat{\psi}$	phase angle of K depends upon $KL^{i\varepsilon}$
ψ_D	phase angle of D
ψ_P	phase angle of P

Upper Case Greek letters

Γ	integration path
$\Gamma(\cdot)$	special function Gamma
${}_k\Sigma_{\alpha\beta}^{(1)}$, ${}_k\Sigma_{\alpha\beta}^{(2)}$	bimaterial interface in-plane stress functions for material k under contracted notation
${}_k\Sigma_{\alpha 3}^{(III)}$	bimaterial interface out-of-plane stress functions for material k under contracted notation
${}_k\Sigma_{\alpha\beta}^{(1)}(\theta)$, ${}_k\Sigma_{\alpha\beta}^{(2)}(\theta)$ $(k=1,2)$	in-plane stress functions for material k
${}_k\Sigma_{3\beta}^{III}(\theta)$ $(k=1,2)$	out-of-plane stress functions for material k

Abbreviation

CC	central crack
CCT	central crack tension
COD	crack opening displacement
DCB	double cantileverbeam
EN	edged notched
FEA	finite element analysis
SC-Si	Single Crystal Silicon
SL	Stroh and Lekhnitskii
UD	unidirectional
VCE	virtual crack extension
VCCT	virtual crack closure technique

Chapter 1

Introduction

Fracture mechanics is an important subject in the field of failure of materials. It explores propagation of cracks in a structure. A crack may initiate in a material as a result of an overload or fatigue loading. It may then propagate during the lifetime of the structure until it propagates catastrophically. The first milestone of fracture mechanics was achieved by Griffith (1920) while investigating propagation of cracks in brittle materials. Griffith (1920) developed a failure criterion based upon a new concept: the energy release rate. Irwin (1958) used the work of Griffith (1920), and developed a new approach, based on the stress intensity factor. Stress intensity factors depend upon the geometry and applied tractions of the problem. By using the stress intensity factors, one may also predict failure.

Fracture mechanics concepts have been applied to composite materials. Composite materials are lightweight and have desirable mechanical properties. Additionally, by changing the direction of the fibers in various plies, tailorable properties may be obtained. Those features satisfy the needs of the sporting, aircraft and aerospace industries. Thus, the use of composite materials has been increasing in those industries with time. An example of the need to understand the behavior and failure of composite materials is the crash of the Airbus A300B4-605R. On November 12, 2001, the Airbus A300B4-605R crashed shortly after takeoff. Two hundred and sixty-five people were killed, including all of the people on board and five people on the ground. The investigation team found that the vertical stabilizer separated from the fuselage causing the airplane to lose control and crash. One of the reasons for the stabilizer separation was a prior delamination between composite plies. The delamination was found by technicians after the crash.

Methods for calculating stress intensity factors numerically have been developed. Some of the popular methods include the J-integral, M-integral and displacement extrapolation. These methods make use of results obtained by means of finite element analyses (FEA). The J and M-integrals are indirect methods, introduced by Rice (1968a), and Chen and Shield (1977), respectively. The stress intensity factors are determined indirectly from energy quantities. By using the J-integral, one may calculate stress intensity factors for

pure mode problems. The M-integral allows calculation of two or three stress intensity factors separately. Those problems are called mixed mode problems. The M-integral requires derivation of the first term of the asymptotic expansion of the displacement field and the stress field on a line ahead of the crack tip. In addition, complex computer software must be developed. This method is considered very accurate. The displacement extrapolation method, introduced by Chan et al. (1970), is a direct method. The stress intensity factors are found by extrapolating the displacement components along the crack faces. This method requires only the first term of the asymptotic expansion of the crack face displacements and is easy to implement. It is considered less accurate than the M-integral.

In this investigation, the Virtual Crack Closure Technique (VCCT), introduced by Rybicki and Kanninen (1977), is considered. The VCCT uses data from a finite element solution of the problem at hand to calculate the stress intensity factors. Only the first term of the asymptotic expansion of the crack face displacements and the stresses on a line ahead of the crack tip are required. In a recent paper (Banks-Sills and Farkash, 2016), it was found that the VCCT allows accurate calculation of stress intensity factors for two-dimensional problems with fine meshes. The goal of this study is to extend the VCCT method to three-dimensional problems in composite materials. In addition, in this study, an extension of Stroh (1958) and Lekhnitskii (1950,1963) formalisms to three-dimensional problems is presented.

In Section 1.1, the basic equations related to a crack in a linear elastic, homogeneous and isotropic material are presented. The equations for an interface crack between two different linear elastic, homogeneous and isotropic materials are discussed in Section 1.2. An overview of the J and M-integrals is presented in Section 1.3. In Section 1.4, the Stroh (1958) and Lekhnitskii (1950,1963) formalisms are presented. Stroh (1958) and Lekhnitskii (1950,1963) developed formalisms that describes mathematically the behavior of anisotropic materials in two dimensions. In Section 1.5, a Clifford algebra is presented. The VCCT, based on the Irwin (1958) crack closure integral, is presented in Section 1.6. In Section 1.7, research objectives are discussed.

1.1 Crack in a linear elastic, homogeneous and isotropic material

In linear elastic fracture mechanics, deformation of the crack faces is used to describe three deformation modes, as shown in Fig. 1.1. In mode I, shown in Fig. 1.1a, the crack faces open so that the displacements are perpendicular to the crack plane. In mode II, the deformation is in the crack plane, as shown in Fig. 1.1b. In this mode, the crack faces slide with respect to one another in the plane perpendicular to the crack plane. Mode

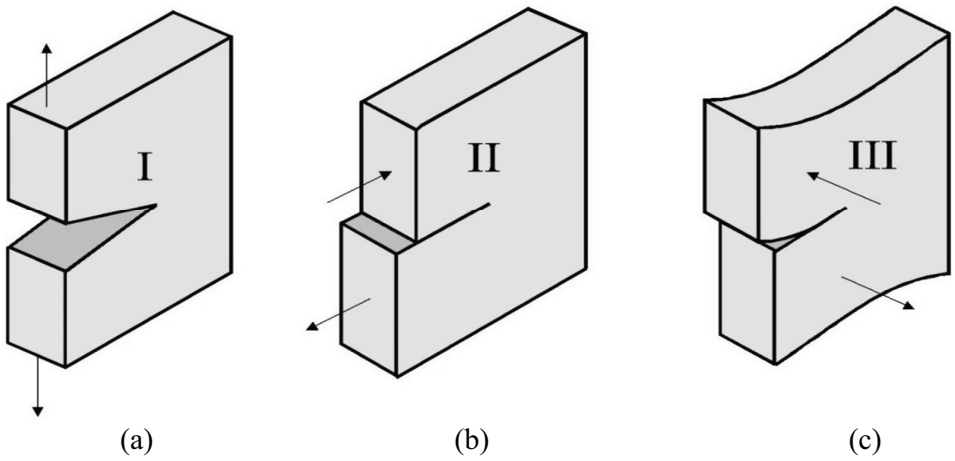

Figure 1.1: Mode deformation: (a) Mode I, (b) Mode II and (c) Mode III.

III is shown in Fig. 1.1c. In this mode, the deformation is characterized by out-of-plane sliding of the crack faces.

The asymptotic stress and displacement fields for mode I were found by Irwin (1957) and Williams (1957). Explicit expressions for the first term in the asymptotic stress field for mode I are given as

$$\left\{ \begin{array}{c} \sigma_{11} \\ \sigma_{12} \\ \sigma_{22} \end{array} \right\} = \frac{K_I}{\sqrt{2\pi r}} \cos\frac{\theta}{2} \left\{ \begin{array}{c} 1 - \sin\frac{\theta}{2}\sin\frac{3\theta}{2} \\ \sin\frac{\theta}{2}\cos\frac{3\theta}{2} \\ 1 + \sin\frac{\theta}{2}\sin\frac{3\theta}{2} \end{array} \right\}, \tag{1.1}$$

$$\sigma_{33} = \left\{ \begin{array}{cc} 2\nu\frac{K_I}{\sqrt{2\pi r}}\cos\frac{\theta}{2} & \text{plane strain} \\ 0 & \text{generalized plane stress} \end{array} \right\} \tag{1.2}$$

and

$$\sigma_{13} = \sigma_{23} = 0 \tag{1.3}$$

where σ_{ij} $(i, j = 1, 2, 3)$ are the stress components corresponding to Fig. 1.2 and ν is Poisson's ratio.

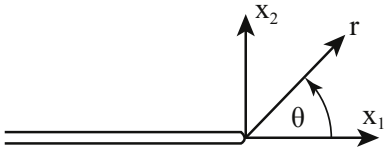

Figure 1.2: Cartesian and polar coordinates systems emanating from the crack tip.

In eqs. (1.1) to (1.3), K_I is the stress intensity factor for mode I and r and θ are polar coordinates emanating from the crack tip as shown in Fig. 1.2.

The first term of the asymptotic expansion for the displacement field for mode I is given as

$$\left\{ \begin{array}{c} u_1 \\ u_2 \end{array} \right\} = \frac{K_I}{2\mu}\sqrt{\frac{r}{2\pi}} \left\{ \begin{array}{c} \cos\frac{\theta}{2}\left(\kappa - 1 + 2\sin^2\frac{\theta}{2}\right) \\ \sin\frac{\theta}{2}\left(\kappa + 1 - 2\cos^2\frac{\theta}{2}\right) \end{array} \right\} \tag{1.4}$$

and

$$u_3 = 0 \tag{1.5}$$

where u_i $(i = 1, 2, 3)$ are the displacement components in the x_1, x_2 and x_3-directions, respectively; μ is the shear modulus and

$$\kappa = \left\{ \begin{array}{ll} 3 - 4\nu\,, & \text{plane strain} \\ \dfrac{3-\nu}{1+\nu}\,, & \text{generalized plane stress.} \end{array} \right. \tag{1.6}$$

For mode II, the first term of the asymptotic expansion for the stress and displacement components are given as

$$\left\{ \begin{array}{c} \sigma_{11} \\ \sigma_{12} \\ \sigma_{22} \end{array} \right\} = \frac{K_{II}}{\sqrt{2\pi r}} \left\{ \begin{array}{c} -\sin\frac{\theta}{2}\left(2 + \cos\frac{\theta}{2}\cos\frac{3\theta}{2}\right) \\ \cos\frac{\theta}{2}\left(1 - \sin\frac{\theta}{2}\sin\frac{3\theta}{2}\right) \\ \sin\frac{\theta}{2}\cos\frac{\theta}{2}\cos\frac{3\theta}{2} \end{array} \right\}, \tag{1.7}$$

$$\sigma_{33} = \left\{ \begin{array}{cl} -2\nu\dfrac{K_{II}}{\sqrt{2\pi r}}\sin\dfrac{\theta}{2} & \text{plane strain} \\ 0 & \text{generalized plane stress} \end{array} \right\}, \tag{1.8}$$

$$\sigma_{13} = \sigma_{23} = 0, \tag{1.9}$$

$$\left\{ \begin{array}{c} u_1 \\ u_2 \end{array} \right\} = \frac{K_{II}}{2\mu}\sqrt{\frac{r}{2\pi}} \left\{ \begin{array}{c} \sin\frac{\theta}{2}\left(\kappa + 1 + 2\cos^2\frac{\theta}{2}\right) \\ -\cos\frac{\theta}{2}\left(\kappa - 1 - 2\sin^2\frac{\theta}{2}\right) \end{array} \right\} \tag{1.10}$$

and

$$u_3 = 0. \tag{1.11}$$

In eqs. (1.7) to (1.11), K_{II} is the stress intensity factor for mode II.

For mode III, the first term of the asymptotic expansion for the stress and displacement components are given as

$$\left\{ \begin{array}{c} \sigma_{13} \\ \\ \sigma_{23} \end{array} \right\} = \frac{K_{III}}{\sqrt{2\pi r}} \left\{ \begin{array}{c} -\sin\dfrac{\theta}{2} \\ \\ \cos\dfrac{\theta}{2} \end{array} \right\}, \tag{1.12}$$

$$\sigma_{11} = \sigma_{22} = \sigma_{33} = \sigma_{12} = 0, \tag{1.13}$$

$$u_3 = 2\frac{K_{III}}{\mu}\sqrt{\frac{r}{2\pi}}\sin\frac{\theta}{2} \tag{1.14}$$

and

$$u_1 = u_2 = 0 \tag{1.15}$$

In eqs. (1.12) to (1.15), K_{III} is the stress intensity factor for mode III.

Irwin (1958) found the relation between the stress intensity factors and $\mathcal{G}_T$, the total energy release rate, given as

$$\mathcal{G}_T = \begin{cases} \dfrac{1}{\bar{E}}\left(K_I^2 + K_{II}^2\right) + \dfrac{1}{2\mu}K_{III}^2\,, & \text{plane strain} \\ \dfrac{1}{\bar{E}}\left(K_I^2 + K_{II}^2\right)\,, & \text{generalized plane stress} \end{cases} \tag{1.16}$$

In eq. (1.16), $\bar{E}$ is given by

$$\frac{1}{\bar{E}} = \begin{cases} \dfrac{1-\nu^2}{E}\,, & \text{plane strain} \\ \dfrac{1}{E}\,, & \text{generalized plane stress.} \end{cases} \tag{1.17}$$

where E is Young's modulus. The energy release rate is the energy that is required to extend the crack by a length Δa.

The stress intensity factors are the amplitude of the singularity at the crack tip and are a function of the applied load and geometry.

The total energy release rate may be separated into three components according to the three deformation modes given as

$$\mathcal{G}_T = \mathcal{G}_I + \mathcal{G}_{II} + \mathcal{G}_{III}, \tag{1.18}$$

where

$$\mathcal{G}_I = \frac{1}{\bar{E}}K_I^2, \tag{1.19}$$

$$\mathcal{G}_{II} = \frac{1}{\bar{E}}K_{II}^2 \tag{1.20}$$

and

$$\mathcal{G}_{III} = \frac{K_{III}^2}{2\mu}. \tag{1.21}$$

The in-plane energy release rate is given as

$$\mathcal{G}_{2D} = \mathcal{G}_I + \mathcal{G}_{II}. \tag{1.22}$$

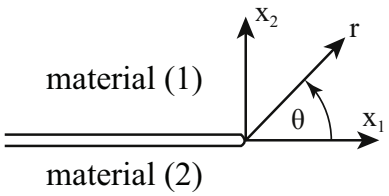

Figure 1.3: Interface crack between two dissimilar materials.

1.2 Interface crack between two isotropic materials

In Fig. 1.3, a crack along an interface between two dissimilar materials is presented. Williams (1959) investigated this problem for two dissimilar linear elastic, homogenous and isotropic materials and found the stress and displacement fields around the crack tip. The dependence of those fields on distance from the crack tip r, was shown to be

$$\sigma \propto r^{-\frac{1}{2}} \left\{ \begin{array}{c} \sin\left(\varepsilon \ln r\right) \\ \cos\left(\varepsilon \ln r\right) \end{array} \right\} \tag{1.23}$$

and

$$u \propto r^{\frac{1}{2}} \left\{ \begin{array}{c} \sin\left(\varepsilon \ln r\right) \\ \cos\left(\varepsilon \ln r\right) \end{array} \right\}. \tag{1.24}$$

The geometry of the problem and the coordinates are shown in Fig. 1.3, and ε, the oscillatory parameter, is given as

$$\varepsilon = \frac{1}{2\pi} \ln\left(\frac{\kappa_1 \mu_2 + \mu_1}{\kappa_2 \mu_1 + \mu_2}\right). \tag{1.25}$$

In eq. (1.25), the subscript $k = 1, 2$ denotes the upper and lower materials, respectively, as shown in Fig. 1.3, μ_k are the shear moduli,

$$\kappa_k = \left\{ \begin{array}{ll} 3 - 4\nu_k \,, & \text{plane strain} \\ \dfrac{3 - \nu_k}{1 + \nu_k} \,, & \text{generalized plane stress} \end{array} \right. \tag{1.26}$$

and ν_k are the Poisson's ratios. Near the crack tip, the asymptotic displacement field shows interpenetration between the upper and lower crack faces which is not realistic.

An interface crack between two isotropic materials was considered by Comninou (1977, 1978) and Comninou and Schmueser (1979). Three regions along the interface and the crack faces were assumed. In the first region, continuity of the traction and displacement components was enforced. In the next region, there is frictionless contact. In the last region, the crack faces are free from traction. Comninou (1977) considered an infinite body containing a finite length crack along the interface. The body was loaded by far field tension normal to the crack faces. The contact length was normalized as s/a, where

s is the length of the contact zone and a is the half crack length. The normalized contact length s/a was found to be $O\left(10^{-4}\right)$ to $O\left(10^{-7}\right)$, depending on the mechanical properties. Thus, for applied tension, the contact zone is very small. For the same infinite body, loaded with far field shear, Comninou (1978) found that for the side of the crack where the shear stress is positive, s/a can reach 0.66. On the other side of the crack, s/a was found to be less than $O\left(10^{-7}\right)$. Again, the value of s/a depends on the mechanical properties. It may be pointed out that $s/a = 0.66$ is its greatest value.

Those investigations led to a return to the singular stress solution determined by Williams (1959), Erdogan (1965), England (1965) and Rice and Sih (1965). In Rice (1988), an approximate expression for the interpenetration zone length was found. It is given by

$$r_c = \hat{L} \exp\left\{\frac{1}{\varepsilon}\left[-\left(\frac{\pi}{2} + \hat{\psi}\right) + \tan^{-1} 2\varepsilon\right]\right\} \tag{1.27}$$

where r_c is the length of the interpenetration zone, $\hat{L}$ is an arbitrary length scale, $\varepsilon > 0$ and is the oscillatory parameter given in eq. (1.25) and $\hat{\psi}$ is the normalized phase angle given as

$$\hat{\psi} = \tan^{-1}\left[\frac{\Im(K\hat{L}^{i\varepsilon})}{\Re(K\hat{L}^{i\varepsilon})}\right] = \tan^{-1}\left[\frac{\sigma_{21}}{\sigma_{22}}\right]\Bigg|_{\theta=0, r=\hat{L}} . \tag{1.28}$$

In eq. (1.28), $\Re$ and $\Im$ denote the real and imaginary parts, respectively, of the parameters in parentheses and K is the complex stress intensity factor given by

$$K = K_1 + iK_2. \tag{1.29}$$

In eq. (1.29), K_1 and K_2 are real and are the stress intensity factors for modes 1 and 2, respectively. Note that for an interface crack the stress intensity factors are not associated with modes I and II deformation. The units of K are $FL^{-i\varepsilon/L^{3/2}}$, where L denotes a length quantity and F denotes force. The complex stress intensity factor may be normalized as

$$\hat{K} = K\hat{L}^{i\varepsilon} . \tag{1.30}$$

The normalized stress intensity factor $\hat{K}$ has regular stress intensity factor units of $F/L^{3/2}$. It was prescribed by Rice (1988) that if the contact zone of Comninou or the interpenetration zone in eq. (1.27) may be included within a small scale nonlinear zone, then the singular crack tip solution may be used. Thus, it may be concluded that for large shear deformation, the singular formulation is questionable.

For an interface crack between two dissimilar isotropic materials, the in-plane stress field was presented in Rice et al. (1990). The in-plane stress field is given as

$${}_k\sigma_{\alpha\beta} = \frac{1}{\sqrt{2\pi r}}\left[\Re\left(Kr^{i\varepsilon}\right)\ {}_k\Sigma^{(1)}_{\alpha\beta}(\theta,\varepsilon) + \Im\left(Kr^{i\varepsilon}\right)\ {}_k\Sigma^{(2)}_{\alpha\beta}(\theta,\varepsilon)\right]. \tag{1.31}$$

In eq. (1.31), the subscripts $k = 1, 2$ denote the upper and lower materials, respectively, as shown in Fig. 1.3, $\alpha, \beta = 1, 2$ represent polar or Cartesian coordinates emanating from

the crack tip, as shown in Fig. 1.3; ε is defined in eq. (1.25) and K is the stress intensity factor given in eq. (1.29). The stress functions ${}_k\Sigma^{(1)}_{\alpha\beta}(\theta,\varepsilon)$ and ${}_k\Sigma^{(2)}_{\alpha\beta}(\theta,\varepsilon)$ are associated with the real and imaginary parts of $Kr^{i\varepsilon}$, respectively. These functions are given in Rice et al. (1990) and Deng (1993) for polar and Cartesian coordinates, respectively. For out-of-plane deformation, the stress components are given as

$$ {}_k\sigma_{\alpha 3} = \frac{K_{III}}{\sqrt{2\pi r}}\, {}_k\Sigma^{(III)}_{\alpha 3}(\theta) \tag{1.32} $$

where K_{III} is the mode III stress intensity factor and ${}_k\Sigma^{(III)}_{\alpha 3}(\theta)$ is a known function of θ given in Deng (1993). The stress intensity factor K_{III} has units of $F/L^{3/2}$. The stress functions ${}_k\Sigma^{(1)}_{\alpha\beta}(\theta,\varepsilon)$, ${}_k\Sigma^{(2)}_{\alpha\beta}(\theta,\varepsilon)$ and ${}_k\Sigma^{(III)}_{\alpha 3}(\theta)$ are dimensionless. The displacement field is given in Deng (1993) in Cartesian coordinates as

$$ {}_k u_\alpha = \sqrt{\frac{1}{2\pi r}}\left[\Re\left(Kr^{i\varepsilon}\right)\, {}_k U^{(1)}_\alpha(\theta) + \Im\left(Kr^{i\varepsilon}\right)\, {}_k U^{(2)}_\alpha(\theta)\right] \tag{1.33} $$

and

$$ {}_k u_3 = \sqrt{\frac{r}{2\pi}} K_{III}\, {}_k U^{(III)}_3(\theta), \tag{1.34} $$

where $\alpha = 1, 2$ and ${}_k U^{(1)}_\alpha(\theta)$, ${}_k U^{(2)}_\alpha(\theta)$ and ${}_k U^{(III)}_\alpha(\theta)$ are known functions of θ and have units of L^2/F.

Using the crack closure integral (Irwin, 1958), the relation between the interface energy release rate and the stress intensity factors was found as

$$ \mathcal{G}_i = \frac{1}{H_1}(K_1^2 + K_2^2) + \frac{1}{H_2} K_{III}^2, \tag{1.35} $$

where the subscript i represents interface. In eq. (1.35),

$$ \frac{1}{H_1} = \frac{1}{2\cosh^2 \pi\varepsilon}\left(\frac{1}{\bar{E}_1} + \frac{1}{\bar{E}_2}\right) \tag{1.36} $$

and

$$ \frac{1}{H_2} = \frac{1}{4}\left(\frac{1}{\mu_1} + \frac{1}{\mu_2}\right). \tag{1.37} $$

In eqs. (1.36) and (1.37), the subscripts $k = 1, 2$ represent the upper and lower materials, respectively; the parameters $\bar{E}_k$ are defined in eq. (1.17). Malyshev and Salganik (1965) were the first to develop the in-plane version of eq. (1.35). Note that for an interface crack, there are no explicit expressions for $\mathcal{G}_I$ and $\mathcal{G}_{II}$. The sum of $\mathcal{G}_I$ and $\mathcal{G}_{II}$ may be shown to be

$$ \mathcal{G}_I + \mathcal{G}_{II} = \frac{1}{H_1}(K_1^2 + K_2^2). \tag{1.38} $$

The parameter $\mathcal{G}_{III}$ is given by

$$ \mathcal{G}_{III} = \frac{1}{H_2} K_{III}^2. \tag{1.39} $$

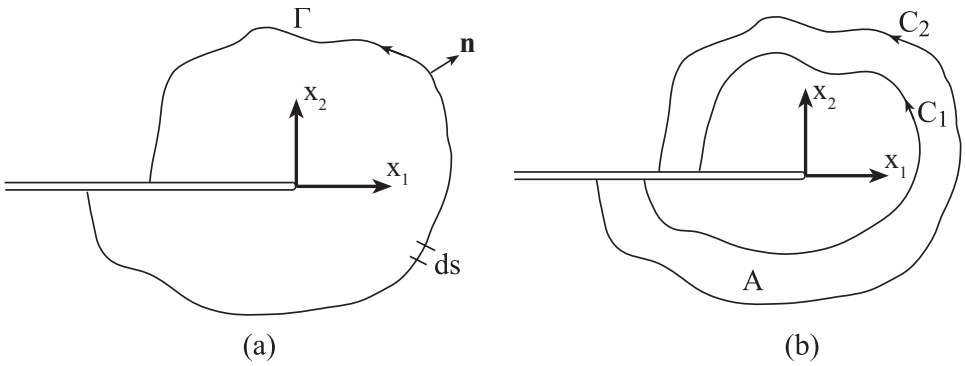

Figure 1.4: (a) A contour for the line J-integral and (b) an integration area for the area J-integral.

In addition to the phase angle in eq. (1.28), a second phase angle between K_1 and K_2 may be defined as

$$\psi = \arctan\left(\frac{K_2}{K_1}\right). \tag{1.40}$$

For three-dimensional problems, a third phase angle is defined as

$$\phi = \tan^{-1}\left[\sqrt{\frac{H_1}{2H_2}}\frac{K_{III}}{\sqrt{K_1^2+K_2^2}}\right] = \tan^{-1}\left[\sqrt{\frac{H_1}{2H_2}}\frac{\sigma_{23}}{\sqrt{\sigma_{22}^2+\sigma_{21}^2}}\right]\Bigg|_{\theta=0,r=\hat{L}}. \tag{1.41}$$

1.3 J- and M-integrals

The J-integral was first introduced by Rice (1968a) for two-dimensional elastic, homogeneous, isotropic, linear and non-linear materials and assuming small strain. The integral is given by

$$J = \int_\Gamma \left(W n_1 - T_i \frac{\partial u_i}{\partial x_1}\right)\, ds. \tag{1.42}$$

In eq. (1.42), Γ is a contour starting from the lower crack face and ending at the upper crack face as presented in Fig. 1.4a. The strain energy density for linear-elastic material is given by

$$W = \frac{1}{2}\sigma_{ij}\varepsilon_{ij}. \tag{1.43}$$

The parameter n_1 is the component of the outward normal to Γ in the x_1-direction; T_i is the traction given as

$$T_i = \sigma_{ij} n_j; \tag{1.44}$$

u_i are the displacement components and ds is differential arc length. The J-integral is independent of path on such a contour Γ.

In the same year, Rice (1968b) proved that the J-integral and the energy release rate are equal such that

$$J = \mathcal{G}. \tag{1.45}$$

By means of eqs. (1.16) and (1.45), J is related to the stress intensity factors; so that, the J-integral allows calculation of the sum of squares of the stress intensity factors. Thus, for pure mode problems, one may use the J-integral to determine a stress intensity factor. For mixed mode problems, the M-integral or interaction energy integral was developed which is presented below.

Using Green's theorem, the line J-integral may be transformed to an area integral. The area J-integral was presented by Li et al. (1985) as

$$J = \int_A \left(\sigma_{ij} \frac{\partial u_i}{\partial x_1} - W \delta_{1j} \right) \frac{\partial q_1}{\partial x_j} \, dA \tag{1.46}$$

where δ_{1j} is the Kronecker delta given by

$$\delta_{ij} = \begin{cases} 1 \, , & i = j \\ \\ 0 \, , & i \neq j \, , \end{cases} \tag{1.47}$$

q_1 is a sufficiently smooth function in the area A in Fig. 1.4 defined as

$$q_1 = \begin{cases} 1 \, , & \text{on } C_1 \\ \\ 0 \, , & \text{on } C_2 \, . \end{cases} \tag{1.48}$$

The parameter q_1 is a normalized virtual crack extension such that $q_1 \Delta a$ is the virtual crack extension. For further details the reader is referred to Banks-Sills (1991).

As mentioned previously, the interaction integral or M-integral was derived in order to calculate stress intensity factors for mixed mode problems. It was firstly introduced by Chen and Shield (1977) for linear elastic, homogenous and isotropic materials. In Yau et al. (1980), the first application of the integral for a homogeneous, isotropic material was presented. The integral was extended by Yau and Wang (1984) for an interface crack between two homogeneous, isotropic materials. A three-dimensional M-integral was first presented for a homogeneous isotropic material by Nakamura and Parks (1989); it was extended to dissimilar monoclinic materials by Freed and Banks-Sills (2005).

In Banks-Sills (2010), a review of the M-integral was presented for isotropic and anisotropic materials of two and three-dimensional mixed mode problems. The M-integral for a three-dimensional problem of a straight through crack in a homogeneous isotropic material is given in Banks-Sills (2010) as

$$M_N^{(1,2\alpha)} = \frac{1}{A_1} \int_V \left\{ \sigma_{ij}^{(1)} \frac{\partial u_i^{(2\alpha)}}{\partial x_1} + \sigma_{ij}^{(2\alpha)} \frac{\partial u_i^{(1)}}{\partial x_1} - W^{(1,2\alpha)} \delta_{1j} \right\} \frac{\partial q_1}{\partial x_j} \, dV. \tag{1.49}$$

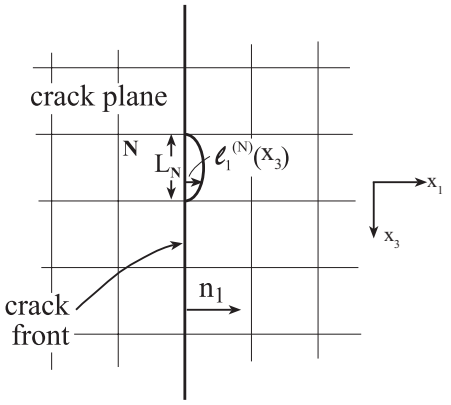

Figure 1.5: Virtual crack extension along the crack front denoted on the finite element mesh (from Banks-Sills, 2010).

In eq. (1.49), $M_N^{(1,2\alpha)}$ is the average value of $M^{(1,2\alpha)}$ for the N^{th} element along the crack front, the superscript $(1, 2\alpha)$ represents the sought after solution, 1, and the three auxiliary solutions $2\alpha = 2a, 2b, 2c$. The auxiliary solutions are obtained as the first term of the asymptotic solution for the material under consideration in this case, homogeneous and isotropic. Three sets of the stress intensity factors are substituted into these expressions which are

$$K_I^{(2a)} = 1, \quad K_{II}^{(2a)} = 0, \quad K_{III}^{(2a)} = 0, \tag{1.50}$$

$$K_I^{(2b)} = 0, \quad K_{II}^{(2b)} = 1, \quad K_{III}^{(2b)} = 0, \tag{1.51}$$

and

$$K_I^{(2c)} = 0, \quad K_{II}^{(2c)} = 0, \quad K_{III}^{(2c)} = 1. \tag{1.52}$$

In eq. (1.49), A_1 is defined as

$$A_1 = \int_0^{L_N} \ell_1^{(N)}(x_3) dx_3, \tag{1.53}$$

where $\ell_1^{(N)}(x_3)$ is the normalized virtual crack extension of element N in the x_1-direction as shown in Fig. 1.5; V is the volume of elements used in the finite element calculation. The cross-section of these elements is shown in grey in Fig. 1.6. The volume is one element

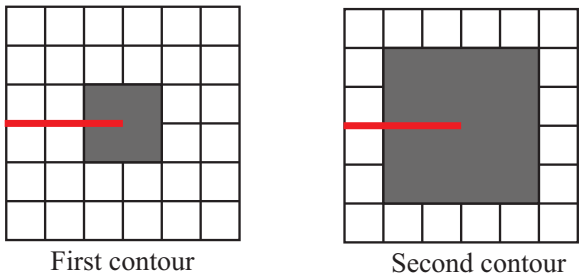

Figure 1.6: Cross-sectional view of the first and second domains for the M-integral.

thick; $i,j=1,2,3$; $W^{(1,2\alpha)}$ is the mutual strain energy density given by

$$W^{(1,2\alpha)}=\sigma_{ij}^{(1)}\varepsilon_{ij}^{(2\alpha)}=\sigma_{ij}^{(2\alpha)}\varepsilon_{ij}^{(1)}\ ; \tag{1.54}$$

q_1 is defined as

$$q_1=\sum_{m=1}^{20}N_m\left(\xi,\eta,\zeta\right)q_{1m}, \tag{1.55}$$

where $N_m\left(\xi,\eta,\zeta\right)$ are the shape functions of a twenty noded, isoparametric element and q_{1m} is a vector which preserves the distance between the nodes after a virtual crack extension.

On the other hand, in Banks-Sills (2010) it is shown that

$$M_N^{(1,2\alpha)}=\frac{2}{\bar{E}}\left[K_{I_N}^{(1)}K_{I_N}^{(2\alpha)}+K_{II_N}^{(1)}K_{II_N}^{(2\alpha)}\right]+\frac{1}{\mu}K_{III_N}^{(1)}K_{III_N}^{(2\alpha)}, \tag{1.56}$$

where $\bar{E}$ is defined in eq.(1.17) and μ is the shear modulus; K_{i_N} for $i=I,II,III$ are the stress intensity factors for the N^{th} element. By using the auxiliary solutions with eqs. (1.50) to (1.52) and substituting them into eqs. (1.49) and (1.56), the stress intensity factors for the N^{th} element are given by

$$K_{I_N}^{(1)}=\frac{\bar{E}}{2A_1}\int_V\left\{\sigma_{ij}^{(1)}\frac{\partial u_i^{(2a)}}{\partial x_1}+\sigma_{ij}^{(2a)}\frac{\partial u_i^{(1)}}{\partial x_1}-W^{(1,2a)}\delta_{1j}\right\}\frac{\partial q_1}{\partial x_j}\,dV, \tag{1.57}$$

$$K_{II_N}^{(1)}=\frac{\bar{E}}{2A_1}\int_V\left\{\sigma_{ij}^{(1)}\frac{\partial u_i^{(2b)}}{\partial x_1}+\sigma_{ij}^{(2b)}\frac{\partial u_i^{(1)}}{\partial x_1}-W^{(1,2b)}\delta_{1j}\right\}\frac{\partial q_1}{\partial x_j}\,dV, \tag{1.58}$$

and

$$K_{III_N}^{(1)}=\frac{\mu}{A_1}\int_V\left\{\sigma_{ij}^{(1)}\frac{\partial u_i^{(2c)}}{\partial x_1}+\sigma_{ij}^{(2c)}\frac{\partial u_i^{(1)}}{\partial x_1}-W^{(1,2c)}\delta_{1j}\right\}\frac{\partial q_1}{\partial x_j}\,dV. \tag{1.59}$$

For further details, the reader is referred to Banks-Sills (2010).

For an interface crack between two different isotropic materials, eq. (1.49) is modified as

$$M_N^{(1,2\alpha)}=\frac{1}{A_1}\sum_{k=1}^{2}\int_{V_k}\left\{{}_k\sigma_{ij}^{(1)}\frac{\partial\,{}_ku_i^{(2\alpha)}}{\partial x_1}+\,{}_k\sigma_{ij}^{(2\alpha)}\frac{\partial\,{}_ku_i^{(1)}}{\partial x_1}-\,{}_kW^{(1,2\alpha)}\delta_{1j}\right\}\frac{\partial q_1}{\partial x_j}\,dV, \tag{1.60}$$

where the subscript $k=1,2$ denotes the upper and lower materials, respectively. On the other hand, the connection between the M-integral and the stress intensity factors is given by

$$M_N^{(1,2\alpha)}=\frac{2}{H_1}\left[K_{1_N}^{(1)}K_{1_N}^{(2\alpha)}+K_{2_N}^{(1)}K_{2_N}^{(2\alpha)}\right]+\frac{2}{H_2}K_{III_N}^{(1)}K_{III_N}^{(2\alpha)} \tag{1.61}$$

where H_1 and H_2 are defined for an interface crack between two isotropic materials in eqs. (1.36) and (1.37), respectively. The auxiliary solutions $2a,2b,2c$ for an interface crack are obtained from the first term of the asymptotic solution of the stress and displacement

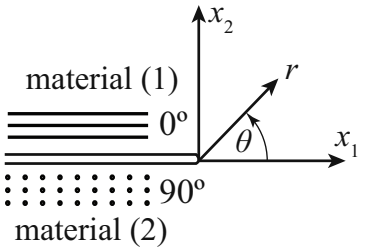

Figure 1.7: An interface crack between two dissimilar linear elastic, transversely isotropic and homogeneous materials.

fields with eqs. (1.50) to (1.52). By equating eqs. (1.60) and (1.61), with the use of eqs. (1.50) to (1.52) the stress intensity factors for the N^{th} element are found as

$$K_1^{(1)} = \frac{H_1}{2A_1}\sum_{k=1}^{2}\int_{V_k}\left[{}_k\sigma_{ij}^{(1)}\,\frac{\partial\,{}_k u_i^{(2a)}}{\partial x_1} + {}_k\sigma_{ij}^{(2a)}\,\frac{\partial\,{}_k u_i^{(1)}}{\partial x_1} - {}_k W^{(1,2a)}\delta_{1j}\right]\frac{\partial q_1}{\partial x_j}\,dV \quad (1.62)$$

$$K_2^{(1)} = \frac{H_1}{2A_1}\sum_{k=1}^{2}\int_{V_k}\left[{}_k\sigma_{ij}^{(1)}\,\frac{\partial\,{}_k u_i^{(2b)}}{\partial x_1} + {}_k\sigma_{ij}^{(2b)}\,\frac{\partial\,{}_k u_i^{(1)}}{\partial x_1} - {}_k W^{(1,2b)}\delta_{1j}\right]\frac{\partial q_1}{\partial x_j}\,dV \quad (1.63)$$

$$K_{III}^{(1)} = \frac{H_2}{2A_1}\sum_{k=1}^{2}\int_{V_k}\left[{}_k\sigma_{ij}^{(1)}\,\frac{\partial\,{}_k u_i^{(2c)}}{\partial x_1} + {}_k\sigma_{ij}^{(2c)}\,\frac{\partial\,{}_k u_i^{(1)}}{\partial x_1} - {}_k W^{(1,2c)}\delta_{1j}\right]\frac{\partial q_1}{\partial x_j}\,dV\,. \quad (1.64)$$

For some pairs of different anisotropic materials, the formulation in eqs. (1.60) and (1.61) may be used. For these pairs, the stress intensity factors are given in eqs. (1.62) to (1.64). For these two different anisotropic materials, H_1 and H_2 depend on the mechanical properties of each material and they are presented in Section 1.4. The asymptotic solution for an interface crack between some anisotropic materials, based on the Stroh (1958) and Lekhnitskii (1950) formalisms, is also presented in Section 1.4.

1.4 Stroh and Lekhnitskii Formalisms

In this investigation, an interface crack between two transversely isotropic and homogeneous materials, as shown in Fig. 1.7, is considered. The upper material is a unidirectional composite with fibers in the x_1- direction. The lower material is the same material as the upper one, rotated about the x_2-axis with fibers in the x_3- direction. Effective mechanical properties of graphite/epoxy AS4/3501-6 were used; the mechanical properties are shown in Table 1.1.

For an interface crack between two different anisotropic materials, the singularities and the eigenvalues take the form

$$\delta_{1,2} = -\frac{1}{2} \pm i\varepsilon \quad (1.65)$$

Table 1.1: Effective mechanical properties of graphite/epoxy AS4/3501-6 (Banks-Sills and Boniface, 2000).

E_A (GPa)	E_T (GPa)	ν_A	ν_T	G_A (GPa)
138.2	10.4	0.3	0.55	5.5

and

$$\delta_3 = -\frac{1}{2}. \tag{1.66}$$

So that, there is a square-root singularity and an oscillatory, square-root singularity. The oscillatory parameter ε is given in Ting (1996) by

$$\varepsilon = \frac{1}{2\pi} \ln\left(\frac{1+\beta}{1-\beta}\right) \tag{1.67}$$

where

$$\beta = \left[-\frac{1}{2}\mathrm{tr}\left(\breve{\mathbf{S}}\right)^2\right]^{1/2}. \tag{1.68}$$

In eq. (1.68), the 3×3 matrix $\breve{\mathbf{S}}$ is given as

$$\breve{\mathbf{S}} = \mathbf{D}^{-1}\mathbf{W}, \tag{1.69}$$

where

$$\mathbf{D} = \mathbf{L}_1^{-1} + \mathbf{L}_2^{-1}, \tag{1.70}$$

and

$$\mathbf{W} = \mathbf{S}_1\mathbf{L}_1^{-1} - \mathbf{S}_2\mathbf{L}_2^{-1}. \tag{1.71}$$

In eqs. (1.70) and (1.71), the subscripts 1 and 2 denote the upper and lower material, respectively; $\mathbf{S}_k$ and $\mathbf{L}_k$ are the Barnett-Lothe (1973) second rank tensors and are real; they may be calculated by using four 3×3 matrices $\mathbf{A}_k$ and $\mathbf{B}_k$ and the relation

$$-\mathbf{A}_k\mathbf{B}_k^{-1} = \mathbf{S}_k\mathbf{L}_k^{-1} + i\mathbf{L}_k^{-1} \tag{1.72}$$

where there is no summation on k.

The matrices $\mathbf{A}_k$ and $\mathbf{B}_k$, are known and depend upon the mechanical properties and the orientation of the transversely isotropic material. For the interface considered, the matrices are given explicitly in Banks-Sills and Boniface (2000). The stress and displacement functions $\boldsymbol{\phi}$ and $\mathbf{u}$ are also presented in Banks-Sills and Boniface (2000). To obtain the stress components, the stress function vector is differentiated as

$$\sigma_{i1} = -\phi_{i,2} \qquad \sigma_{i2} = \phi_{i,1} \tag{1.73}$$

where $i = 1, 2, 3$.

For the interface considered in this investigation, the in-plane stresses in the neighborhood of the crack tip are given by

$$ {}_k\sigma_{\alpha\beta} = \frac{1}{\sqrt{2\pi r}} \left[\Re \left(K r^{i\varepsilon} \right) {}_k\Sigma^{(1)}_{\alpha\beta}(\theta) + \Im \left(K r^{i\varepsilon} \right) {}_k\Sigma^{(2)}_{\alpha\beta}(\theta) \right] \tag{1.74} $$

where $k = 1, 2$ denotes the upper and the lower materials, respectively; $\alpha, \beta = 1, 2$ represent polar or Cartesian coordinates; $\Re$ and $\Im$ represent the real and imaginary parts of the expression in parentheses, respectively. Explicit expressions for the stresses are given in Banks-Sills and Boniface (2000).

For plane deformation, the tractions ahead of the crack tip along the interface and the crack face displacement jumps are given as (Banks-Sills and Boniface, 2000)

$$ \left(\sqrt{\frac{D_{22}}{D_{11}}} \sigma_{yy} + i \sigma_{yx} \right) \Bigg|_{\theta=0} = \frac{K x_1^{i\varepsilon}}{\sqrt{2\pi x_1}} \tag{1.75} $$

and

$$ \sqrt{\frac{D_{11}}{D_{22}}} \Delta u_2 + i \Delta u_1 = \frac{2 D_{11}}{(1 + 2i\varepsilon) \cosh \pi\varepsilon} \sqrt{\frac{\Delta a - x_1}{2\pi}} \, (\Delta a - x_1)^{i\varepsilon} K \, . \tag{1.76} $$

respectively, where the coordinate system is shown in Fig. 1.7. In eqs. (1.75) and (1.76), D_{11} and D_{22} are taken from the matrix $\mathbf{D}$ given in eq. (1.70), ε is defined in eq. (1.67) and the complex stress intensity factor K is defined in eq. (1.29). In Chapters 2 and 3, the VCCT is presented for two and three-dimensional problems, respectively. In order to develop the method for the interface considered, eqs. (1.75) and (1.76) will be used.

1.5 Clifford algebra

Consider a planar crack in a three-dimensional body. Using the Stroh (1958) and Lekhnitskii (1950) formalisms for these problems, the assumption of plane deformation is made. This is a good assumption for an internal crack. For one which intersects a free surface, this is only an approximation. In order to solve this problem without this assumption, another formalism is required. In Liu and Hong (2015), a derivation of Clifford algebra (Clifford, 1873) that may be used for solving three-dimensional problems of anisotropic materials is presented. In this investigation, this derivation will be extended to solve uniform stress problems. Several cases are considered. It may be extended further for solution of the three-dimensional problem of an ellipsoidal void or rigid inclusion. The basic ideas of Clifford algebra for $\mathbb{R}^3$ (three-dimensional space) are presented in this section.

Clifford algebra is based upon quaternions (Hamilton, 1844) and exterior algebra (Grassmann, 1844). A quaternion is an extension of complex numbers given as

$$ q = a_0 + a_1 i + a_2 j + a_3 k, \tag{1.77} $$

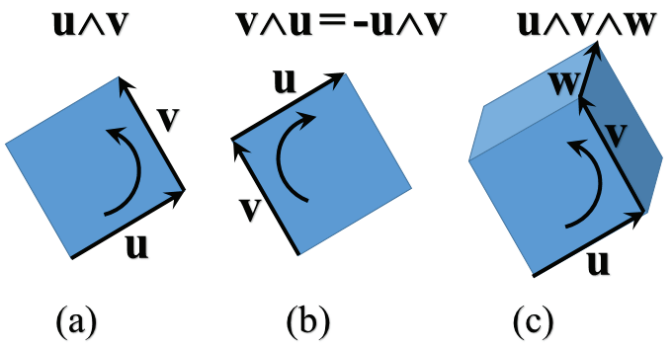

Figure 1.8: Bivectors of (a) $\mathbf{u} \wedge \mathbf{v}$ and (b) $\mathbf{v} \wedge \mathbf{u}$ and (c) a trivector $\mathbf{u} \wedge \mathbf{v} \wedge \mathbf{w}$.

where a_i for $i = 0, .., 3$ are real numbers. The constant a_0 is the real part of the quaternion and $a_1 i + a_2 j + a_3 k$ is the imaginary part. The values of i, j and k are $i = j = k = \sqrt{-1}$ and the multiplication between them is given in Table 1.2.

The exterior algebra presented in Grassmann (1844) defines bivectors and trivectors that are created using the exterior product. The exterior product between two vectors is the area of the parallelogram defined by them with the orientation of the area, as shown in Fig. 1.8a for $\mathbf{u} \wedge \mathbf{v}$, where $\mathbf{u}$ and $\mathbf{v}$ are vectors and $\wedge$ is the symbol for an exterior product denoted as wedge. The orientation is determined as the first vector is swept toward the second one. Note that $\mathbf{v} \wedge \mathbf{u} = -\mathbf{u} \wedge \mathbf{v}$, since the orientation is reversed, as presented in Fig. 1.8b. Clearly, $\mathbf{u} \wedge \mathbf{u} = 0$, since the area of the parallelogram is zero. The exterior product of three vectors $\mathbf{u} \wedge \mathbf{v} \wedge \mathbf{w}$ is the volume of the parallelepiped that they define with its orientation determined by the bivector $\mathbf{u} \wedge \mathbf{v}$ as shown in Fig. 1.8c.

The sybolism $C\ell_3(\mathbb{R})$ is used where $C\ell$ is Clifford algebra, the subscript 3 denotes grade 3 of Clifford algebra and $\mathbb{R}$ represents the set of real numbers. The basic elements of $C\ell_3(\mathbb{R})$ are scalars (grade 0), vectors (grade 1), bivectors (grade 2) and trivectors (grade 3). Thus, a Clifford number, sometimes called a multivector, in $C\ell_3(\mathbb{R})$ is given as

$$a = a_0 + a_1\mathbf{e}_1 + a_2\mathbf{e}_2 + a_3\mathbf{e}_3 + a_4 e_{23} + a_5 e_{31} + a_6 e_{12} + a_7 e_{123}, \tag{1.78}$$

Table 1.2: Multiplication table of quaternions.

$\times$	1	i	j	k
1	1	i	j	k
i	i	-1	k	$-j$
j	j	$-k$	-1	i
k	k	j	$-i$	-1

Table 1.3: Multiplication table of reduced biquaternions.

$\times$	1	e	i	ie
1	1	e	i	ie
e	e	1	i	ie
i	i	ie	-1	$-e$
ie	ie	i	$-e$	1

where a_i for $i = 0...7$ are real scalars, $\mathbf{e}_1$, $\mathbf{e}_2$ and $\mathbf{e}_3$ are the orthonormal unit base vectors of $\mathbb{R}^3$, e_{23}, e_{31} and e_{12} are bivectors and e_{123} is a trivector.

Clifford algebra extends the ideas of exterior algebra such that multiplication between two vectors is defined as

$$\mathbf{a}\ \mathbf{b} = \mathbf{a} \cdot \mathbf{b} + \mathbf{a} \wedge \mathbf{b}, \tag{1.79}$$

where $\cdot$ is the usual dot product. It may be noted that $\mathbf{a}\ \mathbf{b}$ is a bivector. Bivectors and trivectors are not multiplied. The multiplication rule of the Clifford algebra used in this investigation for two unit vectors (grade 1) yielding a bivector (grade 2) is given by

$$\mathbf{e}_i\mathbf{e}_j = \begin{cases} 1 \ , & i = j \\ -\mathbf{e}_j\mathbf{e}_i \ , & i \neq j \end{cases} , \tag{1.80}$$

where $i, j = 1, 2, 3$. Using eq. (1.79),

$$e_{23} = \mathbf{e}_2 \wedge \mathbf{e}_3, \qquad e_{31} = \mathbf{e}_3 \wedge \mathbf{e}_1, \qquad e_{12} = \mathbf{e}_1 \wedge \mathbf{e}_2 \ , \tag{1.81}$$

since $\mathbf{e}_i \cdot \mathbf{e}_j = 0$ for $i \neq j$. The trivector in eq. (1.78), arising from the three unit vectors, is given by

$$e_{123} = \mathbf{e}_1 \wedge \mathbf{e}_2 \wedge \mathbf{e}_3 \ , \tag{1.82}$$

which is unity with the orientation of $\mathbf{e}_1 \wedge \mathbf{e}_2$.

In Liu and Hong (2015), it is suggested to use reduced biquaternions which use the basis 1, e, i and ei. The multiplication between these coefficients for this basis is given in Table 1.3.

The eigenvalue problem for a three-dimensional anisotropic material was derived in Liu and Hong (2015). This derivation is presented next. In order to develop the eigenvalue problem, the stress-strain law is given by

$$\sigma_{ij} = C_{ijkl}\epsilon_{kl} \ , \tag{1.83}$$

where $i, j, k, l = 1, 2, 3$ and repeated indices obey the summation convention. Equation (1.83) may be rewritten using the strain-displacement equations

$$\epsilon_{ij} = \frac{1}{2}\left(\frac{\partial u_i}{\partial x_j} + \frac{\partial u_j}{\partial x_i}\right) \tag{1.84}$$

so that

$$\sigma_{ij} = C_{ijkl}\frac{\partial}{\partial x_l}u_k \ . \tag{1.85}$$

The stiffness tensor C satisfies the symmetry conditions

$$C_{ijkl} = C_{klij} \ , C_{ijkl} = C_{jikl} \ , C_{ijkl} = C_{ijlk} \ . \tag{1.86}$$

The equilibrium equations are given as

$$\frac{\partial \sigma_{ji}}{\partial x_j} = 0 \ . \tag{1.87}$$

The governing equations of anisotropic elasticity are derived by substituting eq. (1.85) into eq. (1.87) and noting that $\sigma_{ji} = \sigma_{ij}$ as

$$C_{ijkl}\frac{\partial}{\partial x_j}\frac{\partial}{\partial x_l}u_k = 0 \ . \tag{1.88}$$

Next, the displacements are defined as a function of the coordinates x_1, x_2 and x_3 as

$$u_k = a_k f(y) \ , \tag{1.89}$$

where $k = 1, 2, 3$, a_k are unknown constants to be determined, $f(y)$ is an arbitrary function and

$$y = P_{11}x_1 + P_{12}x_2 + P_{13}x_3. \tag{1.90}$$

In eq. (1.90), P_{1j} for $j = 1, 2, 3$ are quaternions that will be defined in the sequel. It may be noted that the relation in eq. (1.89) will be defined more precisely in Section 4.3. Substituting eq. (1.89) into the governing equations in eq. (1.88) results in

$$C_{ijkl}P_{1j}P_{1l}a_k f''(y) = 0 \ , \tag{1.91}$$

summation is used on repeated indices, and the prime denotes differentiation with respect to the argument y. Since $f''(y)$ is not identically zero,

$$C_{ijkl}P_{1j}P_{1l}a_k = 0 \ . \tag{1.92}$$

The non-trivial solution for a_k must satisfy

$$\det\left(C_{ijkl}P_{1j}P_{1l}\right) = 0 \ . \tag{1.93}$$

For completeness, eq. (1.92) is given by

$$\begin{aligned}
&(\mathbf{C}_{11}P_{11}^2 + \mathbf{C}_{12}P_{11}P_{12} + \mathbf{C}_{13}P_{11}P_{13} \\
&+\mathbf{C}_{21}P_{12}P_{11} + \mathbf{C}_{22}P_{12}^2 + \mathbf{C}_{23}P_{12}P_{13} \\
&+\mathbf{C}_{31}P_{13}P_{11} + \mathbf{C}_{32}P_{13}P_{11} + \mathbf{C}_{33}P_{13}^2)\,\mathbf{a}_{3\times 1} = \mathbf{0}_{3\times 1} \ ,
\end{aligned} \tag{1.94}$$

where $\mathbf{C}_{jl}$ are 3×3 matrices given by

$$\begin{aligned}
(\mathbf{C}_{11})_{ik} &= C_{i1k1} \ , \quad (\mathbf{C}_{12})_{ik} = C_{i1k2} \ , \quad (\mathbf{C}_{13})_{ik} = C_{i1k3} \ , \\
(\mathbf{C}_{21})_{ik} &= C_{i2k1} \ , \quad (\mathbf{C}_{22})_{ik} = C_{i2k2} \ , \quad (\mathbf{C}_{23})_{ik} = C_{i2k3} \ , \\
(\mathbf{C}_{31})_{ik} &= C_{i3k1} \ , \quad (\mathbf{C}_{32})_{ik} = C_{i3k2} \ , \quad (\mathbf{C}_{33})_{ik} = C_{i3k3} \ ,
\end{aligned} \tag{1.95}$$

and the vector $\mathbf{a}$ is composed of the constants a_k in eq. (1.92). For example, the matrix $\mathbf{C}_{11}$ is given as

$$\begin{bmatrix} C_{1111} & C_{1121} & C_{1131} \\ C_{2111} & C_{2121} & C_{2131} \\ C_{3111} & C_{3121} & C_{3131} \end{bmatrix} . \tag{1.96}$$

Equation (1.94) is the eigenvalue problem of the anisotropic elasticity problem. This equation may be rewritten as

$$(\mathbf{N}_1 + P_{12}\mathbf{N}_2 + P_{13}\mathbf{N}_3)\mathbf{d} = \mathbf{0} \ , \tag{1.97}$$

where, without lost of generality, setting P_{11} to unity, and

$$\mathbf{N}_1 = \begin{bmatrix} \mathbf{C}_{11} & 0 & 0 \\ \mathbf{C}_{21} & -\mathbf{I} & 0 \\ \mathbf{C}_{31} & 0 & -\mathbf{I} \end{bmatrix} , \mathbf{N}_2 = \begin{bmatrix} \mathbf{C}_{12} & \mathbf{I} & 0 \\ \mathbf{C}_{22} & 0 & 0 \\ \mathbf{C}_{32} & 0 & 0 \end{bmatrix} , \ \mathbf{N}_3 = \begin{bmatrix} \mathbf{C}_{13} & 0 & \mathbf{I} \\ \mathbf{C}_{23} & 0 & 0 \\ \mathbf{C}_{33} & 0 & 0 \end{bmatrix} . \tag{1.98}$$

In eq. (1.97), the vector $\mathbf{d}_{9\times 1}$ is defined as

$$\mathbf{d} = \begin{bmatrix} \mathbf{a} \\ \mathbf{b} \\ \mathbf{g} \end{bmatrix} , \tag{1.99}$$

where

$$\mathbf{b} = (\mathbf{C}_{21} + P_{12}\mathbf{C}_{22} + P_{13}\mathbf{C}_{23})\mathbf{a} \ , \tag{1.100}$$

$$\mathbf{g} = (\mathbf{C}_{31} + P_{12}\mathbf{C}_{32} + P_{13}\mathbf{C}_{33})\mathbf{a} \ . \tag{1.101}$$

Equation (1.97) allows solution of three-dimensional problems for anisotropic materials. The eigenvector is $\mathbf{d}$, defined in eq. (1.99), and the eigenvalues are P_{12} and P_{13} which are determined from

$$\det(\mathbf{N}_1 + P_{12}\mathbf{N}_2 + P_{13}\mathbf{N}_3) = 0. \tag{1.102}$$

One of the issues will be to determine the function $f(y)$. Simple problems will be pursued before attempting to solve a crack problem.

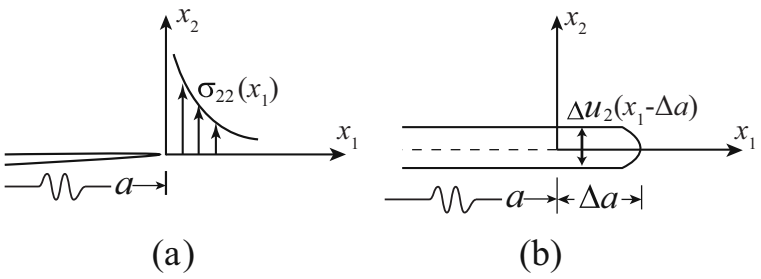

Figure 1.9: (a) Crack of length a and (b) crack of length $a + \Delta a$.

1.6 Virtual crack closure technique (VCCT)

In this section, the virtual crack closure technique (VCCT), first presented by Rybicki and Kanninen (1977) for two dimensions, is described. In addition, this method is presented for three dimensions relying on papers in which it was extended. In Section 1.6.1, the calculation of the energy release rates for the three deformation modes using the VCCT is discussed. The equations needed in order to extract the stress intensity factors from the calculated energy release rates are presented is Section 1.6.2

1.6.1 Calculation of the energy release rates using the virtual crack closure technique

The Irwin (1958) crack closure integral is given in three dimensions as

$$\mathcal{G} = \lim_{\Delta a \to 0} \frac{1}{2\Delta a} \int_0^{\Delta a} [\sigma_{22}(x_1)\Delta u_2(\Delta a - x_1) + \sigma_{21}(x_1)\Delta u_1(\Delta a - x_1) + \sigma_{33}(x_1)\Delta u_3(\Delta a - x_1)]\, dx_1. \tag{1.103}$$

The energy release rate is calculated from this integral as the work done to close a crack which underwent a virtual crack extension of length Δa as shown in Fig. 1.9b. The tractions ahead of the crack tip as illustrated in Fig. 1.9a for σ_{22} are applied in the opposite direction in order to close the extended crack whose displacement is Δu_2. The displacement in the x_2-direction is shown in Fig. 1.9b. Equation (1.103) may be separated into three equations as

$$\mathcal{G}_I = \lim_{\Delta a \to 0} \frac{1}{2\Delta a} \int_0^{\Delta a} [\sigma_{22}(x_1)\Delta u_2(\Delta a - x_1)]\, dx_1, \tag{1.104}$$

$$\mathcal{G}_{II} = \lim_{\Delta a \to 0} \frac{1}{2\Delta a} \int_0^{\Delta a} [\sigma_{21}(x_1)\Delta u_1(\Delta a - x_1)]\, dx_1 \tag{1.105}$$

and

$$\mathcal{G}_{III} = \lim_{\Delta a \to 0} \frac{1}{2\Delta a} \int_0^{\Delta a} [\sigma_{23}(x_1)\Delta u_3(\Delta a - x_1)]\, dx_1. \tag{1.106}$$

The energy release rates for the three deformation modes, mode I, II and III, respectively, may be calculated by means of eqs. (1.104) to (1.106).

Equations (1.104) to (1.106) should be calculated numerically with two finite elements analyses. The nodal point forces are used to approximate $\sigma_{22}(x_1)$, $\sigma_{21}(x_1)$ and $\sigma_{23}(x_1)$ for a crack of length a as presented in Fig. 1.9a for $\sigma_{22}(x_1)$ and in Figs. 1.10a and 1.10b for $F_2^{(m)}$; the second analysis provides values for $\Delta u_2(\Delta a - x_1)$, $\Delta u_1(\Delta a - x_1)$ and $\Delta u_3(\Delta a - x_1)$ for the extended crack as presented in Fig. 1.9b for $\Delta u_2(\Delta a - x_1)$. In Rybicki and Kanninen (1977), Ramamurthy et al. (1986) and Raju (1987), only one FEA for a crack of length a was carried out. The elements in the vicinity of the crack tip have the same length ℓ, as shown in Figs. 1.10a and 1.10b. An approximation is obtained for the displacement jumps from the element behind the virtual crack extension (VCE). This is reasonable when Δa is sufficiently small and ℓ is constant in all elements that participate in the calculations.

In Rybicki and Kanninen (1977), the integrals in eqs. (1.104) and (1.105) were calculated numerically using four-noded isoparametric elements. Use of higher order elements was first suggested in Ramamurthy et al. (1986) and Raju (1987). Analytical derivations were presented for VCCT with four-noded elements, eight-noded regular and singular elements, and twelve-noded regular and singular elements. The equations for calculating the modes I and II energy release rates using four-noded and eight-noded regular elements are given as

$$\mathcal{G}_I = \frac{1}{2\Delta a} \sum_{m=1}^{M} F_2^{(m)} \Delta u_2^{(m')} \tag{1.107}$$

$$\mathcal{G}_{II} = \frac{1}{2\Delta a} \sum_{m=1}^{M} F_1^{(m)} \Delta u_1^{(m')}. \tag{1.108}$$

In eqs. (1.107) and (1.108), for the nodal point forces $F_p^{(m)}$ and the displacement jumps $\Delta u_p^{(m')}$, the subscript represents the x_p-direction and the superscript denotes the node number as illustrated in Figs. 1.10a and 1.10b. For four-noded elements $M = 1$ and for eight-noded elements $M = 2$, as shown in Figs. 1.10a and 1.10b, respectively.

Numerical results were presented in Rybicki and Kanninen (1977) for double cantilever beam (DCB) and central crack (CC) specimens. Differences of up to 0.5% were obtained when compared to results obtained with the J-integral for $\Delta a/a < 0.1$. Poor results were achieved for larger values of Δa. If the lengths of the elements before and after the crack tip are different, eqs. (1.107) and (1.108) cannot be used. For this case, modified equations were derived in Rybicki and Kanninen (1977) and Krueger (2004) for four-noded elements.

As one may see from eq. (1.1), the stresses in the vicinity of the crack tip are square-root singular. Barsoum (1974) and Henshell and Shaw (1975) proposed a method for achieving this behavior using eight-noded quadrilateral elements; the former also suggested use of six and eight-noded triangular elements. In both cases, it was suggested to move the

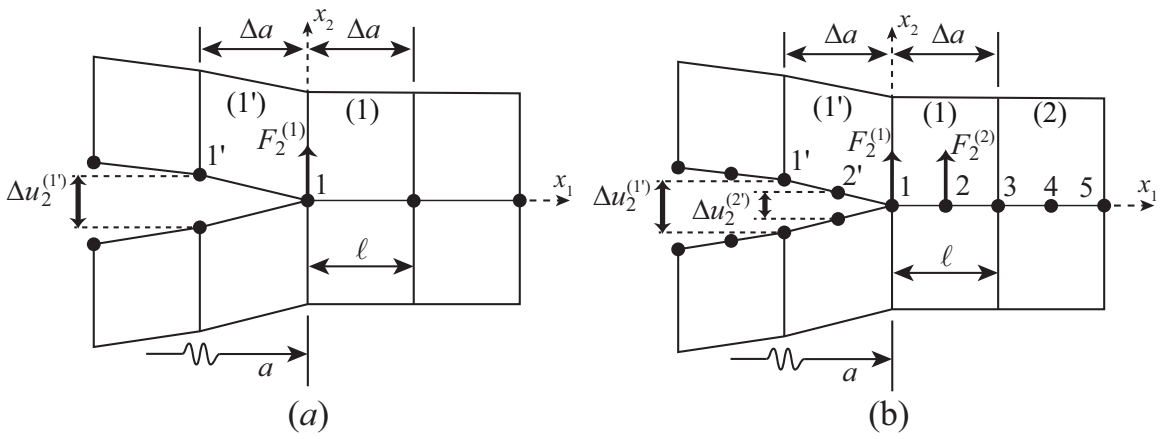

Figure 1.10: Nodal point forces and displacement jumps for (a) four-noded elements and (b) eight-noded elements for VCCT following Ramamurthy et al. (1986) and Raju (1987).

mid-side nodes on the edges of the element emanating from the crack tip to a quarter distance from the crack tip, as shown in Fig. 1.11a for a quadrilateral element. This element is called a quarter-point (QP) element. Henshell and Shaw (1975) showed that the stresses are square-root singular on these edges. In Banks-Sills and Bortman (1984), it was shown that the stresses are square-root singular on all rays emanating from the crack tip in a small region close to it, illustrated as the shaded area in Fig. 1.11b. It was shown also that a square quarter-point element captures the square-root singular stresses more accurately. For an interface crack, the stress singularity is in the form of $r^{-1/2+i\varepsilon}$. In Banks-Sills et al. (1999), it was shown that use of the quarter-point element leads to reliable results. In the three-dimensional case, a quarter-point element is achieved using a 20-noded element, as shown in Fig. 1.12. In Banks-Sills (1988), a proof for the singular behavior of the stresses in a quarter-point, 20-noded element is presented. The stresses are square-root singular on all rays emanating from the crack front in every x_1x_2-plane (orthogonal to the crack front), as presented in Fig. 1.11b.

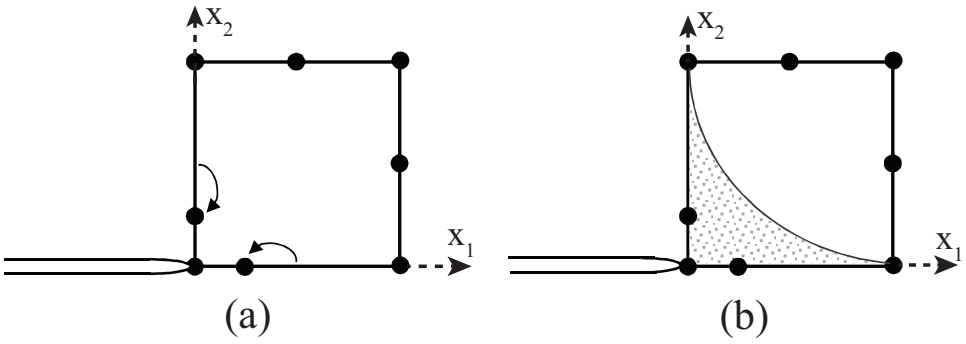

Figure 1.11: (a) Quarter-point element and (b) schematic description of the singularity area of it.

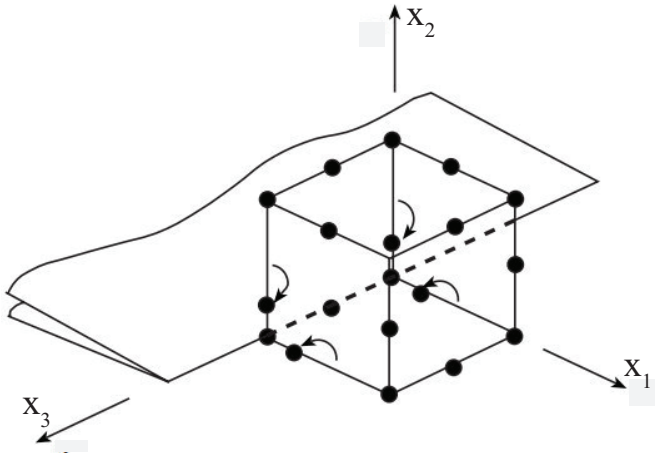

Figure 1.12: Quarter-point twenty-noded element.

The equations for calculating the modes I and II energy release rates using a quarter-point element are given by (Raju, 1987)

$$\mathcal{G}_I = \frac{1}{2\Delta a}\sum_{m=1}^{3}\sum_{n=1}^{3} t_{nm} F_2^{(n)} \Delta u_2^{(m')} \tag{1.109}$$

and

$$\mathcal{G}_{II} = \frac{1}{2\Delta a}\sum_{m=1}^{3}\sum_{n=1}^{3} t_{nm} F_1^{(n)} \Delta u_1^{(m')} \tag{1.110}$$

where

$$\begin{aligned} t_{11} &= 14 - \frac{66\pi}{16} \qquad t_{12} = -52 + \frac{264\pi}{16} \quad t_{13} = 39 - \frac{198\pi}{16} \\ t_{21} &= -3.5 + \frac{21\pi}{16} \quad t_{22} = 17 - \frac{84\pi}{16} \qquad t_{23} = -12.5 + \frac{63\pi}{16} \\ t_{31} &= 8 - \frac{42\pi}{16} \qquad t_{32} = -32 + \frac{168\pi}{16} \quad t_{33} = 25 - \frac{126\pi}{16}\,. \end{aligned} \tag{1.111}$$

The nodal point forces and displacement jumps in the x_2-direction from eq. (1.109) are presented in Fig. 1.13. In order to calculate the work done to close the crack extension Δa, points 2 and $2'$ should be the same distance from points 1 and $1'$, respectively. This case occurs in the four and eight-noded elements. Thus, each force corresponds to a displacement jump in the same relative position in adjoining elements as shown in Figs. 1.10a and 1.10b. In the QP-element, node $2'$ is located at $x_1(\text{node } 1') + 3\Delta a/4$, whereas, node 2 is located at $x_1(\text{node } 1) + \Delta a/4$. To overcome this problem, a derivation was carried out in Raju (1987) leading to eqs. (1.109) and (1.110) in which each nodal force is distributed at each of the displacement jumps, through the factors t_{ij}. Since the displacement jumps $u_1^{(3')}$ and $u_2^{(3')}$ are zero, the final equations for the QP element are given by

$$\mathcal{G}_I = \frac{1}{2\Delta a}\sum_{m=1}^{2}\sum_{n=1}^{3} t_{nm} F_2^{(n)} \Delta u_2^{(m')} \tag{1.112}$$

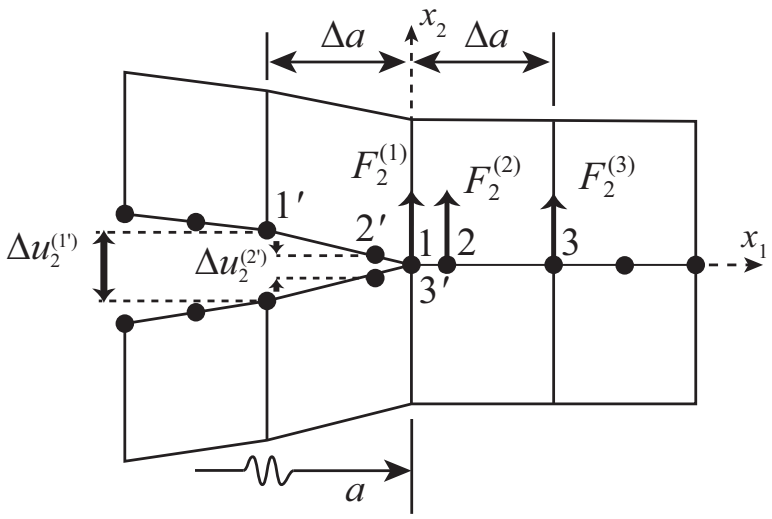

Figure 1.13: The nodal point forces and displacement jumps for VCCT using QP-elements.

and

$$\mathcal{G}_{II} = \frac{1}{2\Delta a} \sum_{m=1}^{2} \sum_{n=1}^{3} t_{nm} F_1^{(n)} \Delta u_1^{(m')} \tag{1.113}$$

where t_{ij} for $i = 1, 2, 3$ and $j = 1, 2$ are given in eqs. (1.111).

Numerical results were presented for a homogenous center cracked tension (CCT) specimen and an edged notched (EN) specimen, as well as an infinite body subjected to crack face pressure. The normalized crack tip element size for the interface crack was $\Delta a/a = 0.05$; for the former examples, it was $\Delta a/a = 0.0625$. This element size for the homogeneous problem should be sufficient to obtain good results. For the CCT specimen, the error with eight-noded elements was -3.0%; for that of the QP-elements, it was -1.7%. For the EN specimen, with eight-noded elements, the error was -10% and -6.5% with QP-elements. It is worth noting that the meshes exterior to the crack tip region were quite coarse. It may be recalled that this investigation was published in 1987. The larger errors for the EN specimen may be related to the large value of $a/W = 0.8$ where a is the crack length and W is specimen width. It is possible that there are errors in the comparative results. For the interface crack, only QP-elements were used with errors in $\mathcal{G}_i$ ranging from 0.9% to 5.2%. The finite element model was not sufficiently large to model well an infinite body and the comparative solution was numerical. For the homogenous bodies, the QP-elements produced more accurate results.

The VCCT uses two elements for the displacements jumps, element (1), presented in Fig. 1.14, and the element directly below it, which is not shown in Fig. 1.14. The forces are taken from the nodes in element (2), as shown in Fig. 1.14. The force $F_2^{(1)}$ in the x_2-direction is the sum of $F_2^{(1L)}$ and $F_2^{(1R)}$, where $F_2^{(1L)}$ and $F_2^{(1R)}$ are the forces which are determined from elements (1) and (2), respectively. The superscripts L and R denote the left and right sides, respectively, of node 1. Similarly, the force $F_2^{(3)}$ is the sum of $F_2^{(3L)}$

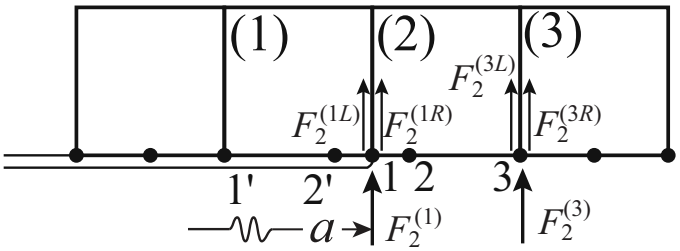

Figure 1.14: The forces obtained at nodes 1 and 3 from the finite elements analysis.

and $F_2^{(3R)}$. The force in node 2, $F_2^{(2)}$, is not shown in Fig. 1.14. It was pointed out in Narayana et al. (1990) with an excellent discussion in Narayana and Dattaguru (1996), that for the forces, only elements (1) and (2) should participate in the calculations. The same discussion applies to the forces and displacements in the x_1-direction. Thus, $F_i^{(3)}$, $i = 1, 2$, are calculated only from the nodal forces from element (2), i.e. only using $F_i^{(3L)}$. It was shown in Narayana and Dattaguru (1996), that by taking the nodal point forces only from elements $(1')$ and (1) and not from (2), the errors obtained in Sethuraman and Maiti (1988) and Pang et al. (1990) for the CCT specimen decreased from 5.9% to less than 1.6%. In Sethuraman and Maiti (1988), use was made of $F_i^{(3)}$. Results with up to a 7% error as compared to analytical solutions were obtained. Therefore, it was demonstrated that only $F_i^{(3L)}$ should be used in the calculations of the energy release rate. It may be noted that in Raju (1987), the nodal point forces were taken only from elements $(1')$ and (1).

In Nairn (2011), general expressions for the energy release rates were introduced for placing the mid-side node of an eight-noded element at an arbitrary location. In addition, the nodal point forces were replaced by nodal edge forces and the energy release rate results were extrapolated for values of $\Delta a \to 0$. For a DCB specimen, numerical results were obtained using eight-noded regular elements. This result was used for comparison. When using QP-elements and global nodal point forces with eqs. (1.109) and (1.110), differences of up to 2.8% were found. It may be noted that the nodal point force at node 3 in Fig. 1.14 was calculated from elements (2) and (3). When using QP-elements, nodal edge forces and extrapolation, the results differed by up to 0.44%. But plane stress elements with reduced integration were used. When using 3×3 integration points, as calculated here, a difference of -1.42% was found. Therefore, it is not possible to categorically recommend use of QP-elements. In fact, using the results from eight-noded regular elements as the standard for comparison in Nairn (2011) demonstrates that the premise that these elements produce the most accurate results appears to be supported. Although the numerical results for the energy release rates when using VCCT with QP-elements were not found to produce more accurate results than regular eight-noded elements, they have been used extensively (Jimenez and Miravete, 2004; Chen et al., 2005; Chiu et al., 2008; Chen et al., 2008; Chiu and Lin, 2009; Wahab, 2015; Peixoto and de Castro, 2016; Khaldi et al., 2016; Burlayenko

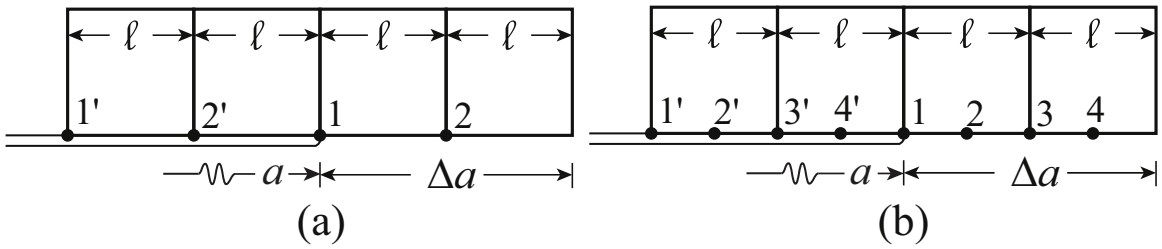

Figure 1.15: The elements used for calculation of the energy release rates when using two elements ahead and four elements behind the crack tip (the two lower elements not shown) for (a) four-noded and (b) eight-noded elements, using the approach of Beuth (1996).

et al., 2016; Salem et al., 2018 and Di Stasio and Ayadi, 2019).

Beuth (1996) and Oneida et al. (2015) suggested use of many elements to calculate energy release rates. In Banks-Sills and Farkash (2016), this method was implemented for an interface crack between two isotropic materials. The elements in the calculations are the same width ℓ, as shown in Fig. 1.15. The equations for calculating the modes I and II energy release rates are given in eqs. (1.107) and (1.108) where M is the number of nodes ahead of the crack tip that participate in the calculations. An example of the elements that are used for the calculation of the energy release rates when the virtual crack extension consists of two elements ahead of the crack tip, is presented in Figs. 1.15a and 1.15b, for four-noded and eight-noded elements, respectively. Note that for eight-noded elements, the number of nodes ahead of the crack tip that participates in the calculation, M, is even. No numerical comparisons were made in Beuth (1996). In Oneida et al. (2015), results were presented for an interface crack problem with errors of less than 0.65%, as compared to an analytical solution. Although eqs. (1.107) and (1.108) are for regular elements, QP-elements were used in the finite element analyses.

In Fig. 1.16a, an example for which the virtual crack extension consists of three elements ahead of the crack tip is illustrated. Elements (3') and (1) are QP-elements. The forces at the nodal points of element (i), $i = 1, 2, 3$, are used to close the displacement jumps at the nodal points of element (i'). In Fig. 1.16b, the primed elements were moved to the right in order to be below their corresponding elements. As may be observed, nodes $2'$ and $6'$ are not located below their corresponding nodes 2 and 6. A basic assumption in eqs. (1.107) and (1.108) is that force $F_p^{(m)}$, $m = 1, ..., M$ and $p = 1, 2$, closes the corresponding displacement jump $\Delta u_p^{(m')}$. When using QP-elements, this assumption does not hold for the second and the last nodes that are used in the calculations. Oneida et al. (2015) suggested that since many small elements are used, the effect of the QP-elements is negligible. It may be noted that Oneida et al. (2015) carried out two finite element analyses, one with the original crack length and the second with the extended crack. To deal with this problem, Raju (1987) derived eqs. (1.112) and (1.113) with the coefficients t_{ij} presented in eq. (1.111). The coefficients t_{ij} determine how the nodal point

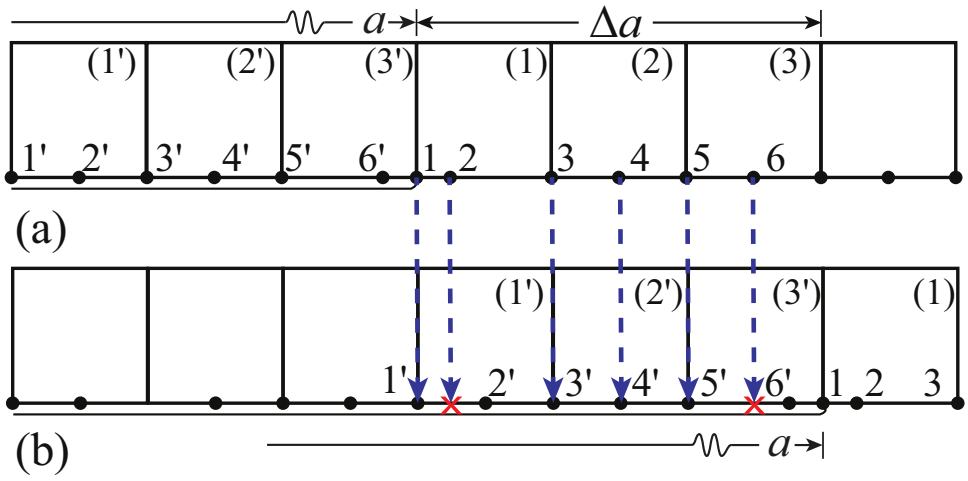

Figure 1.16: (a) The elements used for calculation of the energy release rates when using three elements ahead of the crack tip. (b) The ($i'^{\,th}$) element located below the (i^{th}) element for $i = 1, 2, 3$.

forces are distributed to close the displacement jumps when using QP-elements. Note that Raju (1987) derived these coefficients only for the case when one QP-element ahead of the crack tip is used in the calculations.

Next, the VCCT for three-dimensional problems is considered. The VCCT was first extended to three-dimensional problems, using eqs. (1.104) to (1.106), by Shivakumar et al. (1988). For eight-noded brick elements, the equations are given as

$$\mathcal{G}_I^{(N)} = \frac{1}{2\Delta A^{(N)}} \sum_{n=N}^{N+1} c^{(n)} F_2^{(1,n)} \Delta u_2^{(1',n)} \tag{1.114}$$

$$\mathcal{G}_{II}^{(N)} = \frac{1}{2\Delta A^{(N)}} \sum_{n=N}^{N+1} c^{(n)} F_1^{(1,n)} \Delta u_1^{(1',n)}, \tag{1.115}$$

$$\mathcal{G}_{III}^{(N)} = \frac{1}{2\Delta A^{(N)}} \sum_{n=N}^{N+1} c^{(n)} F_3^{(1,n)} \Delta u_3^{(1',n)}, \tag{1.116}$$

where $\Delta A^{(N)}$ is the area of the virtual crack extension, presented in Fig. 1.17 as the shaded region; it is given by

$$\Delta A^{(N)} = \ell_1 \cdot \ell_3^{(N)}. \tag{1.117}$$

In eq. (1.117), ℓ_1 is the length of virtual crack extension in the x_1-direction. It is also the length of each element in the vicinity of the crack front. The parameter $\ell_3^{(N)}$ is the depth of the N^{th} element in the x_3-direction; it may vary between rows as shown in Fig. 1.17. In eqs. (1.114) to (1.116), for the nodal point forces $F_p^{(m,N)}$ and the displacement jumps $\Delta u_p^{(m',N)}$, the subscript represents the x_p-direction. The first superscript, for the nodal point forces, represents the number of the column proceeding from the crack front; for the displacement jumps, the first superscript is primed denoting the corresponding column

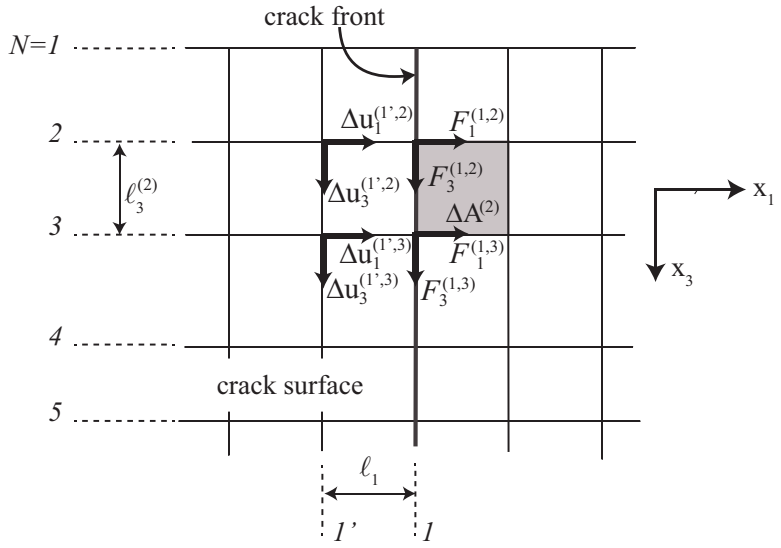

Figure 1.17: Upper view of the nodal point forces and displacement jumps for eight-noded brick elements following Shivakumar et al. (1988).

on the crack surface. The second superscript denotes the row of the node. Shivakumar et al. (1988) assumed that the nodal point force $F_p^{(1,n)}$ is distributed between rows $n-1$ and n. The nodal point force $F_p^{(1,n)}$ is partitioned proportionally by means of the depth ℓ_3 of elements $n-1$ and n in the x_3-direction. To this end, a ratio $c^{(n)}$ is defined such that

$$c^{(n)} \equiv \frac{\ell_3^{(n-1)}}{\ell_3^{(n)} + \ell_3^{(n-1)}}. \tag{1.118}$$

This ratio appears as a multiplicative constant in eqs. (1.114) to (1.116). If ℓ_3 is constant, eqs. (1.114) to (1.116) become

$$\mathcal{G}_I^{(N)} = \frac{1}{4\Delta A^{(N)}} \sum_{n=N}^{N+1} F_2^{(1,n)} \Delta u_2^{(1',n)} \tag{1.119}$$

$$\mathcal{G}_{II}^{(N)} = \frac{1}{4\Delta A^{(N)}} \sum_{n=N}^{N+1} F_1^{(1,n)} \Delta u_1^{(1',n)}, \tag{1.120}$$

$$\mathcal{G}_{III}^{(N)} = \frac{1}{4\Delta A^{(N)}} \sum_{n=N}^{N+1} F_3^{(1,n)} \Delta u_3^{(1',n)}, \tag{1.121}$$

The total energy for each row of elements is given as

$$\mathcal{G}^{(N)} = \mathcal{G}_I^{(N)} + \mathcal{G}_{II}^{(N)} + \mathcal{G}_{III}^{(N)}. \tag{1.122}$$

With the approach of Shivakumar et al.(1988), the average value of the energy release rates over the element is calculated and it is define to occur in the middle of the depth of the element along the crack front.

The energy release rates for twenty-noded brick elements are calculated in Shivakumar et al. (1988) as

$$\mathcal{G}_I^{(N)} = \frac{1}{2\Delta A^{(N)}} \left[\left(\sum_{m=1}^{2} c^{(N-1)} F_2^{(m,N-1)} \Delta u_2^{(m',N-1)} + c^{(N+1)} F_2^{(m,N+1)} \Delta u_2^{(m',N+1)} \right) + F_2^{(1,N)} \Delta u_2^{(1',N)} \right], \tag{1.123}$$

$$\mathcal{G}_{II}^{(N)} = \frac{1}{2\Delta A^{(N)}} \left[\left(\sum_{m=1}^{2} c^{(N-1)} F_1^{(m,N-1)} \Delta u_1^{(m',N-1)} + c^{(N+1)} F_1^{(m,N+1)} \Delta u_1^{(m',N+1)} \right) + F_1^{(1,N)} \Delta u_1^{(1',N)} \right], \tag{1.124}$$

$$\mathcal{G}_{III}^{(N)} = \frac{1}{2\Delta A^{(N)}} \left[\left(\sum_{m=1}^{2} c^{(N-1)} F_3^{(m,N-1)} \Delta u_2^{(m',N-1)} + c^{(N+1)} F_3^{(m,N+1)} \Delta u_3^{(m',N+1)} \right) + F_3^{(1,N)} \Delta u_3^{(1',N)} \right], \tag{1.125}$$

where $\Delta A^{(N)}$ is the area of the virtual crack extension, presented in Fig. 1.18 as the shaded region and given in eq. (1.117). The parameter N defines a row of nodes in the x_3-direction. Equations (1.123) to (1.125) are only for even N. The average value of the energy release rates for each row of elements is defined to occur in row N along the crack front. The nodal point forces and the displacement jumps used in eq. (1.124), are shown in Fig. 1.18. Each nodal point force $F_p^{(m,n)}$, in eqs. (1.123) to (1.125), multiplies its corresponding displacement jump $\Delta u_p^{(m',n)}$. For example, for $N = 4$ in eq. (1.124), the nodal point force in the last term $F_1^{(1,4)}$ multiplies its corresponding displacement jump $\Delta u_1^{(1',4)}$. Similar to eqs. (1.114) to (1.116), the nodal point forces $F_p^{(m,N-1)}$ and $F_p^{(m,N+1)}$ are distributed between two adjacent rows using the ratio $c^{(n)}$, given as

$$c^{(n)} \equiv \frac{\ell_3^{(n-1)}}{\ell_3^{(n+1)} + \ell_3^{(n-1)}} \tag{1.126}$$

where $\ell_3^{(N)}$ is shown in Fig. 1.18. The nodal point forces $F_p^{(1,N)}$ are affected only by the element in row N and, therefore, are not multiplied by $c^{(N)}$. Note that Shivakumar et al. (1988) does not mention how to treat the nodal point forces at the surface of the body. It would appear that the ratio $c^{(n)}$ is equal to unity for those nodal point forces.

Shivakumar et al. (1988) presented results for three finite element models. The VCCT results were compared graphically to the crack opening displacement (COD) method (Barsoum, 1974) and the force method (Raju and Newman, 1977). The results were very similar. For example, the first model that was examined is a semicircular surface crack in a single edge notched tension specimen, shown in Fig. 1.19a. Eight-noded brick elements were used for the VCCT calculations. The dimension of the problem are given

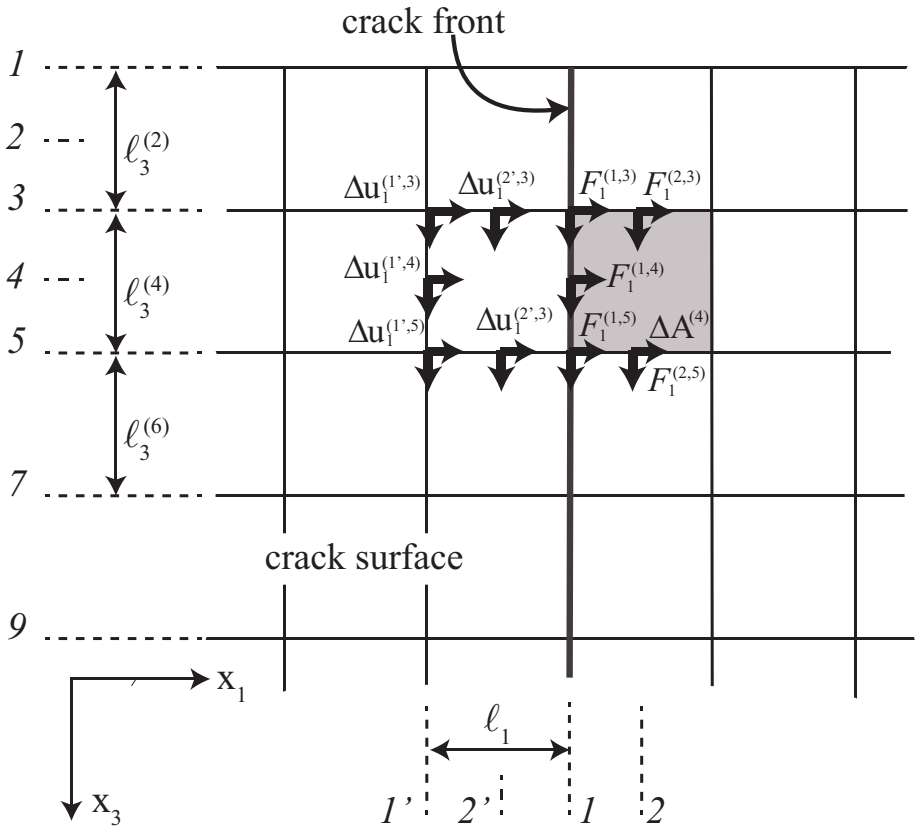

Figure 1.18: Upper view of the nodal point forces and displacement jumps for twenty-noded brick elements following Shivakumar et al. (1988).

as $a/t = 0.2, a/c = 1.0, t/b = 0.09$ and $R/t = 2.78$. Comparative results of a normalized

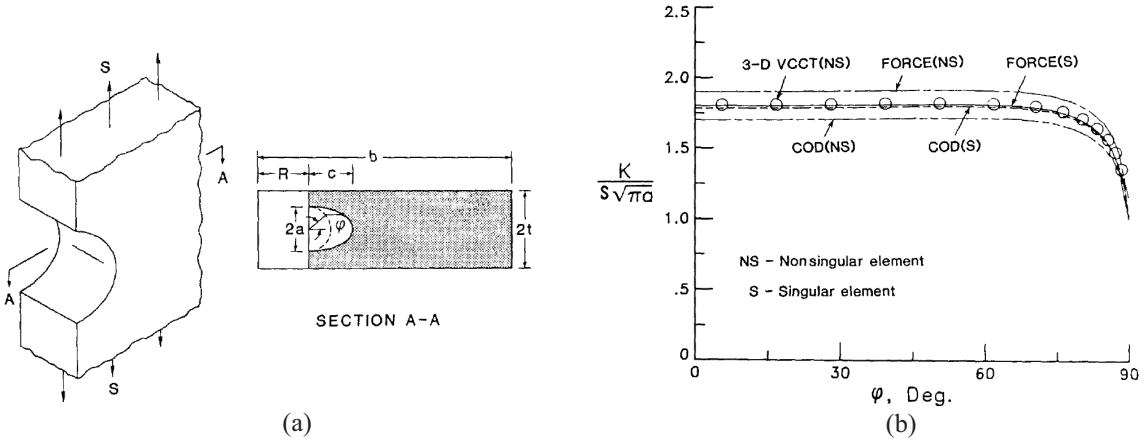

Figure 1.19: (a) Specimen configuration and loading for $a/t = 0.2, a/c = 1.0, t/b = 0.09$ and $R/t = 2.78$ and (b) comparison of normalized K calculated from three-dimensional VCCT, force and COD methods for a semicircular surface crack in a single edge notched tension specimen from Shivakumar et al. (1988).

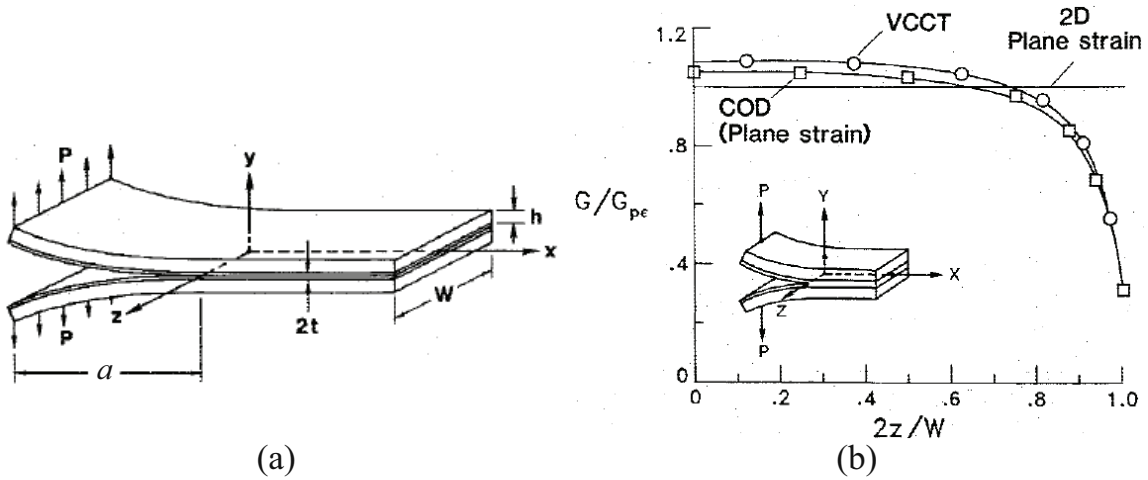

Figure 1.20: (a) DCB specimen dimensions and loading and (b) comparison of $\mathcal{G}/\mathcal{G}_{p\varepsilon}$ calculated from three-dimensional VCCT, COD method and two-dimensional finite element model from Raju, Shivakumar and Crews (1988).

K are shown in Fig. 1.19b. Shivakumar et al. (1988) concluded that the VCCT for three-dimensional problems is an accurate and simple method to use. Additionally, the method does not require singular elements.

In eqs. (1.123) to (1.125), the nodal point forces $F_p^{(m,N-1)}$ and $F_p^{(m,N+1)}$ are distributed between the $N-2$, N and $N+2$ rows using $c^{(n)}$. It was suggested in Raju, Shivakumar and Crews (1988) that for the calculations of the energy release rates of row N, the nodal point forces $F_p^{(m,N-1)}$ and $F_p^{(m,N+1)}$ should be taken only from the elements in row N. In that way, there is no need to use the ratio $c^{(n)}$. Results were presented graphically for a DCB specimen in Raju, Shivakumar and Crews (1988). The specimen consisted of 24 plies of a unidirectional (UD) T300/5208 carbon/epoxy laminate cocured with a thin resin layer in the middle of the specimen. A crack was located in the middle of the resin. The fibers were in the longitudinal direction of the specimen. The dimensions of the specimen shown in Fig. 1.20a are $a = 50.8$ mm, $W = 25.4$ mm, $h = 1.65$ mm and $2t = 0.01$ mm. The specimen was loaded as shown in Fig. 1.20a with $P = 1$ N/m. Collapsed twenty-noded elements were used along the crack front. The VCCT results were compared graphically to the COD method (Barsoum, 1974) and to results obtained from a two-dimensional plane strain finite element model. The graph is shown in Fig. 1.20b. The maximum difference between results obtained by means of the VCCT and the COD methods was 3%. The integrated average value of the VCCT results over the crack front is greater by 1% than the two-dimensional plane strain value. It was concluded that the VCCT, three-dimensional method may be used confidently.

A different approach for a twenty-noded brick elements was presented in Whitcomb (1988). In this approach, the energy release rates are calculated only at the corner nodes of elements along the crack front. For those corner nodes within the body, when N in

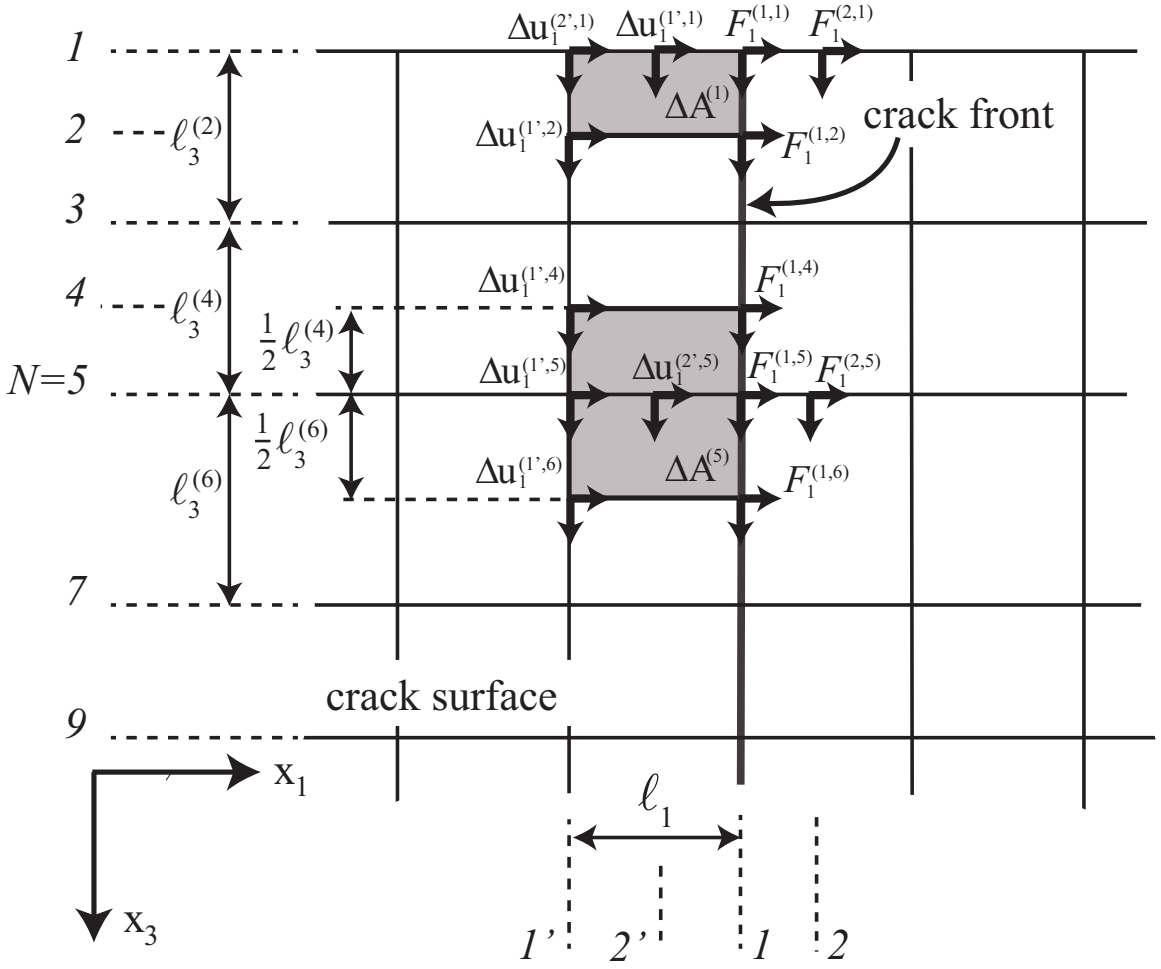

Figure 1.21: Upper view of the nodal point forces and displacement jumps for corner nodes of twenty-noded brick elements along the crack front using the approach of Whitcomb (1988).

Fig. 1.21 is odd, the equations are given by

$$\mathcal{G}_I^{(N)} = \frac{1}{2\Delta A^{(N)}} \left[\left(\sum_{m=1}^{2} F_2^{(m,N)} \Delta u_2^{(m',N)} \right) + \frac{1}{2} \left(F_2^{(m,N-1)} \Delta u_2^{(m',N-1)} + F_2^{(m,N+1)} \Delta u_2^{(m',N+1)} \right) \right] \tag{1.127}$$

$$\mathcal{G}_{II}^{(N)} = \frac{1}{2\Delta A^{(N)}} \left[\left(\sum_{m=1}^{2} F_1^{(m,N)} \Delta u_1^{(m',N)} \right) + \frac{1}{2} \left(F_1^{(m,N-1)} \Delta u_1^{(m',N-1)} + F_1^{(m,N+1)} \Delta u_1^{(m',N+1)} \right) \right] \tag{1.128}$$

$$\mathcal{G}_{III}^{(N)} = \frac{1}{2\Delta A^{(N)}} \left[\left(\sum_{m=1}^{2} F_3^{(m,N)} \Delta u_3^{(m',N)} \right) + \frac{1}{2} \left(F_3^{(m,N-1)} \Delta u_3^{(m',N-1)} + F_3^{(m,N+1)} \Delta u_3^{(m',N+1)} \right) \right] \tag{1.129}$$

where $\Delta A^{(N)}$ is the area of the virtual crack extension, given as

$$\Delta A^{(N)} = \left(\frac{\ell_3^{(N-1)} + \ell_3^{(N+1)}}{2} \right) \ell_1. \tag{1.130}$$

The area of the virtual crack extension in eq. (1.130) is found by multiplying the length between rows $N-1$ and $N+1$ in the x_3-direction and ℓ_1; it is illustrated for $N=5$ as the shaded area $\Delta A^{(5)}$ in Fig. 1.21. In eqs. (1.127) to (1.129), the nodal point forces at even rows are multiplied by 1/2. They are distributed equally between two energy release rate calculations; for example, the nodal point force $F_1^{(1,6)}$ is distributed between the energy release rate calculations of $N=5$ and $N=7$. The nodal point forces and the displacement jumps used in eq. (1.128) for $N=5$, are shown in Fig. 1.21.

For $N=1$, the energy release rates are given by

$$\mathcal{G}_I^{(N)} = \frac{1}{2\Delta A^{(N)}} \left[\left(\sum_{m=1}^{2} F_2^{(m,N)} \Delta u_2^{(m',N)} \right) + \frac{1}{2} F_2^{(m,N+1)} \Delta u_2^{(m',N+1)} \right] \tag{1.131}$$

$$\mathcal{G}_{II}^{(N)} = \frac{1}{2\Delta A^{(N)}} \left[\left(\sum_{m=1}^{2} F_1^{(m,N)} \Delta u_1^{(m',N)} \right) + \frac{1}{2} F_1^{(m,N+1)} \Delta u_1^{(m',N+1)} \right] \tag{1.132}$$

$$\mathcal{G}_{III}^{(N)} = \frac{1}{2\Delta A^{(N)}} \left[\left(\sum_{m=1}^{2} F_3^{(m,N)} \Delta u_3^{(m',N)} \right) + \frac{1}{2} F_3^{(m,N+1)} \Delta u_3^{(m',N+1)} \right] \tag{1.133}$$

where $\Delta A^{(N)}$ is illustrated as the shaded area $\Delta A^{(1)}$ in Fig. 1.21 and is given by

$$\Delta A^{(N)} = \frac{1}{2} \ell_3^{(N+1)} \ell_1 \ . \tag{1.134}$$

The second term in eqs. (1.131) to (1.133) is multiplied by 1/2 similar to that of eqs. (1.127) to (1.129). The nodal point forces and the displacement jumps used in eq. (1.132) for $N=1$, are presented in Fig. 1.21. For calculations of the energy release rates at the corner node at the second edge of the crack front, the term $N+1$, in eqs. (1.131) to (1.134), is replaced with $N-1$. No comparative results were presented.

In Raju et al. (1996), graphical comparisons were made between the approaches described in Raju, Shivakumar and Crews (1988) and Whitcomb (1988); the latter is presented in eqs. (1.127) to (1.134). Recall that in Raju et al. (1996), eqs. (1.127) to (1.134) are also relied upon, with $c^{(n)}=1$; additionally for each energy release rate calculation at row N, the nodal point forces are taken only from the elements in row N. The approaches were found to produce very similar results. For example, a comparison was presented for a stiffener debonded from a skin as shown in Fig. 1.22a. The dimensions and loading are $l_1 = l_2 = 1$ in, $b=1$ in, $h=0.09$ in, $a=0.4$ in and $Q=60$ lb/in. This configuration consists of a $[0]_{36}$ graphite/epoxy laminate divided evenly between the skin and the flange. A comparison of the energy release rates is shown in Fig. 1.22b. Recall that $\mathcal{G}$ is the total energy release rate defined in eq. (1.122). It was concluded that either approach may be used. In Kruger (2004), the approaches of Shivakumar et al. (1988) and Whitcomb (1988) were presented as one method. The approach of Shivakumar et al. (1988), presented in eqs. (1.123) to (1.126), produces results at the mid-nodes of elements along the crack fronti; the approach of Whitcomb (1988), presented in eqs. (1.127) to (1.134), is for corner nodes

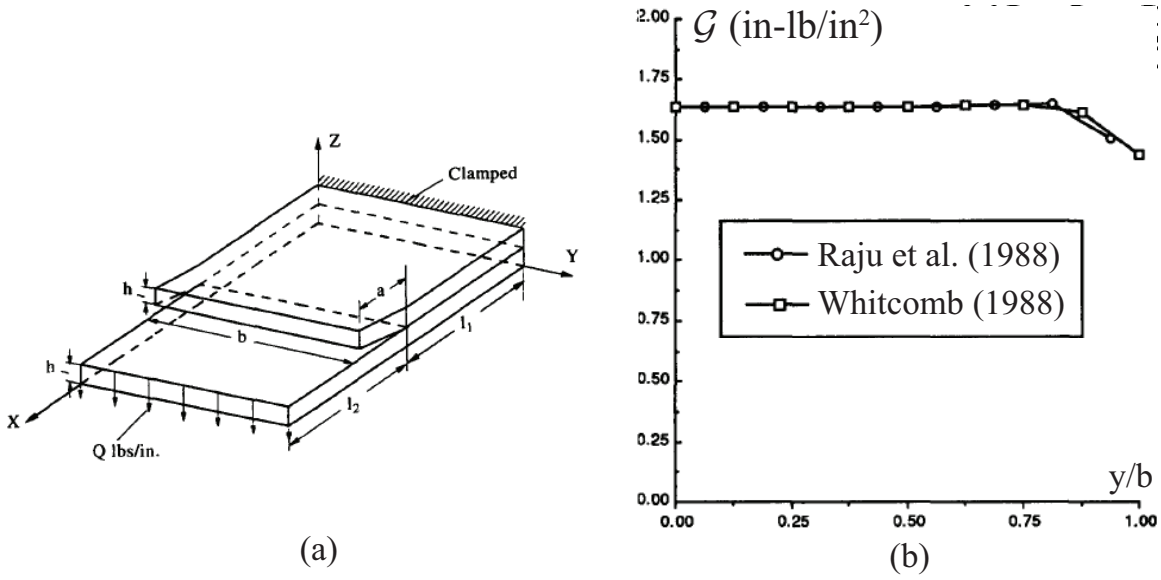

Figure 1.22: (a) Skin-stiffener debonded configuration and (b) comparison between Raju, Shivakumar and Crews (1988) and Whitcomb (1988) approaches presented in Raju et al. (1996).

of elements along the crack front. It was suggested to use the approach described in Raju, Shivakumar and Crews (1988) when elements on the plane of the crack face and along its front are not rectangular; for example, when the crack front is not straight. No numerical comparisons were presented in Kruger (2004).

It may be recalled that Shivakumar et al. (1988) presented results for mode I deformation of a semi-circular surface crack, as shown in Fig. 1.19. In addition, results for mode I deformation of a semi-elliptical crack were also presented. The method for carrying out the calculations of the energy release rates was not described.

In Whitcomb (1988), a method was suggested for obtaining separately the energy release rates $\mathcal{G}_I$, $\mathcal{G}_{II}$ and $\mathcal{G}_{III}$ for circular and elliptic cracks. Use of a local coordinate system, as shown in Fig. 1.23, was suggested. In the new coordinate system, the x_1'-axis is tangent

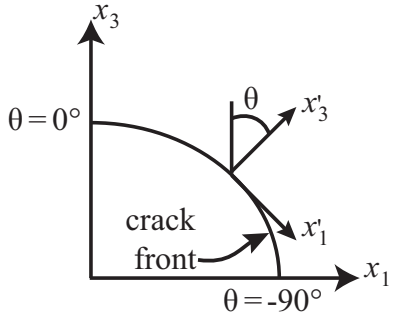

Figure 1.23: Original and transformed coordinate systems.

to the crack front, the x_3'-axis is normal to the crack front in its plane and the x_2'-axis is normal to the crack plane as is the original x_2-axis. Thus, the transformed nodal point forces are given by

$$F_1' = F_1 \cos\theta + F_3 \sin\theta, \tag{1.135}$$

$$F_2' = F_2 \tag{1.136}$$

and

$$F_3' = -F_1 \sin\theta + F_3 \cos\theta, \tag{1.137}$$

where θ is presented in Fig. 1.23. Note that θ is between $-90°$ to $0°$. The same transformation is used for the displacement jumps. In order to use the transformation correctly, it was recommended to use a mesh whose elements are orthogonal to the crack front. A definition of the virtual crack extension ΔA was presented only for a straight through crack.

In Smith and Raju (1998), results were presented for a straight through the thickness crack, an elliptical crack and a semi-elliptical surface crack using orthogonal and non-orthogonal meshes. Eight-noded isoparametric elements were used. It was suggested to determine ΔA using the element ahead of the crack tip. In order to present the approach of Smith and Raju (1998), a mesh of a quarter of a penny-shaped crack is illustrated in Fig. 1.24. The rays are numbered using the perimeter coordinate s and the number of the ray N. The distance between rays is defined with $\ell_s^{(n,p)}$, where n is the arc number and p is the ray number. The coordinate r emanates from the center of the penny-shaped crack. The distance between arcs 1' and 1, ℓ_r, is equal to the distance between arcs 1 and 2. The area $\Delta A^{(N)}$ for ray N is given as

$$\Delta A^{(N)} = \left(\frac{\ell_s^{(1,4)} + \ell_s^{(2,4)}}{2} \right) \ell_r. \tag{1.138}$$

In Smith and Raju (1998), new equations were introduced for meshes in which elements near the crack front did not have orthogonal edges. Those meshes will not be discussed. Results for an elliptical crack in a large body, as shown in Fig. 1.25, using an orthogonal mesh were presented. It is not clear how ΔA in Fig. 1.25 is defined for this case. The dimensions are $a/t = 0.2$, $a/h = 0.01$, $h/W = 0.5$ and $a/c = 0.2$. The body was subjected to a remote tensile stress. As a result of symmetry, one-eighth of the body was modeled. The crack consisted of nine rays. The mesh that was used for carrying out the calculations was not presented. The results were compared to an analytical solution from Green and Sneddon (1950). Except for the last two rays next to the x_1-axis, the errors were less than 1.7%. It was pointed out that close to the x_1-axis, the crack front was not modeled well. It was concluded that orthogonal meshes produced accurate results except where the crack front curvature changed rapidly or where the crack front coincides with a body surface.

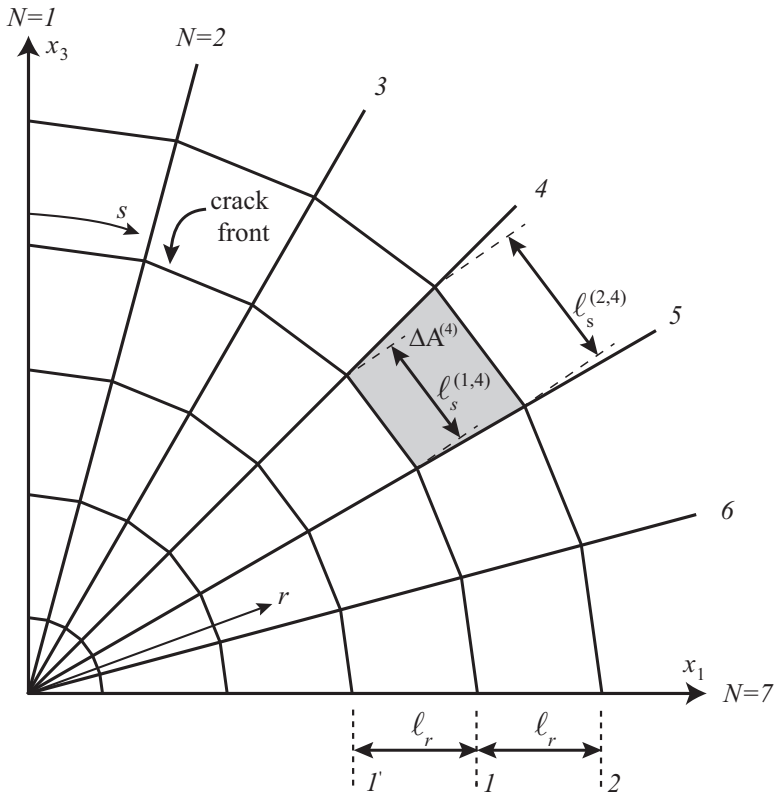

Figure 1.24: Mesh of a quarter of a penny-shaped crack and ΔA following Smith and Raju (1998).

In Okada et al. (2005), new derivations for elements with non-orthogonal edges to the crack front were presented. The crack fronts were circular or elliptical. Further details of this work are shown only for orthogonal meshes. Twenty-noded isoparametric elements were used. Two requirements for creating a mesh were proposed. First, the lines that intersect the crack front should be straight. For example, the lines between nodes $(1', 7)$

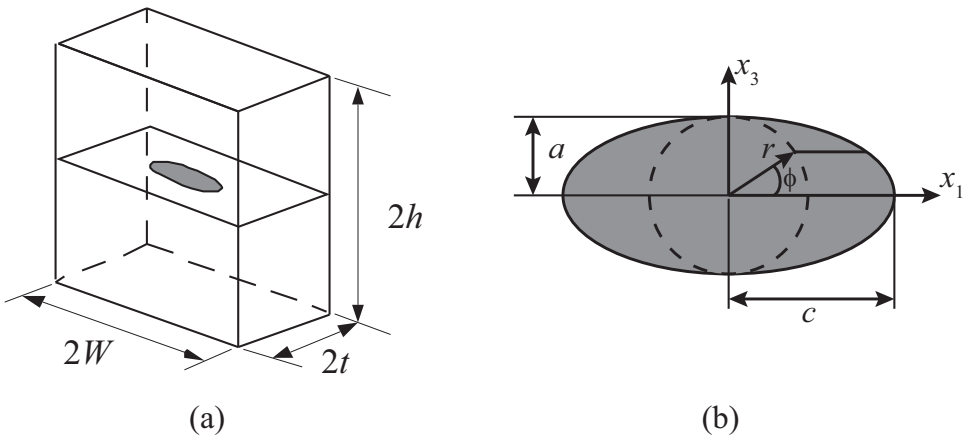

Figure 1.25: (a) A body with an embedded elliptic crack and (b) the embedded crack parameters.

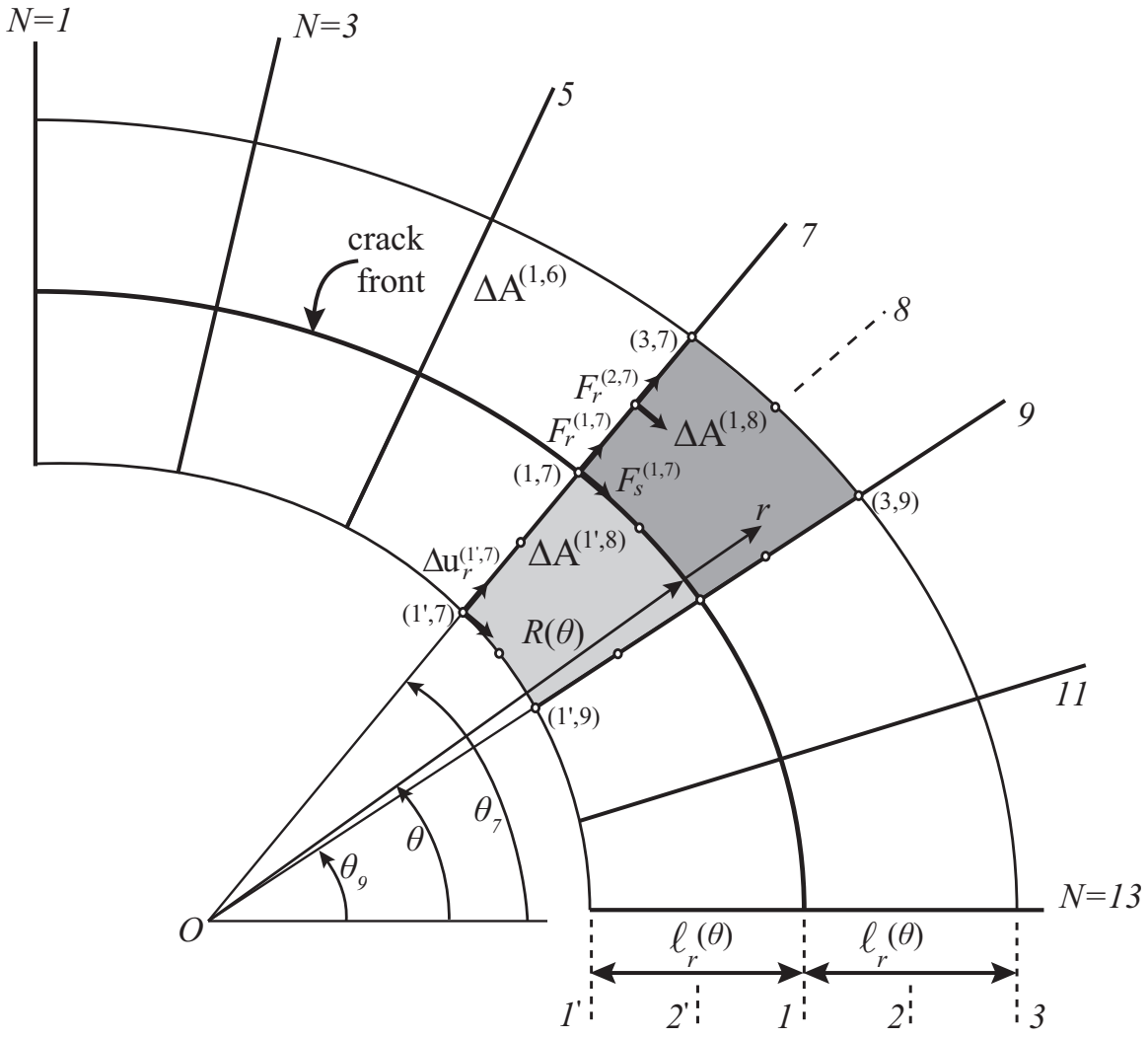

Figure 1.26: A mesh of a quarter of an elliptical crack and ΔA following Okada et al. (2005)

.

and (3,7) and between nodes $(1', 9)$ and (3,9), in Fig. 1.26, should be straight and orthogonal to the crack front. In Fig. 1.26, point O is located at the intersection of those lines. For the case of a penny-shaped crack, this point is at the center of the circle. For an elliptical crack, this point will differ for each pair of elements on either side of the crack front. The angle θ is a polar coordinate, where the angle of ray N is denoted as θ_N. The parameter $R(\theta)$ defines the distance between point O and the crack front as function of θ. The coordinates s and r are local coordinates tangent and perpendicular, respectively, to the crack front; the x_2-axis is perpendicular to the crack surface. For the second requirement, the radial distance $\ell_r(\theta)$, shown in Fig. 1.26, should be the same for elements on the crack surface and that ahead of it. The parameters $R(\theta)$ and $\ell_r(\theta)$ are constant for a penny-shaped crack and vary with respect to θ for an elliptical crack. It is not clear how $R(\theta)$ and $\ell_r(\theta)$ are found for the latter case. The equations for calculating

the energy release rates are similar to eqs. (1.123) to (1.125) presented in Shivakumar et al. (1988) and are given by

$$\mathcal{G}_I^{(N)} = \frac{1}{2\overline{\Delta A}^{(N)}} \left[\left(\sum_{m=1}^{2} c^{(m,N-1)} F_2^{(m,N-1)} \Delta u_2^{(m',N-1)} + c^{(m,N+1)} F_2^{(m,N+1)} \Delta u_2^{(m',N+1)} \right) + F_2^{(1,N)} \Delta u_2^{(1',N)} \right], \tag{1.139}$$

$$\mathcal{G}_{II}^{(N)} = \frac{1}{2\overline{\Delta A}^{(N)}} \left[\left(\sum_{m=1}^{2} c^{(m,N-1)} F_s^{(m,N-1)} \Delta u_s^{(m',N-1)} + c^{(m,N+1)} F_s^{(m,N+1)} \Delta u_s^{(m',N+1)} \right) + F_s^{(1,N)} \Delta u_s^{(1',N)} \right], \tag{1.140}$$

$$\mathcal{G}_{III}^{(N)} = \frac{1}{2\overline{\Delta A}^{(N)}} \left[\left(\sum_{m=1}^{2} c^{(m,N-1)} F_r^{(m,N-1)} \Delta u_r^{(m',N-1)} + c^{(m,N+1)} F_r^{(m,N+1)} \Delta u_r^{(m',N+1)} \right) + F_r^{(1,N)} \Delta u_r^{(1',N)} \right], \tag{1.141}$$

where $\overline{\Delta A}^{(N)}$ is found analytically to be

$$\overline{\Delta A}^{(N)} = \frac{1}{4} \Delta A^{(1',N)} + \frac{3}{4} \Delta A^{(1,N)}. \tag{1.142}$$

The areas $\Delta A^{(1',N)}$ and $\Delta A^{(1,N)}$ are shown in Fig. 1.26 for $N = 8$. After some analysis, they may be expressed as

$$\Delta A^{(1,N)} = \int_{\theta_{N-1}}^{\theta_{N+1}} \left(\ell_r(\theta) R(\theta) + \frac{\ell_r^2(\theta)}{2} \right) d\theta \tag{1.143}$$

and

$$\Delta A^{(1',N)} = \int_{\theta_{N-1}}^{\theta_{N+1}} \left(\ell_r(\theta) R(\theta) - \frac{\ell_r^2(\theta)}{2} \right) d\theta. \tag{1.144}$$

In eqs. (1.139) to (1.141), the ratio $c^{(m,n)}$ is given as

$$c^{(m,N-1)} = \frac{\displaystyle\int_{\Delta A^{(1,N)}} W^{(m,N-1)} dA}{\displaystyle\int_{\Delta A^{(1,N)}} W^{(m,N-1)} dA + \int_{\Delta A^{(1,N-2)}} W^{(m,N-1)} dA} \tag{1.145}$$

and

$$c^{(m,N+1)} = \frac{\int_{\Delta A^{(1,N)}} W^{(m,N+1)} dA}{\int_{\Delta A^{(1,N)}} W^{(m,N+1)} dA + \int_{\Delta A^{(1,N+2)}} W^{(m,N+1)} dA} \tag{1.146}$$

where $W^{(m,p)}$ is the shape function at node (m,p) of the element where integration takes place. For example, for $N = 8$ and $m = 2$, the force $F_r^{(2,7)}$ in eq. (1.141) is multiplied by $c^{(2,7)}$. The ratio $c^{(2,7)}$ is the ratio between the integral of the shape function $W^{(2,7)}$ in the virtual crack extension area $\Delta A^{(1,8)}$ and the sum of the integrals of $W^{(2,7)}$ in areas $\Delta A^{(1,8)}$ and $\Delta A^{(1,6)}$. The virtual crack extension areas $\Delta A^{(1,8)}$ and $\Delta A^{(1,6)}$ are shown in Fig. 1.26. Note that the shape function is different in each virtual crack extension area. In effect, the factors in eqs. (1.145) and (1.146) are used to weight the value of the force at the nodal point.

Results were presented for a through crack, a semi-circular surface crack and a semi-elliptical surface crack in an infinite thin plate subjected to a tensile load far from the crack. The results of the semi-circular and semi-elliptical surface cracks were compared to solutions presented in Newman and Raju (1979). Results obtained differed by no more than 3% from those presented by Newman and Raju (1979).

In this section, the equations for calculating the energy release rates using VCCT were presented. Equations for extracting the stress intensity factors from the energy release rates are presented in the next section.

1.6.2 Extraction of the stress intensity factors from the energy release rates

For problems of linear elastic, homogeneous and isotropic material, the relations between the energy release rates $\mathcal{G}_T, \mathcal{G}_I, \mathcal{G}_{II}$ and $\mathcal{G}_{III}$ and the stress intensity factors K_I, K_{II} and K_{III} are presented in eqs. (1.16) to (1.21). The relation between the interface energy release rate $\mathcal{G}_i$ and the stress intensity factors K_1, K_2 and K_{III} for an interface crack between two dissimilar isotropic materials is presented in eq. (1.35); the relations between the energy release rates $\mathcal{G}_I$, $\mathcal{G}_{II}$ and $\mathcal{G}_{III}$ to those stress intensity factors is presented in eqs. (1.38) and (1.39). In those equations, explicit expressions for the stress intensity factors are not presented.

For linear elastic, homogeneous and isotropic material, explicit expressions for the stress intensity factors may be found by using eqs. (1.19) to (1.21) as

$$K_I = \sqrt{\bar{E}\mathcal{G}_I} \tag{1.147}$$

$$K_{II} = \sqrt{\bar{E}\mathcal{G}_{II}} \tag{1.148}$$

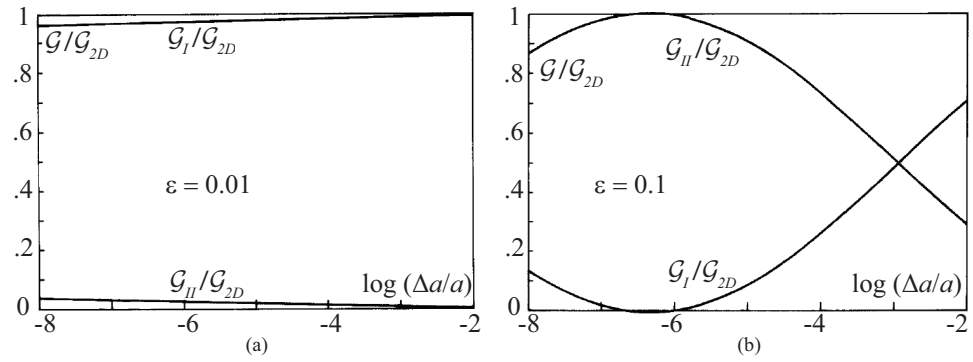

Figure 1.27: The oscillatory behaviour of $\mathcal{G}_I$ and $\mathcal{G}_{II}$ for (a) $\varepsilon = 0.01$ and (b) $\varepsilon = 0.1$ (adapted from Toya, 1992).

and

$$K_{III} = \sqrt{2\mu\mathcal{G}_{III}} \tag{1.149}$$

where $\bar{E}$ is given in eqs. (1.17) and μ is the shear modulus.

For an interface crack between two dissimilar isotropic materials, the stress and displacement fields were introduced in eqs. (1.31) to (1.34). Using these equations, the tractions along the interface ahead of the crack tip and the crack face displacement jumps are given by

$$\sigma_{22} + i\sigma_{21}\Big|_{\theta=0} = \frac{Kx_1^{i\varepsilon}}{\sqrt{2\pi x_1}} \tag{1.150}$$

and

$$\Delta u_2 + i\Delta u_1 = \frac{8\cosh\pi\varepsilon}{(1+2i\varepsilon)H_1}\sqrt{\frac{\Delta a - x_1}{2\pi}}\,(\Delta a - x_1)^{i\varepsilon}K\ , \tag{1.151}$$

respectively, where the coordinate system is shown in Fig. 1.9, ε is defined in eq. (1.25), H_1 is defined in eq. (1.36) and the complex stress intensity factor is defined in eq. (1.29).

The behavior of the energy release rates $\mathcal{G}_I$ and $\mathcal{G}_{II}$ for an interface crack between two dissimilar materials was investigated in Raju, Crews and Aminpour (1988), Sun and Manoharan (1989), Toya (1992), Chow and Atluri (1995), Beuth (1996) and Agrawal and Karlsson (2006). By substituting eqs. (1.150) and (1.151) into the integrals of eqs. (1.104) and (1.105) and integrating them, it was shown that the energy release rates, $\mathcal{G}_I$ and $\mathcal{G}_{II}$ oscillate as a function of $\Delta a^{2i\varepsilon}$. In Raju, Crews and Aminpour (1988), the oscillating behavior was presented for an interface crack between two isotropic materials, two transversely isotropic materials and two monoclinic materials. The numerical results verified the oscillatory behavior. The same oscillatory behavior was shown for an interface crack between two orthotropic materials in Sun and Manoharan (1989). In Toya (1992), the dependence of the energy release rates on ε was illustrated for different values of ε. Numerical results of an interface crack between two isotropic materials in an infinite body subjected to a remote tensile load are presented in Fig. 1.27. The parameter $\mathcal{G}_{2D}$ in Fig. 1.27 is defined in eq. (1.22). In Fig. 1.27a, for $\varepsilon = 0.01$ the energy release rates $\mathcal{G}_I$

and $\mathcal{G}_{II}$ are almost constant. Increasing ε to 0.1 leads to large oscillations of $\mathcal{G}_I$ and $\mathcal{G}_{II}$, as shown in Fig. 1.27b. In Toya (1992), new equations were derived, showing the relation between the energy release rates and the stress intensity factors; but no calculations of the stress intensity factors were carried out.

Numerical calculations of the stress intensity factors for an interface crack were presented first in Chow and Atluri (1995). New sets of equations were derived for an interface crack between two dissimilar isotropic materials, two dissimilar orthotropic materials and two dissimilar generally anisotropic materials. A coupled energy release rate was introduced, given as

$$\mathcal{G}_{I-II} = \lim_{\Delta a \to 0} \frac{1}{2\Delta a} \int_0^{\Delta a} \left[\sigma_{22}(x_1)\Delta u_1(\Delta a - x_1) + \sigma_{21}(x_1)\Delta u_2(\Delta a - x_1)\right] dx_1. \tag{1.152}$$

The set of equations for an interface crack between two dissimilar isotropic materials is given by

$$\begin{bmatrix} a_{11}a_{21} + a_{12}^2 & a_{22}a_{11} - a_{12}^2 \\ a_{22}a_{21} - a_{12}^2 & a_{11}a_{21} + a_{12}^2 \end{bmatrix} \begin{Bmatrix} K_1^2 \\ K_2^2 \end{Bmatrix} = \lambda \begin{Bmatrix} a_{21}\mathcal{G}_I - a_{21}\mathcal{G}_{I-II} \\ a_{21}\mathcal{G}_{II} - a_{12}\mathcal{G}_{I-II} \end{Bmatrix}. \tag{1.153}$$

In eq. (1.153), the constants a_{ij} for $i, j = 1, 2$ are functions of ε and Δa. The parameter λ depends on the mechanical properties. For an interface crack between two dissimilar orthotropic materials, the set of equations is similar to eq. (1.153), but with additional constants that depend upon the mechanical properties. For an interface crack between two dissimilar generally anisotropic materials, a 6×6 matrix which replaces the 2×2 matrix in eq. (1.153) is obtained. Three additional energy release rates are calculated, the energy release rate for mode III, $\mathcal{G}_{III}$, and two coupled energy release rates $\mathcal{G}_{I-III}$ and $\mathcal{G}_{II-III}$.

New equations for the relation between the energy release rates and the stress intensity factors were also derived in Beuth (1996). In Agrawal and Karlsson (2006), it was shown that the different equations in Toya (1992), Chow and Atluri (1995) and Beuth (1996) are mathematically identical. A new quadratic algebraic equation was derived in order to determine the normalized phase angle, $\hat{\psi}$, given in eq. (1.28). The new quadratic equation is given by

$$\begin{aligned} \kappa^2 \left[(I_c + 2\varepsilon I_s)(1+g) + I_0(g-1)\right] + \kappa \left[(4\varepsilon I_c - 2I_s)(1+g)\right] \\ - \left[(I_c + 2\varepsilon I_s)(1+g) - I_0(g-1)\right] = 0, \end{aligned} \tag{1.154}$$

where

$$\hat{\psi} = \tan^{-1}(1/\kappa) \tag{1.155}$$

and

$$\kappa = \frac{K_1}{K_2}. \tag{1.156}$$

The integrals I_c, I_s and I_0 in eq. (1.154) are given as

$$I_c = \frac{1}{\Delta a}\int_0^{\Delta a} \cos\left[\varepsilon \ln\left(\frac{r(\Delta a - r)}{\hat{L}^2}\right)\right]\sqrt{\frac{r}{\Delta a - r}}\, dr, \tag{1.157}$$

$$I_s = \frac{1}{\Delta a}\int_0^{\Delta a} \sin\left[\varepsilon \ln\left(\frac{r(\Delta a - r)}{\hat{L}^2}\right)\right]\sqrt{\frac{r}{\Delta a - r}}\, dr \tag{1.158}$$

and

$$I_0 = \frac{1}{\Delta a}\int_0^{\Delta a} \cos\left[\varepsilon \ln\left(\frac{(\Delta a - r)}{r}\right)\right] - 2\varepsilon \sin\left[\varepsilon \ln\left(\frac{(\Delta a - r)}{r}\right)\right]\, dr = \frac{\pi\,(1+4\varepsilon^2)}{2\cosh(\pi\varepsilon)}. \tag{1.159}$$

In eqs. (1.157) to (1.159), Δa is the virtual crack extension, ε is the oscillatory parameter, r is shown in Fig. 1.3 and $\hat{L}$ is an arbitrary length scale presented in eqs. (1.27) and (1.30). The values of the integrals in eqs. (1.157) and (1.158) were obtained by carrying out numerical integration, with $\hat{L} = 2a$. In Toya (1992), the values of eqs. (1.157) to (1.158) were found in terms of the special function Gamma which is tabulated. In eq. (1.154), the parameter g is given as

$$g \equiv \frac{\mathcal{G}_{II}}{\mathcal{G}_I}. \tag{1.160}$$

Using eqs. (1.154) and (1.155), two solutions are found for $\hat{\psi}$. In order to eliminate the extraneous solution, it was suggested to use an approximation of $\hat{\psi}$. The approximation was derived by combining equations from Smelser (1979) and Matos et al. (1989), and given by

$$\hat{\psi} \cong \tan^{-1}\left(\frac{\Delta u_1(r)}{\Delta u_2(r)}\right) + \tan^{-1}(2\varepsilon) - \varepsilon \ln\left(\frac{r}{\hat{L}}\right). \tag{1.161}$$

For a detailed explanation to choose r in eq. (1.161), the reader is referred to Agrawal and Karlsson (2006). The stress intensity factors are found using the relations

$$|K| = \sqrt{\mathcal{G}_{2D} H_1}, \tag{1.162}$$

and

$$K = |K|\hat{L}^{-i\varepsilon} e^{i\hat{\psi}}. \tag{1.163}$$

The energy release rate $\mathcal{G}_{2D}$ is given in eq. (1.22) and H_1 is defined in eq. (1.36).

In Agrawal and Karlsson (2006), two problems were considered. The first problem is that of an interface crack between two linear elastic, homogeneous and isotropic materials in an infinite body subjected to a remote tensile stress, as shown in Fig. 1.28. The upper and lower materials are denoted as (1) and (2), respectively. The second problem does not have an analytical solution and, therefore, will not be described. The mechanical properties used were $E_1 = 200$ GPa, $E_2 = 5$ GPa, and $\nu_1 = \nu_2 = 0.25$. To model an infinite body, the dimensions of the body in the finite element analysis were taken to be $2h = 2w = 400$ mm and $2a = 10$ mm, as shown in Fig. 1.28. The analytical solution for the infinite body problem is given in Rice (1988) as

$$K = (\sigma_{22} + i\sigma_{12})(1 + 2i\varepsilon)\sqrt{\pi a}(2a)^{-i\varepsilon}. \tag{1.164}$$

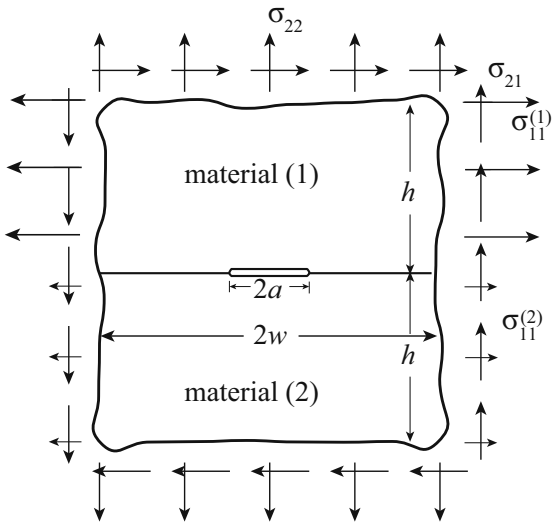

Figure 1.28: Interface crack in an infinite body subjected to remote tensile and shear stresses.

In order to maintain displacement continuity along the interface, stresses $\sigma_{11}^{(1)}$ and $\sigma_{11}^{(2)}$ are applied parallel to the interface, as shown in Fig. 1.28. The relation between those stresses is given as

$$\sigma_{11}^{(2)} = \frac{\bar{E}_2}{\bar{E}_1}\sigma_{11}^{(1)} + \frac{\nu_2}{1-\nu_2}\left[1 - \frac{\nu_1}{\nu_2}\frac{E_2}{E_1}\frac{1+\nu_1}{1+\nu_2}\right]\sigma_{22}, \tag{1.165}$$

where $\bar{E}_i$ is defined in eq. (1.17). The remote stresses in the analysis were assumed to be $\sigma_{22} = 100$ MPa, $\sigma_{21} = \sigma_{11}^{(1)} = 0$. So that, for plane strain conditions, from eq. (1.165), $\sigma_{11}^{(2)} = 32.5$ MPa. The analysis was carried out with the four-noded element CPE4R (4-node bilinear plane strain quadrilateral element with reduced integration) using ABAQUS (2003). Note that reduced integration was used in the calculations and is not recommended for this type of problem. The percent errors for the stress intensity factors were obtained using

$$\%\ \text{error} = \frac{\hat{K}_i - \hat{K}_{i,analytical}}{|\hat{K}_{analytical}|} \cdot 100 \tag{1.166}$$

for $i = 1, 2$, where $\hat{K}$ is defined in eq. (1.30) and

$$|\hat{K}_{analytical}| = \sqrt{\hat{K}_{1,analytical}^2 + \hat{K}_{2,analytical}^2}. \tag{1.167}$$

In this study, the percent errors are calculated as

$$\%\ \text{error} = \frac{\hat{K}_i - \hat{K}_{i,analytical}}{\hat{K}_{i,analytical}} \cdot 100. \tag{1.168}$$

This is a more precise error calculation for small values of $\hat{K}_i$. The numerical errors obtained in Agrawal and Karlsson (2006) for the infinite body were 0.51% and 2.59% for

$\hat{K}_1$ and $\hat{K}_2$, respectively. Using eq. (1.168), the errors are 0.52% and −12.64% for $\hat{K}_1$ and $\hat{K}_2$, respectively.

In Banks-Sills and Farkash (2016), new equations were derived in order to determine the stress intensity factors for an interface crack between two dissimilar isotropic materials. The equations were derived by using the integrals

$$A = \frac{1}{2\Delta a}\int_0^{\Delta a}\Big[\sigma_{22}(x_1)+i\sigma_{21}(x_1)\Big]\Big[\Delta u_2(\Delta a-x_1)-i\Delta u_1(\Delta a-x_1)\Big]\,dx_1 \tag{1.169}$$

$$D = \frac{1}{2\Delta a}\int_0^{\Delta a}\Big[\sigma_{22}(x_1)+i\sigma_{21}(x_1)\Big]\Big[\Delta u_2(\Delta a-x_1)+i\Delta u_1(\Delta a-x_1)\Big]\,dx_1 \tag{1.170}$$

where the coordinate system and the virtual crack extension Δa are shown in Fig. 1.9. The integrals are obtained as

$$A = \frac{1}{H_1}(K_1^2+K_2^2) \tag{1.171}$$

$$D = \frac{\cosh\pi\varepsilon}{\pi H_1}PK^2\Delta a^{2i\varepsilon}\ , \tag{1.172}$$

where H_1 is given in eq. (1.36) and

$$P = \frac{\Gamma\Big(\frac{1}{2}+i\varepsilon\Big)\Gamma\Big(\frac{1}{2}+i\varepsilon\Big)}{\Gamma\Big(2+2i\varepsilon\Big)}\ . \tag{1.173}$$

In eq. (1.173), $\Gamma(\cdot)$, is the special function Gamma.

Noting that

$$\Im\{A\} = 0\ , \tag{1.174}$$

from eq. (1.169), one may write

$$\mathcal{I}_I = \mathcal{I}_{II}, \tag{1.175}$$

where

$$\mathcal{I}_I = \frac{1}{2\Delta a}\int_0^{\Delta a}\sigma_{22}(x_1)\Delta u_1(\Delta a-x_1)dx_1 \tag{1.176}$$

$$\mathcal{I}_{II} = \frac{1}{2\Delta a}\int_0^{\Delta a}\sigma_{21}(x_1)\Delta u_2(\Delta a-x_1)dx_1. \tag{1.177}$$

By considering the expressions in eqs. (1.104) and (1.105) for $\mathcal{G}_I$ and $\mathcal{G}_{II}$, respectively, and manipulating the integrals A and D in eqs. (1.169) and (1.170), respectively, the relations between them are found as

$$\mathcal{G}_I = \frac{1}{2}\lim_{\Delta a\to 0}\Big[\Re(A)+\Re(D)\Big] \tag{1.178}$$

$$\mathcal{G}_{II} = \frac{1}{2}\lim_{\Delta a\to 0}\Big[\Re(A)-\Re(D)\Big]. \tag{1.179}$$

Using eqs. (1.178) and (1.179) and manipulating eqs. (1.171) and (1.172), the phase angle ψ defined in eq. (1.40) is determined as

$$\psi = \frac{1}{2}\cos^{-1}\left(\frac{1}{C}\frac{1-g}{1+g}\right) - \frac{1}{2}\tan^{-1}\left(\frac{P_I}{P_R}\right) - \varepsilon \ln \Delta a. \tag{1.180}$$

In eq. (1.180), the parameter C is defined as

$$C = \frac{\cosh \pi\varepsilon}{\pi}\sqrt{P_R^2 + P_I^2}, \tag{1.181}$$

where the parameters P_R and P_I are the real and imaginary parts of P given in eq. (1.173) and g is defined in eq. (1.160).

The stress intensity factors may be found by manipulating eqs. (1.22), (1.38) and (1.40) as

$$K_1 = \pm\sqrt{H_1 \mathcal{G}_{2D}}\cos\psi\ . \tag{1.182}$$

and

$$K_2 = K_1 \tan\psi\ . \tag{1.183}$$

Two pairs of stress intensity factors are found using eqs. (1.182) and (1.183). The valid pair satisfies the inequality

$$-\frac{\pi}{2} < \tan^{-1}\left(\frac{K_2}{K_1}\right) - \tan^{-1} 2\varepsilon + \varepsilon \ln r < \frac{\pi}{2}, \tag{1.184}$$

where r was chosen as $a/100$.

In order to calculate the stress intensity factors, a finite element analysis is carried out. The two-dimensional analyses were performed with the eight-noded isoparametric element using Abaqus/CAE (2016). The energy release rates are calculated using eqs. (1.107) and (1.108). Recall that in Section 1.6.1, the virtual crack extension, Δa, consisting of more than one element was suggested, as shown in Fig. 1.15. After the energy release rates are calculated, the phase angle is found by using eq. (1.180). The stress intensity factors are found by using $\mathcal{G}_{2D}$, given in eq. (1.22), and eqs. (1.182) and (1.183). The parameters $\mathcal{I}_I$ and $\mathcal{I}_{II}$ are calculated as

$$\mathcal{I}_I = \frac{1}{2\Delta a}\sum_{m=1}^{M} F_2^{(m)} \Delta u_1^{(m')}\ , \tag{1.185}$$

$$\mathcal{I}_{II} = \frac{1}{2\Delta a}\sum_{m=1}^{M} F_1^{(m)} \Delta u_2^{(m')}\ , \tag{1.186}$$

where the nodal point forces and displacements jumps are the same as those used in eqs. (1.107) and (1.108).

Numerical results were presented for an interface crack between two dissimilar isotropic materials in an infinite body, as shown in Fig. 1.28. The body was subjected to a remote

Table 1.4: Data for an interface crack in an infinite body analysis carried out with the finer mesh in Banks-Sills and Farkash (2016).

no. of elements in Δa	1	2	3	6	20	40
percent error K_1	0.9	0.3	0.4	0.3	0.22	0.22
percent error K_2	-0.2	-0.5	0.5	0.2	0.06	0.06
$\mathcal{I}$	9.7	5.4	3.8	2.0	0.6	0.4

tensile stress of $\sigma_{22} = 1$ MPa. The mechanical properties of the materials used were $E_1 = 1$ GPa, $E_2 = 0.1$ GPa and $\nu_1 = \nu_2 = 0.3$. Using eq. (1.165) and plane strain condition, the stresses parallel to the interface crack were $\sigma_{11}^{(1)} = 1$ MPa and $\sigma_{11}^{(2)} = 0.486$ MPa. The dimensions of the body in the finite element analysis were taken to be $a/w = 0.05$ and $w/h = 1$ where $2a = 1$ mm, as shown in Fig. 1.28. The percent difference between $\mathcal{I}_I$ and $\mathcal{I}_{II}$ is defined as

$$\mathcal{I} = \frac{\mathcal{I}_I - \mathcal{I}_{II}}{\mathcal{I}_I} \cdot 100 \, . \tag{1.187}$$

In Banks-Sills and Farkash (2016), two finite element analyses were carried out with two different meshes; the stress intensity factor errors and the value of $\mathcal{I}$ for the finer mesh are shown in Table 1.4 . The percent errors were calculated using eq. (1.168). When using one element for the virtual crack extension Δa, the percent errors of the stress intensity factors are 0.9% and -0.2% for K_1 and K_2, respectively. By using more than 6 elements in Δa, the percent errors of the stress intensity factors are less than 0.3%. The percent error decreases to 0.22%, when using more than 20 elements. The value of $\mathcal{I}$ is 9.7% when using one element in Δa. By increasing the number of elements in Δa, the value of $\mathcal{I}$ decreases. When using 40 elements in Δa, the value of $\mathcal{I}$ is 0.4%.

1.7 Research objectives

One of the aims of this research investigation is to explore and extend the VCCT approach to two and three-dimensional problems, as presented in Banks-Sills and Farkash (2016). Using QP-elements is shown to be unappropriate for VCCT. Equation (1.180) was presented here for extracting the phase angle ψ. This equation is shown to lead to erroneous results for some cases and a new equation with new insights is developed. The extension of VCCT is proposed for an interface crack between two transversely isotropic materials. The Stroh (1958) and Lekhnitskii (1950) formalisms may be used in the analysis of this problem for plane deformation. New equations using VCCT for three-dimensional straight through and penny-shaped cracks are presented. A second aim of this study is to extend the Stroh (1958) and Lekhnitskii (1950) formalisms for a fully three-dimensional description of anisotropic material. This is done by considering a Clifford formalism (Liu

and Hong, 2015). An initial step was taken here to solve the problem of a uniform stress state in a three-dimensional homogenous, anisotropic material.

In Section 1.1, the basic concepts of fracture mechanics for linear elastic, homogeneous and isotropic material were presented. The concepts of fracture mechanics for an interface crack between two dissimilar linear elastic, homogenous and isotropic materials were described in Section 1.2. The conservative J and M-integrals were discussed in Section 1.3. It was shown that by using the M-integral, the individual stress intensity factors may be determined for an interface crack. The conservative integrals, J and M, are considered to be very accurate methods. The VCCT is much simpler to derive for a specific interface compared to the conservative integrals. Thus, the accuracy of results obtained here will be examined. In Section 1.4, the Stroh and Lekhnitskii formalisms for problems involving anisotropic material and plane deformation were briefly presented. The delamination face displacement jumps and the tractions along the interface ahead of the delamination front, for the delamination considered in this study (a delamination between two transversely isotropic materials) were developed using the mentioned formalisms. In Section 1.5, a Clifford algebra was presented. In Section 1.6, the VCCT method was presented. Different approaches to calculate the energy release rates were described in Section 1.6.1. In Section 1.6.2, it was shown how the individual stress intensity factors may be determined by using the energy release rates. The stress intensity factors K_I, K_{II} and K_{III} may be extracted from $\mathcal{G}_I, \mathcal{G}_{II}$ and $\mathcal{G}_{III}$, respectively, for linear elastic, homogeneous and isotropic material in three-dimensional problems. For an interface crack or a delamination, the complex stress intensity factor K, given in eq. (1.29), may be found by using $\mathcal{G}_I$ and $\mathcal{G}_{II}$ and K_{III} may be determined directly from $\mathcal{G}_{III}$.

In order to explore and extend the VCCT approach presented in Banks-Sills and Farkash (2016), new derivations will be described in Chapters 2 and 3. In Chapter 2, two-dimensional problems will be presented. An extension of the VCCT for three-dimensional problems will be discussed in Chapter 3. In order to demonstrate that QP-elements are not appropriate for VCCT, the expressions for calculating the energy release rates from VCCT are rederived in Section 2.1. In Section 2.2, several problems are solved by means of the finite element method to examine the various approaches for calculating the energy release rates with VCCT. The effect of mesh refinement is considered. Use of QP-elements for VCCT is shown to be less accurate than that of eight-noded regular elements and, therefore, not recommended. In Section 2.3, a new equation for extraction of the phase angle is presented. The differences between the numerically calculated dual energy release rates are examined in Section 2.4. In Section 2.5, an extension of the VCCT for an interface crack between two transversely isotropic materials is presented. For this extension, three problems are solved: a crack in an infinite body, a CCT specimen and a DCB specimen.

The equations for determining the energy release rates in Banks-Sills and Farkash (2016)

were developed only for two-dimensional problems. New equations for a straight through crack and a penny-shaped crack will be derived in Section 3.1. In Section 3.2, numerical results for a straight through finite length crack and a penny-shaped crack in an infinite body of isotropic, homogeneous material are presented. Numerical results for an interface crack between two dissimilar linear elastic, homogeneous and isotropic materials are shown in Section 3.3. In Section 3.4, numerical results for an interface crack between two dissimilar transversely isotropic materials are considered.

In Chapter 4, the Clifford formalism is discussed. In Section 4.1, The eigenvalue problem for various anisotropic materials is presented. The eigenvectors for various anisotropic materials are found in Section 4.2. In Section 4.3, a three-dimensional Clifford formalism is extended in an explicit manner. Analytical results using the three-dimensional Clifford formalisms are presented in Section 4.4. In this section, a general solution for a uniform stress field is found. The results are checked by means of finite element analyses. A summary and conclusions are given in Chapter 5.

Chapter 2

VCCT for two-dimensional problems

In this chapter, the VCCT is presented for two-dimensional problems. In Section 2.1, equations for calculating the energy release rates are rederived. The suitability of the VCCT for an eight-noded element, a quarter-point (QP) element, as well as a new element that is suggested, is considered. Numerical results, considering the different element types, are presented in Section 2.2. A new equation for calculating the phase angle, is given in Section 2.3. In Section 2.4, the dual energy release rates are considered. An extension of the VCCT for an interface crack between two transversely isotropic materials is presented in Section 2.5.

2.1 Derivations of equations for calculating the energy release rates

The VCCT was reviewed in Section 1.6.1. In Raju (1987), the first full mathematical derivation for the equations of the VCCT was presented for various element types. Four-noded, eight-noded, QP-elements and also higher order elements were considered. In Bueth (1996), it was suggested to use more than one element for calculating the energy release rates. A simple extension of the four-noded and eight-noded element equations was presented, as shown in eqs. (1.107) and (1.108), where M is the number of nodes in the calculation, and illustrated in Figs. 1.15a and 1.15b, respectively.

Next, the VCCT is reconsidered for both eight-noded regular and QP-elements. The equations for calculating the energy release rates by means of VCCT are rederived. Additional insight is gained from the derivations. It is shown that QP-elements are not appropriate for the VCCT. In Section 2.2, numerical results comparing use of eight-noded and QP-elements are presented.

The rederivation of the VCCT makes use of the basic concepts of the finite element method presented in Hughes (1987). The derivation is presented for $\mathcal{G}_I$ using σ_{22}, F_2 and Δu_2, where σ_{22} is the stress ahead of the crack tip, F_2 is the nodal point force also ahead of

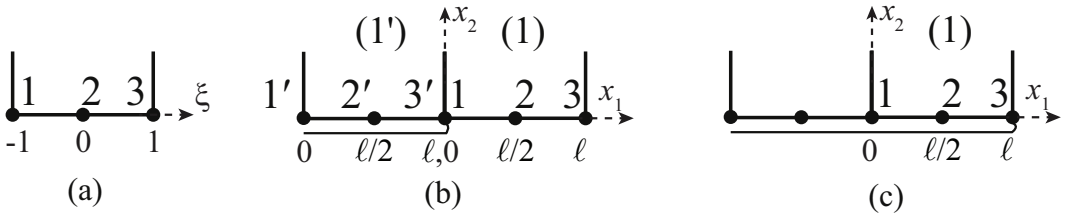

Figure 2.1: (a) The lower edge of an eight-noded isoparametric element using its natural coordinate ξ. For eight-noded regular elements: (b) the crack before and (c) after the VCE in Cartesian coordinates.

the crack tip and Δu_2 is the crack faces opening in the x_2-direction behind the crack tip. The derivation for $\mathcal{G}_{II}$ is similar and final expressions will be given. The lower edge of an eight-noded element using its natural coordinate is illustrated in Fig. 2.1a. The nodes are located permanently at $\xi = -1, 0, 1$, respectively. The lower edges of two eight-noded regular elements in the vicinity of the crack tip in Cartesian coordinates before and after the VCE are presented in Figs. 2.1b and 2.1c, respectively. Two finite element analyses are considered in Figs. 2.1b and 2.1c: one before the VCE and the second after the VCE. The origin of the x_1, x_2 coordinate system is located at the crack tip before the VCE in Fig. 2.1b.

The shape functions $N^{(m)}$ for $m = 1, 2, 3$ may be used to interpolate the displacement components that are obtained from the FEA. For an eight-noded isoparametric element, they are given for nodes 1 to 3 as

$$N^{(1)}(\xi) = \frac{\xi}{2}(\xi - 1) \qquad N^{(2)}(\xi) = 1 - \xi^2 \qquad N^{(3)}(\xi) = \frac{\xi}{2}(\xi + 1) \; . \tag{2.1}$$

Consider element (1) in Figs. 2.1b and 2.1c. For an isoparametric element, the mapping between Cartesian coordinates and natural coordinates is given by

$$x_1(\xi) = \sum_{m=1}^{3} N^{(m)}(\xi) x_1^{(m)} \tag{2.2}$$

where $x_1(\xi)$ is the mapped coordinate in the x_1-direction, and $x_1^{(m)}$ is the coordinate of node m in the physical space. The derivative of $x_1(\xi)$ with respect to ξ is given by

$$x_{1,\xi}(\xi) = \sum_{m=1}^{3} N_{,\xi}^{(m)}(\xi) x_1^{(m)} \tag{2.3}$$

where a comma represents differentiation. The total force F_2 in the x_2-direction on the lower edge of the element in front of the crack tip is given by

$$F_2 = \int_{-1}^{1} \left[\sigma_{22}(x_1(\xi))\right] \; x_{1,\xi}(\xi) \; d\xi \tag{2.4}$$

where $\sigma_{22}(x_1)$ is the stress acting on the element edge in front of the crack tip in Fig. 2.1b and $x_{1,\xi}$ is the Jacobian of the transformation between ξ and x_1. The total force F_2 may

be divided into three forces at nodes 1 to 3 using the shape functions by (Hughes, 1987, p. 67)

$$F_2^{(m)} = \int_{-1}^{1} \left[\sigma_{22}(x_1(\xi))N^{(m)}(\xi)\right]\, x_{1,\xi}(\xi)\, d\xi \tag{2.5}$$

where $N^{(m)}$ are the shape functions given in eqs. (2.1). The crack face opening displacement in natural coordinates is given by

$$\Delta u_2(\Delta a - x_1(\xi)) = \sum_{m=1}^{3} N^{(m)}(\xi)\Delta u_2^{(m)} \tag{2.6}$$

where $\Delta u_2^{(m)}$ is the displacement jump at node m of the VCE in the x_2-direction. The displacement jumps are calculated in element (1) in Fig. 2.1c.

Equation (1.104) for the mode I energy release rate may be rewritten in natural coordinates as

$$\mathcal{G}_I = \lim_{\Delta a\to 0} \frac{1}{2\Delta a} \int_{-1}^{1} \left[\sigma_{22}(x_1(\xi))\Delta u_2(\Delta a - x_1(\xi))\right]\, x_{1,\xi}\, d\xi. \tag{2.7}$$

As mentioned in Section 1.6, the Irwin crack closure integral represents the work done to close the VCE. Substituting eq. (2.6) into eq. (2.7) results in

$$\mathcal{G}_I = \lim_{\Delta a\to 0} \frac{1}{2\Delta a} \sum_{m=1}^{3} \int_{-1}^{1} \left[\sigma_{22}(x_1(\xi))N^{(m)}(\xi)\Delta u_2^{(m)}\right]\, x_{1,\xi}\, d\xi. \tag{2.8}$$

Since element (1) is used to calculate both the stress, in Fig. 2.1b, and displacement jumps, in Fig. 2.1c, and node 2 remains in the same location before and after the VCE, there is no ambiguity with respect to $x_{1,\xi}$. The displacement jumps at the nodes are found from an FEA, so that eq. (2.8) may be rewritten as

$$\mathcal{G}_I = \lim_{\Delta a\to 0} \frac{1}{2\Delta a} \sum_{m=1}^{3} \Delta u_2^{(m)} \int_{-1}^{1} \left[\sigma_{22}(x_1(\xi))N^{(m)}(\xi)\right] x_{1,\xi}\, d\xi. \tag{2.9}$$

Substituting eq. (2.5) into eq. (2.9) and omitting the limit yields

$$\mathcal{G}_I = \frac{1}{2\Delta a} \sum_{m=1}^{3} F_2^{(m)}\Delta u_2^{(m)}. \tag{2.10}$$

Since node 3 is at the crack tip in Fig. 2.1c, $\Delta u_2^{(3)} = 0$ and

$$\mathcal{G}_I = \frac{1}{2\Delta a} \sum_{m=1}^{2} F_2^{(m)}\Delta u_2^{(m)}. \tag{2.11}$$

This derivation is based on two FEAs.

For one FEA, the crack face opening displacements at the nodal points in element (1) in Fig. 2.1c, may be approximated from element (1′) in Fig. 2.1b, so that eq. (1.107) with

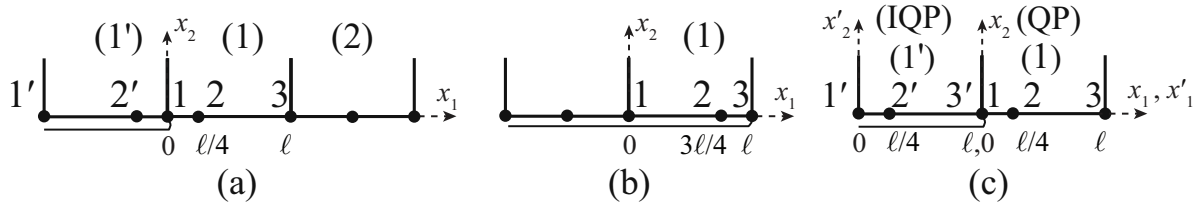

Figure 2.2: For a QP-element: (a) the crack before and (b) after the VCE. (c) IQP-element containing node $2'$ and QP-element containing node 2.

$M = 2$ is found. For the mode II energy release rate, a similar derivation may be carried out beginning with eq. (1.105). Equation (1.108) is found with $M = 2$.

To the best of the authors' knowledge, this development does not appear in the literature. In Ramamurthy et al. (1986), Raju (1987) and Nairn (2011), the first three terms of the asymptotic expansion for the stress on the element edge ahead of the crack tip in a linear elastic and homogeneous material was used to obtain eqs. (1.107) and (1.108) for eight-noded elements. This is seen to be unnecessary as shown here. The derivation of eqs. (1.107) and (1.108) is independent of the stress distribution ahead of the crack tip and, hence, also applicable to interface cracks.

For a QP-element, difficulties arise when using the VCCT. The location of node 2 is not the same in element (1) before and after the VCE as shown in Figs. 2.2a and 2.2b, respectively. Node 2 is at $x_1 = \ell/4$ in Fig. 2.2a and at $x_1 = 3\ell/4$ in Fig. 2.2b. Note that for two FEAs, the displacement jump at node 2 in Fig. 2.2b which is at $x_1 = 3\ell/4$ is closed by the force at node 2 in Fig. 2.2a which is at $x_1 = \ell/4$. Using eq. (2.11) with QP-elements implies that the nodal point force at nodal point 2 in Fig. 2.2a closes the displacements jump at nodal point 2 in Fig. 2.2b. This is not possible. Hence, this method is problematic with QP-elements.

In Ramamurthy et al. (1986) and Raju (1987), a different approach was taken. Equation (1.104) was calculated using the analytic stress distribution from element (1) in Fig. 2.2a. The displacement jumps were taken from element $(1')$ in Fig. 2.2a. To account for the fact that the nodal point force $F_2^{(2)}$ is not located in the same relative position as the displacement jump $\Delta u_2^{(2')}$, the nodal point forces were distributed by means of the weights t_{nm} in eq. (1.111). It may be noted that for an interface crack other weights t_{nm} are required. In Nairn (2011), in addition to the weights t_{nm}, nodal edge forces were used in order to obtain more accurate results. The accuracy of those approaches will be examined in Section 2.2.

Another possibility for using a QP-element ahead of the crack tip with eqs. (1.107) and (1.108), is to change the position of node $2'$ in element $(1')$. For this element, called the inverse quarter-point (IQP) element, node $2'$ is located at $x_2'^{(2')} = \ell/4$, as shown in Fig. 2.2c. Note that for the primed nodes, use is made of the x'_1, x'_2 coordinate system

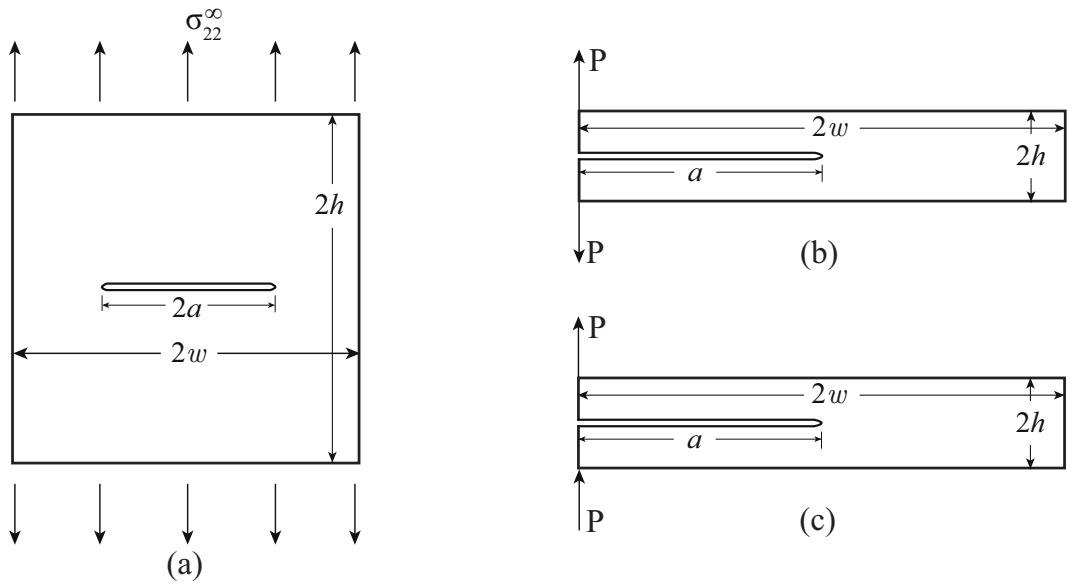

Figure 2.3: Geometry for (a) a CCT specimen, (b) a DCB specimen and (c) a pure mode II beam specimen.

with its origin located at node $1'$, as shown in Fig. 2.2c. In this way, node 2 in the QP-element and node $2'$ in the IQP-element are at the same relative distance $\ell/4$ within their respective elements. The stress singularity of the QP-element ahead of the crack tip is not influenced by the change of the location of node $2'$. The stress singularity of the IQP-element is also of order 1/2 but at node $1'$.

Equation (2.11) is presented for two FEAs using eight-noded elements. It also may be used for two FEAs, where for the first FEA, a QP-element is used as shown in Fig. 2.2a. For the second FEA, element (1) in Fig. 2.2b may be an IQP-element with node 2 moved to $x_1 = \ell/4$. Comparison of the numerical results using eight-noded elements, QP-elements and IQP-elements will be presented in Section 2.2.

2.2 Numerical results for different types of elements

In this section, three problems are solved by means of an FEA using a commercial finite element program Abaqus/CAE (2016). All bodies are linear elastic, homogeneous and isotropic. The material of the bodies is taken to be aluminium where $E = 70$ GPa and $\nu = 0.3$. The first problem is a CCT specimen, as shown in Fig. 2.3a. A double cantilever beam (DCB) specimen subjected to mode I loading as shown in Fig. 2.3b, is the second problem. The third problem is a pure mode II beam specimen shown in Fig. 2.3c. These problems are solved to compare the different approaches of calculating the energy release rates and stress intensity factors.

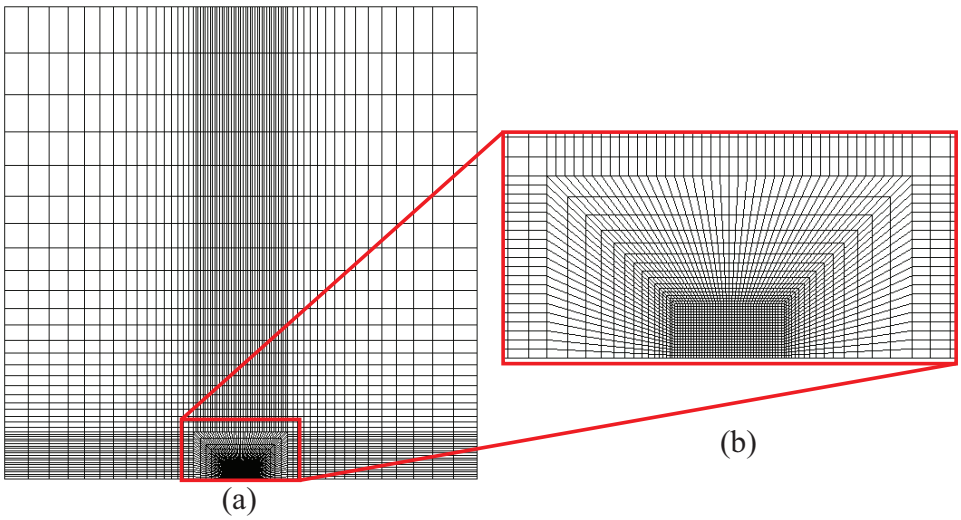

Figure 2.4: Schematic view of (a) the mesh and (b) focused mesh in the crack tip region that is used to carry out the FEA of the CCT specimen for a VCE of 0.5 μm.

The CCT specimen is subjected to a remote tensile traction, as shown in Fig. 2.3a. The length of the crack is $2a = 10$ mm. The width and height of the body are $2w = 2h = 20$ mm. The applied tensile traction is $\sigma_{22}^{\infty} = 1$ MPa and plane strain conditions are imposed using CPE8 elements of Abaqus/CAE (2016). It is noted that these are eight noded isoparametric bi-quadratic elements. The finite element method is used to determine the crack face displacement jumps and the nodal point forces ahead of the crack tip. As a results of symmetry, only one-quarter of the body is modeled. The FEAs are carried out with four different element lengths in the vicinity of the crack tip: 1 mm, 0.5 mm, 50 μm and 0.5 μm. For the first three lengths, uniform meshes are used with all elements being square. For the element length of 0.5 μm, a focused mesh in the vicinity of the crack tip is used. A schematic view of the mesh of the body and the focused mesh in the vicinity of the crack tip are shown in Figs. 2.4a and 2.4b, respectively. In the schematic view, there are only twenty elements ahead of the crack tip. In the actual mesh, the element size in the vicinity of the crack tip is 0.5×0.5 μm^2 with 100 elements of this size ahead, behind, above and below the crack tip. ee elements are surrounded by a focused mesh. Ahead, behind, above and below the focused mesh there is a transition mesh. The greatest aspect ratio of these elements is 50.

The normalized stress intensity factor for mode I is defined as

$$\hat{K}_I = \frac{K_I}{\sigma_{22}^{\infty}\sqrt{\pi a}} \,. \tag{2.12}$$

The solution for this CCT problem is given in Isida (1971) as

$$\hat{K}_I^{(\mathrm{ex})} = 1.334. \tag{2.13}$$

Note that in Isida (1971), the stress intensity factors are found from a convergent series

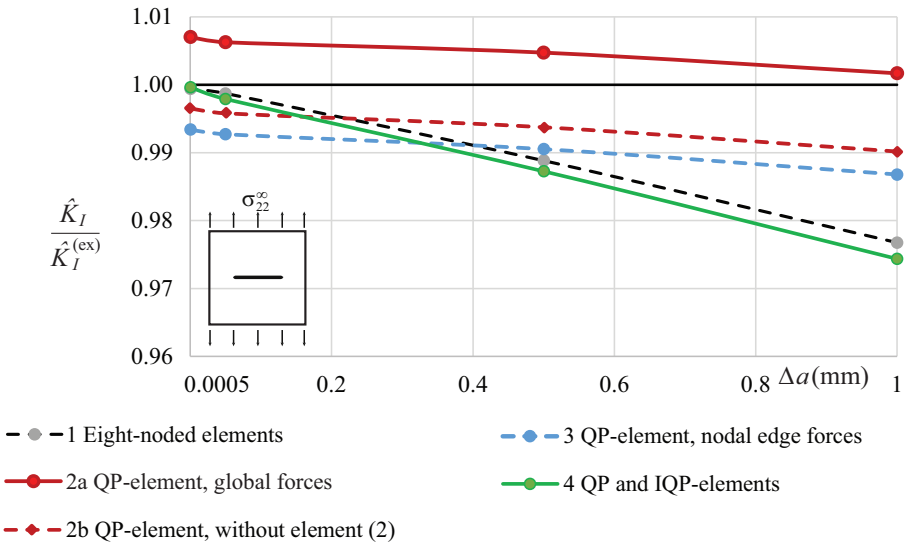

Figure 2.5: The normalized stress intensity factors obtained by the different approaches divided by the analytical solution for the CCT specimen. Solid black line is the exact solution.

solution using boundary collocation. This solution is thought to be exact up to four significant figures.

The normalized stress intensity factors are obtained by five approaches. Use of two eight-noded elements with eq. (1.107) and $M = 2$, is the first approach. In the second approach, the two elements adjacent to the crack tip are replaced by QP-elements and use is made of eq. (1.109). Recall that eq. (1.109) corrects for the mismatch between nodes 2 and 2′ in Fig. 2.2a. For the second approach, the results are shown for two options. The first option, 2a (Sethuraman and Maiti, 1988; Pang et al., 1990), uses the global nodal point forces from elements (1′), (1) and (2) in Fig. 2.2a; in the second approach, 2b (Ramamurthy et al., 1986; Raju, 1987), use is made only of elements (1′) and (1) without element (2) in Fig. 2.2a. In the third approach (Nairn, 2011), QP-elements and nodal edge forces are used, together with eq. (1.109). The fourth approach presented here consists of using one QP-element and one IQP-element, as shown in Fig. 2.2c and eq. (1.107) with $M = 2$. For each of the approaches, FEAs are carried out for the different element sizes. The values of $\mathcal{G}_I$ are obtained and the normalized stress intensity factors are calculated using eqs. (1.147) and (2.12).

The values obtained for $\hat{K}_I$ are normalized by the comparison solution in eq. (2.13) and presented in Fig. 2.5. The errors for $\hat{K}_I$ are shown in Table 2.1. The first and the fourth approaches converge to excellent results. Recall that Δa is the VCE and is also the length of the elements adjacent to the crack tip. For the first approach, the errors converge from -2.3% for $\Delta a = 1$ mm to -0.06% for $\Delta a = 0.5$ μm, as shown in Table 2.1. Using more elements as the VCE, as done in Banks-Sills and Farkash (2016), did not improve the

Table 2.1: Errors of the normalized stress intensity factors obtained by the different approaches for the CCT specimen.

approach	1	2a	2b	3	4
element type	eight-noded	QP	QP	QP	QP and IQP
Δa	$\hat{K}_I(\%)$	$\hat{K}_I(\%)$	$\hat{K}_I(\%)$	$\hat{K}_I(\%)$	$\hat{K}_I(\%)$
1.0 (mm)	-2.32	0.17	-0.98	-1.32	-2.56
0.5 (mm)	-1.12	0.47	-0.63	-0.95	-1.27
50 (μm)	-0.13	0.63	-0.42	-0.73	-0.21
0.5 (μm)	-0.06	0.70	-0.35	-0.66	-0.04

results. For the fourth approach, the errors converge from -2.6% for $\Delta a = 1$ mm to -0.04% for $\Delta a = 0.5$ μm. The behavior of the results for eight-noded elements and a pair of IQP and QP-elements is very similar, as presented in Fig. 2.5. The similar results and behavior show that for the VCCT, nodes 2 and $2'$ should indeed be located at the same relative location with respect to nodes 1 and $1'$, respectively, as shown in Fig. 2.2c. Since an IQP-element requires modification of the mesh that is generated by the finite element program, use of eight-noded elements is preferred. When using only QP-elements, the results are less accurate. For the global nodal point forces for approach 2a, the results diverge from 0.2% for $\Delta a = 1$ mm to 0.7% for $\Delta a = 0.5$ μm. The good result for the coarse mesh seems random. If element (2) in Fig. 2.2a is not used as in option 2b, the results converge to -0.35% for $\Delta a = 0.5$ μm. For the third approach of Nairn (2011) using nodal edge forces, the results converge to -0.66% for $\Delta a = 0.5$ μm. For QP-elements, using approach 2b is found to be the most accurate, but the eight-noded elements are still preferred. From this particular problem, one may conclude that using QP-elements for VCCT results in unnecessary inaccuracy as Δa approaches zero. Moreover, there is no obvious benefit to using a QP approach which involves additional actions during meshing and post-processing.

Two additional FEAs are carried out on CCT specimens with crack lengths of $a = 3$ mm and $a = 7$ mm. The comparison solution for these problems also may be found in Isida (1971) with $\hat{K}_I^{(\text{ex})} = 1.123$ for $a/w = 0.3$ and $\hat{K}_I^{(\text{ex})} = 1.680$ for $a/w = 0.7$. The same behavior of the different approaches is observed as for that of the crack of length $a = 5$ mm. For a crack length $a = 3$ mm, all of the errors for the finest mesh converge to the same errors as for $a = 5$ mm with a difference of 0.06%. For example, for the first approach the error of the finest mesh is 0.00% instead of -0.06%, and for the fourth approach, the error is 0.02% instead of -0.04%. For a crack length $a = 7$ mm, the errors for the finest mesh converge to the same errors, once again, but with a difference of -0.13% as compared to that of $a/w = 0.5$.

Next, the DCB specimen shown in Fig. 2.3b is discussed. This problem was solved in

Nairn (2011). From simple beam theory (SBT) and plane stress conditions

$$\mathcal{G}_{SBT} = \frac{12\mathrm{P}^2 a^2}{B^2 h^3 E} \tag{2.14}$$

where P is the applied load, a is the crack length, B and h are the specimen depth and half-height and E is Young's modulus. Accounting for shear deformation and crack root rotation as presented in Williams (1989)

$$\mathcal{G}_I = \left(1 + 0.67\,\frac{h}{a}\right)^2 \mathcal{G}_{SBT}. \tag{2.15}$$

In the FEA, the DCB specimen is subjected to an applied load P = 1 N, as shown in Fig. 2.3b; $a = 20$ mm; $2h =$ 4 mm, and the length of the body is $2w =$ 40 mm. Plane stress conditions are imposed using CPS8 elements of Abaqus/CAE (2016). It is noted that these are eight noded isoparametric bi-quadratic elements. The FEAs are carried out with four different element lengths in the vicinity of the crack tip: 1 mm, 0.5 mm, 100 μm and 0.5 μm. For the first three lengths, uniform meshes were used with all elements being square. For the element length of 0.5 μm, a focused mesh is used, similar to that in Fig. 2.4b. In Nairn (2011), ten different element lengths which were not explicitly specified were used, with a size between 1 mm and 0.1 mm with uniform meshes.

For the DCB specimen investigated here and in Nairn (2011), using eq. (2.15),

$$\mathcal{G}_I = 1.1385\ \mathcal{G}_{SBT}. \tag{2.16}$$

The result for eight-noded elements converged in Nairn (2011) to

$$\mathcal{G}_I = 1.1392\ \mathcal{G}_{SBT}. \tag{2.17}$$

The other approaches used there were compared to this latter result. Recall that in Nairn (2011), the results were extrapolated to $\Delta a = 0$. It may also be noted that although in Nairn (2011), results for quadratic elements appear to be constant for all element sizes, this is an illusion created by the large scale used to plot the results. The values obtained here for $\mathcal{G}_I$ are normalized by $\mathcal{G}_{SBT}$ and are presented in Fig. 2.6. The errors for $\mathcal{G}_I$ are shown in Table 2.2. But the ratio using eight-noded elements with the element length of 0.5 μm was found here to be 1.1385; the same as the result presented in eq. (2.16). The errors here are compared to that solution and the value of the solid black line in Fig. 2.6 is 1.1385. For the third approach (Nairn, 2011), results are also shown for CPS8R elements. It appears that in Nairn (2011), CPS8R elements with reduced integration were used, resulting in a difference of less than -0.33% for the smallest elements as observed in Table 2 column 6. In Nairn (2011), for eight-noded regular elements, the results were extrapolated without that at $\Delta a = 0.5$ μm in Table 2.2 to obtain the ratio between $\mathcal{G}_I$ and $\mathcal{G}_{SBT}$ as 1.1392. Note that in Nairn (2011), the results were extrapolated to $\Delta a = 0$, whereas here in Fig. 2.6 and Table 2.2 results are shown for $\Delta a = 0.5$ μm. In Fig. 2.6, the

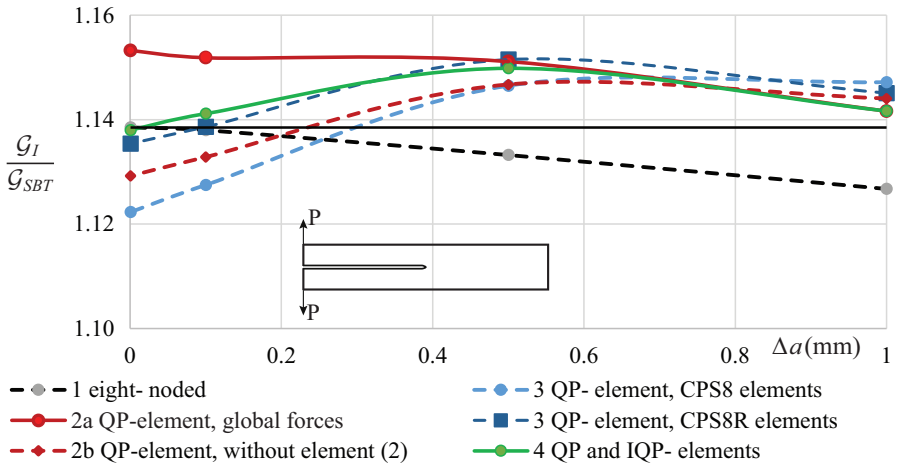

Figure 2.6: The mode I energy release rates $\mathcal{G}_I$ obtained by the different approaches normalized by $\mathcal{G}_{SBT}$ for the DCB specimen in eq. (2.14). Solid black line is the comparison solution.

Table 2.2: Errors of $\mathcal{G}_I$ obtained by the different approaches for the DCB specimen.

approach element type	1 eight-noded	2a QP	2b QP	3 QP CPS8	3 QP CPS8R	4 QP and IQP
Δa	$\mathcal{G}_I(\%)$	$\mathcal{G}_I(\%)$	$\mathcal{G}_I(\%)$	$\mathcal{G}_I(\%)$	$\mathcal{G}_I(\%)$	$\mathcal{G}_I(\%)$
1.0 (mm)	-1.03	0.27	0.49	0.76	0.52	0.28
0.5 (mm)	-0.46	1.11	0.72	0.70	1.08	1.00
0.1 (mm)	-0.04	1.17	-0.50	-0.97	-0.05	0.23
0.5 (μm)	0.00	1.30	-0.81	-1.42	-0.33	-0.05

results for $\Delta a = 0.5$ μm appear to be on the ordinate because of the relatively large scale of the abscissa. The results for the eight-noded elements of approach 1 are the same when using either CPS8 or CPS8R elements. There does not appear to be any justification for using reduced integration. The CPS8 elements are preferred for the problems investigated here.

Next, the results obtained here with CPS8 elements are discussed. The first and the fourth approaches converge again to excellent results. For the first approach, the errors converge from -1.03% for $\Delta a = 1$ mm to 0.00% for $\Delta a = 0.5$ μm, as shown in Table 2.2. For the fourth approach, the errors converge from 0.28% for $\Delta a = 1$ mm to -0.05% for $\Delta a = 0.5$ μm. The behavior of the results for eight-noded elements and a pair of IQP and QP-elements are not similar, as may be observed for the DCB specimen in Fig. 2.6. When using only QP-elements, the results are less accurate. When using the global nodal point forces for approach 2a, the results diverge from 0.27% for $\Delta a = 1$ mm to 1.30% for $\Delta a = 0.5$ μm. If element (2) in Fig. 2.2a is not used as in option 2b, the results diverge

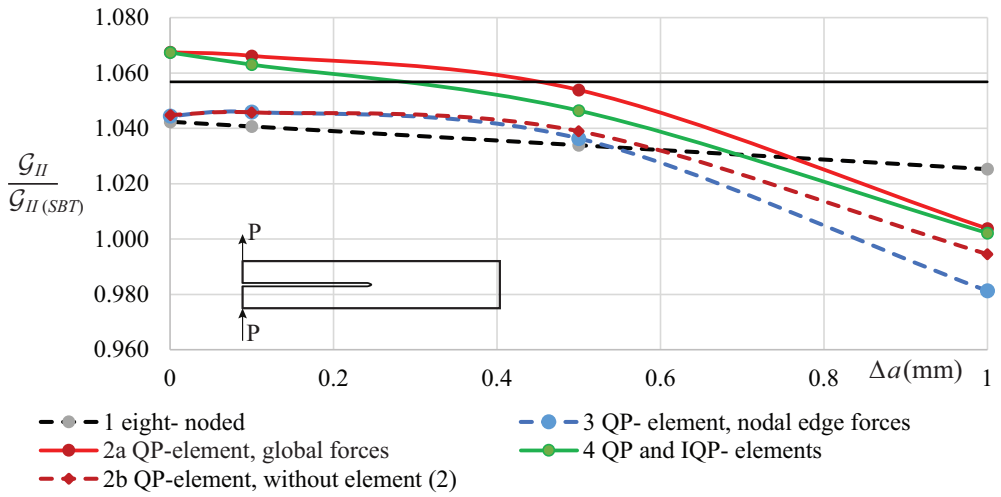

Figure 2.7: The mode II energy release rates $\mathcal{G}_{II}$ obtained by the different approaches normalized by $\mathcal{G}_{II(SBT)}$ for the pure mode II beam specimen. Solid black line is the solution in eq. (2.20).

from 0.49% for $\Delta a = 1$ mm to -0.81% for $\Delta a = 0.5$ μm. For the third approach in Nairn (2011), the results diverge to -1.42% for $\Delta a = 0.5$ μm. When using only QP-elements, approach 2b is found to be the most accurate. Nonetheless, the eight-noded elements lead to the best results.

The pure mode II beam specimen shown in Fig. 2.3c is discussed next. This problem was also solved in Nairn (2011). From SBT and plane stress conditions

$$\mathcal{G}_{II(SBT)} = \frac{9\mathrm{P}^2 a^2}{B^2 h^3 E} \tag{2.18}$$

where P is the applied load, a is the crack length, B and h are the specimen depth and half-height and E is Young's modulus. Accounting for shear deformation and crack root rotation presented in Wang and Williams (1992)

$$\mathcal{G}_{II} = \left(1 + 0.67\sqrt{\frac{11}{63}}\,\frac{h}{a}\right)^2 \mathcal{G}_{II(SBT)}. \tag{2.19}$$

In the FEA, the pure mode II beam specimen is subjected to an applied load P = 1 N, as shown in Fig. 2.3c. The dimensions of the body and the meshes are the same as those for the DCB specimen. For the pure mode II beam specimen, using eq. (2.19),

$$\mathcal{G}_{II} = 1.0568\ \mathcal{G}_{II(SBT)}\ . \tag{2.20}$$

The values obtained here for $\mathcal{G}_{II}$ are normalized by $\mathcal{G}_{II(SBT)}$ and are presented in Fig. 2.7. The errors for $\mathcal{G}_{II}$ are shown in Table 2.3. When compared to the solution in eq. (2.20), approaches 1, 2b and 3 converge to similar results with errors between -1.1% and -1.4%. Approaches 2a and 4 converge to similar results with errors of 0.9% and 1.0%, respectively.

Table 2.3: Errors of $\mathcal{G}_{II}$ obtained by the different approaches for the pure mode II beam specimen in Fig. 2.3c as compared to eq. (2.20); errors in parenthesis obtained as compared to the J-integral result in eq. (2.21).

approach element type	1 eight-noded	2a QP	2b QP	3 QP	4 QP and IQP
Δa	$\mathcal{G}_{II}(\%)$	$\mathcal{G}_{II}(\%)$	$\mathcal{G}_{II}(\%)$	$\mathcal{G}_{II}(\%)$	$\mathcal{G}_{II}(\%)$
1.0 (mm)	-3.0 (-1.6)	-5.0 (-3.7)	-5.9 (-4.6)	-7.1 (-5.9)	-5.2 (-3.9)
0.5 (mm)	-2.2 (-0.81)	-0.3 (1.1)	-1.7 (-0.32)	-1.9 (-0.57)	-1.0 (0.39)
0.1 (mm)	-1.5 (-0.16)	0.9 (2.3)	-1.0 (0.33)	-1.0 (0.35)	0.6 (2.0)
0.5 (μm)	-1.4 (0.00)	0.9 (2.4)	-1.1 (0.24)	-1.2 (0.20)	1.0 (2.4)

Using the J-integral with either eight-noded regular elements or QP-elements and the finest mesh, eq. (2.20) was found to be

$$\mathcal{G}_{II} = 1.0423\ \mathcal{G}_{II(SBT)}\ . \tag{2.21}$$

This is the same value found in Nairn (2011) by means of VCCT and eight-noded elements. The errors as compared to the J-integral result in eq. (2.21) are presented in parenthesis in Table 2.3. The errors for the finest mesh as compared to the J-integral for approaches 1, 2b and 3 are 0.0%, 0.24% and 0.20%, respectively. For the other two approaches, the error is 2.4%. It would appear that the results in eqs. (2.19) and (2.20) are only approximate.

Thus, the most consistent approach with the best results for all three problems is the first approach of eight-noded regular elements, which is clearly preferred. Using an IQP-element was found to be accurate here only for mode I problems. For the mode II problem, using an IQP-element produces poor results. Recall that the stress singularity of the IQP-element is of order 1/2 but at node $1'$ in Fig. 2.2c. Perhaps this is the reason for the poor results. Thus, QP and IQP-elements used together, as well as QP-elements used alone are not recommended. Part of this section appears in Farkash and Banks-Sills (2020).

2.3 A new equation for calculation of the phase angle

In Banks-Sills and Farkash (2016), the relations between the complex stress intensity factor for an interface crack between two linear elastic, isotropic and homogeneous materials and the energy release rates were found. The stress intensity factors are related to the energy release rates through the phase angle. In this section, first, the relations between the stress intensity factors for a crack in a linear elastic, isotropic and homogeneous material and the energy release rates and the dual energy release rates are found. Second, new relations between the energy release rates and the complex stress intensity factor for an interface crack between two linear elastic, isotropic and homogeneous materials and new relations between the energy release rates and the phase angle of the complex stress intensity factor

are determined. It will be shown that one of the new relations for the phase angle is valid for any value of the phase angle whereas, others, of which one of them was found in Banks-Sills and Farkash (2016), are not.

For a crack in a linear elastic, homogeneous and isotropic material, explicit expressions for the in-plane stress intensity factors are given in eqs. (1.147) and (1.148). The relation between the dual energy release rates and the stress intensity factors for a crack in this material is obtained. Using eqs. (1.1) and (1.7), the stress components ahead of the crack tip are given by

$$\left\{ \begin{array}{c} \sigma_{22} \\ \sigma_{21} \end{array} \right\} = \left\{ \begin{array}{c} \dfrac{K_I}{\sqrt{2\pi x_1}} \\ \dfrac{K_{II}}{\sqrt{2\pi x_1}} \end{array} \right\} . \tag{2.22}$$

Using eqs. (1.4) and (1.10), the crack face displacement jumps are given as

$$\left\{ \begin{array}{c} \Delta u_2 \\ \Delta u_1 \end{array} \right\} = \frac{8}{\bar{E}} \sqrt{\frac{-x_1}{2\pi}} \left\{ \begin{array}{c} K_I \\ K_{II} \end{array} \right\} , \tag{2.23}$$

where $\bar{E}$ is defined in eq. (1.17). Substituting the stresses ahead of the crack tip and the crack face displacement jumps into eqs. (1.176) and (1.177) results in

$$\mathcal{I}_I = \lim_{\Delta a \to 0} \frac{1}{2\Delta a} \int_0^{\Delta a} \left(\frac{K_I}{\sqrt{2\pi x_1}} \frac{8K_{II}}{\bar{E}} \sqrt{\frac{\Delta a - x_1}{2\pi}} \right) dx_1 \tag{2.24}$$

$$\mathcal{I}_{II} = \lim_{\Delta a \to 0} \frac{1}{2\Delta a} \int_0^{\Delta a} \left(\frac{K_{II}}{\sqrt{2\pi x_1}} \frac{8K_I}{\bar{E}} \sqrt{\frac{\Delta a - x_1}{2\pi}} \right) dx_1. \tag{2.25}$$

In eqs. (2.24) and (2.25), $\mathcal{I}_I$ and $\mathcal{I}_{II}$ are defined as the dual energy release rates. From eqs. (2.24) and (2.25) it may be observed that

$$\mathcal{I}_I = \mathcal{I}_{II}. \tag{2.26}$$

From Gradshteyn and Ryzhik (2015, p. 318) it may be shown that

$$\int_0^{\Delta a} \left(\sqrt{\frac{\Delta a - x_1}{x_1}} \right) dx_1 = \frac{\pi \Delta a}{2} . \tag{2.27}$$

Substituting the expression in eq. (2.27) into eqs. (2.24) and (2.25) and using the equality in eq. (2.26) leads to

$$\mathcal{I}_I = \mathcal{I}_{II} = \frac{K_I K_{II}}{\bar{E}} . \tag{2.28}$$

Noting eqs. (1.152), (1.176) and (1.177)

$$\mathcal{G}_{I-II} = \mathcal{I}_I + \mathcal{I}_{II}. \tag{2.29}$$

Using the relation between $\mathcal{G}_{I-II}$ and $\mathcal{I}_I$ and $\mathcal{I}_{II}$ given in eqs. (2.29), (1.147), (1.148) and (2.28) results in

$$\mathcal{G}_{I-II} = 2\mathcal{I}_I = 2\mathcal{I}_{II} = \frac{2K_I K_{II}}{\bar{E}} = 2\sqrt{\mathcal{G}_I \mathcal{G}_{II}} \ . \tag{2.30}$$

Noting eqs. (1.22) and (2.30)

$$\mathcal{G}_{I-II}^2 + (\mathcal{G}_I - \mathcal{G}_{II})^2 = \mathcal{G}_I^2 + \mathcal{G}_{II}^2 + 2\ \mathcal{G}_I \mathcal{G}_{II} = (\mathcal{G}_I + \mathcal{G}_{II})^2 = \mathcal{G}^2 \tag{2.31}$$

where in this section $\mathcal{G}$ is equal to the in-plane energy release rate, $\mathcal{G}_{2D}$. From Gradshteyn and Ryzhik (2015, p. 59) it may be shown that

$$\tan^{-1}\left(\frac{2xy}{x^2 - y^2}\right) = 2\tan^{-1}(y/x) \ . \tag{2.32}$$

Noting eqs. (1.19), (1.20) and (2.30) and using the identity from eq. (2.32), the angle between $\mathcal{G}_{I-II}$ and $(\mathcal{G}_I - \mathcal{G}_{II})$ is given as

$$\tan^{-1}\left(\frac{\mathcal{G}_{I-II}}{\mathcal{G}_I - \mathcal{G}_{II}}\right) = \tan^{-1}\left(\frac{2K_I K_{II}}{K_I^2 - K_{II}^2}\right) = 2\tan^{-1}\left(\frac{K_{II}}{K_I}\right) \tag{2.33}$$

From eqs. (2.31) to (2.33), it is found that

$$\psi = \tan^{-1}\left(\frac{K_{II}}{K_I}\right) = \frac{1}{2}\tan^{-1}\left(\frac{\mathcal{G}_{I-II}}{\mathcal{G}_I - \mathcal{G}_{II}}\right) \tag{2.34}$$

where ψ is the phase angle related to the mode mixity ratio K_{II}/K_I. From eqs. (2.31) and $(2.34)_2$, $\mathcal{G}_{I-II}$ and $(\mathcal{G}_I - \mathcal{G}_{II})$ are the sides of a right triangle, 2ψ is the angle between $(\mathcal{G}_I - \mathcal{G}_{II})$ and $\mathcal{G}$ where the latter is the hypotenuse.

Next, an interface crack between two dissimilar isotropic materials is considered. For clarity, some of the equations from Section 1.6.2 are repeated here. Using the stress and displacement fields from Rice et al. (1990) and Deng (1993), the tractions along the interface ahead of the crack tip and the crack face displacement jumps are found and given in eqs. (1.150) and (1.151), respectively. The coordinate system is shown in Fig. 1.9a; the complex stress intensity factor is given in eq. (1.29). In eqs. (1.150) and (1.151), the oscillatory parameter is given in eq. (1.25).

In order to relate the stress intensity factors K_1 and K_2 to the energy release rates, two auxiliary integrals were considered in Banks-Sills and Farkash (2016) and Farkash (2016), namely,

$$A = \frac{1}{2\Delta a}\int_0^{\Delta a} \Big[\sigma_{22}(x_1) + i\sigma_{21}(x_1)\Big]\Big[\Delta u_2(\Delta a - x_1) - i\Delta u_1(\Delta a - x_1)\Big]\, dx_1 \tag{2.35}$$

$$D = \frac{1}{2\Delta a}\int_0^{\Delta a} \Big[\sigma_{22}(x_1) + i\sigma_{21}(x_1)\Big]\Big[\Delta u_2(\Delta a - x_1) + i\Delta u_1(\Delta a - x_1)\Big]\, dx_1 \ . \tag{2.36}$$

These integrals are repeated from eqs. (1.169) and (1.170), respectively. Using the real and imaginary parts of the auxiliary integrals, it may be shown that

$$\mathcal{G}_i = \mathcal{G}_I + \mathcal{G}_{II} = \lim_{\Delta a \to 0} \Re(A) \tag{2.37}$$

$$\mathcal{G}_I - \mathcal{G}_{II} = \lim_{\Delta a \to 0} \Re(D) \tag{2.38}$$

$$\mathcal{G}_I = \frac{1}{2} \lim_{\Delta a \to 0} \Re(A + D) \tag{2.39}$$

$$\mathcal{G}_{II} = \frac{1}{2} \lim_{\Delta a \to 0} \Re(A - D) \tag{2.40}$$

$$\mathcal{G}_{I-II} = \mathcal{I}_I + \mathcal{I}_{II} = \lim_{\Delta a \to 0} \Im(D) \tag{2.41}$$

$$\mathcal{I}_{II} - \mathcal{I}_I = \lim_{\Delta a \to 0} \Im(A) \tag{2.42}$$

where $\mathcal{G}_i$ is the interface energy release rate, and $\Re(\cdot)$ and $\Im(\cdot)$ represent the real and imaginary parts of the quantity in parentheses.

It was shown in Banks-Sills and Farkash (2016) that the two auxiliary integrals are obtained as

$$A = \frac{1}{H_1}(K_1^2 + K_2^2) = \mathcal{G}_i \tag{2.43}$$

$$D = \frac{\cosh \pi\varepsilon}{\pi H_1} P K^2 \Delta a^{2i\varepsilon} \tag{2.44}$$

where H_1 is given in eq. (1.36) and P is given in eq. (1.173). The expressions for A and D are from eqs. (1.171) and (1.172), respectively.

Since A is real and noting eq. (2.42)

$$\mathcal{I}_I = \mathcal{I}_{II}. \tag{2.45}$$

By using the expressions found for the auxiliary integrals in eqs. (2.43) and (2.44), the values for eqs. (2.38) to (2.41) are obtained as

$$\mathcal{G}_I - \mathcal{G}_{II} = \Re(D) = C\mathcal{G}_i \cos\psi_D \tag{2.46}$$

$$\mathcal{G}_I = \frac{1}{2}\Re(A + D) = \frac{1}{2}\, \mathcal{G}_i\, (1 + C\cos\psi_D) \tag{2.47}$$

$$\mathcal{G}_{II} = \frac{1}{2}\Re(A - D) = \frac{1}{2}\, \mathcal{G}_i\, (1 - C\cos\psi_D) \tag{2.48}$$

$$\mathcal{G}_{I-II} = \Im(D) = C\mathcal{G}_i \sin\psi_D \tag{2.49}$$

where, the parameter C is defined in eq. (1.181) and

$$\psi_D = \tan^{-1}\left[\frac{\Im(D)}{\Re(D)}\right] = 2\psi + \psi_P + 2\varepsilon \ln \Delta a\ . \tag{2.50}$$

The last equality in eq. (2.50) is obtained from eq. (2.44), where ψ is the phase angle of the complex stress intensity factor, namely

$$\psi = \tan^{-1}\left(\frac{K_2}{K_1}\right) \tag{2.51}$$

and ψ_P is the phase angle of P defined as

$$\psi_P = \tan^{-1}\left(\frac{P_I}{P_R}\right)\ . \tag{2.52}$$

Noting eqs. (2.50) to (2.52), the phase angles ψ and ψ_P are constants for each specific problem; however, the phase angle ψ_D is a function of Δa through the term $2\varepsilon \ln \Delta a$. By using eqs. (2.41), (2.45) and (2.49), the dual energy rates are found to be

$$\mathcal{I}_I = \mathcal{I}_{II} = \frac{1}{2}\mathcal{G}_{I-II} = \frac{1}{2}C\mathcal{G}_i \sin \psi_D. \tag{2.53}$$

Since the stress intensity factors K_1 and K_2 are unknown, eq. (2.51) may not be used for determining the phase angle. However, it may be obtained by rearranging eq. (2.50) as

$$\psi = \frac{1}{2}\psi_D - \frac{1}{2}\psi_P - \varepsilon \ln \Delta a. \tag{2.54}$$

Note that ψ_D was found in Banks-Sills and Farkash (2016) and Farkash (2016) as

$$\psi_D = \cos^{-1}\left(\frac{1}{C}\frac{1-g}{1+g}\right) \tag{2.55}$$

where g is defined in Agrawal and Karlsson (2006) and is given in eq. (1.160). Substituting eq. (1.160) into eq. (2.55) or noting eq. (2.46) results in

$$\psi_D = \cos^{-1}\left(\frac{\mathcal{G}_I - \mathcal{G}_{II}}{C\mathcal{G}_i}\right) . \tag{2.56}$$

From eq. (2.49), ψ_D may also be defined as

$$\psi_D = \sin^{-1}\left(\frac{\mathcal{G}_{I-II}}{C\mathcal{G}_i}\right) . \tag{2.57}$$

Finally, using eqs. (2.46) and (2.49),

$$\psi_D = \tan^{-1}\left(\frac{\mathcal{G}_{I-II}}{\mathcal{G}_I - \mathcal{G}_{II}}\right) . \tag{2.58}$$

Noting eq. (2.56), ψ_D is the angle between $\mathcal{G}_I - \mathcal{G}_{II}$ and $C\mathcal{G}_i$ in a right triangle. The length $C\mathcal{G}_i$ is the hypotenuse of the right triangle. The side opposite ψ_D, from eq (2.57), is $\mathcal{G}_{I-II}$. From eqs. (2.46) and (2.49), it may be shown that $C\mathcal{G}_i$ is the magnitude of D. It may be pointed out that for a crack in a linear elastic, homogeneous and isotropic material, $\varepsilon = 0$, so that P in eq. (1.173) is real, equal to π, and from eq. (2.52), $\psi_P = 0$. Moreover, from eq. (1.181), $C = 1$. Thus, using eq. (2.50)

$$\psi_D = 2\psi \tag{2.59}$$

and $\mathcal{G}$, the total energy release rate for this crack, is the hypotenuse of the right triangle. Equation (2.59) is compatible with eq. (2.34).

In eqs. (2.56) and (2.57), the inverse trigonometric functions $\cos^{-1}(\cdot)$ and $\sin^{-1}(\cdot)$ produce the correct angle ψ_D only for $0 \le \psi_D \le \pi$ and $-\pi/2 \le \psi_D \le \pi/2$, respectively. The angle ψ_D, may be less than $-\pi/2$ or greater than π. For these cases, eqs. (2.56) and (2.57) are not useful. Therefore, use is made of eq. (2.58) which produces the correct value of ψ_D in

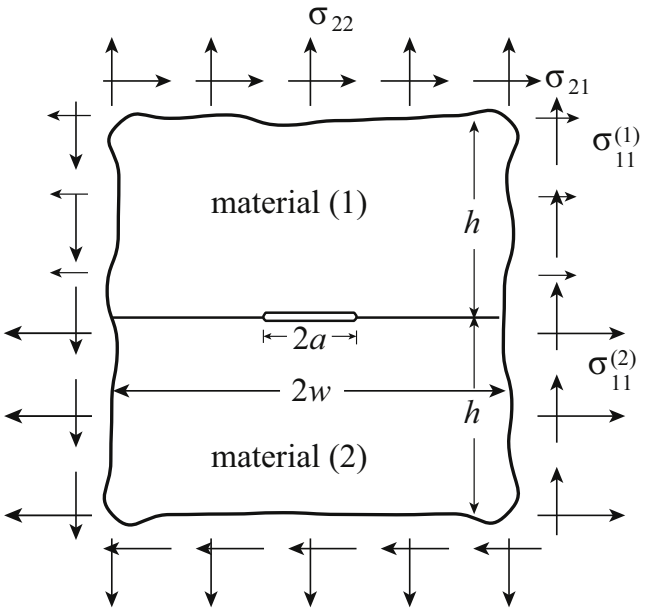

Figure 2.8: An interface crack of length $2a$ between two dissimilar linear elastic, isotropic and homogeneous materials in an infinite body subjected to tension σ_{22} and shear σ_{12} stresses. The width and height of the body $2w/2a = 2h/2a = 40$, respectively, are used in the finite element analysis.

the range $-\pi \leq \psi_D \leq \pi$ up to $\psi_D \pm 2\pi k$ for $k = ... -1, 0, 1, ...$. It may be pointed out that eq. (1.180) which appears in Banks-Sills and Farkash (2016) should be replaced by

$$\psi = \frac{1}{2}\tan^{-1}\left(\frac{\mathcal{G}_{I-II}}{\mathcal{G}_I - \mathcal{G}_{II}}\right) - \frac{1}{2}\tan^{-1}\left(\frac{P_I}{P_R}\right) - \varepsilon \ln \Delta a. \tag{2.60}$$

The stress intensity factors are obtained in Banks-Sills and Farkash (2016) and Farkash (2016) as

$$K_1 = \pm\sqrt{H_1 \mathcal{G}_i}\cos\psi \qquad K_2 = K_1 \tan\psi \tag{2.61}$$

where ψ is calculated from eq. (2.60). In eq. (2.61), two pairs of values for K_1 and K_2 are obtained. An assumption was made in Banks-Sills and Farkash (2016) that the crack is open; so that, the valid pair satisfies the inequality in eq. (1.184). The applicability of eqs. (2.56) to (2.58) is examined below.

Next, a problem in which ψ_D in eqs. (2.56) and (2.57) may not be found by using the inverse trigonometric functions $\cos^{-1}(\cdot)$ and $\sin^{-1}(\cdot)$ is presented. In Banks-Sills and Farkash (2016), the inverse trigonometric function $\cos^{-1}(\cdot)$ from eq. (2.55) was used to obtain ψ_D. Recall that $\cos^{-1}(\cdot)$ produces the correct value of ψ_D for $0 \leq \psi_D \leq \pi$. In Banks-Sills and Farkash (2016), the problem of a finite length interface crack between two dissimilar linear elastic, homogeneous and isotropic materials was considered. In that case, the oscillatory parameter $\varepsilon = -0.0758$ and $0.1\pi \leq \psi_D \leq 0.5\pi$. Recall that $\mathcal{G}_I$, $\mathcal{G}_{II}$, $\mathcal{G}_{I-II}$ and ψ_D depend on Δa, the VCE.

Table 2.4: Data for the solved problem in Fig. 2.8.

E_1 (GPa)	E_2 (GPa)	ν_1	ν_2	σ_{22} (MPa)	σ_{12} (MPa)	$\sigma_{11}^{(1)}$ (MPa)	$\sigma_{11}^{(2)}$ (MPa)
0.1	1	0.3	0.3	1	-1	1	6.143

Here, a different problem of a finite length interface crack between two dissimilar linear elastic, isotropic and homogeneous materials in an infinite body is considered, as illustrated in Fig. 2.8. This problem is solved by means of the finite element method using ABAQUS/CAE (2017). The analytical solution for the complex stress intensity factor is given in Rice (1988) as

$$K = (\sigma_{22} + i\sigma_{21})(1 + 2i\varepsilon)\sqrt{\pi a}(2a)^{-i\varepsilon} \tag{2.62}$$

where σ_{22} and σ_{21} are the far field tension and shear stresses given in Table 2.4 and shown in Fig. 2.8. The mechanical properties of the upper (1) and lower (2) materials are Young's moduli, $E_1 = 0.1$ GPa and $E_2 = 1$ GPa, respectively, and Poisson's ratios $\nu_1 = \nu_2 = 0.3$; these are also given in Table 2.4. In order to maintain displacement continuity along the interface, tractions are applied in the far field in the x_1-direction. The traction in the upper material $\sigma_{11}^{(1)}$ is chosen as unity and $\sigma_{11}^{(2)}$ is defined in eq. (1.165) for plane strain conditions. The values of $\sigma_{11}^{(1)}$ and $\sigma_{11}^{(2)}$ are given in Table 2.4. Using eqs. (2.51) and (2.62), the stress intensity factors and the phase angle ψ are found as $K_1 = 1.9594$ N/mm$^{3/2+i\varepsilon}$, $K_2 = -1.6088$ N/mm$^{3/2+i\varepsilon}$ and $\psi = -0.2\pi$, respectively. The analytical value of C in eq. (1.181) is $C = 1.0074$. The length of the crack is $2a = 2$ mm. To model the infinite body for the finite element analysis, w/a is taken to be 40 and h/w is taken to be unity. A schematic illustration of the mesh is shown in Fig. 2.9. A schematic view of the focused mesh in the vicinity of the crack tip and above the crack is shown in Fig. 2.4b. Outside

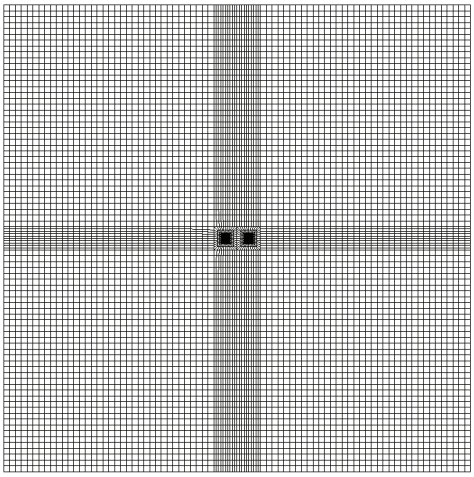

Figure 2.9: A schematic view of the mesh that was used to carry out the finite element analysis for the body in Fig. 2.8.

Table 2.5: Numerical values for the energy release rates and ψ_D using the inverse trigonometric functions in eqs. (2.56) to (2.58).

$\mathcal{G}_I$(N/m)	$\mathcal{G}_{II}$(N/m)	$\mathcal{I}_I$(N/m)	$\mathcal{I}_{II}$(N/m)	C$\mathcal{G}_i$(N/m)	$\mathcal{G}_{I-II}$(N/m)	$\mathcal{G}_I - \mathcal{G}_{II}$(N/m)
3.9	26.6	-10.3	-10.3	30.7	-20.6	-22.7
	analytic value	$\cos^{-1}(\cdot)$	$\sin^{-1}(\cdot)$	$\tan^{-1}(\cdot)$		
ψ_D	-0.8π	0.8π	-0.2π	-0.8π		

the refined sections of the mesh, the element size is 1×1 mm^2. The element size in the vicinity of the crack tips is 0.5×0.5 μm^2. There are 50 elements of this size ahead, behind, above and below the crack tip. Those elements are surrounded by a focused mesh. Ahead, behind, above and below the focused mesh there is a transition mesh. The greatest aspect ratio of these elements is 50.

A finite element analysis was carried out for this problem. The energy release rates, $\mathcal{G}_I$ and $\mathcal{G}_{II}$, are found using eqs. (1.107) and (1.108), respectively; the dual energy release rates, $\mathcal{I}_I$ and $\mathcal{I}_{II}$, are found using eqs. (1.185) and (1.186), respectively. The interface energy release rate is the sum of $\mathcal{G}_I$ and $\mathcal{G}_{II}$. The difference between $\mathcal{I}_I$ and $\mathcal{I}_{II}$, $\mathcal{I}$, was calculated using eq. (1.187). The values of the numerically calculated energy release rates are presented in Table 2.5 for a VCE consisting of 24 elements where $\Delta a = 12$ μm. Values of $\mathcal{I}_I$ and $\mathcal{I}_{II}$ are also presented in Table 2.5. This value of Δa produced the lowest value of $\mathcal{I} = 0$ to a high degree of accuracy. Value of $C\mathcal{G}_i$ from eq. (2.37) and (1.181), $\mathcal{G}_{I-II}$ from eq. (2.41) and $\mathcal{G}_I - \mathcal{G}_{II}$ are also presented in Table 2.5. In order to determine the stress intensity factors, the value of ψ in eq. (2.54) is required. To this end, eqs. (2.56) to (2.58) may be used to calculate ψ_D. These values are also shown in Table 2.5. From the

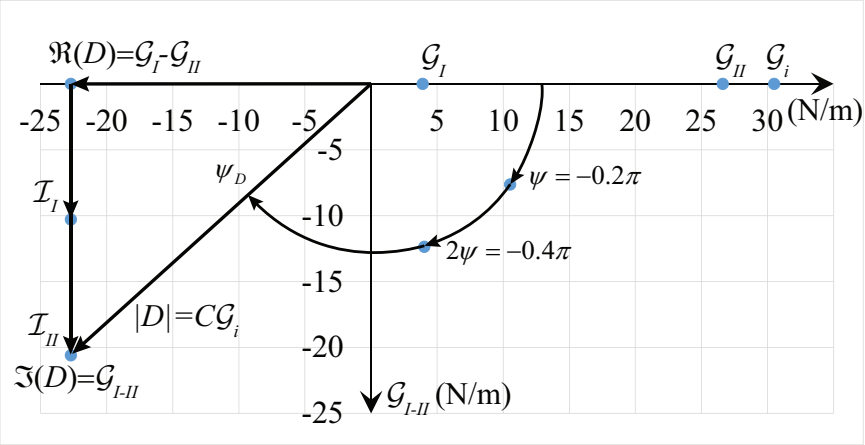

Figure 2.10: An illustration of the energy release rates and the phase angles obtained numerically.

analytical solution, ψ_D is found and presented in Table 2.5. It may be observed that only the $\tan^{-1}(\cdot)$ function yields the correct results. The purpose of this numerical exercise was to show that functions $\cos^{-1}(\cdot)$ and $\sin^{-1}(\cdot)$ cannot be used in the calculation of ψ_D.

A graphical illustration of the values from Table 2.5 is shown in Fig. 2.10. On the abscissa, the energy release rates $\mathcal{G}_I$, $\mathcal{G}_{II}$, $\mathcal{G}_i$ and $\mathcal{G}_I - \mathcal{G}_{II}$ related to the real parts of A and D, from eqs. (2.46) to (2.48) are plotted. The coupled energy release rate $\mathcal{G}_{I-II}$ and the dual energy release rates $\mathcal{I}_I$ and $\mathcal{I}_{II}$ are related to the imaginary part of D in eqs. (2.49) and $(2.53)_1$; they are plotted parallel to the ordinate in Fig. 2.10. Recall that the analytically calculated value of the phase angle ψ from eq. (2.51) is -0.2π. The numerical values of the terms ψ_P and $2\varepsilon \ln \Delta a$ from eq. (2.50), are -0.1π and -0.3π, respectively. The relation between ψ and $\psi_D = -0.8\pi$ is presented in Fig. 2.10.

In order to calculate ψ_D, eqs. (2.56) to (2.58) were used. The values of $C\mathcal{G}_i$, $\mathcal{G}_{I-II}$ and $\mathcal{G}_I - \mathcal{G}_{II}$ used in these equations are also shown in Table 2.5. In the fourth row of Table 2.5, values obtained for ψ_D are shown. As mentioned earlier, the inverse trigonometric functions $\cos^{-1}(\cdot)$ and $\sin^{-1}(\cdot)$ may be used to produce the correct value of ψ_D for various ranges of $-\pi/2 \leq \psi_D \leq \pi$. The function $\cos^{-1}(\cdot)$ produced ψ_D with an error in sign, as shown in Table 2.5. The function $\sin^{-1}(\cdot)$ produced a value of ψ_D which also differed from the exact value. When the signs of the numerator and dominator of the argument of the function $\tan^{-1}(\cdot)$ are considered properly, the correct value of ψ_D is produced. Thus, the function $\tan^{-1}(\cdot)$ is recommended in these calculations.

2.4 The coupled energy release rate and the dual energy release rates

In this section, analytic expressions for the crack face opening displacement jumps and the nodal point forces on the line ahead of the crack tip for a crack in a linear elastic, homogeneous and isotropic material are found. These will enable comparison of the dual energy release rates in eqs. (1.176) and (1.177), and their numerically calculated values, given in eqs. (1.185) and (1.186). It may be pointed out that analytically, the dual energy release rates are equal. It has been observed in Banks-Sills and Farkash (2016) that they are not equal when calculated numerically. The aim here is to shed light on this difference.

The crack face displacement jumps in the neighborhood of the crack tip are given in eq. (2.23). The normalized crack face displacement jumps will be used below and may be defined as

$$\Delta\hat{u}_1 = \frac{\bar{E}\Delta u_1}{8\sqrt{\frac{\ell}{2\pi}}\, K_{II}} \qquad \Delta\hat{u}_2 = \frac{\bar{E}\Delta u_2}{8\sqrt{\frac{\ell}{2\pi}}\, K_I} \tag{2.63}$$

where ℓ is the length of the element and $\bar{E}$ is given in eq. (1.17).

For the comparison mentioned above, the nodal point forces ahead of the crack tip are required. Details are given for obtaining the nodal point forces in the first two elements ahead of the crack tip. In a similar manner, one may obtain the additional nodal point forces ahead of the crack tip. The first ten nodal point forces are tabulated at the end of this section. The first term of the asymptotic expansion for the stresses ahead of the crack tip are given in eq. (2.22). Here, element (1) in Fig. 2.1b is considered. Using eqs. (2.2) and (2.3) and noting that $x_1^{(i)} = 0, \ell/2, \ell$ for $i = 1, 2, 3$, the mapping of the element and its derivative are given by

$$x_1(\xi) = \frac{\ell}{2}(1+\xi) \qquad x_{1,\xi} = \frac{\ell}{2} \, . \tag{2.64}$$

The total force F_2 may be found by substituting σ_{22} from eq. (2.22) and $x_{1,\xi}$ from eq. $(2.64)_2$ into eq. (2.4) as

$$F_2 = \sqrt{\frac{2\ell}{\pi}} \, K_I \, . \tag{2.65}$$

The nodal point forces in element (1) in Fig. 2.1b may be found using eq. (2.5). For example, for $F_2^{(1)}$, substituting σ_{22} from eq. (2.22), $N^{(1)}(\xi)$ from eq. $(2.1)_1$ and $x_{1,\xi}$ from eq. $(2.64)_2$ into eq. (2.5) results in

$$F_2^{(1)} = \frac{2}{5} \sqrt{\frac{2\ell}{\pi}} \, K_I \, . \tag{2.66}$$

By substituting eqs. $(2.1)_2$ or $(2.1)_3$ into eq. (2.5) instead of eq. $(2.1)_1$, the nodal point forces $F_2^{(2)}$ and $F_2^{(3)}$ are found as

$$F_2^{(2)} = \frac{8}{15} \sqrt{\frac{2\ell}{\pi}} \, K_I \qquad F_2^{(3)} = \frac{1}{15} \sqrt{\frac{2\ell}{\pi}} \, K_I \, . \tag{2.67}$$

As expected, the sum of $F_2^{(1)}$, $F_2^{(2)}$ and $F_2^{(3)}$ is F_2.

For the second element ahead of the crack tip, element (2) in Fig. 1.10b, the mapping of this element and its derivative are given by

$$x_1(\xi) = \frac{\ell}{2}(3+\xi) \qquad x_{1,\xi} = \frac{\ell}{2} \, . \tag{2.68}$$

By substituting eqs. $(2.22)_1$, (2.1) and $(2.68)_2$ into eq. (2.5), the nodal point forces are found to be

$$\begin{gathered} F_2^{(3)} = \frac{(88-61\sqrt{2})}{15} \sqrt{\frac{\ell}{\pi}} \, K_I \qquad F_2^{(4)} = \frac{8(3\sqrt{2}-4)}{15} \sqrt{\frac{\ell}{\pi}} \, K_I \\ F_2^{(5)} = \frac{2(19-13\sqrt{2})}{15} \sqrt{\frac{\ell}{\pi}} \, K_I \qquad . \end{gathered} \tag{2.69}$$

The total force at node 3 is the sum of the forces at that node from elements (1) and (2), so that

$$F_2^{(3)} = \frac{(88-60\sqrt{2})}{15} \sqrt{\frac{\ell}{\pi}} \, K_I \, . \tag{2.70}$$

Table 2.6: The analytic expressions for the normalized nodal point forces at nodes $i = 1$ to 10 ahead of the crack tip in the x_p-direction ($p = 1, 2$).

i	$\hat{F}_p^{(i)}$	i	$\hat{F}_p^{(i)}$
1	$\frac{2\sqrt{2}}{5}$	6	$\frac{(21\sqrt{6}-52)8}{15}$
2	$\frac{8\sqrt{2}}{15}$	7	$\frac{(-56+144\sqrt{2}-60\sqrt{6})}{5}$
3	$\frac{(88-60\sqrt{2})}{15}$	8	$\frac{(51\sqrt{6}-88)8}{15}$
4	$\frac{(3\sqrt{2}-4)8}{15}$	9	$\frac{(-240\sqrt{2}-87\sqrt{6}+175\sqrt{10})2}{15}$
5	$\frac{2(-120-13\sqrt{2})}{15}$	10	$\frac{8(56-25\sqrt{10})}{15}$

Additional analytically obtained nodal point forces at consecutive nodes are found in the same way. The normalized nodal point forces may be defined as

$$\hat{F}_1 = \frac{F_1}{\sqrt{\frac{\ell}{\pi}}\, K_{II}} \qquad \hat{F}_2 = \frac{F_2}{\sqrt{\frac{\ell}{\pi}}\, K_I} \tag{2.71}$$

where ℓ is the length of the element and they are tabulated in Table 2.6. It may be noted that elements (3) to (5) are not shown in Fig. 1.10b; they are the succeeding elements after element (2). From eq. $(2.22)_2$, the nodal point forces in the x_1-direction may be obtained by replacing K_I by K_{II}. The normalized nodal point forces are the same for both directions x_p, $p = 1, 2$.

It has been shown at the end of Section 1.6.2 that the lowest value of $\mathcal{I}$ may be used for choosing the best length of the VCE for a problem of an interface crack. In addition, it has been shown that although the dual energy release rates are analytically equal, numerically they differ. In Section 2.2, it was shown that only one element is required as the VCE in homogeneous material. Hence, there is no need to calculate $\mathcal{I}_I$ and $\mathcal{I}_{II}$ for this problem type. Nonetheless, a problem of a finite length crack in a linear elastic, homogeneous and isotropic infinite body is solved next. This allows use of the analytical expressions of the normalized nodal point forces in Table 2.6 and normalized crack face displacement jumps in eq. (2.63), to examine the behavior of $\mathcal{I}_I$ and $\mathcal{I}_{II}$.

The problem of a finite length crack in a linear elastic, homogeneous and isotropic infinite body, shown in Fig. 2.11 is solved by means of the finite element method using ABAQUS/CAE (2017). This problem is solved to examine the numerical and analytical difference between the dual energy release rates. The material of the body is taken to be aluminium where $E = 70$ GPa and $\nu = 0.3$. To model the infinite body for the finite element analysis, w/a is taken to be 40 and h/w is taken to be unity. The dimensions of the body and the mesh used in the finite element analysis are identical to those used in

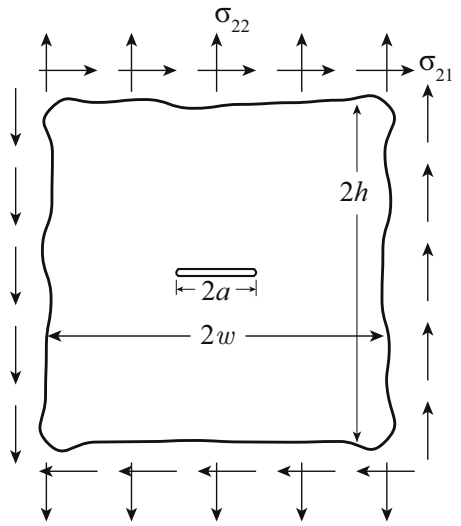

Figure 2.11: A crack of length $2a$ in a linear elastic, homogeneous and isotropic infinite body subjected to remote tensile and shear tractions. The width and height $w/a = h/a = 40$, respectively, are used in the finite element analysis.

Section 2.3 for the problem of an interface crack in an infinite body. A schematic view of the mesh of the body is shown in Fig. 2.9. Recall that in the vicinity of the crack tips, the element size is 0.5×0.5 μm^2. The remote tensile and shear tractions are $\sigma_{22} = 1$ MPa and $\sigma_{21} = 1$ MPa, respectively, and plane strain conditions are imposed. The finite element method is used to determine the crack face displacement jumps behind the crack tip and the nodal point forces ahead of the crack tip.

The normalized stress intensity factors are defined as

$$\hat{K}_I = \frac{K_I}{\sigma_{22}\sqrt{\pi a}} \qquad \hat{K}_{II} = \frac{K_{II}}{\sigma_{21}\sqrt{\pi a}} \,. \tag{2.72}$$

The analytical solution for this problem is given in Irwin (1957), so that

$$\hat{K}_I = \hat{K}_{II} = 1. \tag{2.73}$$

Noting eqs. (1.147), (1.148), (2.28) and (2.29), the normalized energy release rates are found to be

$$\hat{\mathcal{G}}_I = 1 \qquad \hat{\mathcal{G}}_{II} = 1 \tag{2.74}$$

$$\hat{\mathcal{I}}_I = \hat{\mathcal{I}}_{II} = 1 \qquad \hat{\mathcal{G}}_{I-II} = 1 \tag{2.75}$$

where

$$\begin{gathered} \hat{\mathcal{G}}_I = \frac{\bar{E}\mathcal{G}_I}{\sigma_{22}^2\pi a} \qquad \hat{\mathcal{G}}_{II} = \frac{\bar{E}\mathcal{G}_{II}}{\sigma_{21}^2\pi a} \\ \hat{\mathcal{I}}_I = \frac{\bar{E}\mathcal{I}_I}{\sigma_{22}\sigma_{21}\pi a} \qquad \hat{\mathcal{I}}_{II} = \frac{\bar{E}\mathcal{I}_{II}}{\sigma_{22}\sigma_{21}\pi a} \qquad \hat{\mathcal{G}}_{I-II} = \frac{\bar{E}\mathcal{G}_{I-II}}{2\sigma_{22}\sigma_{21}\pi a} \,. \end{gathered} \tag{2.76}$$

Table 2.7: Percent errors of the normalized energy release rates obtained with eight-noded isoparametric elements.

$\Delta a(\mu\text{m})$	$\hat{\mathcal{G}}_I(\%)$	$\hat{\mathcal{G}}_{II}(\%)$	$\hat{\mathcal{G}}_{I-II}(\%)$	$\hat{\mathcal{I}}_I(\%)$	$\hat{\mathcal{I}}_{II}(\%)$	$\mathcal{I}$ (%)
0.5	0.15	0.05	-0.69	-5.41	4.04	-9.99
1.0	0.15	0.05	0.06	-2.69	2.82	-5.65
1.5	0.15	0.05	0.10	-1.85	2.03	-3.96
2.0	0.15	0.05	0.10	-1.34	1.54	-2.92
2.5	0.15	0.05	0.10	-1.06	1.25	-2.33
3.0	0.15	0.05	0.10	-0.86	1.06	-1.94
3.5	0.15	0.05	0.10	-0.73	0.92	-1.66
4.0	0.15	0.05	0.10	-0.62	0.82	-1.45
4.5	0.15	0.05	0.10	-0.54	0.74	-1.29
5.0	0.15	0.05	0.10	-0.48	0.67	-1.16
10.0	0.15	0.05	0.10	-0.19	0.38	-0.58
15.0	0.15	0.05	0.10	-0.10	0.29	-0.38
20.0	0.15	0.05	0.10	-0.05	0.24	-0.29
25.0	0.15	0.05	0.10	-0.02	0.21	-0.23

The differences between the numerically calculated normalized dual energy release rates are considered using the first approach from Section 2.2. For this approach, only eight-noded elements are used to calculate $\mathcal{G}_I$, $\mathcal{G}_{II}$, $\mathcal{I}_I$ and $\mathcal{I}_{II}$ with eqs. (1.107) and (1.108), (1.185) and (1.186), respectively. The coupled energy release rate $\mathcal{G}_{I-II}$ is calculated using eq. (2.29) and the differences between the dual energy release rates, $\mathcal{I}$, are calculated using eq. (1.187). The energy release rates are normalized using eqs. (2.76).

The percent errors of the normalized energy release rates and the values of $\mathcal{I}$ are presented in Table 2.7. The first column, in Table 2.7, presents the length of the VCE with increments of 0.5 μm. In the next columns, the errors of $\hat{\mathcal{G}}_I$, $\hat{\mathcal{G}}_{II}$, $\hat{\mathcal{G}}_{I-II}$, $\hat{\mathcal{I}}_I$, and $\hat{\mathcal{I}}_{II}$ and the

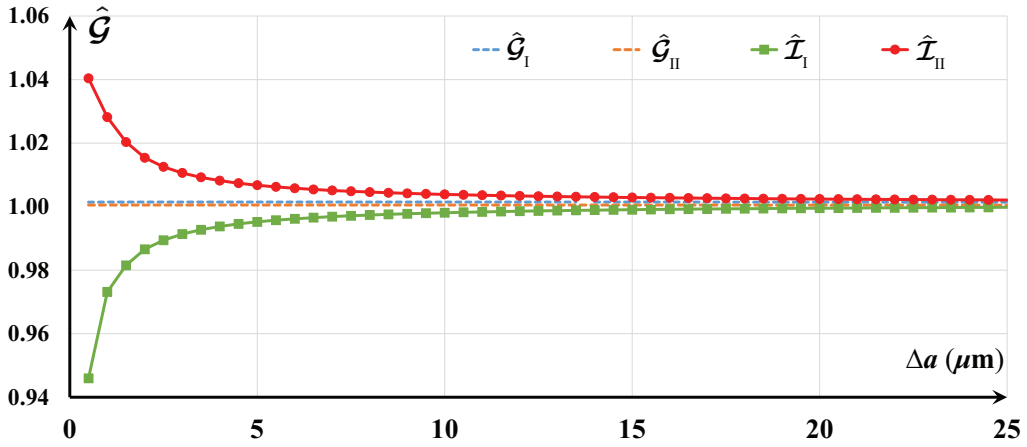

Figure 2.12: Numerical results of the energy release rates for the problem in Fig. 2.11.

value of $\mathcal{I}$ are shown, respectively. The values of the normalized energy release rates are shown in Fig. 2.12. The errors of $\hat{\mathcal{G}}_I$ and $\hat{\mathcal{G}}_{II}$ are 0.15% and 0.05%, respectively, and they are constant for all values of Δa. These results illustrate once again that only one element is required to calculate the energy release rates. The errors of $\hat{\mathcal{G}}_{I-II}$ are -0.69% and 0.06% for a VCE consisting of one and two elements, respectively. For a VCE that consists of more than two elements, the error is 0.10%. The errors of the dual energy release rates $\hat{\mathcal{I}}_I$, and $\hat{\mathcal{I}}_{II}$ for a VCE that consists of one element are greater than 4% in absolute value. As the number of elements of the VCE increases, the errors decrease. For a VCE that consists of 50 elements, the errors are -0.02% and 0.21% for $\hat{\mathcal{I}}_I$ and $\hat{\mathcal{I}}_{II}$, respectively. The value of $\mathcal{I}$ decreases from -9.99% to -0.23% as the errors of $\hat{\mathcal{I}}_I$ and $\hat{\mathcal{I}}_{II}$ decrease. It may be noted that the errors of the normalized dual energy release rates are of opposite sign, so that for $\Delta a > 0.5$ μm, the errors of $\hat{\mathcal{G}}_{I-II}$ are low.

The energy release rates are obtained using the nodal point forces and the crack face displacement jumps as shown in eqs. (1.107), (1.108), (1.185) and (1.186). In order to understand the difference between the excellent results obtained for the modes I and II energy release rates and the poor results for the dual energy release rates, the nodal point forces and the crack face displacement jumps are considered next. The analytical values of the normalized nodal point forces are tabulated in Table 2.6. In eq. (2.23), analytical expressions for the crack face displacement jumps are given. The normalized crack face displacement jumps and the normalized nodal point forces are given in eqs. (2.63) and (2.71), respectively.

The values of $\hat{F}_i^{(m)}$ and $\Delta\hat{u}_i^{(m')}$ for $i = 1, 2$ and $m = 1, ..10$, obtained for ten nodal points are considered, i.e. node $1'$ is the tenth node behind the crack tip on the crack face; nodes $10'$ and 1 coincide and are located at the crack tip; node 10 is the tenth node ahead of the crack tip (see Fig. 2.13). The VCE $\Delta a = 2.5$ μm and $\ell = 0.5$ μm where ℓ is the length of each element. Note that in the calculation of the energy release rates, node m pairs with node m'. The crack face displacement jumps at node $10'$ are zero. The percent errors of the normalized nodal point forces and normalized crack face displacement jumps are tabulated in Table 2.8; their values are illustrated in Figs. 2.13a and 2.13b, respectively.

In Table 2.8, the first column is the node number. The next two pairs of columns present the errors of the normalized nodal point forces and normalized crack face displacement jumps, respectively. The errors in the elements adjacent to the crack tip are large. Note that the elements adjacent to the crack tip consist of nodes 1, 2, 3, for the nodal point forces, and nodes $8'$ and $9'$ for the displacement jumps. The errors of the normalized nodal point forces in the first element ahead of the crack tip are 76%, -52% and 36% for $\hat{F}_1^{(1)}$, $\hat{F}_1^{(2)}$ and $\hat{F}_1^{(3)}$, respectively, and the errors for $\hat{F}_2^{(1)}$, $\hat{F}_2^{(2)}$ and $\hat{F}_2^{(3)}$ are 45% , -26% and 1.9%. The errors of the normalized crack face displacement jumps in the element behind the crack tip are -7.1% and -27% for $\Delta\hat{u}_1^{(8')}$ and $\Delta\hat{u}_1^{(9')}$, and the errors of $\Delta\hat{u}_2^{(8')}$ and $\Delta\hat{u}_2^{(9')}$ are -6.1% and -14%. These errors are caused by the stress singularity at the crack tip.

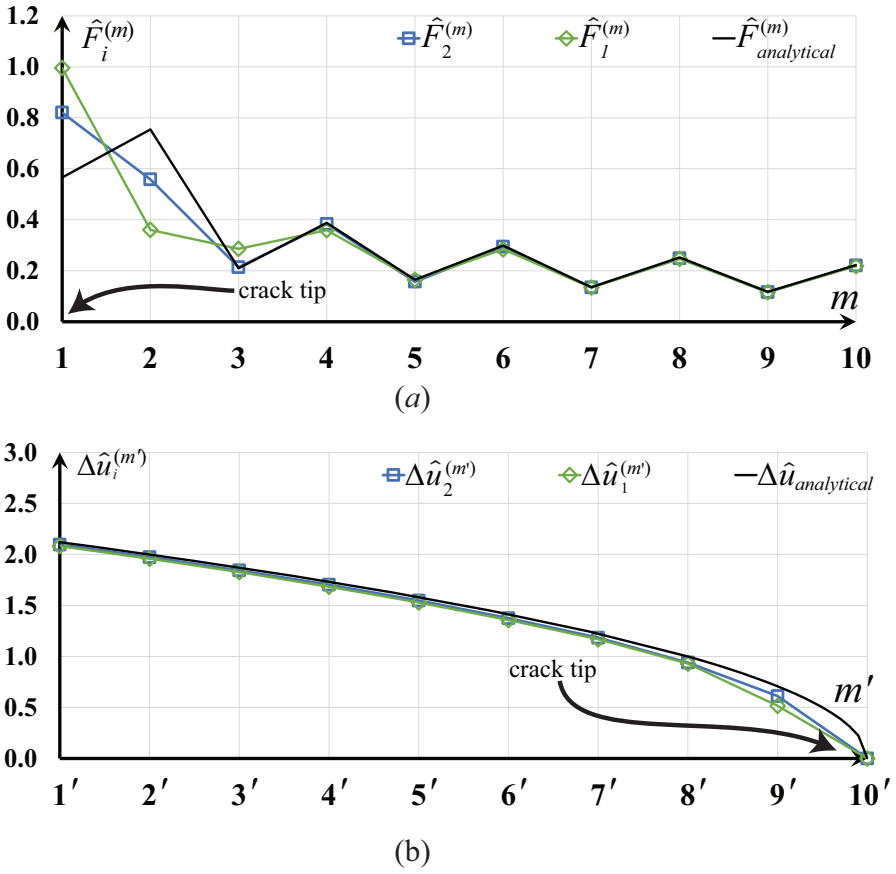

Figure 2.13: Numerical results and analytical values of the (a) normalized nodal point forces and (b) normalized crack face displacement jumps.

The positive errors in nodes 1 and 3 and the negative errors in the remaining nodes appear to cancel each other when the modes I and II energy release rates are calculated. Indeed, it is surprising that even when only one element is used as the VCE, excellent results

Table 2.8: Percent errors of the normalized nodal point forces and normalized crack face displacement jumps.

m, m'	$\hat{F}_1^{(m)}(\%)$	$\hat{F}_2^{(m)}(\%)$	$\Delta\hat{u}_1^{(m')}(\%)$	$\Delta\hat{u}_2^{(m')}(\%)$
1	76	45	-1.9	-1.2
2	-52	-26	-2.1	-1.3
3	36	1.9	-2.4	-1.5
4	-7.5	-1.2	-2.8	-1.7
5	-0.2	-4.8	-3.3	-2.1
6	-5.0	-1.6	-4.1	-2.8
7	-1.2	-0.6	-4.6	-3.4
8	-2.3	-1.3	-7.1	-6.1
9	-1.5	-1.3	-27	-14
10	-1.7	-0.9	-	-

are obtained as shown in Table 2.7, despite the large errors in the nodal point forces and displacement jumps. It may be pointed out that by adding more significant figures to the results for $\mathcal{G}_I$ and $\mathcal{G}_{II}$, the errors shown in Table 2.7 remain the same. Apparently, there is energy conservation that produces excellent results for the modes I and II energy release rates. Recall that in the finite element method, the potential energy is minimized.

The same constant behavior found for the results of the energy release rates is not maintained for the dual and coupled energy release rates. When calculating $\hat{\mathcal{I}}_I$, the nodal point forces in the x_2-direction are multiplied by the crack face displacement jumps in the x_1-direction as shown in eq. (1.185) instead of those in the x_2-direction as for $\hat{\mathcal{G}}_I$. The values of $\Delta\hat{u}_1^{(8')}$ and $\Delta\hat{u}_1^{(9')}$ are less than the values of $\Delta\hat{u}_2^{(8')}$ and $\Delta\hat{u}_2^{(9')}$, as illustrated in Fig. 2.13b, and thus $\hat{\mathcal{I}}_I$ is less than $\hat{\mathcal{G}}_I$, as shown in Fig. 2.12 by the green curve. For $\hat{\mathcal{I}}_{II}$, the nodal point forces in the x_1-direction are multiplied by the crack face displacement jumps in the x_2-direction as shown in eq. (1.186) instead of those in the x_1-direction as for $\hat{\mathcal{G}}_{II}$; thus its numerically obtained value is greater than $\hat{\mathcal{G}}_{II}$, as shown in Fig. 2.12 by the red curve. When using many elements in the VCE, the significant errors caused by the stress singularity in the neighborhood of the crack tip become negligible, as shown in Fig. 2.12 for large values of Δa and the errors in the first two elements are minimized. With the high errors in $\hat{F}_i^{(m)}$ and $\Delta\hat{u}_i^{(m')}$, it is surprising that the VCCT produces such accurate results.

In Banks-Sills and Farkash (2016), coarse and finer finite element meshes were employed for an interface crack between two dissimilar linear elastic, isotropic and homogeneous materials. For coarser meshes, the best results were obtained for the VCE producing the lowest value of $\mathcal{I}$ in eq. (1.187), i.e., the lowest difference between $\hat{\mathcal{I}}_I$ and $\hat{\mathcal{I}}_{II}$ (or $\mathcal{I}_I$ and $\mathcal{I}_{II}$). For finer meshes, excellent results were obtained even when $\mathcal{I}$ was large. But for the smallest value of $\mathcal{I}$, accurate energy release rates values were also found. Thus, it was proposed to use $\mathcal{I}_{\min}$ as a criterion for choosing the number of elements in the VCE. It is shown here, that for a fine mesh with a crack in a linear elastic, homogeneous and isotropic material, excellent results are obtained for $\mathcal{G}_I$ and $\mathcal{G}_{II}$ with a VCE consisting of one element but resulting in a large value of $\mathcal{I}$. From this investigation, it is understood that the reason for the difference between the dual energy release rates $\mathcal{I}_I$ and $\mathcal{I}_{II}$ is the stress singularity at the crack tip. For coarser meshes, with interface cracks when the dual energy release rates converge nearly to the same value, the errors resulting from the stress singularity at the crack tip have been overcome. In addition, it was shown here that the dual energy release rates are analytically equal with analytical expressions given in eqs. (2.28) and (2.53), for a crack in a linear elastic, homogeneous and isotropic material and an interface crack between two dissimilar linear elastic, isotropic and homogeneous materials, respectively.

2.5 VCCT for an interface crack between two transversely isotropic materials

In this section, an interface crack between two dissimilar linear elastic, transversely isotropic and homogeneous materials, as shown in Fig. 1.7, is investigated. The upper material is a unidirectional composite with fibers in the x_1- direction. The lower material is the same material as the upper one, rotated about the x_2-axis with fibers in the x_3-direction. The interface energy release rate is given in eq. (1.35) where $K_{III} = 0$ and

$$\frac{1}{H_1} = \frac{D_{11}}{4\cosh^2 \pi\varepsilon}. \tag{2.77}$$

In eq. (2.77), D_{11} is taken from the matrix $\mathbf{D}$ and is given explicitly as (Banks-Sills and Boniface, 2000)

$$D_{11} = \frac{\beta_1 + \beta_2}{E_A}\left(1 - \nu_A^2 \frac{E_T}{E_A}\right) + \frac{1 + 2\kappa}{4G_T}\,, \tag{2.78}$$

where $i\beta_1$ and $i\beta_2$ are eigenvalues of the compatibility equations; $i = \sqrt{-1}$; E_A and E_T are the Young's moduli in the axial and transverse directions, respectively; G_T is the shear modulus in the transverse direction given by

$$G_T = \frac{E_T}{2(1 + \nu_T)}\,; \tag{2.79}$$

ν_A and ν_T are the Poisson's ratios in the axial and transverse directions, respectively; and κ is given by

$$\kappa = \frac{3 - \nu_T - \nu_A^2 E_T/E_A}{2(1 + \nu_T)}\,. \tag{2.80}$$

The oscillatory parameter ε is defined in eq. (1.67).

In order to determine the phase angle ψ, defined in eq. (1.40), two new auxiliary integrals are presented

$$A_T = \frac{1}{2\Delta a}\int_0^{\Delta a}\left[\sqrt{\frac{D_{22}}{D_{11}}}\sigma_{22}(x_1) + i\sigma_{21}(x_1)\right]\left[\sqrt{\frac{D_{11}}{D_{22}}}\Delta u_2(\Delta a - x_1) - i\Delta u_1(\Delta a - x_1)\right]dx_1\,, \tag{2.81}$$

$$D_T = \frac{1}{2\Delta a}\int_0^{\Delta a}\left[\sqrt{\frac{D_{22}}{D_{11}}}\sigma_{22}(x_1) + i\sigma_{21}(x_1)\right]\left[\sqrt{\frac{D_{11}}{D_{22}}}\Delta u_2(\Delta a - x_1) + i\Delta u_1(\Delta a - x_1)\right]dx_1\,, \tag{2.82}$$

where the subscript T denotes transversely isotropic material, D_{22} is taken from the matrix $\mathbf{D}$ and is given explicitly as (Banks-Sills and Boniface, 2000)

$$D_{22} = \frac{\beta_1\beta_2(\beta_1 + \beta_2)}{E_A}\left(1 - \nu_A^2 \frac{E_T}{E_A}\right) + \frac{1 + 2\kappa}{4G_T}\,. \tag{2.83}$$

The coordinate system and the virtual crack extension, Δa, are shown in Figs. 1.7 and 1.9, respectively. Noting the expressions for A and D in eqs. (1.169) to (1.172) and substituting eqs. (1.75) and (1.76) into eqs. (2.81) and (2.82), it may be shown that

$$A_T = \frac{1}{H_1}\left(K_1^2 + K_2^2\right) \tag{2.84}$$

and

$$D_T = \frac{\cosh \pi\varepsilon}{\pi H_1} P K^2 \Delta a^{2i\varepsilon} \ , \tag{2.85}$$

where H_1 is defined in eq. (2.77) and P is defined in eq. (1.173).

Noting that A_T is real, one may write

$$\sqrt{\frac{D_{22}}{D_{11}}}\mathcal{I}_I = \sqrt{\frac{D_{11}}{D_{22}}}\mathcal{I}_{II}, \tag{2.86}$$

where $\mathcal{I}_I$ and $\mathcal{I}_{II}$ are defined in eqs. (1.176) and (1.177), respectively. The dual energy release rates for this interface crack may be redefined, following eq. (2.86), as

$$\mathcal{I}_I^{(T)} = \frac{1}{2\Delta a}\sqrt{\frac{D_{22}}{D_{11}}}\sum_{m=1}^{M} F_2^{(m)} \Delta u_1^{(m')} \tag{2.87}$$

$$\mathcal{I}_{II}^{(T)} = \frac{1}{2\Delta a}\sqrt{\frac{D_{11}}{D_{22}}}\sum_{m=1}^{M} F_1^{(m)} \Delta u_2^{(m')} \ . \tag{2.88}$$

The coupled energy release rate in eq. (2.41) for two isotropic materials is extended here to be

$$\mathcal{G}_{I-II}^{(T)} = \mathcal{I}_I^{(T)} + \mathcal{I}_{II}^{(T)} \ . \tag{2.89}$$

The percent difference between the left and the right hand sides of eq. (2.86) is defined as

$$\mathcal{I}_T = \frac{\mathcal{I}_{II}^{(T)} - \mathcal{I}_I^{(T)}}{\mathcal{I}_I^{(T)}} \cdot 100 \ . \tag{2.90}$$

The phase angle of D_T may be extracted from eq. (2.82) as

$$\psi_{D_T} = \tan^{-1}\left[\frac{\Im(D_T)}{\Re(D_T)}\right] = \tan^{-1}\left(\frac{\mathcal{G}_{I-II}^{(T)}}{\mathcal{G}_I - \mathcal{G}_{II}}\right) \ . \tag{2.91}$$

From eq. (2.85), it may also be written as

$$\psi_{D_T} = 2\psi + \psi_P + 2\varepsilon \ln \Delta a \ , \tag{2.92}$$

where ψ_P is define in eq. (2.52) and ψ is the phase angle of the stress intensity factors given in eq. (2.51). Using eq. (2.92), ψ may be found as

$$\psi = \frac{1}{2}\psi_{D_T} - \frac{1}{2}\psi_P - \varepsilon \ln \Delta a. \tag{2.93}$$

The stress intensity factors are determined using eqs. (2.61) and (1.184).

In Section 2.5.1, an expression for calculating the length of the interpenetration zone is derived. This phenomenon was also considered in Toya (1992), Sun and Qian (1997), Hemanth et al. (2005) and Agrawal and Karlsson (2006). In Toya (1992) and Sun and Qian (1997), it was pointed out that Δa should be larger than the interpenetration zone. In this study, this suggestion is questioned. In Sections 2.5.2 and 2.5.3, numerical results are presented for three problems of an interface crack between two dissimilar transversely isotropic materials. An interface crack in an infinite body is presented in Section 2.5.2. In Section 2.5.3, a CCT specimen and a DCB specimen are presented. The mechanical properties that are used for all problems are shown in Table 1.1. Recall that the upper material is a unidirectional composite with fibers in the x_1- direction and the lower material is the same material as the upper one, rotated about the x_2-axis with fibers in the x_3- direction as shown in Fig. 1.7.

2.5.1 Interpenetration zone

Using the method presented in Rice (1988), one may derive an expression for the length of the interpenetration zone for an interface crack between two transversely isotropic materials. Taking the real part of eq. (1.76), one may write

$$\Delta u_2 = \tilde{C}\sqrt{r}\Re\left[\frac{K}{1+2i\varepsilon}r^{i\varepsilon}\right] \tag{2.94}$$

where $\tilde{C}$ is a constant given by

$$\tilde{C} = \sqrt{\frac{D_{22}}{D_{11}}}\frac{2D_{11}}{\sqrt{2\pi}\cosh\pi\varepsilon} \tag{2.95}$$

and r has been substituted for $\Delta a - x$ in eq. (1.76). Since $\hat{L}$ is an arbitrary length scale, one may write

$$\hat{K} = |K|e^{i\hat{\psi}} \tag{2.96}$$

where it is possible to define another phase angle

$$\hat{\psi} = \tan^{-1}\left[\frac{\Im(K\hat{L}^{i\varepsilon})}{\Re(K\hat{L}^{i\varepsilon})}\right]. \tag{2.97}$$

Solving eq. (1.30) for K and substituting eq. (2.96) into it, leads to

$$K = |K|\hat{L}^{-i\varepsilon}e^{i\hat{\psi}}. \tag{2.98}$$

Use of eq. (2.98) in eq. (2.94) yields

$$\Re\left[\frac{K}{1+2i\varepsilon}r^{i\varepsilon}\right] = \frac{|K|}{\sqrt{1+4\varepsilon^2}}\cos\left[\hat{\psi}+\varepsilon\ln\left(\frac{r}{\hat{L}}\right)-\tan^{-1}2\varepsilon\right]. \tag{2.99}$$

In order to determine r_c, the length of the interpenetration zone, one may require $\Delta u_2 = 0$; thus, from eqs. (2.94) and (2.99)

$$\cos\left[\hat{\psi} + \varepsilon \ln\left(\frac{r_c}{\hat{L}}\right) - \tan^{-1} 2\varepsilon\right] = 0. \tag{2.100}$$

For $\varepsilon < 0$, eq. (2.100) implies that

$$\left[\hat{\psi} + \varepsilon \ln\left(\frac{r_c}{\hat{L}}\right) - \tan^{-1} 2\varepsilon\right] = \frac{\pi}{2}. \tag{2.101}$$

Therefore

$$r_c = \hat{L} \exp\left\{\frac{1}{\varepsilon}\left[\left(\frac{\pi}{2} - \hat{\psi}\right) + \tan^{-1} 2\varepsilon\right]\right\}. \tag{2.102}$$

Equation (2.102) depends explicitly on $\hat{L}$ and implicitly on this quantity through $\hat{\psi}$. However, it may be shown that r_c does not depend on $\hat{L}$.

2.5.2 An interface crack in an infinite body

In this section, the problem of an infinite body containing a finite crack of length $2a$, with $a = 1$ mm, along an interface between two dissimilar linear elastic, transversely isotropic and homogeneous materials is considered, as shown in Fig. 2.14. Three different cases of applied tractions are examined. In order to approximate an infinite body, the dimensions of the body are taken to be $w/a = 40$ and $h/w = 1$; $2h$ and $2w$ are, respectively, the height and width of the analyzed body. The material that is used in this problem is a fiber reinforced composite made of graphite/epoxy AS4/3501-6. The effective mechanical properties were taken from Banks-Sills and Boniface (2000), and are shown in Table 1.1. For the upper material, the fibers are in the x_1- direction, and for the lower material, they are in the x_3- direction as shown in Fig. 2.14. The body is subjected to remote tensile and shear tractions. The analytical solution for this problem is given in Boniface and Banks-Sills (2002) as

$$K = \left(\sqrt{\frac{D_{22}}{D_{11}}}\sigma_{22} + i\sigma_{12}\right)(1 + 2i\varepsilon)\sqrt{\pi a}(2a)^{-i\varepsilon}. \tag{2.103}$$

The stresses $\sigma_{11}^{(1)}$ and $\sigma_{11}^{(2)}$ are imposed parallel to the interface, as shown in Fig. 2.14, to maintain displacement continuity along the interface. Assuming plane deformation, the relation between $\sigma_{11}^{(1)}$ and $\sigma_{11}^{(2)}$ is given as

$$\sigma_{11}^{(2)} = \frac{E_T}{E_A}\sigma_{11}^{(1)} + \left\{\frac{E_A\nu_T - E_T\nu_A[1 - (\nu_A - \nu_T)]}{E_A - E_T\nu_A^2}\right\}\sigma_{22}, \tag{2.104}$$

where E_A and E_T are the Young's moduli in the axial and transverse directions, respectively, and ν_A and ν_T are the Poisson's ratios in the axial and transverse directions, respectively.

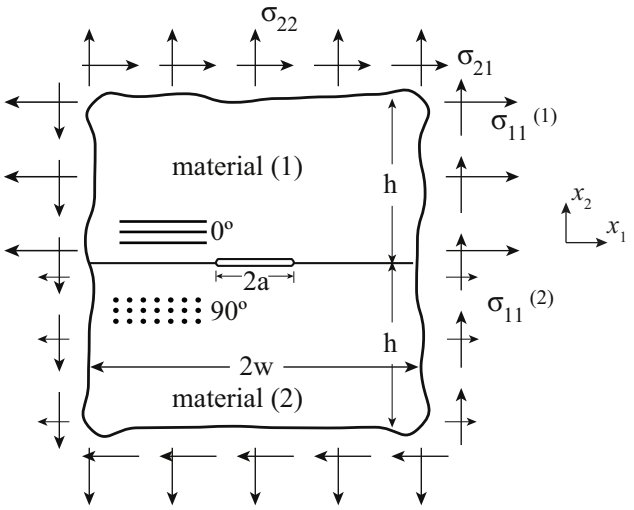

Figure 2.14: An interface crack between two dissimilar transversely isotropic materials in an infinite body subjected to remote tensile and shear stresses.

Table 2.9: Parameters used to calculate the stress intensity factors.

D_{11} (1/GPa)	D_{22} (1/GPa)	$1/H_1$ (1/GPa)	ε	P	C	ψ_P
0.2307	0.3122	0.0572	-0.02780	$3.1053+0.4141i$	1.0010	0.1326

The values of D_{11}, D_{22}, $1/H_1$, ε, P, C and ψ_P from eqs. (2.78), (2.83), (2.77), (1.67), (1.173), (1.181) and (2.52), respectively, are given in Table 2.9. The parameter ε is given explicitly as (Boniface and Banks-Sills, 2002)

$$\varepsilon = \frac{W_{12}}{\sqrt{D_{11}D_{22}}} , \tag{2.105}$$

where W_{12} is taken from the matrix $\mathbf{W}$ in eq. (1.71) and explicitly given by (Boniface and Banks-Sills, 2002)

$$W_{12} = -\frac{(1+\nu_T)\nu_A}{E_A} + \beta_1\beta_2\left(1-\nu_A^2\frac{E_T}{E_A}\right)\frac{1}{E_A} + \frac{1-2\kappa}{4G_T} . \tag{2.106}$$

Three cases of applied tractions have been examined in this study. The applied tractions and the analytic solution for the stress intensity factors are presented in Table 2.10.

Three meshes were constructed using Abaqus/CAE 6.14 (2014) with eight noded isoparametric elements (CPE8). In each case, the entire body was modeled. The size of the elements near the crack tip, ℓ, and number of elements and nodes, for each mesh, are presented in Table 2.11.

The applied tensile stress is $\sigma_{22} = 1$ MPa and $\sigma_{11}^{(1)} = 1$ MPa. Using eq. (2.104), the stress $\sigma_{11}^{(2)}$ was found to be 0.6006 MPa. A schematic figure of part of mesh A is shown

in Fig. 2.15. The parts of the mesh that are far from the crack, at the corners of the body, contain uniform elements whose dimensions are about 2×2 mm^2. Note that the crack length $2a$ is 2 mm. There is a uniform mesh of elements surrounding the crack tips, where each element is 5×5 μm^2. Therefore, $\ell = 5$ μm. Above, below and on the sides of the crack, there are transition zones between the two regions with elements which have a large aspect ratio, the largest being 400. The stress gradients are low in those regions; so that these elements should not adversely affect the accuracy of the results. In addition, meshes B and C presented in Table 2.11 with smaller values of ℓ were constructed. For those two meshes, a focused region around the crack tip was utilized as shown schematically in Fig. 2.16. For the elements in the vicinity of the crack tip, $\ell = 0.05$ μm and $\ell = 0.5$ μm, respectively, for meshes B and C. A uniform mesh with an element size of $\ell \times \ell$, was constructed only in the crack tip region, as shown schematically in Fig. 2.16b. An enlargement of the region surrounded by a dotted red line in Fig. 2.16a is illustrated in Fig. 2.16b.

For Mesh B, the size of the uniform mesh in the crack tip region, is 10×10 μm^2, and there are 200×200 elements with $\ell = 0.05$ μm. Note that there are 100 such elements in front of the crack tip and 100 elements on each crack face behind the crack tip. To allow for this small element size, the mesh is focused towards the crack tip, as shown in Fig. 2.16a. In the focused zone there are 70 square rings, each one smaller and thinner than the outer one. Three inner rings are shown in Fig. 2.16b. In the outer region, a uniform coarse mesh was constructed, similar to that in Fig. 2.15. The elements in that region are 1×1 mm^2. The largest aspect ratio of the transition elements is 100.

For mesh C, the size of the uniform mesh in the crack tip region, is 25×25 μm^2; there are 50×50 elements with $\ell = 0.5$ μm, instead of 200×200 elements with $\ell = 0.05$ μm in mesh B. Note that there are 25 elements in front of the crack and 25 elements on each crack face behind the crack tip. In the focused zone, there are 25 square rings instead of 70 square rings as in mesh B. In the outer region, elements are 1×1 mm^2, with no change compared to mesh B. The largest aspect ratio of the transition elements is 25. It may be noted that for meshes B and C, there are no stress gradients in the transition regions. One of the aims of this study is to determine accurate stress intensity factors values for

Table 2.10: Applied tractions and the analytic solutions for the cases investigated in this study.

	σ_{22} (MPa)	σ_{21} (MPa)	$\sigma_{11}^{(1)}$ (MPa)	$\sigma_{11}^{(2)}$ (MPa)	K_1 (N/mm$^{3/2+i\varepsilon}$)	K_2 (N/mm$^{3/2+i\varepsilon}$)
case 1	1	0	1	0.6006	2.0638	-0.0749
case 2	1	1	1	0.6006	2.1282	1.6991
case 3	1	4	1	0.6006	2.3213	7.0212

Table 2.11: The size ℓ of the elements near the crack tip and the number of elements and nodes for each mesh.

Mesh	ℓ (μm)	elements	nodes
Mesh A	5.0	1,037,444	3,117,284
Mesh B	0.05	244,328	735,172
Mesh C	0.5	30,528	92,372

meshes which are as coarse as possible. Hence, elements in the transition region have high aspect ratios.

Using the finite element results, the values of the energy release rates $\mathcal{G}_I$ and $\mathcal{G}_{II}$ are calculated by means of eqs. (1.107) and (1.108), respectively. The values of the dual and coupled energy release rates, $\mathcal{I}_I^{(T)}$, $\mathcal{I}_{II}^{(T)}$ and $\mathcal{G}_{I-II}^{(T)}$ are calculated using eqs. (2.87) to (2.89), respectively. In order to compute the stress intensity factors, $\mathcal{G}_I$, $\mathcal{G}_{II}$ and $\mathcal{G}_{I-II}^{(T)}$ are substituted into eq. (2.91) to determine ψ_{D_T}. This value is substituted into eq. (2.93) to obtain ψ. The interface energy release rate, $\mathcal{G}_i$, is found from eq. $(2.37)_1$. Two pairs of stress intensity factors are determined by substituting $\mathcal{G}_i$ and ψ into eq. (2.61), where H_1 is given in eq. (2.77) and Table 2.9. Using the condition in eq. (1.184), the valid solution is found. By means of eq. (2.90), the parameter $\mathcal{I}_T$ is also computed. This parameter is used to indicate a best solution.

The first two cases in Table 2.10 were considered using all three meshes described above. The results for the first and second cases are shown in Tables 2.12 through 2.14 and 2.15 through 2.17, respectively. The third case in Table 2.10 was carried out only with mesh B presented in Table 2.11. The results for this case are shown in Table 2.18. In Tables 2.12

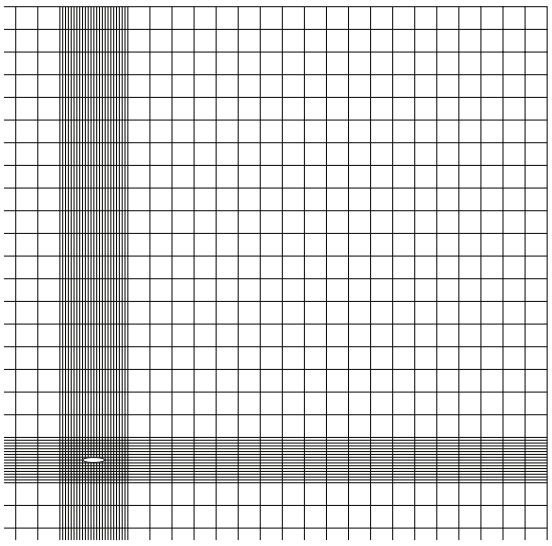

Figure 2.15: Schematic view of part of mesh A presented in Table 2.11. This mesh contains 1,037,444 eight noded isoparametric elements and 3,117,284 nodal points.

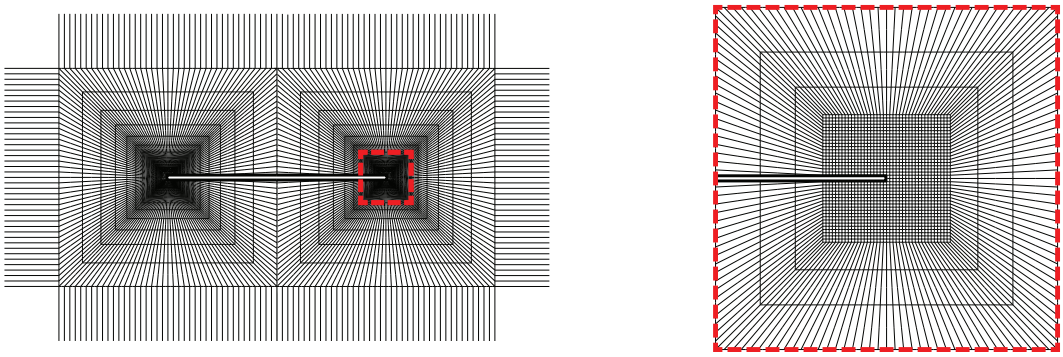

(a) (b)

Figure 2.16: Schematic view of (a) the crack region and (b) the crack tip region of meshes B and C presented in Table 2.11.

Table 2.12: Data for case 1 in Table 2.10, solved with mesh A ($\ell = 5$ μm) in Table 2.11.

$N/2$	$\Delta a(\mu\text{m})$	K_1 (%)	K_2 (%)	$\mathcal{I}_T$ (%)
1	5	0.02	-15.5	-42.9
2	10	0.02	-4.01	-16.7
3	15	0.02	1.34	-12.3
4	20	0.02	0.40	-9.7
5	25	0.02	0.40	-8.5
6	30	0.02	0.40	-7.4
7	35	0.02	0.27	-6.2
8	40	0.02	0.27	-5.7
15	75	0.00	0.27	-4.5
16	80	0.00	0.27	-4.2
17	85	0.00	0.27	-4.3
18	90	0.00	0.27	-4.3
19	95	0.00	0.27	-4.0
20	100	-0.01	0.27	-4.5
25	125	-0.02	0.27	-4.3
26	130	-0.03	0.40	-4.4
31	155	-0.05	0.40	-4.6
32	160	-0.06	0.40	-4.7
40	200	-0.10	0.40	-5.7
50	250	-0.17	0.53	-6.2

through 2.18, the first column represents the number of elements used for Δa, the virtual crack extension, which is given in the second column. Since Δa consists of N nodes and eight noded elements are employed in the analyses, the number of elements is $N/2$. In the next two columns, errors in the stress intensity factors K_1 and K_2 appear. The percentage $\mathcal{I}_T$ in eq. (2.90) is shown in column 5. Recall that $\mathcal{I}_T$ should be zero.

In Table 2.12, the results are shown for case 1 in Table 2.10, using mesh A presented in

Table 2.13: Data for case 1 in Table 2.10, solved with mesh B ($\ell = 0.05$ μm) in Table 2.11.

$N/2$	$\Delta a(\mu\text{m})$	K_1 (%)	K_2 (%)	$\mathcal{I}_T$ (%)
1	0.05	0.11	-15.8	-27.5
2	0.10	0.07	-1.60	-11.5
3	0.15	0.06	1.34	-8.3
4	0.20	0.06	0.40	-6.3
5	0.25	0.06	0.40	-5.2
6	0.30	0.06	0.27	-4.4
50	2.50	0.06	0.27	-0.64
100	5.00	0.06	0.27	-0.24

Table 2.11. Since there is a difference of two orders of magnitude between the two stress intensity factors, as shown in Table 2.10, it is difficult to obtain an accurate solution. For K_1, the absolute value of the percent error is less than 0.06% for $\Delta a = 5$ μm to 155 μm. For $\Delta a = 35$ μm to 125 μm, the percent error for K_2 is 0.27%. The lowest value of $\mathcal{I}_T$ is obtained for $\Delta a = 95$ μm. For this value of Δa, K_1 has no error to 3 significant figures and K_2 has an error of 0.27%. This is a very good result for K_2. Note, that by using one element for Δa, the error for K_2 is -15.5%.

Mesh A consists of over 1,000,000 elements making this method impractical for extension to three dimensions. Hence, the focused mesh B was used to reduce the required computer memory and CPU time in the finite element analyses. By using a focused mesh, a smaller value of ℓ was also achieved. In Table 2.13, the results are shown for case 1 in Table 2.10 using mesh B in Table 2.11 and shown schematically in Fig. 2.16. For $\Delta a \geq 0.3$ μm, the percent error converges to 0.06% for K_1 and 0.27% for K_2. The value of $\mathcal{I}_T$ decreases as Δa increases. For the greatest value of Δa used in the calculation, the value of $\mathcal{I}_T$ is -0.24%. Note that the largest value of Δa in Mesh B is the smallest one in mesh A. As a result of the stress singularity, using only the elements that are in the vicinity of the crack tip leads to poor results for K_2. For example, in Table 2.12, for $\Delta a = 15$ μm and comprising the first 3 elements, the percent error for K_2 is larger than 1.3%. This behavior was also observed for other methods such as the M-integral and displacement extrapolation (see, Freed and Banks-Sills, 2005). For the M-integral, use of the first volume of elements surrounding the crack front produced poor results. For displacement extrapolation, good results were obtained from elements that are at least two or more elements distant from the crack tip. On the other hand, as one may see in eq. (1.103), Δa should be small for VCCT. Therefore, there is a range of values for Δa which produce good results. The lowest value of $\mathcal{I}_T$ is a good indicator for the choice of Δa and, hence, the values for K_1 and K_2.

A further step to reduce the number of elements was made with mesh C. Recall that the number of elements in the uniform mesh surrounding the crack tip and the number of

Table 2.14: Data for case 1 in Table 2.10, solved with mesh C ($\ell = 0.5$ μm) in Table 2.11.

$N/2$	$\Delta a(\mu\text{m})$	K_1 (%)	K_2 (%)	$\mathcal{I}_T$ (%)
1	0.5	0.07	-15.1	-36.5
2	1.0	0.06	-4.01	-14.6
3	1.5	0.06	0.93	-10.5
4	2.0	0.06	0.27	-8.0
5	2.5	0.06	0.40	-6.6
6	3.0	0.06	0.27	-5.6
25	12.5	0.06	0.27	-1.9

rings used for mesh C is less than those of mesh B. As presented in Table 2.11, the number of elements in mesh C is about 30,000, a decrease of about one-eighth as compared to mesh B. In Table 2.14, the results are shown for case 1 in Table 2.10 using mesh C. For $\Delta a \geq 3$ μm, the percent error converges to 0.06% for K_1 and 0.27% for K_2. The value of $\mathcal{I}_T$ decreases as Δa increases. For the greatest value of Δa used in the calculation, the value of $\mathcal{I}_T$ is -1.9%. The values obtained for K_1 and K_2 using meshes B and C, as a function of the number of elements are very similar. Note that for both meshes B and C, by using one element for Δa the error for K_2 is quite large. It may be noted that the lowest values of $\mathcal{I}_T$ are obtained with use of mesh B. Although this mesh is quite fine, mesh C which is much coarser than mesh B is recommended (see Table 2.11). It may be observed in Table 2.14 that values of $\mathcal{I}_T$ are not as small as those presented in Table 2.13 for mesh B. But convergence is obtained with small errors in the stress intensity factors.

In Tables 2.15 through 2.17, the results are presented for case 2 from Table 2.10 using meshes A, B and C. In this case, in addition to tensile traction, a shear traction is applied at the outer boundary of the body as shown in Fig. 2.14, which is the same magnitude as the tensile stress, σ_{22}. Since the stress intensity factors are the same order of magnitude for this problem, it should be easier to obtain accurate results. In Table 2.15, the results are shown for case 2 in Table 2.10, using mesh A in Table 2.11. The absolute values of the percent errors are less than 0.06% for both K_1 and K_2, when $\Delta a = 15$ μm to 165 μm for the former and $\Delta a = 15$ μm to 90 μm for the latter. The lowest value of $\mathcal{I}_T$ is obtained for $\Delta a = 150$ μm. For this value of Δa, K_1 has an error of -0.04% and K_2 has an error of -0.11%. Note that by using one element for Δa, the errors are less than 1% for both stress intensity factors.

In Table 2.16, the results are presented for case 2 in Table 2.10, using mesh B in Table 2.11. For $\Delta a \geq 0.25$ μm, the percent error converges to 0.07% for K_1 and 0.02% for K_2. For the greatest value of Δa used in the calculation, the value of $\mathcal{I}_T$ is -0.14%.

In Table 2.17, the results are presented for case 2 in Table 2.10, using mesh C in Table 2.11. For $\Delta a \geq 3.5$ μm, the percent error converges to 0.06% for K_1 and 0.02% for K_2. For the greatest value of Δa used in the calculation, the value of $\mathcal{I}_T$ is -0.72%. Also here, by

using one element for Δa the errors are less than 1% for both stress intensity factors. It is shown that a mesh (mesh C) consisting of fewer elements in the vicinity of the crack tip and fewer square rings, as compared to mesh B, leads to excellent results.

In case 3 presented in Table 2.10, the applied shear traction is increased to 4 MPa with the tensile traction remaining at 1 MPa. Using eq. (2.102) for this case, $r_c = 0.076$ μm. In eq. (2.102), $\hat{\psi}$ is calculated by means of eq. (2.97) with ε given in eq. (2.105) and Table 2.9. Recall that r_c does not depend on $\hat{L}$. Hence, the interpenetration zone occurs for a distance $r \leq 0.076$ μm from the crack tip. Only mesh B presented in Table 2.11 was used for this calculation. Since the size of one element is $\ell = 0.05$ μm, the first two elements behind the crack tip are in the interpenetration zone. It is expected that interpenetration should occur between the third and fourth nodes from the crack tip. In Fig. 2.17, the deformed configuration of the crack faces in the vicinity of the crack tip are plotted. As may be observed, the first two elements penetrate each other. Indeed, the interpenetration ends between the third and fourth nodes from the crack tip. For cases 1 and 2 in Table 2.10, there will be an interpenetration zone; but it will be smaller than the smallest distance between the nodes in the vicinity of the crack tip in mesh B.

In Table 2.18, the results are shown for case 3 from Table 2.10 obtained using mesh B. Since interpenetration occurs for $\Delta a \leq 0.076$ μm, results for the first and the second elements where $\Delta a = 0.05$ μm and 0.1 μm, produce zero and a negative value for $\mathcal{G}_I$,

Table 2.15: Data for case 2 in Table 2.10, solved with mesh A ($\ell = 5$ μm) in Table 2.11.

$N/2$	$\Delta a(\mu\text{m})$	K_1 (%)	K_2 (%)	$\mathcal{I}_T$ (%)
1	5	-0.43	0.65	-20.9
2	10	-0.08	0.14	-9.4
3	15	0.03	-0.04	-6.6
4	20	0.03	-0.03	-4.8
5	25	0.03	-0.04	-3.9
6	30	0.03	-0.04	-3.2
7	35	0.03	-0.04	-2.8
8	40	0.02	-0.04	-2.4
16	80	0.01	-0.05	-1.3
17	85	0.01	-0.05	-1.3
18	90	0.00	-0.05	-1.2
19	95	0.00	-0.06	-1.2
20	100	0.00	-0.06	-1.2
29	145	-0.03	-0.10	-1.04
30	150	-0.04	-0.11	-0.99
31	155	-0.04	-0.11	-1.04
33	165	-0.05	-0.12	-1.04
34	170	-0.06	-0.12	-1.00
50	250	-0.16	-0.24	-1.05

Table 2.16: Data for case 2 in Table 2.10, solved with mesh B ($\ell = 0.05$ μm) in Table 2.11.

$N/2$	$\Delta a(\mu\text{m})$	K_1 (%)	K_2 (%)	$\mathcal{I}_T$ (%)
1	0.05	-0.36	0.74	-15.9
2	0.10	0.01	0.11	-7.5
3	0.15	0.09	-0.01	-5.3
4	0.20	0.07	0.01	-3.9
5	0.25	0.07	0.02	-3.1
30	1.50	0.07	0.02	-0.49
50	2.50	0.07	0.02	-0.34
100	5.00	0.07	0.02	-0.14

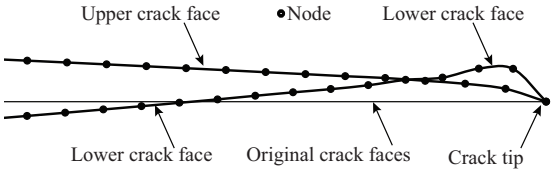

Figure 2.17: For case 3 in Table 2.10 using mesh B, a schematic view of the deformed configuration of the crack faces using data obtained from the finite element analysis.

respectively, they are not presented. For $\Delta a \geq 0.85$ μm, the percent error converges to 0.09% for K_1 and 0.02% for K_2. For the greatest value of Δa used in the calculation, the value of $\mathcal{I}_T$ is 0.09%. The percent error of -2.33% for K_1 when $\Delta a = 0.15$ μm and values of more than 25% for $\mathcal{I}_T$ when 0.15 μm $\leq \Delta a \leq$ 0.20 μm are higher than the corresponding values for cases 1 and 2 using mesh B (see Tables 2.13 and 2.16). These high values appear to be a result of the negative crack face displacements jumps from the interpenetration zone that are used at the calculation. Using the elements that are in the interpenetration zone, together with other elements beyond them, for the calculation does not cause the results to deteriorate. On the contrary, in order to obtain accurate results, those elements should be used in the calculation. It may be pointed out that contact

Table 2.17: Data for case 2 in Table 2.10, solved with mesh C ($\ell = 0.5$ μm) in Table 2.11.

$N/2$	$\Delta a(\mu\text{m})$	K_1 (%)	K_2 (%)	$\mathcal{I}_T$ (%)
1	0.5	-0.38	0.70	-20.3
2	1.0	-0.05	0.19	-9.2
3	1.5	0.06	0.02	-6.3
4	2.0	0.06	0.02	-4.7
5	2.5	0.07	0.01	-3.7
6	3.0	0.07	0.01	-3.1
7	3.5	0.06	0.02	-2.6
25	12.5	0.06	0.02	-0.72

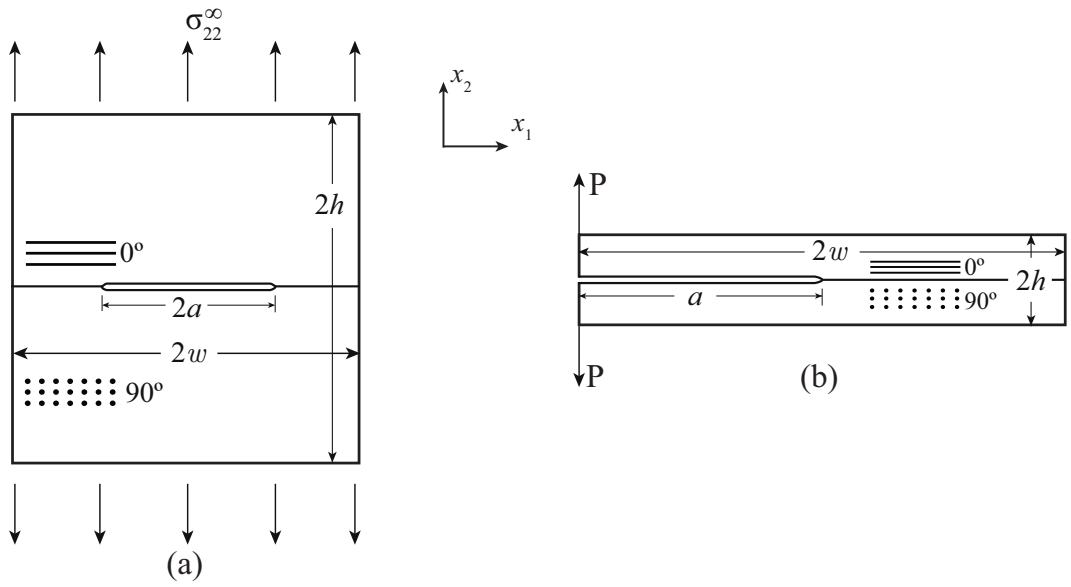

Figure 2.18: Geometry for (a) a CCT specimen and (b) a DCB specimen with an interface crack.

elements may be used to prevent interpenetration. However, using contact elements will cause small errors in the calculation of $\mathcal{G}_I$ and $\mathcal{G}_{II}$. Hence, contact elements were not used. Sections 2.5.1 and 2.5.2 were published in Farkash and Banks-Sills (2017).

2.5.3 Interface cracks in a CCT and a DCB specimens

In this section, two problems are solved by means of an FEA using a commercial finite element program Abaqus/CAE (2017). The results in this section are new. The first problem is a CCT specimen with an interface crack, as shown in Fig. 2.18a. A DCB specimen with an interface crack subjected to mode I loading, as shown in Fig. 2.18b, is the second problem. Recall that the upper material of the specimens is a unidirectional composite with fibers in the x_1- direction. The material that is used in this problem is a

Table 2.18: Data for case 3 in Table 2.10, solved with mesh B ($\ell = 0.05$ μm) in Table 2.11.

$N/2$	$\Delta a(\mu\text{m})$	K_1 (%)	K_2 (%)	$\mathcal{I}_T$ (%)
3	0.15	-2.33	0.29	53.1
4	0.20	-0.04	0.04	25.3
5	0.25	0.05	0.03	15.6
6	0.30	0.07	0.03	11.0
17	0.85	0.09	0.02	2.0
30	1.50	0.09	0.02	0.88
50	2.50	0.09	0.02	0.41
100	5.00	0.09	0.02	0.09

Table 2.19: Data for the CCT specimen.

$N/2$	$\Delta a(\mu\text{m})$	K_1 (N/mm$^{3/2+i\varepsilon}$)	K_2 (N/mm$^{3/2+i\varepsilon}$)	$\mathcal{I}_T$ (%)
1	0.5	5.5417	0.4290	30.5
2	1.0	5.5429	0.4137	12.6
3	1.5	5.5437	0.4069	9.0
4	2.0	5.5435	0.4070	6.8
5	2.5	5.5434	0.4071	5.5
30	15	5.5434	0.4073	1.2
50	25	5.5434	0.4073	0.9
100	50	5.5434	0.4073	0.9

fiber reinforced composite made of graphite/epoxy AS4/3501-6. The effective mechanical properties are given in Table 1.1. The lower material is the same material as the upper one, rotated about the x_2-axis with fibers in the x_3- direction.

The CCT specimen is subjected to a remote tensile traction, as shown in Fig. 2.18a. The length of the crack is $2a = 10$ mm. The width and height of the body are $2w = 2h = 20$ mm. The applied tensile traction is $\sigma_{22}^{\infty} = 1$ MPa and plane strain conditions are imposed using CPE8 elements of Abaqus/CAE (2017). It is noted that these are eight noded isoparametric elements. The finite element method is used to determine the crack face displacement jumps behind the crack tip and the nodal point forces ahead of the crack tip. The FEA ia carried out with an element length of 0.5 μm in the vicinity of the crack tip. A focused mesh in the vicinity of the crack tip is used. A schematic view of a quarter of the mesh and the focused mesh in the vicinity of the crack tip are presented in Figs. 2.4a and 2.4b, respectively. Recall that in the schematic view, there are only twenty elements ahead of the crack tip. In the actual mesh, the element size in the vicinity of the crack tip is 0.5×0.5 μm^2 with 100 elements of this size ahead, behind, above and below the crack tip. The number of elements and nodal points for this mesh is 274,144 and 824,716, respectively.

Using the finite element results, the values of the energy release rates $\mathcal{G}_i$, $\mathcal{G}_I$, $\mathcal{G}_{II}$, $\mathcal{I}_I^{(T)}$, $\mathcal{I}_{II}^{(T)}$ and $\mathcal{G}_{I-II}^{(T)}$ are calculated using eqs. $(2.37)_1$, (1.107), (1.108), (2.87), (2.88) and (2.89), respectively. The stress intensity factors are calculated using eq. (2.61), where H_1 is given in eq. (2.77) and Table 2.9, as described in Section 2.5.2. Equation (2.90) is used to calculate the parameter $\mathcal{I}_T$. The results obtained for the stress intensity factors are presented in Table 2.19. Recall that N is the number of nodal points in the calculation and Δa is the VCE. The value of $\mathcal{I}_T$ given in eq. (2.90) decreases as Δa increases. For the greatest value of Δa used in the calculation, the value of $\mathcal{I}_T$ is 0.9%. The values of the stress intensity factors converged to $K_1 = 5.5434$ N/mm$^{3/2+i\varepsilon}$ and $K_2 = 0.4073$ N/mm$^{3/2+i\varepsilon}$, respectively.

Next, the DCB specimen shown in Fig. 2.18b is discussed. In the FEAs, the DCB specimen

Table 2.20: Data for the DCB specimen using the first mesh.

$N/2$	$\Delta a(\mu\text{m})$	K_1 (N/mm$^{3/2+i\varepsilon}$)	K_2 (N/mm$^{3/2+i\varepsilon}$)	$\mathcal{I}_T$ (%)
1	0.5	21.084	12.772	21.6902
2	1.0	21.141	12.676	9.6901
3	1.5	21.160	12.647	6.7826
4	2.0	21.158	12.648	5.0106
5	2.5	21.158	12.647	4.0231
30	15.0	21.158	12.648	1.1282
31	15.5	21.158	12.648	1.1234
32	16.0	21.158	12.648	1.1198
33	16.5	21.158	12.648	1.1176
34	17.0	21.158	12.648	1.1163
35	17.5	21.158	12.648	1.1160
36	18.0	21.158	12.648	1.1168
37	18.5	21.158	12.648	1.1182
38	19.0	21.158	12.648	1.1205
50	25.0	21.158	12.648	1.1915
100	50.0	21.158	12.647	1.8125

is subjected to an applied load P = 1 N, as shown in Fig. 2.18b; $a = 20$ mm; $2h = 4$ mm, and the length of the body is $2w = 40$ mm. Plane strain conditions are imposed using CPE8 elements of Abaqus/CAE (2017). The first FEA is carried out with an element length in the vicinity of the crack tip of 0.5 μm. The second is carried out with an element length in the vicinity of the crack tip of 0.05 μm. In both cases, a focused mesh is used, similar to that in Fig. 2.4b. The number of elements and nodal points for the first mesh is 61,360 and 185,189, respectively; for the second mesh they are 125,360 and 377,349, respectively.

The results obtained for the stress intensity factors using the first mesh, are presented in Table 2.20. The lowest value of $\mathcal{I}_T$ is obtained for $\Delta a = 17.5$ μm. The values of the stress intensity factors for this value of Δa are found to be $K_1 = 21.158$ N/mm$^{3/2+i\varepsilon}$ and $K_2 = 12.648$ N/mm$^{3/2+i\varepsilon}$, respectively.

The results obtained for the stress intensity factors using the second mesh, are presented in Table 2.21. The value of $\mathcal{I}_T$ given in eq. (2.90) decreases as Δa increases. For the greatest value of Δa used in the calculation, the value of $\mathcal{I}_T$ is 0.9%. The values of the stress intensity factors converged to $K_1 = 21.164$ N/mm$^{3/2+i\varepsilon}$ and $K_2 = 12.651$ N/mm$^{3/2+i\varepsilon}$, respectively. The difference between the values of the stress intensity factors obtained using the first and the second meshes is less than 0.03%. Hence, convergence is fulfilled.

Table 2.21: Data for the DCB specimen using the second mesh.

$N/2$	$\Delta a(\mu\text{m})$	K_1 (N/mm$^{3/2+i\varepsilon}$)	K_2 (N/mm$^{3/2+i\varepsilon}$)	$\mathcal{I}_T$ (%)
1	0.05	21.051	12.784	21.0
2	0.10	21.163	12.687	9.3
3	0.15	21.171	12.655	6.5
4	0.20	21.164	12.650	4.7
5	0.25	21.165	12.650	3.8
10	0.50	21.165	12.652	1.9
50	2.50	21.164	12.651	0.4
100	5.00	21.164	12.651	0.3

2.5.4 Summary

In Section 2.5, an interface crack between two dissimilar linear elastic, transversely isotropic and homogeneous materials, as shown in Fig. 1.7, was investigated. The upper material is a unidirectional composite with fibers in the x_1- direction. The lower material is the same material as the upper one, rotated about the x_2-axis with fibers in the x_3- direction. The equations for this interface crack using the VCCT were derived. The interpenetration zone was found in Section 2.5.1. Numerical results for a finite length interface crack in an infinite body were presented in Section 2.5.2. The errors for the stress intensity factors, compared to analytical solution, were less than 0.3%. In Section 2.5.3, numerical results for a CCT and a DCB specimens were presented. For the CCT specimen, a mesh with an element length in the vicinity of the crack tip of 0.5 μm was used. The value of $\mathcal{I}_T$ decreases as Δa increases. The values of the stress intensity factors were taken for the largest Δa that was used. For the DCB specimen, two FEAs were carried out. The value of $\mathcal{I}_T$ using an element length in the vicinity of the crack tip of 0.5 μm decreased up to $\Delta a = 17.5$ μm; with a greater VCE the value of $\mathcal{I}_T$ increased. The values of the stress intensity factors were taken for $\Delta a = 17.5$ μm. Using an element length in the vicinity of the crack tip of 0.05 μm, the value of $\mathcal{I}_T$ decreases as Δa increases. The values of the stress intensity factors were taken for the largest Δa that was used. The values of the stress intensity factors obtained using the first and second meshes were almost the same with a difference of less than 0.03% difference. Based on this criterion, it was found in Sections 2.5.2 and 2.5.3 that a mesh consisting of fewer elements in the vicinity of the crack tip and fewer square rings, as compared to finer meshes, leads to the same results. With this information, meshes with fewer elements may be used for three-dimensional problems to decrease the FEA run-time.

Chapter 3

VCCT for three-dimensional problems

In this chapter, the VCCT is considered for three-dimensional problems. In Section 3.1, equations for calculating the energy release rates using a VCE that consists of many elements in three-dimensional problems are derived. Numerical results, considering the equations from Section 3.1, are presented in Section 3.2 for a straight through finite length crack and a penny-shaped crack in infinite bodies of linear-elastic, homogeneous and isotropic material. These problems are carried out for interface cracks between two dissimilar linear elastic, homogeneous and isotropic materials in Section 3.3. In Section 3.4, numerical results for an interface crack between two dissimilar transversely isotropic materials are presented.

3.1 Derivations of equations for calculating the energy release rates in three-dimensional problems

The VCCT was reviewed in Section 1.6.1. Recall that in Shivakumar et al. (1988), the first full mathematical derivation of the VCCT for eight-noded and twenty-noded brick elements was presented. Additional methods were reviewed in Section 1.6.1. One element was used in front of the crack front for the VCE in all cases. The equations for calculating the energy release rates are presented here using many elements for the VCE, as shown in Fig. 3.1 for a straight through crack.

The equations for a straight through crack are presented next. In Fig. 3.1, the VCE consists of two elements which are shaded for two different cases. Each node is denoted by its column m and row n in parentheses as (m, n). For the nodes ahead of the crack front and at the crack front, the columns are numbered by proceeding from the crack front. The node numbers for columns on the crack surface are primed. The primed numbers refer to the corresponding column on the crack surface. The derivation follows

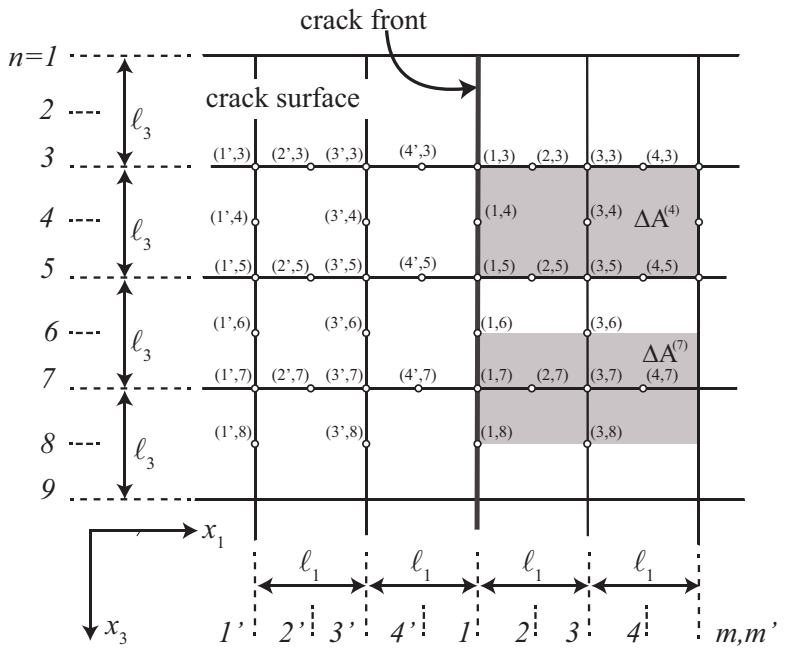

Figure 3.1: View from above of the nodes that are used for calculating the energy release rates in rows 4 and 7, using twenty-noded brick elements.

the approaches, presented in Section 1.6.1, of Shivakumar et al. (1988) for mid-nodes in eqs. (1.123) to (1.125) and of Whitcomb (1988) for corner nodes along the crack front in eqs. (1.127) to (1.129) using a VCE which consists of one element. The equation for the mode I energy release rate at mid-nodes along the crack front (even values of n) in Fig. 3.1 is given as

$$\mathcal{G}_I^{(n)} = \frac{1}{2\Delta A^{(n)}} \left[\left(\frac{1}{2} \sum_{m=1}^{2M} F_2^{(m,n-1)} \Delta u_2^{(m',n-1)} + F_2^{(m,n+1)} \Delta u_2^{(m',n+1)} \right) + \sum_{m=1}^{M} F_2^{(2m-1,n)} \Delta u_2^{(2m'-1,n)} \right], \tag{3.1}$$

where $\Delta A^{(n)}$ is the area of the virtual crack extension, presented in Fig. 3.1 as the shaded region for row 4 so that $n = 4$; it is given by

$$\Delta A^{(n)} = M \cdot \ell_1 \cdot \ell_3. \tag{3.2}$$

In eqs. (3.1) and (3.2), M is the number of elements used for the VCE, in this case, $M = 2$ (see Fig. 3.1). The length and the depth of the elements in the x_1 and x_3-directions are ℓ_1 and ℓ_3, respectively. In eq. (3.1), for the nodal point forces $F_p^{(m,n)}$ and the displacement jumps $\Delta u_p^{(m',n)}$, the subscript p represents the x_p-direction and the superscript denotes the node numbers. It is assumed that the nodal point forces $F_p^{(m,n-1)}$ and $F_p^{(m,n+1)}$ are distributed equally between two adjacent rows of elements. Therefore, they are multiplied by one-half in eq. (3.1).

The equation for the mode I energy release rate at corner nodes along the crack front (odd values of n) is given as

$$\mathcal{G}_I^{(n)} = \frac{1}{2\Delta A^{(n)}} \Bigg[\sum_{m=1}^{2M} F_2^{(m,n)} \Delta u_2^{(m',n)} + \frac{1}{2} \left(\sum_{m=1}^{M} F_2^{(2m-1,n-1)} \Delta u_2^{(2m'-1,n-1)} + F_2^{(2m-1,n+1)} \Delta u_2^{(2m'-1,n+1)} \right) \Bigg], \tag{3.3}$$

where $\Delta A^{(n)}$ is given in eq. (3.2) and is the shaded region surrounding $n = 7$ in Fig. 3.1. In eq. (3.3), it is assumed that the nodal point forces $F_p^{(2m-1,n-1)}$ and $F_p^{(2m-1,n+1)}$ are distributed equally between the calculations for the current corner-node and the former or the next corner node, respectively.

In order to calculate the modes II and III energy release rates, the subscript 2 in eqs. (3.1) and (3.3) is replaced by 1 and 3, respectively. Hence, the equation for the energy release rates at mid-nodes along the crack front for even values of n in Fig. 3.1 are given as

$$\mathcal{G}_{II}^{(n)} = \frac{1}{2\Delta A^{(n)}} \Bigg[\left(\frac{1}{2} \sum_{m=1}^{2M} F_1^{(m,n-1)} \Delta u_1^{(m',n-1)} + F_1^{(m,n+1)} \Delta u_1^{(m',n+1)} \right) + \sum_{m=1}^{M} F_1^{(2m-1,n)} \Delta u_1^{(2m'-1,n)} \Bigg], \tag{3.4}$$

$$\mathcal{G}_{III}^{(n)} = \frac{1}{2\Delta A^{(n)}} \Bigg[\left(\frac{1}{2} \sum_{m=1}^{2M} F_3^{(m,n-1)} \Delta u_3^{(m',n-1)} + F_3^{(m,n+1)} \Delta u_3^{(m',n+1)} \right) + \sum_{m=1}^{M} F_3^{(2m-1,n)} \Delta u_3^{(2m'-1,n)} \Bigg]. \tag{3.5}$$

In order to calculate $\mathcal{I}_I$ and $\mathcal{I}_{II}$, the subscript 2 in eqs. (3.1) and (3.3) is replaced by 1 only for the displacement jumps or only for the nodal point forces, respectively. The equations for the dual energy release rates at mid-nodes along the crack front are given by

$$\mathcal{I}_I^{(n)} = \frac{1}{2\Delta A^{(n)}} \Bigg[\left(\frac{1}{2} \sum_{m=1}^{2M} F_2^{(m,n-1)} \Delta u_1^{(m',n-1)} + F_2^{(m,n+1)} \Delta u_1^{(m',n+1)} \right) + \sum_{m=1}^{M} F_2^{(2m-1,n)} \Delta u_1^{(2m'-1,n)} \Bigg], \tag{3.6}$$

$$\mathcal{I}_{II}^{(n)} = \frac{1}{2\Delta A^{(n)}} \Bigg[\left(\frac{1}{2} \sum_{m=1}^{2M} F_1^{(m,n-1)} \Delta u_2^{(m',n-1)} + F_1^{(m,n+1)} \Delta u_2^{(m',n+1)} \right) + \sum_{m=1}^{M} F_1^{(2m-1,n)} \Delta u_2^{(2m'-1,n)} \Bigg]. \tag{3.7}$$

The equation for the energy release rates at corner-nodes along the crack front for odd values of n in Fig. 3.1 are given by

$$\mathcal{G}_{II}^{(n)} = \frac{1}{2\Delta A^{(n)}} \Bigg[\sum_{m=1}^{2M} F_1^{(m,n)} \Delta u_1^{(m',n)} + \frac{1}{2} \left(\sum_{m=1}^{M} F_1^{(2m-1,n-1)} \Delta u_1^{(2m'-1,n-1)} + F_1^{(2m-1,n+1)} \Delta u_1^{(2m'-1,n+1)} \right) \Bigg]. \tag{3.8}$$

$$\mathcal{G}_{III}^{(n)} = \frac{1}{2\Delta A^{(n)}} \Bigg[\sum_{m=1}^{2M} F_3^{(m,n)} \Delta u_3^{(m',n)} + \frac{1}{2} \left(\sum_{m=1}^{M} F_3^{(2m-1,n-1)} \Delta u_3^{(2m'-1,n-1)} + F_3^{(2m-1,n+1)} \Delta u_3^{(2m'-1,n+1)} \right) \Bigg], \tag{3.9}$$

For the dual energy release rates the equations are given by

$$\mathcal{I}_{I}^{(n)} = \frac{1}{2\Delta A^{(n)}} \Bigg[\sum_{m=1}^{2M} F_2^{(m,n)} \Delta u_1^{(m',n)} + \frac{1}{2} \left(\sum_{m=1}^{M} F_2^{(2m-1,n-1)} \Delta u_1^{(2m'-1,n-1)} + F_2^{(2m-1,n+1)} \Delta u_1^{(2m'-1,n+1)} \right) \Bigg], \tag{3.10}$$

$$\mathcal{I}_{II}^{(n)} = \frac{1}{2\Delta A^{(n)}} \Bigg[\sum_{m=1}^{2M} F_1^{(m,n)} \Delta u_2^{(m',n)} + \frac{1}{2} \left(\sum_{m=1}^{M} F_1^{(2m-1,n-1)} \Delta u_2^{(2m'-1,n-1)} + F_1^{(2m-1,n+1)} \Delta u_2^{(2m'-1,n+1)} \right) \Bigg]. \tag{3.11}$$

Next, the equations for calculating the energy release rates for a penny-shaped crack are presented. In Fig. 3.2, the view from above of a quarter of a penny-shaped crack is shown. The nodal point forces and the displacement jumps perpendicular and tangent to the crack front are denoted with subscripts r and θ, respectively. The x_2-axis is perpendicular to the crack plane. The equations for the energy release rates are given for even values of n at the mid-side nodes by

$$\mathcal{G}_{I}^{(n)} = \frac{1}{2\Delta A^{(n)}} \Bigg[\left(\frac{1}{2} \sum_{m=1}^{2M} F_2^{(m,n-1)} \Delta u_2^{(m',n-1)} + F_2^{(m,n+1)} \Delta u_2^{(m',n+1)} \right) + \sum_{m=1}^{M} F_2^{(2m-1,n)} \Delta u_2^{(2m'-1,n)} \Bigg], \tag{3.12}$$

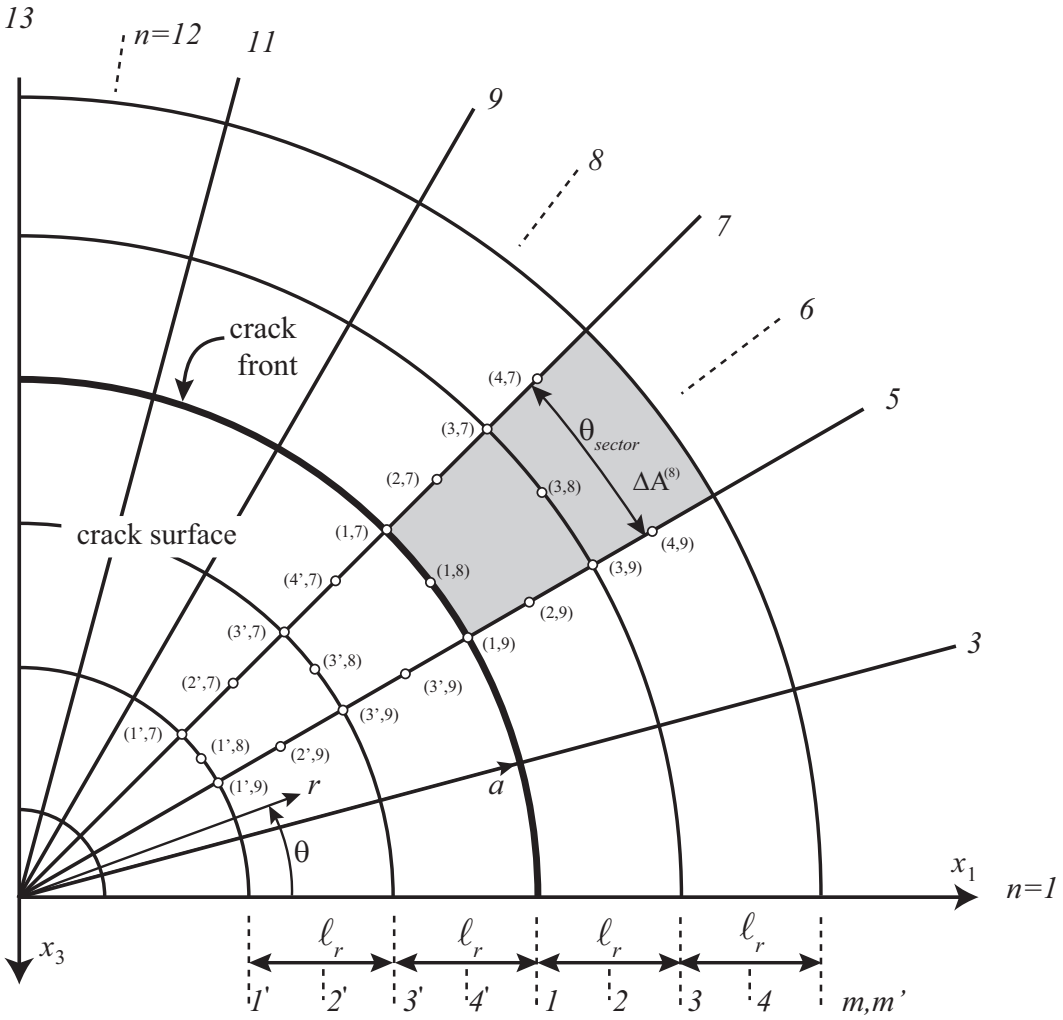

Figure 3.2: View from above of the nodes that are used for calculating the energy release rates in row 6 for a penny-shaped crack.

$$\mathcal{G}_{II}^{(n)} = \frac{1}{2\Delta A^{(n)}} \Bigg[\left(\frac{1}{2} \sum_{m=1}^{2M} F_r^{(m,n-1)} \Delta u_r^{(m',n-1)} + F_r^{(m,n+1)} \Delta u_r^{(m',n+1)} \right) + \sum_{m=1}^{M} F_r^{(2m-1,n)} \Delta u_r^{(2m'-1,n)} \Bigg], \tag{3.13}$$

$$\mathcal{G}_{III}^{(n)} = \frac{1}{2\Delta A^{(n)}} \Bigg[\left(\frac{1}{2} \sum_{m=1}^{2M} F_\theta^{(m,n-1)} \Delta u_\theta^{(m',n-1)} + F_\theta^{(m,n+1)} \Delta u_\theta^{(m',n+1)} \right) + \sum_{m=1}^{M} F_\theta^{(2m-1,n)} \Delta u_\theta^{(2m'-1,n)} \Bigg]. \tag{3.14}$$

where $\Delta A^{(n)}$ is the area of the virtual crack extension, presented in Fig. 3.2 as the shaded region for $n = 8$; it is given as

$$\Delta A^{(n)} = \left[(a + M \cdot \ell_r)^2 - a^2 \right] \frac{\theta_{sector}}{2} \tag{3.15}$$

where M is the number of elements used for the VCE and θ_{sector} is the angle of each sector

in radians. For odd values of n, the the energy release rates are given as

$$\mathcal{G}_I^{(n)} = \frac{1}{2\Delta A^{(n)}}\Bigg[\sum_{m=1}^{2M} F_2^{(m,n)}\Delta u_2^{(m',n)} + \frac{1}{2}\left(\sum_{m=1}^{M} F_2^{(2m-1,n-1)}\Delta u_2^{(2m'-1,n-1)} + F_2^{(2m-1,n+1)}\Delta u_2^{(2m'-1,n+1)}\right)\Bigg], \tag{3.16}$$

$$\mathcal{G}_{II}^{(n)} = \frac{1}{2\Delta A^{(n)}}\Bigg[\sum_{m=1}^{2M} F_r^{(m,n)}\Delta u_r^{(m',n)} + \frac{1}{2}\left(\sum_{m=1}^{M} F_r^{(2m-1,n-1)}\Delta u_r^{(2m'-1,n-1)} + F_r^{(2m-1,n+1)}\Delta u_r^{(2m'-1,n+1)}\right)\Bigg], \tag{3.17}$$

$$\mathcal{G}_{III}^{(n)} = \frac{1}{2\Delta A^{(n)}}\Bigg[\sum_{m=1}^{2M} F_\theta^{(m,n)}\Delta u_\theta^{(m',n)} + \frac{1}{2}\left(\sum_{m=1}^{M} F_\theta^{(2m-1,n-1)}\Delta u_\theta^{(2m'-1,n-1)} + F_\theta^{(2m-1,n+1)}\Delta u_\theta^{(2m'-1,n+1)}\right)\Bigg], \tag{3.18}$$

The dual energy release rates, $\mathcal{I}_I$ and $\mathcal{I}_{II}$, are given for even values of n at the mid-side nodes by

$$\mathcal{I}_I^{(n)} = \frac{1}{2\Delta A^{(n)}}\Bigg[\left(\frac{1}{2}\sum_{m=1}^{2M} F_2^{(m,n-1)}\Delta u_r^{(m',n-1)} + F_2^{(m,n+1)}\Delta u_r^{(m',n+1)}\right) + \sum_{m=1}^{M} F_2^{(2m-1,n)}\Delta u_r^{(2m'-1,n)}\Bigg], \tag{3.19}$$

$$\mathcal{I}_{II}^{(n)} = \frac{1}{2\Delta A^{(n)}}\Bigg[\left(\frac{1}{2}\sum_{m=1}^{2M} F_r^{(m,n-1)}\Delta u_2^{(m',n-1)} + F_r^{(m,n+1)}\Delta u_2^{(m',n+1)}\right) + \sum_{m=1}^{M} F_r^{(2m-1,n)}\Delta u_2^{(2m'-1,n)}\Bigg], \tag{3.20}$$

and for odd values of n as

$$\mathcal{I}_I^{(n)} = \frac{1}{2\Delta A^{(n)}}\Bigg[\sum_{m=1}^{2M} F_2^{(m,n)}\Delta u_r^{(m',n)} + \frac{1}{2}\left(\sum_{m=1}^{M} F_2^{(2m-1,n-1)}\Delta u_r^{(2m'-1,n-1)} + F_2^{(2m-1,n+1)}\Delta u_r^{(2m'-1,n+1)}\right)\Bigg], \tag{3.21}$$

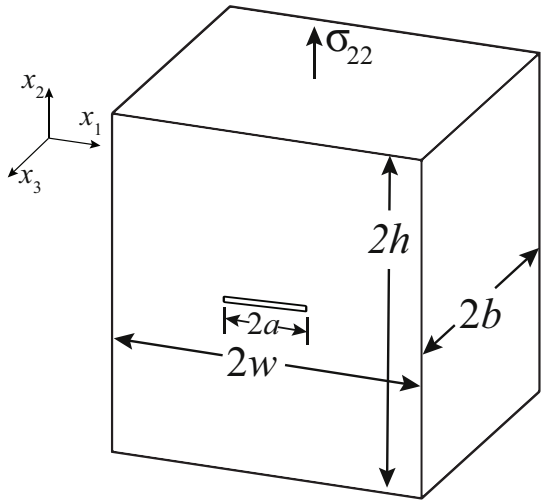

Figure 3.3: A straight through crack in an infinite body.

$$\mathcal{I}_{II}^{(n)} = \frac{1}{2\Delta A^{(n)}} \left[\sum_{m=1}^{2M} F_r^{(m,n)} \Delta u_2^{(m',n)} + \frac{1}{2} \left(\sum_{m=1}^{M} F_r^{(2m-1,n-1)} \Delta u_2^{(2m'-1,n-1)} + F_r^{(2m-1,n+1)} \Delta u_2^{(2m'-1,n+1)} \right) \right], \tag{3.22}$$

3.2 Numerical results for a straight through finite length crack and a penny-shaped crack in an infinite body of isotropic, homogeneous material

In this section, two problems are solved by means of an FEA using a commercial finite element program Abaqus/CAE (2017). The first problem is a straight through finite length crack of length $2a$ in an infinite body of a linear-elastic, homogeneous and isotropic material; a schematic view of the body is shown in Fig. 3.3. The half crack length is $a = 1$ mm. In order to approximate an infinite body, the ratio between the crack length and the body width in the finite element model is $w/a = 40$ and $h = w$. The crack is situated at the center of the body. Three different thicknesses are chosen for study, $2b = 4, 8$ and 15 mm. The origin of the coordinate system is located on the right crack front, at the mid-body thickness. The body is subjected to far field tension, where $\sigma_{22} = 1$ MPa as shown in Fig. 3.3. The mechanical properties of aluminium are used, where $E = 70$ MPa and $\nu = 0.3$.

The solution for the stress intensity factor for a crack in an infinite two-dimensional body is given in Irwin (1957) and presented in eqs. $(2.72)_1$ and $(2.73)_1$. Using eq. (1.19), one

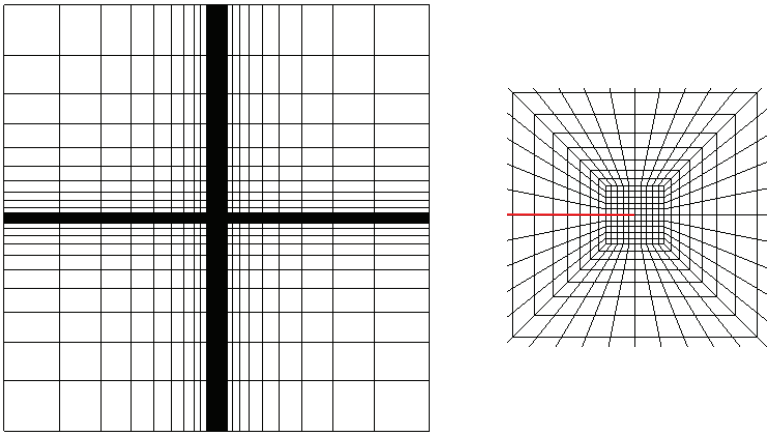

Figure 3.4: A schematic view of (a) the x_1x_2-plane of the mesh that was used for a straight through crack in an infinite body and (b) a close up of the vicinity of the crack tip for this mesh.

may calculate the mode I stress intensity factor for two-dimensional problems by assuming plane stress or plane strain conditions. When solving a three-dimensional problem, if the body is sufficiently thick, one may assume that plane strain conditions prevail at the mid-plane of the body. By using eq. (1.19) and assuming plane strain, the stress intensity factor for mode I is given as

$$K_I = \sqrt{\frac{E}{1-\nu^2}\,\mathcal{G}_I}\,. \tag{3.23}$$

Thus, for $\sigma_{22} = 1$ MPa the mode I energy release rate and the normalized stress intensity factor are $\mathcal{G}_I = 40.8$ N/m and $\hat{K}_I = 1$, respectively.

For $2b = 4$ mm, two meshes are used to check convergence. The coarser mesh is denoted as A1 and the finer mesh is denoted as A2. A schematic view of the x_1x_2-plane of the meshes that are used here, is presented in Fig. 3.4a. At the corners of the body, the elements are large and they become smaller as one approaches the crack, as shown in Fig. 3.4a. The dimensions of the biggest elements at the corners of the body are $\sim 10 \times 10$ mm^2 for both meshes. Around each crack tip there is a focused mesh containing 15 rings. In the vicinity of the crack tips, for mesh A1, there is a uniform mesh of 10×10 elements, as shown in Fig. 3.4b. For mesh A2, there is a uniform mesh of 20×20 elements. The dimensions of the elements in the vicinity of the crack tip in the x_1x_2-plane are 10×10 μm^2 and 5×5 μm^2 for meshes A1 and A2, respectively. There are transition elements between the outer mesh and the focused mesh. The greatest aspect ratio of those elements is ~ 50 and ~ 100 for meshes A1 and A2, respectively. The meshes were extruded through the half-thickness of the body and symmetry conditions were used at the center plane of the body, where $x_3 = 0$. This plane is constrained in the x_3-direction for translation and in the x_1 and x_2-directions for rotation. The thickness of the elements is 0.1 mm so that there are 20 elements through the thickness. The number of elements and nodes of the

Table 3.1: The number of elements and nodes for each three-dimensional mesh for a straight through finite length crack in Fig. 3.3.

Mesh	Thickness ($2b$) (mm)	elements	nodes
A1	4	46,800	200,916
A2	4	94,400	400,936
B	8	188,800	787,416
C	15	354,000	1,463,756

meshes is presented in Table 3.1.

The results obtained for $\mathcal{G}_I$ using eq. (3.3) at the mid-plane of meshes A1 and A2, which is a corner node, are presented in Table 3.2. In this table, M is the number of elements used for the VCE. The results for $\mathcal{G}_I$ for mesh A1 and A2 are nearly constant as a function of Δa with a difference of up to 0.02% for each mesh. The difference between the results for meshes A1 and A2 is less than 0.07% indicating convergence of the results. Thus, mesh A2 is extruded through the thickness for $2b = 8$ and 15 mm resulting in meshes B and C in Table 3.1. The number of elements and nodes of meshes B and C are presented in Table 3.1. It may be noted from Table 3.2 that for homogeneous material it is possible to use one element for the VCE with accurate results produced.

In Fig. 3.5 the results for the mode I energy release rate normalized by the mode I energy release rate for the two-dimensional plane strain problem are presented. The results are shown for $2b = 4, 8$ and 15 mm as function of x_3/b, where $x_3 = 0$ is the mid-plane of the body. Mesh A2 was used for $2b = 4$ mm. The results achieved with the VCCT using eq. (3.1) for mid-side nodes and eq. (3.3) for corner nodes are plotted in blue. The results

Table 3.2: Numerical results for a straight through finite length crack using two-dimensional meshes from Table 3.1.

M	mesh A1		mesh A2	
	Δa (μm)	$\mathcal{G}_I$ (N/m)	Δa (μm)	$\mathcal{G}_I$ (N/m)
1	10	42.15	5	42.16
2	20	42.15	10	42.17
3	30	42.15	15	42.17
4	40	42.14	20	42.17
5	50	42.14	25	42.17
6			30	42.17
7			35	42.17
8			40	42.17
9			45	42.17
10			50	42.16

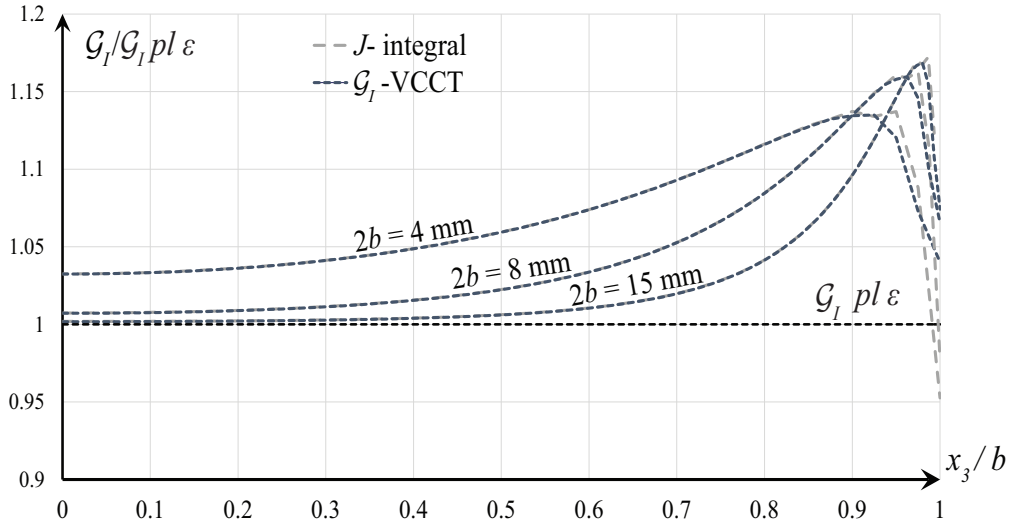

Figure 3.5: Numerical results for a straight through finite length crack in an infinite body.

presented were taken for ΔA with ten elements used for the VCE. The gray lines show the results of the J-integral. The results presented were taken from the tenth contour. The black line is the analytical energy release rate for the two-dimensional plane strain problem.

As one may observe, the results at the mid-plane ($x_3 = 0$) converged to the plane strain solution as the thickness of the body is increased. For $2b = 15$ mm, the results differ by 0.17% from the plane strain solution at the mid-plane. The results differ by less than 0.5% for $x_3/b < 0.45$ for this thickness. The difference between the results obtained by the VCCT and the J-integral is less than 0.02% for $x_3/b < 0.95$. For $x_3/b > 0.95$, there are significant differences between results obtained with the two methods.

Next, a penny-shaped crack in an infinite linear elastic, isotropic and homogeneous body is considered. The mechanical properties of the body are $E = 70$ GPa and $\nu = 0.3$. The dimensions of the body are $a = 1$ mm, $R/a = 40$ and $h/R = 1$ where $2a$ and $2R$ are the crack and the body diameters, respectively, and $2h$ is the height of the body, as shown in Fig. 3.6. The crack is situated at the center of the body. The analytical solution of the problem is given by Sneddon (1946) as

$$K_I = \frac{2}{\pi}\,\sigma_{22}\sqrt{\pi a} \tag{3.24}$$

where the value of σ_{22} is 1 MPa.

First, a convergence study is carried out using two-dimensional axisymmetric meshes. Two axisymmetric meshes are constructed using Abaqus (2017) with eight noded isoparametric axisymmetric elements (CAX8). The axis of symmetry is at the center of the cylinder, as shown in Fig. 3.7a. In the vicinity of the crack tip, there are uniform elements of a size of $\ell \times \ell$, shown as an empty rectangle in Fig. 3.7a; the inner mesh is shown in Fig. 3.7b. The

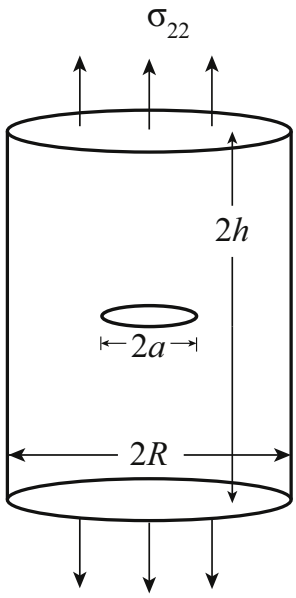

Figure 3.6: A penny-shaped crack in an infinite body.

length ℓ differs from mesh to mesh. The values of ℓ and the number of the elements and nodes for each mesh are shown in Table 3.3. Mesh B is shown in Fig. 3.7. In Fig. 3.7a, one may observe that the elements become smaller towards the vicinity of the crack tip. An area of 1×1 mm^2 around the crack tip contains the uniform mesh.

The energy release rate $\mathcal{G}_I$ is calculated using eq. (1.107) where Δa is replaced by ΔA given as

$$\Delta A = \pi \left[(a + \Delta a)^2 - a^2 \right]. \tag{3.25}$$

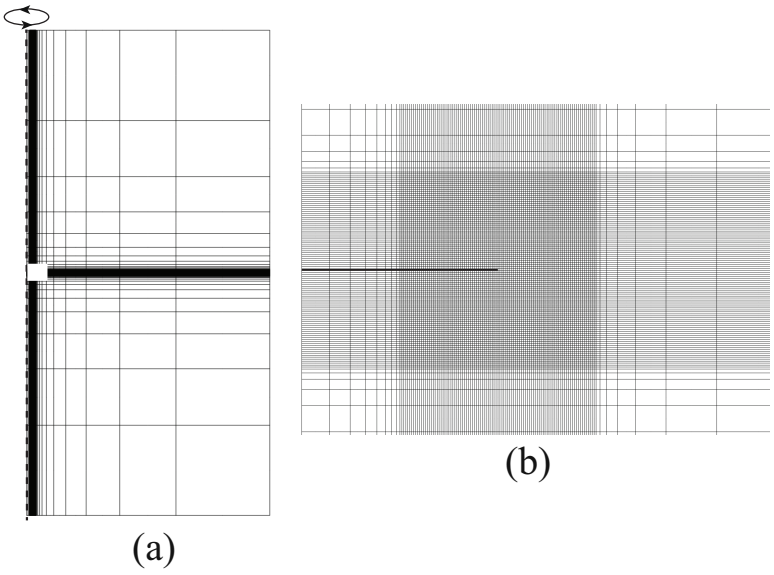

Figure 3.7: A view of (a) the mesh that was used for a penny-shaped crack in an infinite body and (b) a close up of the vicinity of the crack tip for this mesh.

Table 3.3: The size ℓ of the elements near the crack tip and the total number of elements and nodes for each mesh for the penny-shaped crack and axisymmetric mesh.

Mesh	ℓ (μm)	elements	nodes
A	50	1,656	5,159
B	10	15,860	48,201

In eq. (3.25), ΔA is the area of an annulus, as shown in Fig. 3.8. For a penny-shaped crack, the crack front satisfies plane-strain conditions. The stress intensity factor K_I is found from $\mathcal{G}_I$ using eq. (3.23). From eq. (3.24), the analytical solution is $K_I = 1.1284$ N/mm$^{3/2}$. The numerical results for meshes A and B are shown, respectively, in Tables 3.4 and 3.5. The greatest error for meshes A and B is -0.52% and -0.12%, respectively. The errors obtained for K_I are nearly constant for each mesh with a difference of up to 0.07% and 0.06% for meshes A and B, respectively. The results converged to the analytical solution for the finest mesh.

Hence, for the three dimensional analysis, mesh B is swept through 90° with ten divisions. The isoparametric and upper views are shown in Figs. 3.9a and 3.9b, respectively. The plane of the crack is similar to that in Fig. 3.2, with ten divisions in the angular direction and a much more refined mesh in the radial direction. The eight-noded elements were swept to twenty-noded elements (C3D20) except for the elements touching the x_2-axis. The inner elements were swept to fifteen-noded wedge elements (C3D15). The mesh consists of 158,600 brick elements, 1,300 wedge elements and 693,603 nodes. The size of the elements in the vicinity of the crack front is $\ell_r \times \ell_2 \times \ell_\theta = 10 \times 10 \times 157\mu$m^3. Symmetry conditions were applied at $x_1 = 0$ and $x_3 = 0$. The $x_1 = 0$ plane is constrained in the x_1-direction for translation and in the x_2 and x_3-directions for rotation. The $x_3 = 0$

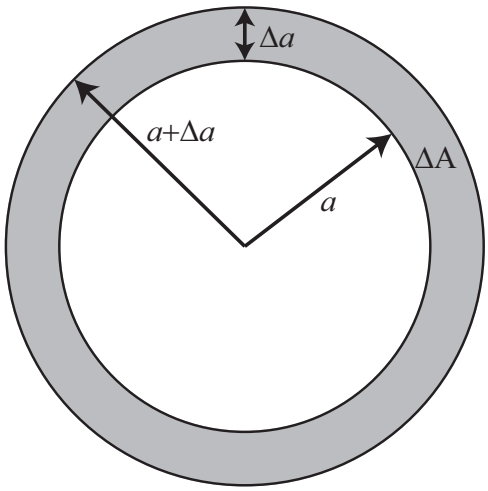

Figure 3.8: Upper view of the virtual crack extension of a penny-shaped crack for an axisymmetric problem.

Table 3.4: Data for mesh A in Table 3.3 ($\ell = 50$ μm).

M	$\Delta a(\mu\text{m})$	K_I (N/mm$^{3/2}$)	K_I (% error)
1	50	1.1225	-0.52
2	100	1.1227	-0.51
3	150	1.1228	-0.49
4	200	1.1230	-0.48
5	250	1.1231	-0.47
6	300	1.1232	-0.46
7	350	1.1233	-0.45
8	400	1.1233	-0.45
9	450	1.1232	-0.46
10	500	1.1231	-0.47

plane is constrained in the x_3-direction for translation and in the x_1 and x_2-directions for rotation. The mode I energy release rate was calculated by using eqs. (3.12) for mid-side nodes and (3.16) for corner nodes along the crack front. For each ray, both corner nodes and mid-side nodes, the same results were obtained. The stress intensity factor K_I is found using eq. (3.23).

The results for one ray are shown in Table 3.6. The greatest error for this mesh is -0.11%. The biggest different between the errors in Tables 3.5 and 3.6 for a specific value of Δa is 0.02%. These results are logical, since the axisymmetric mesh represents a simplification of the three-dimensional mesh. Acceptable results are obtained when one element is used

Table 3.5: Data for mesh B in Table 3.3 ($\ell = 10$ μm).

M	$\Delta a(\mu\text{m})$	K_I (N/mm$^{3/2}$)	K_I (% error)
1	10	1.1271	-0.12
2	20	1.1272	-0.11
7	70	1.1272	-0.11
8	80	1.1273	-0.10
13	130	1.1273	-0.10
14	140	1.1274	-0.09
23	230	1.1275	-0.08
24	240	1.1276	-0.07
32	320	1.1276	-0.07
33	330	1.1277	-0.06
37	370	1.1277	-0.06
38	380	1.1276	-0.07
39	390	1.1276	-0.07
44	440	1.1276	-0.07
50	500	1.1274	-0.09

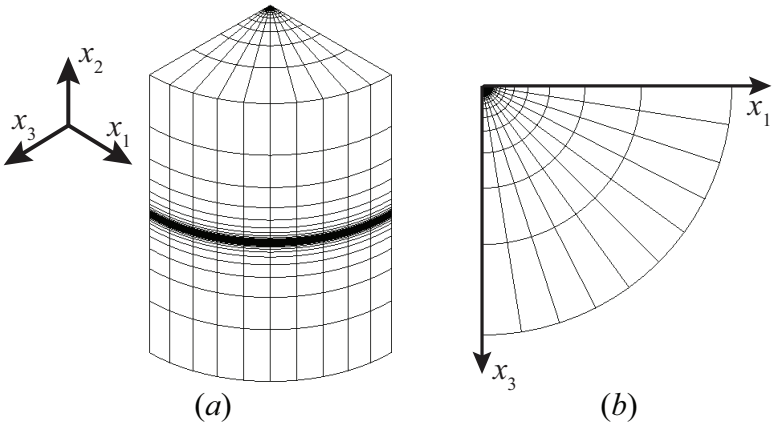

Figure 3.9: (a) Isoparametric and (b) upper views of the mesh used for the penny-shaped crack.

as the VCE.

Table 3.6: Numerical results for a penny-shaped crack using a three-dimensional mesh ($\ell_r \times \ell_2 \times \ell_\theta = 10 \times 10 \times 157\mu\text{m}^3$).

M	$\Delta a(\mu\text{m})$	K_I (N/mm$^{3/2}$)	K_I (% error)
1	10	1.1272	-0.11
2	20	1.1272	-0.11
7	70	1.1272	-0.10
8	80	1.1273	-0.10
9	90	1.1273	-0.10
13	130	1.1273	-0.09
14	140	1.1274	-0.09
23	230	1.1275	-0.07
24	240	1.1276	-0.07
32	320	1.1276	-0.07
33	330	1.1276	-0.06
37	370	1.1276	-0.06
38	380	1.1276	-0.07
39	390	1.1276	-0.07
44	440	1.1276	-0.07
50	500	1.1274	-0.09

3.3 Numerical results for an interface crack between two dissimilar linear elastic, homogeneous and isotropic materials

In this section, two problems of an interface crack between two linear elastic, homogeneous and isotropic materials are solved by means of an FEA using a commercial finite element program Abaqus/CAE (2017). The first problem is a straight through interface crack with a finite length of $2a$ in an infinite body; a schematic view of the body is shown in Fig. 3.10. In the finite element analyses, the width, height and thickness of the body are $2w$, $2h$ and $2b$, respectively, and the length of the crack is $2a$, where $a/w = 0.025$, and $h/w = 1$, as shown schematically in Fig. 3.10. The length of the crack is $2a = 2$ mm. Two different thicknesses are chosen for study, $2b = 4$ and 15 mm. The mechanical properties are $E_1 = 1$ GPa, $\nu_1 = 0.3$, $E_2/E_1 = 0.1$ and $\nu_2/\nu_1 = 1$. The origin of the coordinate system is located on the right crack front, at the mid-body thickness. Meshes A2 and C, presented in Table 3.1, are used for $2b = 4$ and 15 mm. Recall that in Section 3.2, a convergence study was made for mesh A2.

The stress intensity factor for a finite length interface crack between two dissimilar linear elastic, isotropic and homogeneous materials in an infinite two-dimensional body is given in Rice (1988) and in eq. (2.62). In order to maintain displacement continuity along the interface, the stresses $\sigma_{11}^{(1)}$, $\sigma_{11}^{(2)}$, $\sigma_{33}^{(1)}$ and $\sigma_{33}^{(2)}$ are applied parallel to the crack, as shown in Fig. 3.10. Using Hooke's law for a three-dimensional problem and requiring that the

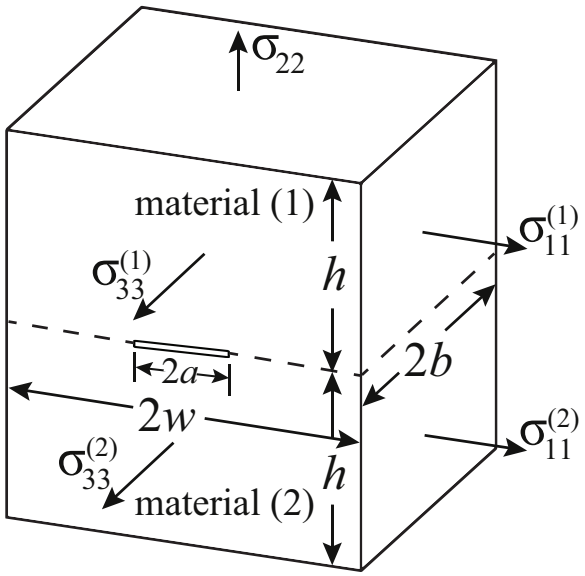

Figure 3.10: An infinite, bimaterial body subjected to tension σ_{22} and tractions $\sigma_{11}^{(1)}$, $\sigma_{11}^{(2)}$, $\sigma_{33}^{(1)}$ and $\sigma_{33}^{(2)}$ parallel to the interface plane. The width, height and thickness are $2w$, $2h$ and $2b$, respectively.

strains in the upper and the lower materials will be equal in x_1 and x_3-directions along the interface results in

$$\sigma_{11}^{(2)} = \frac{E_2}{E_1}\left[\frac{1-\nu_1\nu_2}{1-\nu_2^2}\right]\sigma_{11}^{(1)} + \frac{E_2}{E_1}\left[\frac{\nu_2-\nu_1}{1-\nu_2^2}\right]\sigma_{33}^{(1)} + \left[\nu_2(1+\nu_2) - \frac{E_2}{E_1}\nu_1(1+\nu_2)\right]\frac{\sigma_{22}}{1-\nu_2^2} \tag{3.26}$$

and

$$\sigma_{33}^{(2)} = \frac{E_2}{E_1}\left[\frac{1-\nu_1\nu_2}{1-\nu_2^2}\right]\sigma_{33}^{(1)} + \frac{E_2}{E_1}\left[\frac{\nu_2-\nu_1}{1-\nu_2^2}\right]\sigma_{11}^{(1)} + \left[\nu_2(1+\nu_2) - \frac{E_2}{E_1}\nu_1(1+\nu_2)\right]\frac{\sigma_{22}}{1-\nu_2^2}. \tag{3.27}$$

The tractions $\sigma_{11}^{(1)}$ and $\sigma_{33}^{(1)}$ are chosen arbitrarily, and $\sigma_{11}^{(2)}$ and $\sigma_{33}^{(2)}$ are calculated by using eqs. (3.26) and (3.27). Equations (3.26) and (3.27) are similarly developed to that between $\sigma_{11}^{(1)}$ and $\sigma_{11}^{(2)}$ for a plane strain two-dimensional problem, given in eq. (1.165) and presented by Rice and Sih, (1965). Using eqs. (3.26) and (3.27), the body is subjected to $\sigma_{22} = 1$ MPa, $\sigma_{11}^{(1)} = 1$ MPa, $\sigma_{33}^{(1)} = 1$ MPa, $\sigma_{11}^{(2)} = 0.4857$ MPa and $\sigma_{33}^{(2)} = 0.4857$ MPa.

By using eq. (2.62), the two-dimensional analytical solution for plane strain conditions is $K_1 = 1.7841$ N/mm$^{3/2+i\varepsilon}$ and $K_2 = -0.1753$ N/mm$^{3/2+i\varepsilon}$, where

$$\varepsilon = -0.0758. \tag{3.28}$$

For a two-dimensional solution, there is no value for K_{III}. Using the two-dimensional analytical solution, the interface energy release rate, $\mathcal{G}_i$, is obtained using eq. (1.35) as $\mathcal{G}_i = 15.2058$ N/m. The values of $1/H_1$ and $1/H_2$ in eq. (1.35) are

$$\frac{1}{H_1} = 211.3497 \text{ (MPa}^{-1}\text{)} \quad , \quad \frac{1}{H_2} = 139.8601 \text{ (MPa}^{-1}\text{)}. \tag{3.29}$$

Numerical results for the energy release rates $\mathcal{G}_I^{(n)}$, $\mathcal{G}_{II}^{(n)}$ and $\mathcal{G}_{III}^{(n)}$, were obtained using eqs. (3.1), (3.4) and (3.5) for mid-side nodes, and eqs. (3.3), (3.8) and (3.9) for corner nodes. The values for the dual energy release rates $\mathcal{I}_I^{(n)}$ and $\mathcal{I}_{II}^{(n)}$ were obtained using eqs. (3.6) and (3.7) for mid-side nodes, and eqs. (3.10) and (3.11) for corner nodes. It is noted that n is the row number as shown in Fig. 3.1. The interface energy release rate, $\mathcal{G}_i$, is obtained for each row using eq. (1.122), where $N = n$. Numerical results of the energy release rates obtained for $2b = 15$ mm at the mid-plane, where $n = 1$, $x_3/b = 0$, and this is a corner node; and for $n = 145$, $x_3/b = 0.96$, which is also a corner node, where the maximum value of the interface energy release rate is obtained. These results are presented in Table 3.7. Recall that the element length in the x_3-direction is 0.1 mm, so that for $2b = 15$ mm there are 151 rows of nodes when using symmetry conditions. In addition, M is the number of elements used as the VCE. The lowest difference between the dual energy release rates, $\mathcal{I}_I^{(n)}$ and $\mathcal{I}_{II}^{(n)}$, for each row was found for ΔA with ten elements used for the VCE. Hence, the best results are considered to be taken for $M = 10$ elements. The results are compared to the M-integral of Abaqus/CAE (2017) which are taken from the tenth contour. The results presented below the results obtained for $M = 10$. The

Table 3.7: Numerical results of $\mathcal{G}_i^{(n)}$, $\mathcal{G}_I^{(n)}$, $\mathcal{G}_{II}^{(n)}$, $\mathcal{G}_{III}^{(n)}$, $\mathcal{I}_I^{(n)}$, $\mathcal{I}_{II}^{(n)}$ and $\mathcal{I}^{(n)}$ for $2b = 15$ mm in rows $n = 1$ and $n = 145$ using mesh C in Table 3.1 for an interface crack in Fig. 3.10.

$n = 1$, $x_3/b = 0$							
M	$\mathcal{G}_i^{(1)}$ (N/m)	$\mathcal{G}_I^{(1)}$ (N/m)	$\mathcal{G}_{II}^{(1)}$ (N/m)	$\mathcal{G}_{III}^{(1)}$ (N/m)	$\mathcal{I}_I^{(1)}$ (N/m)	$\mathcal{I}_{II}^{(1)}$ (N/m)	$\mathcal{I}^{(1)}$ (%)
1	15.2285	11.9043	3.3242	0.0000	5.7691	6.7484	-17.0
2	15.2322	12.5932	2.6390	0.0000	5.6012	6.0583	-8.2
3	15.2330	12.9545	2.2785	0.0000	5.3475	5.6741	-6.1
4	15.2331	13.1893	2.0439	0.0000	5.1494	5.3965	-4.8
5	15.2327	13.3649	1.8678	0.0000	4.9795	5.1831	-4.1
6	15.2328	13.5035	1.7293	0.0000	4.8330	5.0079	-3.6
7	15.2326	13.6169	1.6157	0.0000	4.7038	4.8591	-3.3
8	15.2323	13.7123	1.5199	0.0000	4.5882	4.7296	-3.1
9	15.2318	13.7942	1.4375	0.0000	4.4835	4.6147	-2.9
10	15.2313	13.8658	1.3655	0.0000	4.3879	4.5114	-2.8
M-integral	15.2339						
$n = 145$, $x_3/b = 0.96$							
M	$\mathcal{G}_i^{(145)}$ (N/m)	$\mathcal{G}_I^{(145)}$ (N/m)	$\mathcal{G}_{II}^{(145)}$ (N/m)	$\mathcal{G}_{III}^{(145)}$ (N/m)	$\mathcal{I}_I^{(145)}$ (N/m)	$\mathcal{I}_{II}^{(145)}$ (N/m)	$\mathcal{I}^{(145)}$ (%)
1	16.8911	12.8642	3.9621	0.0648	6.5638	7.6408	-17.0
2	16.8956	13.6467	3.1841	0.0648	6.4091	6.9128	-8.2
3	16.8967	14.0598	2.7722	0.0648	6.1467	6.5042	-6.1
4	16.8970	14.3295	2.5027	0.0649	5.9402	6.2075	-4.8
5	16.8968	14.5319	2.2999	0.0649	5.7620	5.9790	-4.1
6	16.8969	14.6920	2.1399	0.0649	5.6078	5.7911	-3.6
7	16.8967	14.8234	2.0083	0.0650	5.4715	5.6311	-3.3
8	16.8964	14.9341	1.8972	0.0650	5.3493	5.4916	-3.1
9	16.8957	15.0293	1.8013	0.0651	5.2385	5.3676	-2.9
10	16.8951	15.1127	1.7173	0.0651	5.1370	5.2561	-2.8
M-integral	16.9147						

value obtained for $\mathcal{G}_i^{(1)}$, differs by 0.17% from the plane strain analytical solution. The difference between the values obtained for $\mathcal{G}_i^{(n)}$, where $n = 1$ and 145, compared to the M-integral are -0.02% and -0.12%, respectively.

In Fig. 3.11, the results for the interface energy release rate $\mathcal{G}_i$ normalized by the interface energy release rate for the two-dimensional plane strain problem are presented. The results are shown for $2b = 4$ and 15 mm as function of x_3/b, where $x_3 = 0$ is the mid-plane of the body. As a result of symmetry, the results are shown only for one-half of the body. The results achieved with the VCCT are plotted in blue. Except for the three closest element rows at the outer surface of the body, the same results were obtained by means of the

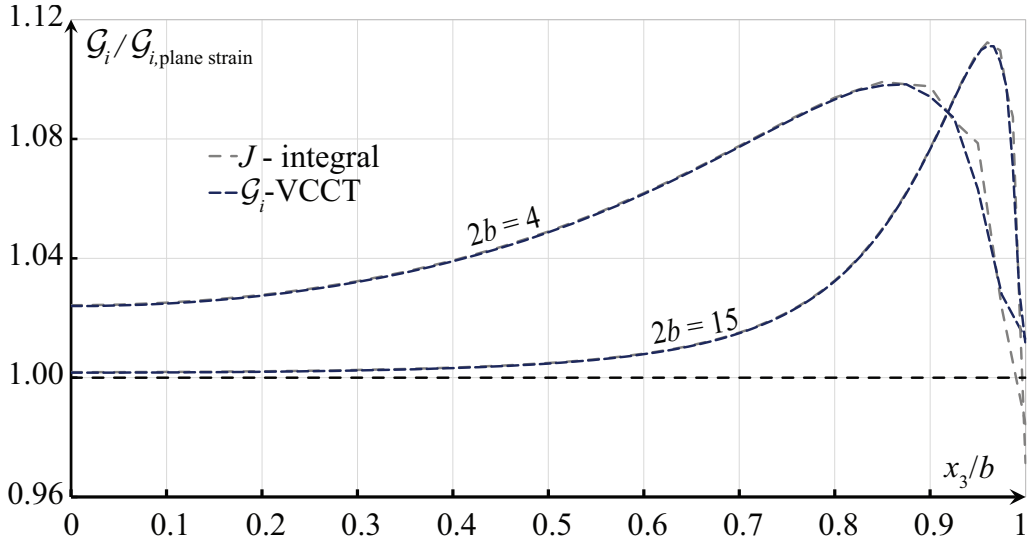

Figure 3.11: Numerical results of a straight through interface crack, shown in Fig. 3.10, where the mechanical properties are $E_1 = 1$ GPa, $\nu_1 = 0.3$, $E_2/E_1 = 0.1$ and $\nu_2/\nu_1 = 1$.

VCCT and the M-integral to three significant figures, as shown in Fig. 3.11. There are 20 rows of elements in the x_3-direction for $2b = 4$ mm, and 150 rows for $2b = 15$ mm. As for the straight through crack in an infinite body of an isotropic material from Section 3.2, the results at the mid-plane ($x_3 = 0$) converged to the plane strain solution as the thickness of the body is increased. The results differ by less than 0.5% for $0 \leq x_3/b \leq 0.5$ for this thickness.

Numerical results for the stress intensity factors obtained for $2b = 15$ mm at the mid-plane, where $n = 1$ and $x_3/b = 0$, and at $n = 145$ and $x_3/b = 0.96$, where the maximum value of the interface energy release rate is obtained, are presented in Table 3.8. The stress intensity factors were calculated using eq. (2.61) for K_1 and K_2 and eq. (1.39) for K_{III}. Recall that, the lowest difference between the dual energy release rates, $\mathcal{I}_I^{(n)}$ and $\mathcal{I}_{II}^{(n)}$, for each row was found for ΔA with ten elements used as the VCE. Hence, the best results are considered to be obtained for ΔA consisting of ten elements. The results are compared to those obtained by the M-integral of Abaqus/CAE (2017) and taken from the tenth contour. These results are presented below the results obtained for $M = 10$. The values obtained for K_1 and K_2 in $n = 1$, differ by 0.09% and -0.29%, respectively, from the plane strain solution. The differences between the results obtained for K_1, K_2 and K_{III} from the VCCT compared to the M-integral are -0.02%, -0.03% and 0.00%, respectively, for row $n = 1$. For row $n = 145$, The differences between the results obtained for K_1, K_2 and K_{III} from the VCCT compared to the M-integral are -0.12%, -0.07% and -0.83%, respectively. For ΔA with one element used as the VCE, where $M = 1$, the differences between the results obtained for K_1, K_2 and K_{III} from the VCCT compared to the M-integral are 0.00%, -4.81% and 0.00%, respectively, for row $n = 1$; for row $n = 145$, The differences are -0.05%, -5.27% and -1.04%, respectively. As was shown in the two-dimensional cases

Table 3.8: Numerical results of the stress intensity factors for $2b = 15$ mm in rows $n = 1$ and $n = 145$ using mesh C in Table 3.1 for an interface crack in Fig. 3.10.

$n = 1$, $x_3/b = 0$			
M	K_1 (N/mm$^{3/2+i\varepsilon}$)	K_2 (N/mm$^{3/2+i\varepsilon}$)	K_{III} (N/mm)
1	1.7863	-0.1663	-0.0001
2	1.7859	-0.1728	-0.0001
3	1.7858	-0.1746	-0.0001
4	1.7858	-0.1745	-0.0001
5	1.7858	-0.1747	-0.0001
6	1.7858	-0.1747	-0.0001
7	1.7857	-0.1748	-0.0001
8	1.7857	-0.1748	-0.0001
9	1.7857	-0.1748	-0.0001
10	1.7857	-0.1748	-0.0001
M-integral	1.7863	-0.1747	-0.0001
$n = 145$, $x_3/b = 0.96$			
M	K_1 (N/mm$^{3/2+i\varepsilon}$)	K_2 (N/mm$^{3/2+i\varepsilon}$)	K_{III} (N/mm)
1	1.8808	-0.1367	-0.0952
2	1.8806	-0.1433	-0.0952
3	1.8805	-0.1451	-0.0952
4	1.8806	-0.1449	-0.0952
5	1.8805	-0.1450	-0.0953
6	1.8805	-0.1450	-0.0953
7	1.8805	-0.1450	-0.0953
8	1.8805	-0.1450	-0.0954
9	1.8805	-0.1450	-0.0954
10	1.8804	-0.1450	-0.0954
M-integral	1.9195	-0.1443	-0.0962

in Chapter 2, if K_1 and K_2 differ by one order of magnitude, many elements should be used as the VCE in order to obtain accurate results.

In Figs. 3.12a, 3.12b and 3.12c, the results for the stress intensity factors K_1, K_2 and K_{III} using mesh C from Table 3.1, where $2b = 15$ mm, are presented, respectively. The analytical solutions for K_1 and K_2 are plotted by a dashed black line in Figs. 3.12a and 3.12b, respectively. The results are compared to the stress intensity factors obtained by means of the M-integral of Abaqus/CAE (2017) and the results presented are taken from the tenth contour. Similar behavior as presented for the interface energy release rate was obtained for the stress intensity factors. All rows have been examined including mid-node

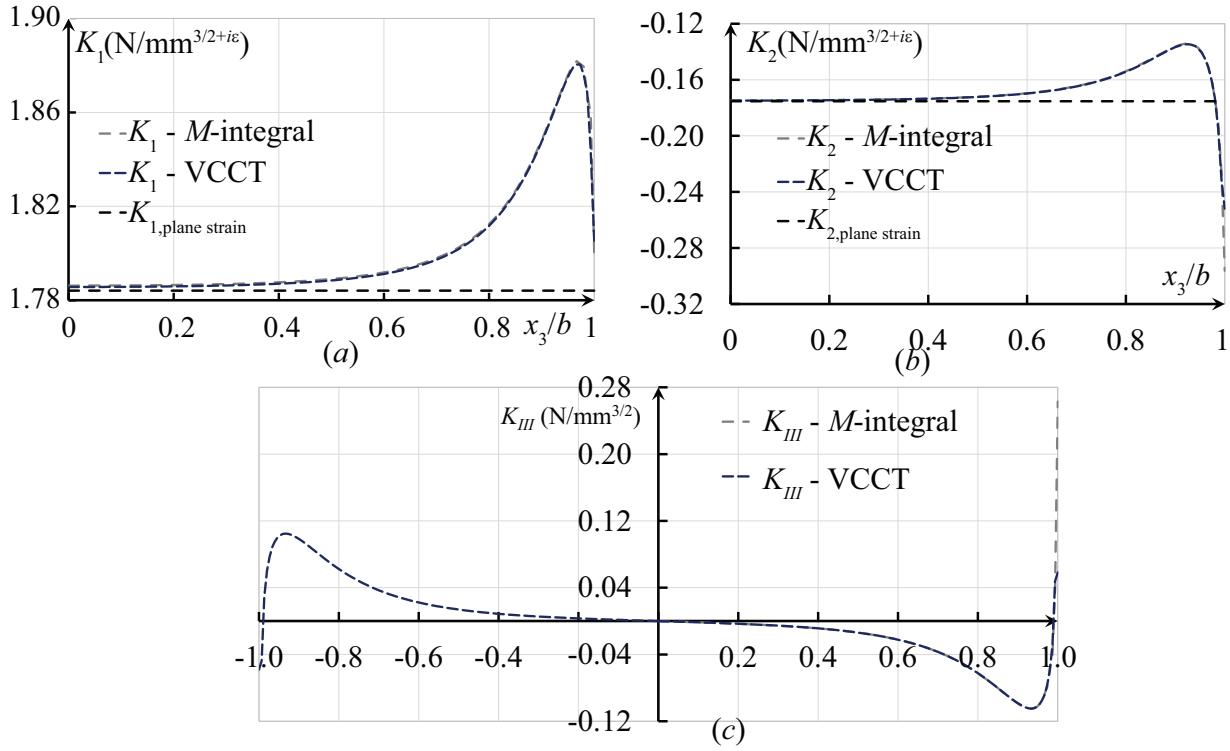

Figure 3.12: Numerical results of a straight through interface crack, shown in Fig. 3.10, for $2b = 15$ mm, for (a) K_1, (b) K_2 and (c) K_{III}.

rows. The differences between the values obtained using the VCCT and the M-integral for K_1, except for the three element rows closest to the outer surface is less than 0.05%; for K_2, the difference is less than 0.45%; for K_{III}, the difference is less than 1.9%. Note that K_{III} is anti-symmetric. If symmetry is not used in the FEA, the same results are obtained for K_{III} to 4 significant figures for $0 \leq x_3/b \leq 1$ for $2b = 4$ mm. Thus, the results obtained for K_{III} using the VCCT are shown to be anti-symmetric in 3.12c for $-1 \leq x_3/b \leq 1$. It is interesting that the symmetry conditions provide the correct values of K_{III} for $0 \leq x_3/b \leq 1$.

Next, a penny-shaped interface crack problem in an infinite body is considered. The mechanical properties of the upper and lower materials, respectively, are $E_1 = 1$ GPa, $E_1 = 0.1$ GPa and $\nu_1 = \nu_2 = 0.3$. The dimensions of the body are $a = 1$ mm, $R/a = 40$ and $h/R = 1$ where $2a$ and $2R$ are the crack and the body diameters, respectively, and $2h$ is the height of the body, as shown in Fig. 3.13. The crack is situated at the center of the body. The analytical solution of the problem is given by Kassir and Bregman (1972) as

$$K = \frac{2\Gamma(2 + i\varepsilon)}{\Gamma(0.5 + i\varepsilon)} \sigma_{22} \sqrt{a} (2a)^{-i\varepsilon} \tag{3.30}$$

where the value of σ_{22} is 1 MPa, and the value of ε is given in eq. (3.28). As in the two-dimensional problem in Fig. 2.8 and the three-dimensional problem presented in Fig. 3.10, stresses $\sigma_{rr}^{(1)}$ and $\sigma_{rr}^{(2)}$ are required to maintain displacement continuity along the interface.

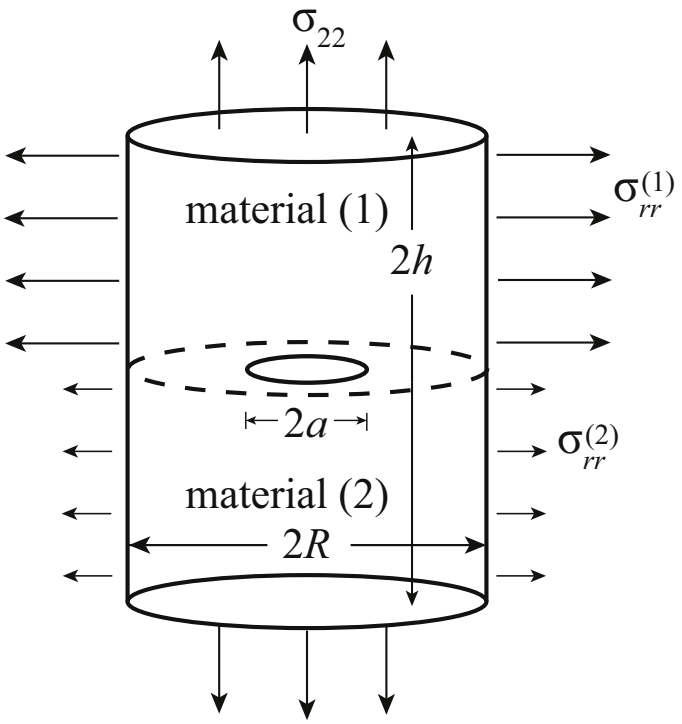

Figure 3.13: A penny-shaped interface crack problem.

They are found as

$$\sigma_{rr}^{(2)} = \frac{\bar{E}_2}{\bar{E}_1}\sigma_{rr}^{(1)} + \frac{\nu_2}{1-\nu_2}\left[1 - \frac{\nu_1}{\nu_2}\frac{E_2}{E_1}\frac{1+\nu_1}{1+\nu_2}\right]\sigma_{22}. \tag{3.31}$$

Recall that $\bar{E}_k$ are defined in eq. (1.17). Using eq. (3.31), $\sigma_{rr}^{(1)}$ is chosen to be 1 MPa and $\sigma_{rr}^{(2)}$ is found to be 0.4857 MPa.

First, a convergence study is carried out using two-dimensional axisymmetric meshes. Meshes A and B in Table 3.3 are used. The energy release rates $\mathcal{G}_I$ and $\mathcal{G}_{II}$ were calculated using eqs. (1.107) and (1.108) where Δa is replaced by ΔA given in eq. (3.25). For a penny-shaped crack, the crack front satisfies plane-strain conditions. The stress intensity factors were calculated using eq. (2.61). By using eq. (3.30), the analytical solution is $K_1 = 1.1330$ N/mm$^{3/2+i\varepsilon}$ and $K_2 = -0.1449$ N/mm$^{3/2+i\varepsilon}$. The percentage errors in comparison to the analytical solution obtained using meshes A and B in Table 3.3 are shown, respectively, in Tables 3.9 and 3.10. For mesh A in Table 3.9, the lowest value of $\mathcal{I}$ is obtained for $M = 4$. For this value of M, K_1 and K_2 have errors of -0.50% and -1.04%, respectively, in comparison to the analytical solution. For mesh B in Table 3.10, the lowest value of $\mathcal{I}$ is obtained for $M = 8$. For this value of M, K_1 has an error of -0.11% and K_2 has an error of -0.21%. The results converged to the analytical solution for the finest mesh.

In order to carry out a fully three-dimensional analysis, the same three-dimensional mesh, based on mesh B in Table 3.10, that was used in Section 3.2 for a penny-shaped crack

Table 3.9: Data for an interface penny-shaped crack in Fig. 3.13 using the axisymmetric mesh A in Table 3.3 ($\ell = 50$ μm).

M	$\Delta a(\mu\text{m})$	K_1 (% error)	K_2 (% error)	$\mathcal{I}(\%)$
1	50	-0.49	-5.73	-23.1
2	100	-0.53	-1.73	-7.8
3	150	-0.53	-0.69	-3.3
4	200	-0.50	-1.04	0.2
5	250	-0.48	-1.31	2.8
6	300	-0.45	-1.66	5.0
7	350	-0.43	-2.07	6.9
8	400	-0.41	-2.48	8.5
9	450	-0.41	-2.97	9.9
10	500	-0.41	-3.52	11.2

is used here. For each ray, both corner nodes and mid-side nodes, the same results were obtained. The results for one ray are shown in Table 3.10. The lowest value of $\mathcal{I}$ is obtained for $M = 8$. For this value of M, K_1 has an error of -0.11% and K_2 has an error of -0.21%. The largest difference between the numerical errors of mesh B for the axisymmetric analysis and the three-dimensional mesh in Table 3.10 for the results obtained is 0.05%. As may be observed in Table 3.10, using a VCE which consists of one element leads to poor results for K_2, with an error of about 4.3%.

3.4 Numerical results for an interface crack between two dissimilar transversely isotropic materials

In this section, a penny-shaped interface crack between two transversely isotropic materials in an infinite body is solved by means of an FEA using a commercial finite element program Abaqus/CAE (2017). A schematic view of the body is shown in Fig. 3.13. The material that is used in this problem is a fiber reinforced composite made of graphite/epoxy AS4/3501-6. The effective mechanical properties were taken from Banks-Sills and Boniface (2000), and are shown in Table 1.1. For the upper material, the fibers are in the x_1-direction, and for the lower material, they are in the x_3- direction. The directions are shown in Fig. 3.2. The body is subjected to remote tensile traction $\sigma_{22} = 1$ MPa. The dimensions of the body are $a = 1$ mm, $R/a = 40$ and $h/R = 1$ where $2a$ and $2R$ are the crack and the body diameters, respectively, and $2h$ is the height of the body, as shown in Fig. 3.13. The crack is situated at the center of the body. Note that there is no analytical solution for this problem. Due to symmetry, only one-quarter of the body is modeled. Axisymmetric meshes A and B in Table 3.3 are used and swept through 90° with ten divisions. Hence, there are 21 rays of nodes. The eight-noded elements were swept to twenty-noded elements (C3D20) except for the elements touching the x_2-axis. The inner

Table 3.10: Numerical results for a penny-shaped interface crack in Fig. 3.13 using the axisymmetric mesh B in Table 3.3 ($\ell = 10$ μm) and using three-dimensional mesh ($\ell_r \times \ell_2 \times \ell_\theta = 10 \times 10 \times 157 \mu\text{m}^3$).

		axisymmetric mesh B			three-dimensional mesh B		
M	Δa (μm)	K_1 (% error)	K_2 (% error)	$\mathcal{I}$ (%)	K_1 (% error)	K_2 (% error)	$\mathcal{I}$ (%)
1	10	-0.06	-4.28	-18.9	-0.06	-4.24	-18.9
2	20	-0.11	-1.04	-8.3	-0.11	-1.05	-8.3
3	30	-0.12	-0.14	-5.6	-0.12	-0.16	-5.6
4	40	-0.11	-0.21	-3.6	-0.12	-0.23	-3.6
5	50	-0.11	-0.21	-2.4	-0.11	-0.18	-2.4
6	60	-0.11	-0.21	-1.3	-0.11	-0.18	-1.4
7	70	-0.11	-0.21	-0.5	-0.11	-0.19	-0.6
8	80	-0.11	-0.21	0.1	-0.11	-0.21	0.1
9	90	-0.11	-0.28	0.8	-0.11	-0.24	0.8
10	100	-0.11	-0.28	1.3	-0.10	-0.27	1.4
11	110	-0.10	-0.35	1.9	-0.10	-0.30	1.9
15	150	-0.08	-0.48	3.8	-0.08	-0.48	3.8
20	200	-0.06	-0.76	5.8	-0.06	-0.77	5.9
30	300	-0.03	-1.52	9.2	-0.02	-1.51	9.3
35	350	-0.01	-1.93	10.7	-0.01	-1.95	10.7
36	360	-0.01	-2.07	11.0	-0.01	-2.04	11.0
37	370	0.00	-2.14	11.2	0.00	-2.13	11.3
38	380	0.00	-2.21	11.6	0.00	-2.23	11.6
39	390	0.00	-2.35	11.8	0.00	-2.33	11.8
40	400	0.01	-2.42	12.1	0.00	-2.43	12.1
50	500	0.01	-3.52	14.5	0.01	-3.50	14.4

elements were swept to fifteen-noded wedge elements (C3D15). The new meshes are called A3D and B3D. The values of ℓ_r, in Fig. 3.2, and the number of the elements and nodes for each mesh are shown in Table 3.11. The isoparametric and upper views of mesh B3D are shown in Figs. 3.14a and 3.14b, respectively. At the outer edge of the body at $r = R$, the tractions

$$\sigma_{rr}^{(1)} = \cos^2\theta + 0.6114 \sin^2\theta \quad , \quad \sigma_{r\theta}^{(1)} = (1 - 0.6114) \sin\theta \cos\theta \tag{3.32}$$

Table 3.11: The size ℓ_r of the elements near the crack tip and the total number of elements and nodes for each mesh for the penny-shaped interface crack and three-dimensional meshes.

Mesh	ℓ_r (μm)	elements	nodes
A3D	50	16,560	72,849
B3D	10	159,900	693,603

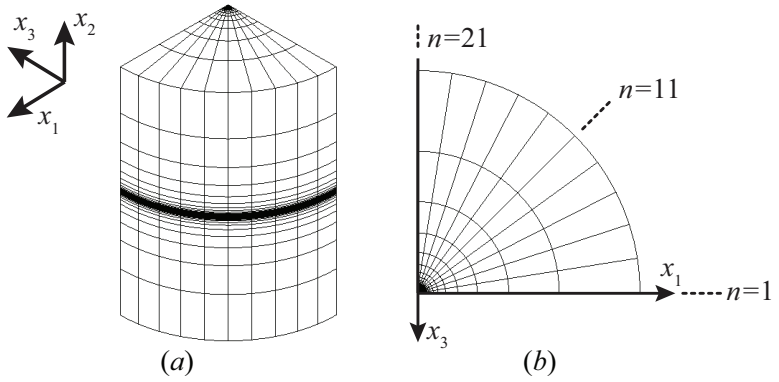

Figure 3.14: (a) Isoparametric and (b) upper views of the mesh used for the penny-shaped crack.

$$\sigma_{rr}^{(2)} = 0.6114\cos^2\theta + \sin^2\theta \quad , \quad \sigma_{r\theta}^{(2)} = (0.6114 - 1)\sin\theta\cos\theta \tag{3.33}$$

are applied to enforce displacement continuity across the interface. Equations (3.32) and (3.33) are developed in Appendix A.

Next, the dual energy release rates for $n = 1$ and 21 are defined. It is noted that n is the ray number as shown in Fig. 3.14b. For $n = 1$, the interface crack is between two transversely isotropic materials where the fibers in the upper material are in the 0°-direction and in the 90°-direction in the lower one. For $n = 21$, the interface crack is between two transversely isotropic materials where the fibers in the upper material are in the 90°-direction and in the 0°-direction in the lower one. The dual energy release rates for an interface crack between two transversely isotropic materials in two-dimensions, $\mathcal{I}_I^{(T)}$ and $\mathcal{I}_{II}^{(T)}$, are defined in eqs. (2.87) and (2.88). The values for the dual energy release rates $\mathcal{I}_I^{(T,n)}$ and $\mathcal{I}_{II}^{(T,n)}$ for rays $n = 1$ and 21 are obtained as

$$\mathcal{I}_I^{(T,n)} = \frac{1}{2\Delta A^{(n)}}\sqrt{\frac{D_{22}}{D_{11}}}\left[\sum_{m=1}^{2M} F_2^{(m,n)}\Delta u_r^{(m',n)} + \frac{1}{2}\left(\sum_{m=1}^{M} F_2^{(2m-1,n-1)}\Delta u_r^{(2m'-1,n-1)} + F_2^{(2m-1,n+1)}\Delta u_r^{(2m'-1,n+1)}\right)\right], \tag{3.34}$$

$$\mathcal{I}_{II}^{(T,n)} = \frac{1}{2\Delta A^{(n)}}\sqrt{\frac{D_{11}}{D_{22}}}\left[\sum_{m=1}^{2M} F_r^{(m,n)}\Delta u_2^{(m',n)} + \frac{1}{2}\left(\sum_{m=1}^{M} F_r^{(2m-1,n-1)}\Delta u_2^{(2m'-1,n-1)} + F_r^{(2m-1,n+1)}\Delta u_2^{(2m'-1,n+1)}\right)\right]. \tag{3.35}$$

For numerical applications, the percent difference between $\mathcal{I}_I^{(T,n)}$ and $\mathcal{I}_{II}^{(T,n)}$ is defined as

$$\mathcal{I}_T^{(n)} \equiv \frac{\mathcal{I}_{II}^{(T,n)} - \mathcal{I}_I^{(T,n)}}{\mathcal{I}_I^{(T,n)}} \cdot 100\,. \tag{3.36}$$

For the mid-row, $n = 11$, which is also a corner node, the interface crack is between two transversely isotropic materials where the fibers in the upper material are in the $+45°$-direction and in the $-45°$-direction in the lower one. For this row, a new set of equations for VCCT may be obtained using the derivations in Freed and Banks-Sills (2005). The tractions ahead of the crack tip along the interface and the crack face displacement jumps are given in Freed and Banks-Sills (2005) as

$$\left(\sigma_{22} + i\sqrt{\frac{E_{33}}{E_{22}}}\sigma_{32}\right)\bigg|_{\theta=0} = \frac{Kx_1^{i\varepsilon}}{\sqrt{2\pi x_1}} \tag{3.37}$$

$$\sigma_{12} = \frac{K_{II}}{\sqrt{2\pi x_1}} \tag{3.38}$$

and

$$\Delta u_2 + i\sqrt{\frac{E_{22}}{E_{33}}}\Delta u_3 = \frac{4\ \mathrm{sgn}(E_{22})|E_{22}|}{(1+2i\varepsilon)\cosh\pi\varepsilon}\sqrt{\frac{\Delta a - x_1}{2\pi}}\,(\Delta a - x_1)^{i\varepsilon}K \tag{3.39}$$

$$\Delta u_1 = 4\ \mathrm{sgn}(E_{11})|E_{11}|\sqrt{\frac{\Delta a - x_1}{2\pi}}K_{II} \tag{3.40}$$

where

$$K = K_1 + iK_3. \tag{3.41}$$

Note that for the previous interface, K was related to K_1 and K_2. The parameters E_{11}, E_{22}, E_{23} and E_{33} and ε are given explicitly in Freed and Banks-Sills (2005) and Appendix B.

Following the derivations in Section 2.5, two new auxiliary integrals are presented

$$A_E = \frac{1}{2\Delta a}\int_0^{\Delta a}\left[\sigma_{22}(x_1) + i\sqrt{\frac{E_{33}}{E_{22}}}\sigma_{32}(x_1)\right]\left[\Delta u_2(\Delta a - x_1) - i\sqrt{\frac{E_{22}}{E_{33}}}\Delta u_3(\Delta a - x_1)\right]dx_1\ , \tag{3.42}$$

$$D_E = \frac{1}{2\Delta a}\int_0^{\Delta a}\left[\sigma_{22}(x_1) + i\sqrt{\frac{E_{33}}{E_{22}}}\sigma_{32}(x_1)\right]\left[\Delta u_2(\Delta a - x_1) + i\sqrt{\frac{E_{22}}{E_{33}}}\Delta u_3(\Delta a - x_1)\right]dx_1\ , \tag{3.43}$$

where the subscript E denotes the current interface. The coordinate system and the virtual crack extension, Δa, are shown in Figs. 1.3 and 1.9, respectively. By considering the expressions in eqs. (1.104) and (1.106) for $\mathcal{G}_I$ and $\mathcal{G}_{III}$, respectively, and manipulating the integrals A_E and D_E in eqs. (3.42) and (3.43), respectively, the relations between them are found as

$$\mathcal{G}_I + \mathcal{G}_{III} = \lim_{\Delta a\to 0}\Re(A_E) \tag{3.44}$$

$$\mathcal{G}_I - \mathcal{G}_{III} = \lim_{\Delta a\to 0}\Re(D_E) \tag{3.45}$$

$$\mathcal{G}_I = \frac{1}{2}\lim_{\Delta a\to 0}\Re(A_E + D_E) \tag{3.46}$$

$$\mathcal{G}_{III} = \frac{1}{2}\lim_{\Delta a\to 0}\Re(A_E - D_E) \tag{3.47}$$

$$\mathcal{G}^{(E)}_{I-III} = \mathcal{I}^{(E)}_{I} + \mathcal{I}^{(E)}_{III} = \lim_{\Delta a \to 0} \Im(D_E) \tag{3.48}$$

$$\mathcal{I}^{(E)}_{I} - \mathcal{I}^{(E)}_{III} = \lim_{\Delta a \to 0} \Im(A_E) \tag{3.49}$$

where $\Re(\cdot)$ and $\Im(\cdot)$ represent the real and imaginary parts of the quantity in parentheses. The dual energy release rates are defined as

$$\mathcal{I}^{(E)}_{I} = \frac{1}{2\Delta a}\sqrt{\frac{E_{33}}{E_{22}}}\int_0^{\Delta a} \sigma_{32}(x_1)\Delta u_2(\Delta a - x_1)dx_1 \tag{3.50}$$

$$\mathcal{I}^{(E)}_{III} = \frac{1}{2\Delta a}\sqrt{\frac{E_{22}}{E_{33}}}\int_0^{\Delta a} \sigma_{22}(x_1)\Delta u_3(\Delta a - x_1)dx_1. \tag{3.51}$$

Substituting eqs. (3.37) and (3.39) into eqs. (3.42) and (3.43), it may be shown that

$$A_E = \frac{1}{H_1}\left(K_1^2 + K_3^2\right) \tag{3.52}$$

and

$$D_E = \frac{\cosh \pi\varepsilon}{\pi H_1} P K^2 \Delta a^{2i\varepsilon}\ , \tag{3.53}$$

where H_1 is defined as

$$\frac{1}{H_1} = \frac{\mathrm{sgn}(E_{22})|E_{22}|}{2\cosh^2 \pi\varepsilon} \tag{3.54}$$

and P is given in eq. (1.173). Noting that A_E is real, one may write from eq. (3.49) that

$$\mathcal{I}^{(E)}_{I} = \mathcal{I}^{(E)}_{III}. \tag{3.55}$$

Although analytically the equality in eq. (3.55) holds, numerically this does not occur. Thus, the percent difference between the left and the right hand sides of eq. (3.55) is defined as

$$\mathcal{I}_E \equiv \frac{\mathcal{I}^{(E)}_{III} - \mathcal{I}^{(E)}_{I}}{\mathcal{I}^{(E)}_{I}} \cdot 100 \tag{3.56}$$

for numerical applications.

The phase angle of D_E may be extracted from eqs. (3.45) and (3.48) as

$$\psi_{D_E} = \tan^{-1}\left[\frac{\Im(D_E)}{\Re(D_E)}\right] = \tan^{-1}\left(\frac{\mathcal{G}^{(E)}_{I-III}}{\mathcal{G}_I - \mathcal{G}_{III}}\right)\ . \tag{3.57}$$

From eq. (3.53), it may also be written as

$$\psi_{D_E} = 2\psi + \psi_P + 2\varepsilon \ln \Delta a\ , \tag{3.58}$$

where ψ_P is defined in eqs. (2.52) and (1.173) and ψ is the phase angle of the stress intensity factors given as

$$\psi = \tan^{-1}\left(\frac{K_3}{K_1}\right). \tag{3.59}$$

Using eq. (3.58), ψ may be found as

$$\psi = \frac{1}{2}\psi_{D_E} - \frac{1}{2}\psi_P - \varepsilon \ln \Delta a. \tag{3.60}$$

The stress intensity factors are determined using

$$K_1 = \pm\sqrt{H_1 \mathcal{G}_i}\cos\psi \qquad K_3 = K_1 \tan\psi\ . \tag{3.61}$$

The valid pair of stress intensity factors satisfies the inequality

$$-\frac{\pi}{2} < \tan^{-1}\left(\frac{K_3}{K_1}\right) - \tan^{-1} 2\varepsilon + \varepsilon \ln r < \frac{\pi}{2}, \tag{3.62}$$

where r was chosen as $a/100$.

Noting eqs. (3.21), (3.22), (3.50) and (3.51), the dual energy release rates, $\mathcal{I}_I^{(E,n)}$ and $\mathcal{I}_{III}^{(E,n)}$, are given for odd values of n at the corner-nodes by

$$\mathcal{I}_I^{(E,n)} = \frac{1}{2\Delta A^{(n)}}\sqrt{\frac{E_{33}}{E_{22}}}\Bigg[\sum_{m=1}^{2M} F_\theta^{(m,n)} \Delta u_2^{(m',n)} + \frac{1}{2}\left(\sum_{m=1}^{M} F_\theta^{(2m-1,n-1)}\Delta u_2^{(2m'-1,n-1)} + F_\theta^{(2m-1,n+1)}\Delta u_2^{(2m'-1,n+1)}\right)\Bigg], \tag{3.63}$$

$$\mathcal{I}_{III}^{(E,n)} = \frac{1}{2\Delta A^{(n)}}\sqrt{\frac{E_{22}}{E_{33}}}\Bigg[\sum_{m=1}^{2M} F_2^{(m,n)} \Delta u_\theta^{(m',n)} + \frac{1}{2}\left(\sum_{m=1}^{M} F_2^{(2m-1,n-1)}\Delta u_\theta^{(2m'-1,n-1)} + F_2^{(2m-1,n+1)}\Delta u_\theta^{(2m'-1,n+1)}\right)\Bigg], \tag{3.64}$$

and

$$\mathcal{I}_E^{(n)} \equiv \frac{\mathcal{I}_{III}^{(E,n)} - \mathcal{I}_I^{(E,n)}}{\mathcal{I}_I^{(E,n)}} \cdot 100\ . \tag{3.65}$$

Next, numerical results are presented for meshes A3D and B3D in Table 3.11. Recall that the energy release rates $\mathcal{G}_I^{(n)}$, $\mathcal{G}_{II}^{(n)}$ and $\mathcal{G}_{III}^{(n)}$, are obtained using eqs. (3.12), (3.13) and (3.14) for mid-side nodes, and eqs. (3.16), (3.17) and (3.18) for corner nodes. The interface energy release rate, $\mathcal{G}_i$, is obtained for each row using eq. (1.122), where $N = n$. Recall that there are 21 rays of nodes. It is noted that n is the ray number, as shown in Fig. 3.14b. For $n = 1$, the interface crack is between two transversely isotropic materials where the fibers in the upper material are in the 0°-direction and in the 90°-direction in the lower one. For $n = 11$, the interface crack is between two transversely isotropic materials where the fibers in the upper material are in the +45°-direction and in the −45°-direction in the lower one. For $n = 21$, the interface crack is between two transversely isotropic materials where the fibers in the upper material are in the 90°-direction and in the 0°-direction in

Table 3.12: Parameters used to calculate the stress intensity factors for the $+45°//-45°$ interface.

E_{22} (1/GPa)	E_{33} (1/GPa)	$1/H_1$ (1/GPa)	ε
$0.1541i$	$0.1316i$	0.0768	0.0182

the lower one. For rows $n = 1$ and 21, the dual energy release rates $\mathcal{I}_I^{(T,n)}$ and $\mathcal{I}_{II}^{(T,n)}$ are obtained using eqs. (3.34) and (3.35). The parameter $\mathcal{I}_T^{(n)}$ is found using eq. (3.36). For row $n = 11$, the dual energy release rates $\mathcal{I}_I^{(E,11)}$ and $\mathcal{I}_{III}^{(E,11)}$ and $\mathcal{I}_E^{(11)}$ are obtained using eqs. (3.63) to (3.65). The parameters E_{22} and E_{33} are given in Table 3.12.

The interface energy release rates and the percent differences between the dual energy release rates for rows $n = 1$ and 11 are presented in Table 3.13. The results for rows 1 and 21 are identical. Recall that M is the number of elements used for the VCE. For the lowest absolute value of $\mathcal{I}_T^{(1)}$, the results for $\mathcal{G}_i^{(1)}$ are 0.0972 N/m and 0.0978 N/m, for meshes A3D and B3D, respectively; the lowest absolute values of $\mathcal{I}_T^{(1)}$ are obtained for $M = 2$ and $M = 3$, respectively. The difference between the interface energy release rates obtained for meshes A3D and B3D, for ray $n = 1$, is -0.5%. The energy release rate values are rather small. Consider the penny-shaped crack between two isotropic materials with $E_2/E_1 = 0.1$, $E_1 = 1$ GPa and $\sigma_{11} = 1$ MPa. The value of $\mathcal{G}_i^{(\text{iso})}$, where the superscript (iso) is used here to denote that the interface is between two isotropic materials, was 6.2 N/m. The value of $\mathcal{G}_i^{(\text{iso})}$ is related to the stress intensity factors and $1/H_1^{(\text{iso})}$ in eq. (1.36). Here, the values of $\mathcal{G}_i^{(1)}$ and $\mathcal{G}_i^{(11)}$ are related to $1/H_1$ defined in eqs. (2.77) and (3.54), respectively. Using eq. (1.36), the value of $1/H_1$ for the two isotropic materials

Table 3.13: Numerical results for a penny-shaped interface crack in Fig. 3.14 using meshes A3D and B3D in Table 3.11 ($\ell_r = 50$ μm).

	mesh A3D				mesh B3D			
M	$\mathcal{G}_i^{(1)}$ (N/m)	$\mathcal{I}_T^{(1)}$ (%)	$\mathcal{G}_i^{(11)}$ (N/m)	$\mathcal{I}_E^{(11)}$ (%)	$\mathcal{G}_i^{(1)}$ (N/m)	$\mathcal{I}_T^{(1)}$ (%)	$\mathcal{G}_i^{(11)}$ (N/m)	$\mathcal{I}_E^{(11)}$ (%)
1	0.0972	-51.8	0.0979	-523	0.0978	-57.7	0.0987	75
2	0.0972	33.2	0.0979	-208	0.0978	-12.1	0.0986	34
3	0.0973	67.1	0.0978	-135	0.0978	-1.7	0.0986	61
4	0.0974	98.1	0.0978	-115	0.0978	7.3	0.0986	107
5	0.0974	126.8	0.0977	-106	0.0978	14.8	0.0986	213
6	0.0975	153.9	0.0977	-102	0.0978	21.8	0.0986	658
7	0.0975	179.4	0.0977	-99	0.0978	28.4	0.0985	-1338
8	0.0976	203.6	0.0977	-98	0.0978	34.8	0.0985	-411
9	0.0976	226.5	0.0976	-96	0.0978	41.0	0.0985	-269
10	0.0976	248.2	0.0976	-96	0.0978	47.1	0.0985	-211

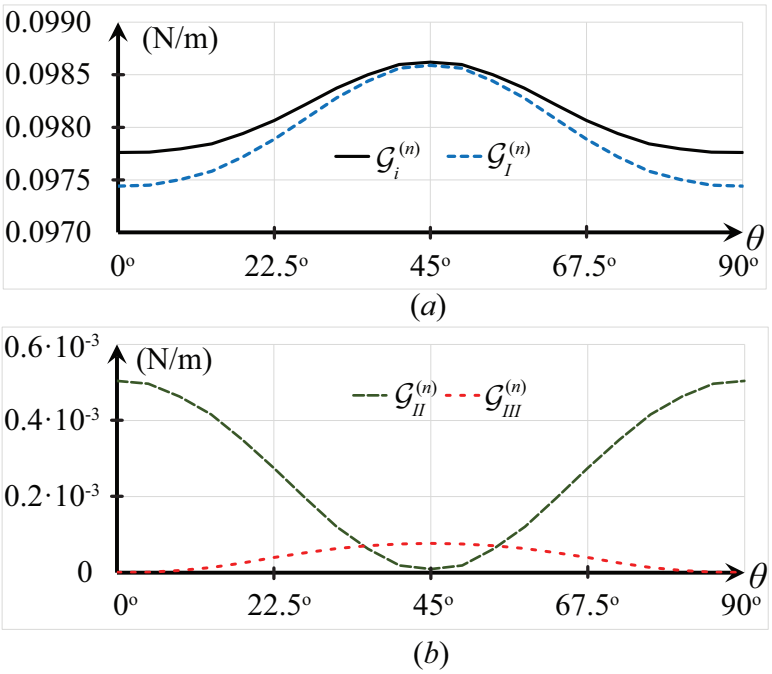

Figure 3.15: Numerical results for an interface penny-shaped crack using mesh B3D in Table 3.11.

is 4.73 1/GPa; for the $0°//90°$ interface, for $\mathcal{G}_i^{(1)}$, $1/H_1 = 0.0572$ 1/GPa in Table 2.9; for the $+45°//-45°$ interface, for $\mathcal{G}_i^{(11)}$, $1/H_1 = 0.0768$ 1/GPa in Table 3.12. There are two orders of magnitude difference between $1/H_1$ for the interface considered here and $1/H_1^{(\text{iso})}$. Hence, the values of $\mathcal{G}_i^{(1)}$ and $\mathcal{G}_i^{(11)}$ are reasonable.

For the lowest absolute value of $\mathcal{I}_E^{(11)}$, the results for $\mathcal{G}_i^{(11)}$ are 0.0976 N/m and 0.0986 N/m, for meshes A3D and B3D, respectively; the lowest absolute values of $\mathcal{I}_E^{(11)}$ are obtained for $M = 9$ and $M = 2$, respectively. The difference between the interface energy release rates obtained for meshes A3D and B3D, for ray $n = 11$, is -1.1%. Note that $\mathcal{G}_i^{(1)}$ obtained for mesh B3D is constant and $\mathcal{G}_i^{(11)}$ is almost constant up to a difference of 0.0002 N/m which is 0.2% of $\mathcal{G}_i^{(11)}$. For mesh B3D, the lowest absolute values of $\mathcal{I}_T^{(1)}$ and $\mathcal{I}_E^{(11)}$ are obtained for $M = 3$ and $M = 2$, respectively.

For each ray $(n = 1, ..., 21)$, the values obtained using mesh B3D for $\mathcal{G}_i^{(n)}$ with $M = 2$ and 3 are the same up to three significant figures. Recall that the energy release rates, $\mathcal{G}_I^{(n)}$, $\mathcal{G}_{II}^{(n)}$ and $\mathcal{G}_{III}^{(n)}$, oscillate for each ray as shown in Figs. 1.27a and 1.27b. In Fig. 3.15, the energy release rates obtained for mesh B3D in Table 3.11 and $M = 2$, are presented. In Fig. 3.15a, the results obtained for $\mathcal{G}_i^{(n)}$ and $\mathcal{G}_I^{(n)}$ are presented. The results obtained for $\mathcal{G}_{II}^{(n)}$ and $\mathcal{G}_{III}^{(n)}$ are presented in Fig. 3.15b. The angle θ defines the position along the delamination front as shown in Fig. 3.2. In Fig. 3.15b, the values obtained for $\mathcal{G}_{II}^{(n)}$ and $\mathcal{G}_{III}^{(n)}$ are very small. The values of $\mathcal{G}_{II}^{(11)}$ and $\mathcal{G}_{III}^{(1)}$ are zero up to the fifth and sixth decimal point at $\theta = 45°$ and $0°$, respectively. The maximum values of $\mathcal{G}_{II}^{(n)}$ and $\mathcal{G}_{III}^{(n)}$ are $\mathcal{G}_{II}^{(1)} = 5.0 \cdot 10^{-4}$ N/m and $\mathcal{G}_{III}^{(11)} = 7.7 \cdot 10^{-5}$ N/m, respectively.

Next, the stress intensity factors for $n = 1$ and 11 are calculated using mesh B3D in Table 3.11. For row $n = 1$ and $M = 3$, K_1 and K_2 are determined using eqs. (2.61) and (1.184) as $K_1 = 1.3001$ N/mm$^{3/2+i\varepsilon}$ and $K_2 = -0.1335$ N/mm$^{3/2+i\varepsilon}$. Noting eq. (1.39) and that $\mathcal{G}_{III}^{(1)}$ is zero, $K_{III} = 0$. For row $n = 11$ and $M = 2$, K_1 and K_3 are determined using eqs. (3.61) and (3.62) as $K_1 = 1.1293$ N/mm$^{3/2+i\varepsilon}$ and $K_3 = 0.0971$ N/mm$^{3/2+i\varepsilon}$. Noting the relation for the $+45°//-45°$ interface from Freed and Banks-Sills (2005)

$$\mathcal{G}_{II} = \frac{1}{H_2} K_{II}^2 \tag{3.66}$$

and that $\mathcal{G}_{II}^{(11)}$ is zero, $K_{II} = 0$.

Obtaining stress intensity factors at other positions along the crack front involves use of the Stroh and Lekhnitskii formalisms at each position. This is beyond the scope of this investigation.

Chapter 4

A Clifford formalism

In Section 1.5, the basic concepts of a Clifford algebra were presented. In addition, the eigenvalue equation for a three-dimensional anisotropic material was developed. In Section 4.1, the eigenvalue problem for various anisotropic materials will be derived. For these materials, the eigenvalue problem provides a bi-sextic equation in the eigenvalues P_{12} and P_{13}. In fact, the eigenvalue problem is one equation with two unknowns. In Section 4.2, explicit expressions are obtained for the eigenvectors of various materials. A three-dimensional Clifford formalism is developed in Section 4.3. In Section 4.4, specific problems are solved and a general solution for a uniform stress problem is developed. These are compared to numerical results obtained by means of the finite element method.

4.1 The eigenvalue problem for various anisotropic materials

Linear elastic, homogeneous, anisotropic materials are considered here. The solution is developed by means of the eigenvalue problem given in eq. (1.97) for generally anisotropic material as

$$(\mathbf{N}_1 + P_{12}\mathbf{N}_2 + P_{13}\mathbf{N}_3)\mathbf{d} = \mathbf{0} \; . \tag{4.1}$$

In eq, (4.1), P_{12} and P_{13} are the eigenvalues, the 9×9 matrices $\mathbf{N}_1$, $\mathbf{N}_2$ and $\mathbf{N}_3$ are given in eqs. (1.98) and $\mathbf{d}$ is the 9×1 eigenvector in eqs. (1.99) to (1.101). The matrices $\mathbf{N}_1$, $\mathbf{N}_2$ and $\mathbf{N}_3$ are composed the sub-matrices $\mathbf{C}_{ij}$ given by eq. (1.95).

To simplify the problem and make it tractable, it is possible to use contracted notation with

$$11 \to 1 \; , \; 22 \to 2 \; , \; 33 \to 3 \; , \; 32 \to 4 \; , \; 31 \to 5 \; , \; 21 \to 6 \; . \tag{4.2}$$

The stiffness tensor may be written as a 6×6 matrix as

$$C_{\alpha\beta} = \begin{bmatrix} C_{11} & C_{12} & C_{13} & C_{14} & C_{15} & C_{16} \\ C_{21} & C_{22} & C_{23} & C_{24} & C_{25} & C_{26} \\ C_{31} & C_{23} & C_{33} & C_{34} & C_{35} & C_{36} \\ C_{41} & C_{24} & C_{34} & C_{44} & C_{45} & C_{46} \\ C_{51} & C_{25} & C_{35} & C_{45} & C_{55} & C_{56} \\ C_{61} & C_{26} & C_{36} & C_{46} & C_{46} & C_{66} \end{bmatrix} . \tag{4.3}$$

where $\alpha, \beta = 1, ..., 6$. Note that $C_{\alpha\beta}$ is symmetric. So that for a general anisotropic material, there are 21 independent constants.

The matrix $\mathbf{C}_{11}$ in eq. (1.95) is given by

$$\mathbf{C}_{11} = \begin{bmatrix} C_{1111} & C_{1112} & C_{1131} \\ C_{1211} & C_{1212} & C_{1231} \\ C_{3111} & C_{3112} & C_{3131} \end{bmatrix} = \begin{bmatrix} C_{11} & C_{16} & C_{15} \\ C_{61} & C_{66} & C_{65} \\ C_{51} & C_{56} & C_{55} \end{bmatrix} \tag{4.4}$$

The matrix $\mathbf{C}_{12}$ is given by

$$\mathbf{C}_{12} = \begin{bmatrix} C_{16} & C_{12} & C_{14} \\ C_{66} & C_{62} & C_{64} \\ C_{56} & C_{52} & C_{54} \end{bmatrix} \tag{4.5}$$

The matrix $\mathbf{C}_{13}$ is given by

$$\mathbf{C}_{13} = \begin{bmatrix} C_{15} & C_{14} & C_{13} \\ C_{65} & C_{64} & C_{63} \\ C_{55} & C_{54} & C_{53} \end{bmatrix} \tag{4.6}$$

The matrices $\mathbf{C}_{21}$, $\mathbf{C}_{22}$ and $\mathbf{C}_{23}$ are given by

$$\begin{aligned} \mathbf{C}_{21} &= \begin{bmatrix} C_{61} & C_{66} & C_{65} \\ C_{21} & C_{26} & C_{25} \\ C_{41} & C_{46} & C_{45} \end{bmatrix} \qquad \mathbf{C}_{22} = \begin{bmatrix} C_{66} & C_{62} & C_{64} \\ C_{26} & C_{22} & C_{24} \\ C_{46} & C_{42} & C_{44} \end{bmatrix} \\ \mathbf{C}_{23} &= \begin{bmatrix} C_{65} & C_{64} & C_{63} \\ C_{25} & C_{24} & C_{23} \\ C_{45} & C_{44} & C_{43} \end{bmatrix} \end{aligned} \tag{4.7}$$

The matrices $\mathbf{C}_{31}$, $\mathbf{C}_{32}$ and $\mathbf{C}_{33}$ are given by

$$\mathbf{C}_{31} = \begin{bmatrix} C_{51} & C_{56} & C_{55} \\ C_{41} & C_{46} & C_{45} \\ C_{31} & C_{36} & C_{35} \end{bmatrix} \qquad \mathbf{C}_{32} = \begin{bmatrix} C_{56} & C_{52} & C_{54} \\ C_{46} & C_{42} & C_{44} \\ C_{36} & C_{32} & C_{34} \end{bmatrix}$$
$$\mathbf{C}_{33} = \begin{bmatrix} C_{55} & C_{54} & C_{53} \\ C_{45} & C_{44} & C_{43} \\ C_{35} & C_{34} & C_{33} \end{bmatrix} \tag{4.8}$$

Thus, the matrices $\mathbf{N}_1$, $\mathbf{N}_2$ and $\mathbf{N}_3$, given in eq. (1.98), for generally anisotropic media are found to be

$$\mathbf{N}_1 = \begin{bmatrix} C_{11} & C_{16} & C_{15} & 0 & 0 & 0 & 0 & 0 & 0 \\ C_{61} & C_{66} & C_{65} & 0 & 0 & 0 & 0 & 0 & 0 \\ C_{51} & C_{56} & C_{55} & 0 & 0 & 0 & 0 & 0 & 0 \\ C_{61} & C_{66} & C_{65} & -1 & 0 & 0 & 0 & 0 & 0 \\ C_{21} & C_{26} & C_{25} & 0 & -1 & 0 & 0 & 0 & 0 \\ C_{41} & C_{46} & C_{45} & 0 & 0 & -1 & 0 & 0 & 0 \\ C_{51} & C_{56} & C_{55} & 0 & 0 & 0 & -1 & 0 & 0 \\ C_{41} & C_{46} & C_{45} & 0 & 0 & 0 & 0 & -1 & 0 \\ C_{31} & C_{36} & C_{35} & 0 & 0 & 0 & 0 & 0 & -1 \end{bmatrix}, \tag{4.9}$$

$$\mathbf{N}_2 = \begin{bmatrix} C_{16} & C_{12} & C_{14} & 1 & 0 & 0 & 0 & 0 & 0 \\ C_{66} & C_{62} & C_{64} & 0 & 1 & 0 & 0 & 0 & 0 \\ C_{56} & C_{52} & C_{54} & 0 & 0 & 1 & 0 & 0 & 0 \\ C_{66} & C_{62} & C_{64} & 0 & 0 & 0 & 0 & 0 & 0 \\ C_{26} & C_{22} & C_{24} & 0 & 0 & 0 & 0 & 0 & 0 \\ C_{46} & C_{42} & C_{44} & 0 & 0 & 0 & 0 & 0 & 0 \\ C_{56} & C_{52} & C_{54} & 0 & 0 & 0 & 0 & 0 & 0 \\ C_{45} & C_{42} & C_{44} & 0 & 0 & 0 & 0 & 0 & 0 \\ C_{36} & C_{32} & C_{34} & 0 & 0 & 0 & 0 & 0 & 0 \end{bmatrix}, \tag{4.10}$$

and

$$\mathbf{N}_3 = \begin{bmatrix} C_{15} & C_{14} & C_{13} & 0 & 0 & 0 & 1 & 0 & 0 \\ C_{65} & C_{64} & C_{63} & 0 & 0 & 0 & 0 & 1 & 0 \\ C_{55} & C_{54} & C_{53} & 0 & 0 & 0 & 0 & 0 & 1 \\ C_{65} & C_{64} & C_{63} & 0 & 0 & 0 & 0 & 0 & 0 \\ C_{25} & C_{24} & C_{23} & 0 & 0 & 0 & 0 & 0 & 0 \\ C_{45} & C_{44} & C_{43} & 0 & 0 & 0 & 0 & 0 & 0 \\ C_{55} & C_{54} & C_{53} & 0 & 0 & 0 & 0 & 0 & 0 \\ C_{45} & C_{44} & C_{43} & 0 & 0 & 0 & 0 & 0 & 0 \\ C_{35} & C_{34} & C_{33} & 0 & 0 & 0 & 0 & 0 & 0 \end{bmatrix}. \tag{4.11}$$

which are 9×9 matrices.

In Section 4.1.1, the general solution for an orthotropic material is presented leading to a cubic equation for one of the eigenvalues. The cubic equation is solved for various specific materials, namely, isotropic, cubic, transversely isotropic, tetragonal and orthotropic. These results are presented in Section 4.1.2.

4.1.1 Eigenvalue solution for orthotropic materials

To simplify the eigenvalue problem, it is assumed that the material is orthotropic with nine independent elastic constants. The stiffness tensor may be written as

$$\mathbf{C} = \begin{bmatrix} C_{11} & C_{12} & C_{13} & 0 & 0 & 0 \\ C_{21} & C_{22} & C_{23} & 0 & 0 & 0 \\ C_{31} & C_{32} & C_{33} & 0 & 0 & 0 \\ 0 & 0 & 0 & C_{44} & 0 & 0 \\ 0 & 0 & 0 & 0 & C_{55} & 0 \\ 0 & 0 & 0 & 0 & 0 & C_{66} \end{bmatrix}. \tag{4.12}$$

Thus, for orthotropic media, the matrices $\mathbf{N}_1$, $\mathbf{N}_2$ and $\mathbf{N}_3$ are given by

$$\mathbf{N}_1 = \begin{bmatrix} C_{11} & 0 & 0 & 0 & 0 & 0 & 0 & 0 & 0 \\ 0 & C_{66} & 0 & 0 & 0 & 0 & 0 & 0 & 0 \\ 0 & 0 & C_{55} & 0 & 0 & 0 & 0 & 0 & 0 \\ 0 & C_{66} & 0 & -1 & 0 & 0 & 0 & 0 & 0 \\ C_{21} & 0 & 0 & 0 & -1 & 0 & 0 & 0 & 0 \\ 0 & 0 & 0 & 0 & 0 & -1 & 0 & 0 & 0 \\ 0 & 0 & C_{55} & 0 & 0 & 0 & -1 & 0 & 0 \\ 0 & 0 & 0 & 0 & 0 & 0 & 0 & -1 & 0 \\ C_{31} & 0 & 0 & 0 & 0 & 0 & 0 & 0 & -1 \end{bmatrix}, \tag{4.13}$$

$$\mathbf{N}_2 = \begin{bmatrix} 0 & C_{12} & 0 & 1 & 0 & 0 & 0 & 0 & 0 \\ C_{66} & 0 & 0 & 0 & 1 & 0 & 0 & 0 & 0 \\ 0 & 0 & 0 & 0 & 0 & 1 & 0 & 0 & 0 \\ C_{66} & 0 & 0 & 0 & 0 & 0 & 0 & 0 & 0 \\ 0 & C_{22} & 0 & 0 & 0 & 0 & 0 & 0 & 0 \\ 0 & 0 & C_{44} & 0 & 0 & 0 & 0 & 0 & 0 \\ 0 & 0 & 0 & 0 & 0 & 0 & 0 & 0 & 0 \\ 0 & 0 & C_{44} & 0 & 0 & 0 & 0 & 0 & 0 \\ 0 & C_{32} & 0 & 0 & 0 & 0 & 0 & 0 & 0 \end{bmatrix}, \tag{4.14}$$

$$\mathbf{N}_3 = \begin{bmatrix} 0 & 0 & C_{13} & 0 & 0 & 0 & 1 & 0 & 0 \\ 0 & 0 & 0 & 0 & 0 & 0 & 0 & 1 & 0 \\ C_{55} & 0 & 0 & 0 & 0 & 0 & 0 & 0 & 1 \\ 0 & 0 & 0 & 0 & 0 & 0 & 0 & 0 & 0 \\ 0 & 0 & C_{23} & 0 & 0 & 0 & 0 & 0 & 0 \\ 0 & C_{44} & 0 & 0 & 0 & 0 & 0 & 0 & 0 \\ C_{55} & 0 & 0 & 0 & 0 & 0 & 0 & 0 & 0 \\ 0 & C_{44} & 0 & 0 & 0 & 0 & 0 & 0 & 0 \\ 0 & 0 & C_{33} & 0 & 0 & 0 & 0 & 0 & 0 \end{bmatrix} \tag{4.15}$$

Substituting eqs. (4.13) to (4.15) into eq. (1.102), the eigenvalue problem for orthotropic material is found as

$$\begin{vmatrix} C_{11} & P_{12}C_{12} & P_{13}C_{13} & P_{12} & 0 & 0 & P_{13} & 0 & 0 \\ P_{12}C_{66} & C_{66} & 0 & 0 & P_{12} & 0 & 0 & P_{13} & 0 \\ P_{13}C_{55} & 0 & C_{55} & 0 & 0 & P_{12} & 0 & 0 & P_{13} \\ P_{12}C_{66} & C_{66} & 0 & -1 & 0 & 0 & 0 & 0 & 0 \\ C_{21} & P_{12}C_{22} & P_{13}C_{23} & 0 & -1 & 0 & 0 & 0 & 0 \\ 0 & P_{13}C_{44} & P_{12}C_{44} & 0 & 0 & -1 & 0 & 0 & 0 \\ P_{13}C_{55} & 0 & C_{55} & 0 & 0 & 0 & -1 & 0 & 0 \\ 0 & P_{13}C_{44} & P_{12}C_{44} & 0 & 0 & 0 & 0 & -1 & 0 \\ C_{31} & P_{12}C_{32} & P_{13}C_{33} & 0 & 0 & 0 & 0 & 0 & -1 \end{vmatrix} = 0 \,. \tag{4.16}$$

Equation (4.16) may be rewritten as

$$
\begin{aligned}
&\big(C_{22}\,C_{44}\,C_{66}\big)\,{P_{12}}^{6}+\\
&+\Big[\,\big(C_{22}\,C_{33}\,C_{66}+C_{22}\,C_{44}\,C_{55}-C_{23}\,C_{32}\,C_{66}-C_{23}\,C_{44}\,C_{66}-C_{32}\,C_{44}\,C_{66}\big)\,{P_{13}}^{2}\\
&\quad+\big(C_{11}\,C_{22}\,C_{44}-C_{12}\,C_{21}\,C_{44}-C_{12}\,C_{44}\,C_{66}-C_{21}\,C_{44}\,C_{66}+C_{22}\,C_{55}\,C_{66}\big)\Big]\,{P_{12}}^{4}\\
&+\Big[\,\big(C_{22}\,C_{33}\,C_{55}-C_{23}\,C_{32}\,C_{55}-C_{23}\,C_{44}\,C_{55}-C_{32}\,C_{44}\,C_{55}+C_{33}\,C_{44}\,C_{66}\big)\,{P_{13}}^{4}\\
&\quad+\big(C_{11}\,C_{22}\,C_{33}-C_{11}\,C_{23}\,C_{32}-C_{11}\,C_{23}\,C_{44}-C_{11}\,C_{32}\,C_{44}-C_{12}\,C_{21}\,C_{33}\\
&\quad+C_{12}\,C_{23}\,C_{31}+C_{12}\,C_{23}\,C_{55}+C_{12}\,C_{31}\,C_{44}-C_{12}\,C_{33}\,C_{66}+C_{12}\,C_{44}\,C_{55}\\
&\quad+C_{13}\,C_{21}\,C_{32}+C_{13}\,C_{21}\,C_{44}-C_{13}\,C_{22}\,C_{31}-C_{13}\,C_{22}\,C_{55}+C_{13}\,C_{32}\,C_{66}\\
&\quad+C_{13}\,C_{44}\,C_{66}+C_{21}\,C_{32}\,C_{55}-C_{21}\,C_{33}\,C_{66}+C_{21}\,C_{44}\,C_{55}-C_{22}\,C_{31}\,C_{55}\\
&\quad+C_{23}\,C_{31}\,C_{66}+C_{23}\,C_{55}\,C_{66}+C_{31}\,C_{44}\,C_{66}+C_{32}\,C_{55}\,C_{66}+4\,C_{44}\,C_{55}\,C_{66}\big)\,{P_{13}}^{2}\\
&\quad+\big(C_{11}\,C_{22}\,C_{55}+C_{11}\,C_{44}\,C_{66}-C_{12}\,C_{21}\,C_{55}-C_{12}\,C_{55}\,C_{66}-C_{21}\,C_{55}\,C_{66}\big)\,\Big]\,{P_{12}}^{2}\\
&+\big(C_{33}\,C_{44}\,C_{55}\big)\,{P_{13}}^{6}\\
&+\big(C_{11}\,C_{33}\,C_{44}-C_{13}\,C_{31}\,C_{44}-C_{13}\,C_{44}\,C_{55}-C_{31}\,C_{44}\,C_{55}+C_{33}\,C_{55}\,C_{66}\big)\,{P_{13}}^{4}\\
&+\big(C_{11}\,C_{33}\,C_{66}+C_{11}\,C_{44}\,C_{55}-C_{13}\,C_{31}\,C_{66}-C_{13}\,C_{55}\,C_{66}-C_{31}\,C_{55}\,C_{66}\big)\,{P_{13}}^{2}\\
&+\big(C_{11}\,C_{55}\,C_{66}\big)=0\,.
\end{aligned}
\tag{4.17}
$$

Noting the stiffness tensor symmetry, eq. (4.17) reduces to

$$
\begin{aligned}
&\big(C_{22}\,C_{44}\,C_{66}\,\big)\,{P_{12}}^{6}\\
&+\Big[\,\big(C_{22}\,C_{33}\,C_{66}+C_{22}\,C_{44}\,C_{55}-{C_{32}}^{2}C_{66}-2\,C_{32}\,C_{44}\,C_{66}\big)\,{P_{13}}^{2}\\
&\quad+\big(C_{11}\,C_{22}\,C_{44}-{C_{12}}^{2}C_{44}-2\,C_{12}\,C_{44}\,C_{66}+C_{22}\,C_{55}\,C_{66}\big)\Big]\,{P_{12}}^{4}\\
&+\Big[\big(C_{22}\,C_{33}\,C_{55}-{C_{32}}^{2}C_{55}-2\,C_{32}\,C_{44}\,C_{55}+C_{33}\,C_{44}\,C_{66}\big)\,{P_{13}}^{4}\\
&\quad+\big(C_{11}\,C_{22}\,C_{33}-C_{11}\,{C_{32}}^{2}-2\,C_{11}\,C_{32}\,C_{44}-{C_{12}}^{2}C_{33}+2\,C_{12}\,C_{13}\,C_{32}\\
&\quad+2\,C_{12}\,C_{13}\,C_{44}+2\,C_{12}\,C_{32}\,C_{55}-2\,C_{12}\,C_{33}\,C_{66}+2\,C_{12}\,C_{44}\,C_{55}-{C_{13}}^{2}C_{22}\\
&\quad-2\,C_{13}\,C_{22}\,C_{55}+2\,C_{13}\,C_{32}\,C_{66}+2\,C_{13}\,C_{44}\,C_{66}+2\,C_{32}\,C_{55}\,C_{66}+4\,C_{44}\,C_{55}\,C_{66}\big)\,{P_{13}}^{2}\\
&\quad+\big(C_{11}\,C_{22}\,C_{55}+C_{11}\,C_{44}\,C_{66}-{C_{12}}^{2}C_{55}-2\,C_{12}\,C_{55}\,C_{66}\big)\,\Big]\,{P_{12}}^{2}\\
&+\big(C_{33}\,C_{44}\,C_{55}\,\big)\,{P_{13}}^{6}\\
&+\big(C_{11}\,C_{33}\,C_{44}-{C_{13}}^{2}C_{44}-2\,C_{13}\,C_{44}\,C_{55}+C_{33}\,C_{55}\,C_{66}\big)\,{P_{13}}^{4}\\
&+\big(C_{11}\,C_{33}\,C_{66}+C_{11}\,C_{44}\,C_{55}-{C_{13}}^{2}C_{66}-2\,C_{13}\,C_{55}\,C_{66}\big)\,{P_{13}}^{2}
\end{aligned}
$$

$$+ \left(C_{11}\, C_{55}\, C_{66}\right) = 0\ . \tag{4.18}$$

Equation (4.18) may be rewritten as

$$\begin{aligned} &A_{30}{P_{12}}^6 + A_{21}{P_{12}}^4{P_{13}}^2 + A_{20}{P_{12}}^4 + A_{12}{P_{12}}^2{P_{13}}^4 + A_{11}{P_{12}}^2{P_{13}}^2 + A_{10}{P_{12}}^2 \\ &+ A_{03}{P_{13}}^6 + A_{02}{P_{13}}^4 + A_{01}{P_{13}}^2 + A_{00} = 0 \end{aligned} \tag{4.19}$$

where

$$\begin{aligned} A_{31} =&\ C_{22}\, C_{44}\, C_{66} \\ A_{21} =&\ C_{22}\, C_{33}\, C_{66} + C_{22}\, C_{44}\, C_{55} - {C_{32}}^2 C_{66} - 2\, C_{32}\, C_{44}\, C_{66} \\ A_{20} =&\ C_{11}\, C_{22}\, C_{44} - {C_{12}}^2 C_{44} - 2\, C_{12}\, C_{44}\, C_{66} + C_{22}\, C_{55}\, C_{66} \\ A_{12} =&\ C_{22}\, C_{33}\, C_{55} - {C_{32}}^2 C_{55} - 2\, C_{32}\, C_{44}\, C_{55} + C_{33}\, C_{44}\, C_{66} \\ A_{11} =&\ C_{11}\, C_{22}\, C_{33} - C_{11}\, {C_{32}}^2 - 2\, C_{11}\, C_{32}\, C_{44} - {C_{12}}^2 C_{33} + 2\, C_{12}\, C_{13}\, C_{32} \\ &+ 2\, C_{12}\, C_{13}\, C_{44} + 2\, C_{12}\, C_{32}\, C_{55} - 2\, C_{12}\, C_{33}\, C_{66} + 2\, C_{12}\, C_{44}\, C_{55} - {C_{13}}^2 C_{22} \\ &- 2\, C_{13}\, C_{22}\, C_{55} + 2\, C_{13}\, C_{32}\, C_{66} + 2\, C_{13}\, C_{44}\, C_{66} + 2\, C_{32}\, C_{55}\, C_{66} + 4\, C_{44}\, C_{55}\, C_{66} \\ A_{10} =&\ C_{11}\, C_{22}\, C_{55} + C_{11}\, C_{44}\, C_{66} - {C_{12}}^2 C_{55} - 2\, C_{12}\, C_{55}\, C_{66} \\ A_{03} =&\ C_{33}\, C_{44}\, C_{55} \\ A_{02} =&\ C_{11}\, C_{33}\, C_{44} - {C_{13}}^2 C_{44} - 2\, C_{13}\, C_{44}\, C_{55} + C_{33}\, C_{55}\, C_{66} \\ A_{01} =&\ C_{11}\, C_{33}\, C_{66} + C_{11}\, C_{44}\, C_{55} - {C_{13}}^2 C_{66} - 2\, C_{13}\, C_{55}\, C_{66} \\ A_{00} =&\ C_{11}\, C_{55}\, C_{66}\ . \end{aligned} \tag{4.20}$$

Equation (4.19) is defined as a bi-sextic equation; that is, the two unknowns P_{12} and P_{13} are raised to the maximum power 6 with power combinations less than or equal to 6.

Equation (4.19) may be rewritten as

$$\begin{aligned} &A_{30}{Q_{12}}^3 + A_{21}{Q_{12}}^2 Q_{13} + A_{20}{Q_{12}}^2 + A_{12} Q_{12} {Q_{13}}^2 + A_{11} Q_{12} Q_{13} + A_{10} Q_{12} \\ &+ A_{03}{Q_{13}}^3 + A_{02}{Q_{13}}^2 + A_{01} Q_{13} + A_{00}\ = 0 \end{aligned} \tag{4.21}$$

where

$$P_{12} = \pm\sqrt{Q_{12}} \qquad P_{13} = \pm\sqrt{Q_{13}}\ . \tag{4.22}$$

Equation (4.21) is a bi-cubic equation in Q_{12} and Q_{13}.

4.1.2 Equations for various material symmetries

As an example, if P_{12} has three identical roots a or ae where $e^2 = 1$, as may be seen in eq. (1.80), and a is a positive real quantity, $Q_{12} = a^2$ and eq. (4.21), reduces to

$$A_{03}{Q_{13}}^3 + D_{02}{Q_{13}}^2 + D_{01} Q_{13} + D_{00}\ = 0 \tag{4.23}$$

where

$$D_{02} = a^2 A_{12} + A_{02} \qquad D_{01} = a^4 A_{21} + a^2 A_{11} + A_{01} \qquad D_{00} = a^6 A_{30} + a^4 A_{20} + a^2 A_{10} + A_{00} \; . \tag{4.24}$$

If P_{12} has three identical roots ai and a is a positive real quantity, $Q_{12} = -a^2$ and eq. (4.21), reduces to

$$A_{03} {Q_{13}}^3 + E_{02} {Q_{13}}^2 + E_{01} Q_{13} + E_{00} = 0 \tag{4.25}$$

where

$$E_{02} = -a^2 A_{12} + A_{02} \qquad E_{01} = a^4 A_{21} - a^2 A_{11} + A_{01} \qquad E_{00} = -a^6 A_{30} + a^4 A_{20} - a^2 A_{10} + A_{00} \; . \tag{4.26}$$

Next, several specific materials are considered. For a linear elastic, homogeneous, isotropic material the stiffness matrix is given as

$$\mathbf{C} = \begin{bmatrix} 2\mu + \lambda & \lambda & \lambda & 0 & 0 & 0 \\ \lambda & 2\mu + \lambda & \lambda & 0 & 0 & 0 \\ \lambda & \lambda & 2\mu + \lambda & 0 & 0 & 0 \\ 0 & 0 & 0 & \mu & 0 & 0 \\ 0 & 0 & 0 & 0 & \mu & 0 \\ 0 & 0 & 0 & 0 & 0 & \mu \end{bmatrix} \tag{4.27}$$

where μ is the shear modulus given by

$$\mu = \frac{E}{2(1+\nu)} \tag{4.28}$$

and

$$\lambda = \frac{\nu E}{(1+\nu)(1-2\nu)} \; . \tag{4.29}$$

In eqs. (4.28) and (4.29), E and ν are, respectively, Young's modulus and Poisson's ratio. Equation (4.21) for this material is given as

$$(Q_{12} + Q_{13} + 1)^3 = 0 \; . \tag{4.30}$$

Noting eqs. (4.30) and (4.22),

$$P_{13} = \pm i \sqrt{P_{12}^2 + 1} \; . \tag{4.31}$$

That is, P_{13} has three identical pairs of roots given in eq. (4.31). It is clearly seen that there are two unknowns and one equation. If $P_{12} = a$ or ae, then

$$P_{13} = \pm i \sqrt{a^2 + 1} \; . \tag{4.32}$$

If $P_{12} = ai$ or aei,

$$P_{13} = \pm i \sqrt{1 - a^2} \; . \tag{4.33}$$

Table 4.1: Effective mechanical properties of SC-Si.

E (GPa)	ν (GPa)	μ (GPa)
130.23	0.25	79.37

If $a > 1$

$$P_{13} = \mp\sqrt{a^2 + 1}\ . \tag{4.34}$$

When using the Stroh formalism (Ting, 1996, page 139), it is seen that isotropic material is mathematically degenerate having three identical eigenvalues. It is anticipated that the same problem may exist here.

Next, the cubic material Single Crystal Silicon (SC-Si) is considered. The mechanical properties are given in Wortman and Evans (1965) and are presented in Table 4.1. These elastic constant are independent of each other. If P_{12} is taken to be a triple root given by

$$P_{12} = 1 \quad \text{or} \quad P_{12} = -1 \tag{4.35}$$

eq. (4.19) leads to

$$P_{13}^6 + 4.1670 P_{13}^4 + 8.4450 P_{13}^2 + 6.1670 = 0 \tag{4.36}$$

The solution of eq. (4.36) results in three complex conjugate pairs. For this material, the eigenvalue pairs are given by

$$P_{13}^{(1)} = \alpha + i\beta\ ,\ P_{13}^{(2)} = -\alpha + i\beta\ ,\ P_{13}^{(3)} = i\beta_3 \tag{4.37}$$

and

$$P_{13}^{(\gamma+3)} = \bar{P}_{13}^{(\gamma)} \tag{4.38}$$

where $\gamma = 1, 2, 3$. For the material constants in Table 4.1,

$$P_{13}^{(1)} = 0.6084 + 1.3407i \quad , \quad P_{13}^{(2)} = -0.6084 + 1.3407i \quad , \quad P_{13}^{(3)} = 1.1457i \tag{4.39}$$

so that

$$P_{13}^{(4)} = 0.6084 - 1.3407i \quad , \quad P_{13}^{(5)} = -0.6084 - 1.3407i \quad , \quad P_{13}^{(6)} = -1.1457i\ . \tag{4.40}$$

This same eigenvalue solution in eqs. (4.39) and (4.40) is also obtained if

$$P_{12} = e \quad \text{or} \quad P_{12} = -e\ . \tag{4.41}$$

If

$$P_{12} = \pm i \quad \text{or} \quad P_{12} = \pm ei \tag{4.42}$$

is a triple root, eq. (4.19) leads to

$$P_{13}^6 - 0.1110 P_{13}^2 = 0 \tag{4.43}$$

Solution of eq. (4.43) results in six eigenvalues. Since not all of the roots are complex, it is not clear how to group them. However, they will be arranged as

$$P_{13}^{(1)} = 0 \ , \ P_{13}^{(2)} = 0.5771 \ , \ P_{13}^{(3)} = 0.5771i \tag{4.44}$$

$$P_{13}^{(4)} = 0 \ , \ P_{13}^{(5)} = -0.5771 \ , \ P_{13}^{(6)} = -0.5771i \ . \tag{4.45}$$

If P_{13} is taken to be a triple root given by

$$P_{13} = 1 \ \text{ or } \ P_{13} = -1 \ \text{ or } \ P_{13} = e \ \text{ or } \ P_{13} = -e \tag{4.46}$$

eq. (4.19) leads to

$$P_{12}^6 + 4.1670 P_{12}^4 + 8.4450 P_{12}^2 + 6.1670 = 0 \tag{4.47}$$

The solution of eq. (4.47) results in three complex conjugate pairs for P_{12}. For this material, the eigenvalue pairs are given by

$$P_{12}^{(1)} = \alpha + i\beta \ , \ P_{12}^{(2)} = -\alpha + i\beta \ , \ P_{12}^{(3)} = i\beta_3 \tag{4.48}$$

and

$$P_{12}^{(\gamma+3)} = \bar{P}_{12}^{(\gamma)} \tag{4.49}$$

where $\gamma = 1, 2, 3$. For the material constants in Table 4.1,

$$P_{12}^{(1)} = 0.6084 + 1.3407i \ , \ P_{12}^{(2)} = -0.6084 + 1.3407i \ , \ P_{12}^{(3)} = 1.1457i \tag{4.50}$$

so that

$$P_{12}^{(4)} = 0.6084 - 1.3407i \ , \ P_{12}^{(5)} = -0.6084 - 1.3407i \ , \ P_{12}^{(6)} = -1.1457i \ . \tag{4.51}$$

Next, the eigenvalues are calculated for the effective mechanical properties of graphite/epoxy AS4/3501-6, shown in Table 1.1. Recall that, E_A and E_T are the Young's moduli in the axial and transverse directions, respectively, ν_A and ν_T are the Poisson's ratios in the axial and transverse directions, respectively, and G_A is the axial shear modulus. The compliance matrix is given as

$$\mathbf{S} = \begin{bmatrix} \frac{1}{E_A} & -\frac{\nu_A}{E_A} & -\frac{\nu_A}{E_A} & 0 & 0 & 0 \\ & \frac{1}{E_T} & -\frac{\nu_T}{E_T} & 0 & 0 & 0 \\ & & \frac{1}{E_T} & 0 & 0 & 0 \\ & \text{sym} & & \frac{2(1+\nu_T)}{E_T} & 0 & 0 \\ & & & & \frac{1}{G_A} & 0 \\ & & & & & \frac{1}{G_A} \end{bmatrix} . \tag{4.52}$$

Table 4.2: Effective mechanical properties of a graphite/epoxy plain weave with yarn in the 0° and 90° directions.

$E_{11} = E_{33}$ (GPa)	E_{22} (GPa)	ν_{13}	$\nu_{21} = \nu_{23}$	G_{13} (GPa)	$G_{21} = G_{23}$ (GPa)
52.8	6.2	0.036	0.049	3.2	2.2

The stiffness matrix is given by

$$C_{\alpha\beta} = S_{\alpha\beta}^{-1} \, . \tag{4.53}$$

In order to obtain the eigenvalues P_{12} and P_{13} in eq. (4.17), an assumption is made such that

$$P_{12} = 1 \text{ or } P_{12} = -1 \text{ or } P_{12} = e \text{ or } P_{12} = -e \, . \tag{4.54}$$

Substituting each of these values into eq. (4.19) leads to

$$P_{13}^6 + 0.2781 P_{13}^4 + 0.0096 P_{13}^2 + 0.8782 = 0 \, . \tag{4.55}$$

For this material, the eigenvalues $P_{13}^{(\gamma)}$ are pure imaginary and given by

$$P_{13}^{(1)} = 1.1787i \quad , \quad P_{13}^{(2)} = 1.6246i \quad , \quad P_{13}^{(3)} = 4.9973i \tag{4.56}$$

so that

$$P_{13}^{(4)} = -1.1787i \quad , \quad P_{13}^{(5)} = -1.6246i \quad , \quad P_{13}^{(6)} = -4.9973i \, . \tag{4.57}$$

If

$$P_{12} = \pm i \text{ or } P_{12} = \pm ie \tag{4.58}$$

eq. (4.19) leads to

$$P_{13}^6 + 3.7231 P_{13}^4 + 85.6402 P_{13}^2 - 33.4022 = 0 \, . \tag{4.59}$$

Solution of eq. (4.59) results in three pairs

$$P_{13}^{(1)} = 0.7815 \quad , \quad P_{13}^{(2)} = 0.7996i \quad , \quad P_{13}^{(3)} = 4.7930i \, ; \tag{4.60}$$

so that

$$P_{13}^{(4)} = -0.7815 \quad , \quad P_{13}^{(5)} = -0.7996i \quad , \quad P_{13}^{(6)} = -4.7930i \, . \tag{4.61}$$

Next, the eigenvalues are calculated for a plain weave with yarn oriented in the 0°/90°-directions. The mechanical properties are taken from Mega and Banks-Sills (2019), Table S8, and are given in Table 4.2. The young's moduli E_{11}, E_{22} and E_{33} are in the x_1, x_2 and x_3-directions, respectively, ν_{13}, ν_{23} and ν_{21} are the Poisson's ratios, and there are shear moduli G_{13}, G_{21} and G_{23}. Additional Poisson ratio's may be found using

$$\frac{\nu_{ij}}{E_{ii}} = \frac{\nu_{ji}}{E_{jj}} \tag{4.62}$$

where there is no summation of indices. The compliance matrix is given as

$$\mathbf{S} = \begin{bmatrix} \frac{1}{E_{11}} & -\frac{\nu_{12}}{E_{11}} & -\frac{\nu_{13}}{E_{11}} & 0 & 0 & 0 \\ & \frac{1}{E_{22}} & -\frac{\nu_{23}}{E_{22}} & 0 & 0 & 0 \\ & & \frac{1}{E_{11}} & 0 & 0 & 0 \\ & \text{sym} & & \frac{1}{G_{23}} & 0 & 0 \\ & & & & \frac{1}{G_{13}} & 0 \\ & & & & & \frac{1}{G_{23}} \end{bmatrix} . \tag{4.63}$$

The stiffness matrix is given in eq. (4.53).

In order to obtain the eigenvalues P_{12} and P_{13} in eq. (4.17), an assumption is made such that

$$P_{12} = 1 \text{ or } P_{12} = -1 \text{ or } P_{12} = e \text{ or } P_{12} = -e \tag{4.64}$$

are triple roots. Substituting these values into eq. (4.19) leads to

$$P_{13}^6 + 21.190 P_{13}^4 + 64.167 P_{13}^2 + 6.570 = 0 \tag{4.65}$$

For this material, the eigenvalues $P_{13}^{(\gamma)}$ are pure imaginary and given by

$$P_{13}^{(1)} = 0.3257i \quad , \quad P_{13}^{(2)} = 1.8781i \quad , \quad P_{13}^{(3)} = 4.1900i \tag{4.66}$$

so that

$$P_{13}^{(4)} = -0.3257i \quad , \quad P_{13}^{(5)} = -1.8781i \quad , \quad P_{13}^{(6)} = -4.1900i \, . \tag{4.67}$$

If

$$P_{12} = \pm i \quad \text{or} \quad \pm ei \tag{4.68}$$

eq. (4.17) leads to

$$P_{13}^6 + 14.2683 P_{13}^4 - 24.65577 P_{13}^2 - 0.5168 = 0 \tag{4.69}$$

Solution of eq. (4.69) results in three complex conjugate pairs

$$P_{13}^{(1)} = 0.1439i \quad , \quad P_{13}^{(2)} = 1.2557 \quad , \quad P_{13}^{(3)} = 3.9780i \tag{4.70}$$

so that

$$P_{13}^{(4)} = -0.1439i \quad , \quad P_{13}^{(5)} = -1.2557 \quad , \quad P_{13}^{(6)} = -3.9780i \, . \tag{4.71}$$

Next, the eigenvalues are calculated for a Single-Crystal Forsterite. The elastic constants are taken from Isaak et al. (1989), Table 3, for 300 K degrees, and are given in Table 4.3. The stiffness matrix is given by

Table 4.3: Elastic constants of Single-Crystal Forsterite. The units are GPa.

C_{11}	C_{22}	C_{33}	C_{44}	C_{55}	C_{66}	C_{23}	C_{13}	C_{12}
329.97	199.98	235.96	67.18	81.50	81.18	72.12	67.96	66.19

$$\mathbf{C} = \begin{bmatrix} C_{11} & C_{12} & C_{13} & 0 & 0 & 0 \\ & C_{22} & C_{23} & 0 & 0 & 0 \\ & & C_{33} & 0 & 0 & 0 \\ & \text{sym} & & C_{44} & 0 & 0 \\ & & & & C_{55} & 0 \\ & & & & & C_{66} \end{bmatrix} . \tag{4.72}$$

In order to obtain the eigenvalues P_{12} and P_{13} in eq. (4.17), an assumption is made such that

$$P_{12} = 1 \text{ or } P_{12} = -1 \text{ or } P_{12} = e \text{ or } P_{12} = -e \tag{4.73}$$

are triple roots. Substituting these values into eq. (4.19) leads to

$$P_{13}^6 + 7.4743 P_{13}^4 + 16.6755 P_{13}^2 + 10.8042 = 0 \tag{4.74}$$

For the solution of eq. (4.74), the eigenvalues $P_{13}^{(\gamma)}$ are pure imaginary and given by

$$P_{13}^{(1)} = 1.0712i \quad , \quad P_{13}^{(2)} = 1.5472i \quad , \quad P_{13}^{(3)} = 1.9831i, \tag{4.75}$$

$$P_{13}^{(4)} = -1.0712i \quad , \quad P_{13}^{(5)} = -1.5472i \quad , \quad P_{13}^{(6)} = -1.9831i \, . \tag{4.76}$$

If

$$P_{12} = \pm i \quad \text{or} \quad \pm ei \tag{4.77}$$

eq. (4.17) leads to

$$P_{13}^6 + 1.4075 P_{13}^4 - 0.3126 P_{13}^2 - 0.0869 = 0 \tag{4.78}$$

Solution of eq. (4.78) results in three complex conjugate pairs

$$P_{13}^{(1)} = 0.4088i \quad , \quad P_{13}^{(2)} = 0.5752 \quad , \quad P_{13}^{(3)} = 1.2535i, \tag{4.79}$$

$$P_{13}^{(4)} = -0.4088i \quad , \quad P_{13}^{(5)} = -0.5752 \quad , \quad P_{13}^{(6)} = -1.2535i \, . \tag{4.80}$$

4.2 The eigenvector for various anisotropic materials

In this section, explicit expressions for calculation of the eigenvector for various anisotropic materials are presented. The eigenvector is defined in eq. (1.94) as

$$\begin{aligned}&(\mathbf{C}_{11}+\mathbf{C}_{12}P_{12}+\mathbf{C}_{13}P_{13}\\&+\mathbf{C}_{21}P_{12}+\mathbf{C}_{22}P_{12}^2+\mathbf{C}_{23}P_{12}P_{13}\\&+\mathbf{C}_{31}P_{13}+\mathbf{C}_{32}P_{13}P_{12}+\mathbf{C}_{33}P_{13}^2)\,\mathbf{a}_{3\times1}=\mathbf{0}_{3\times1}\ ,\end{aligned}\tag{4.81}$$

where $P_{11}=1$, $\mathbf{C}_{ij}$ are 3×3 matrices given in eq. (1.95) and

$$\mathbf{a}=(a_1\ a_2\ a_3)^T\tag{4.82}$$

For an orthotropic material, using the matrices from eqs. (4.4) to (4.8), this equation is given as

$$\begin{aligned}&\left(\begin{bmatrix}C_{11}&0&0\\0&C_{66}&0\\0&0&C_{55}\end{bmatrix}+\begin{bmatrix}0&C_{12}&0\\C_{66}&0&0\\0&0&0\end{bmatrix}P_{12}+\begin{bmatrix}0&0&C_{13}\\0&0&0\\C_{55}&0&0\end{bmatrix}P_{13}\right.\\&\begin{bmatrix}0&C_{66}&0\\C_{12}&0&0\\0&0&0\end{bmatrix}P_{12}+\begin{bmatrix}C_{66}&0&0\\0&C_{22}&0\\0&0&C_{44}\end{bmatrix}P_{12}^2+\begin{bmatrix}0&0&0\\0&0&C_{23}\\0&C_{44}&0\end{bmatrix}P_{12}P_{13}\\&\left.\begin{bmatrix}0&0&C_{55}\\0&0&0\\C_{13}&0&0\end{bmatrix}P_{13}+\begin{bmatrix}0&0&0\\0&0&C_{44}\\0&C_{23}&0\end{bmatrix}P_{13}P_{12}+\begin{bmatrix}C_{55}&0&0\\0&C_{44}&0\\0&0&C_{33}\end{bmatrix}P_{13}^2\right)\begin{pmatrix}a_1\\a_2\\a_3\end{pmatrix}=\\&\begin{bmatrix}C_{11}+C_{66}P_{12}^2+C_{55}P_{13}^2&(C_{12}+C_{66})P_{12}&(C_{13}+C_{55})P_{13}\\(C_{12}+C_{66})P_{12}&C_{66}+C_{22}P_{12}^2+C_{44}P_{13}^2&(C_{23}+C_{44})P_{12}P_{13}\\(C_{13}+C_{55})P_{13}&(C_{23}+C_{44})P_{12}P_{13}&C_{55}+C_{44}P_{12}^2+C_{33}P_{13}^2\end{bmatrix}\begin{pmatrix}a_1\\a_2\\a_3\end{pmatrix}=0\end{aligned}\tag{4.83}$$

For given values of P_{12} and P_{13}, the eigenvector $\mathbf{a}$ may be found using eq. (4.83).

For a linear elastic, homogeneous, isotropic material, substituting eq. (4.27) into eq. (4.83) results in

$$\begin{bmatrix}2\mu+\lambda+\left({P_{12}}^2+{P_{13}}^2\right)\mu&P_{12}\,(\lambda+\mu)&P_{13}\,(\lambda+\mu)\\P_{12}\,(\lambda+\mu)&\mu+{P_{12}}^2\,(2\mu+\lambda)+{P_{13}}^2\mu&P_{12}P_{13}\,(\lambda+\mu)\\P_{13}\,(\lambda+\mu)&P_{12}P_{13}\,(\lambda+\mu)&\mu+{P_{12}}^2\mu+{P_{13}}^2\,(2\mu+\lambda)\end{bmatrix}\begin{pmatrix}a_1\\a_2\\a_3\end{pmatrix}=0\tag{4.84}$$

By substituting the first value of P_{13} from eq. (4.31), namely $i\sqrt{P_{12}^2+1}$, into eq. (4.84), one obtains

$$\begin{bmatrix} 1 & P_{12} & i\sqrt{P_{12}^2+1} \\ P_{12} & {P_{12}}^2 & iP_{12}\sqrt{P_{12}^2+1} \\ i\sqrt{P_{12}^2+1} & iP_{12}\sqrt{P_{12}^2+1} & -(P_{12}^2+1) \end{bmatrix} \begin{pmatrix} a_1 \\ a_2 \\ a_3 \end{pmatrix} = 0 \, . \tag{4.85}$$

Each row in the 3×3 matrix in eq. (4.85) is linearly dependent. Solution of eq. (4.85) leads to the eigenvector

$$\mathbf{a} = \begin{pmatrix} P_{12} + i\sqrt{P_{12}^2+1} \\ \text{-1} \\ \text{-1} \end{pmatrix} \, . \tag{4.86}$$

Since there are three identical eigenvalues, there are three identical eigenvectors making this system mathematically degenerate. Following Ting (1996, p.487-488), it is possible to treat this case. This will not be pursued here. It may be pointed out that there is a second triple eigenvalue which is the complex conjugate of the first (triple) eigenvalue. This case will be treated in the sequel.

Next, the eigenvectors are calculated for the cubic material, SC-Si, presented in Section 4.1.2. Substituting $P_{12} = 1$ and eq. (4.39) into eq. (4.83) results in three complex eigenvectors which may be arranged so that the 3×3 matrix $\mathbf{A}$ is given by

$$\mathbf{A} = \begin{bmatrix} \mathbf{a}^{(1)} & \mathbf{a}^{(2)} & \mathbf{a}^{(3)} \end{bmatrix} \tag{4.87}$$

and

$$\mathbf{a}^{(i)} = \begin{pmatrix} a_1^{(i)} & a_2^{(i)} & a_3^{(i)} \end{pmatrix}^T \, . \tag{4.88}$$

In eq. (4.88), $i = 1, 2, 3$ corresponds to the three eigenvalues with positive imaginary part. Thus,

$$\mathbf{A} = \begin{pmatrix} \text{-0.5311-0.4234}i & \text{0.5311-0.4234}i & 1 \\ \text{-0.5311-0.4234}i & \text{0.5311-0.4234}i & \text{-1} \\ 1 & 1 & 0 \end{pmatrix} \, . \tag{4.89}$$

For $P_{12} = 1$ and the complex conjugate eigenvalues given in eq. (4.40), eq. (4.83) results in

$$\tilde{\mathbf{A}} = \bar{\mathbf{A}} \tag{4.90}$$

where,

$$\tilde{\mathbf{A}} = \begin{bmatrix} \mathbf{a}^{(4)} & \mathbf{a}^{(5)} & \mathbf{a}^{(6)} \end{bmatrix} \tag{4.91}$$

and

$$\bar{\mathbf{A}} = \begin{bmatrix} \bar{\mathbf{a}}^{(1)} & \bar{\mathbf{a}}^{(2)} & \bar{\mathbf{a}}^{(3)} \end{bmatrix} \tag{4.92}$$

and the bar over a quantity represents the complex conjugate. Next, $P_{12} = -1$ and eq. (4.39) is substituted into eq. (4.83) to obtain

$$\mathbf{A} = \begin{pmatrix} \text{-0.5311-0.4234i} & \text{0.5311-0.4234i} & 1 \\ \text{0.5311+0.4234i} & \text{-0.5311+0.4234i} & 1 \\ 1 & 1 & 0 \end{pmatrix} . \tag{4.93}$$

Note that essentially the second row of $\mathbf{A}$ in eq. (4.89) is multiplied by -1 to obtain eq. (4.93). Substituting $P_{12} = -1$ and (4.40) into eq. (4.83) leads to eq. (4.90). Substituting $P_{12} = e$ and eq. (4.39) into eq. (4.83) results in

$$\mathbf{A} = \begin{pmatrix} \text{-0.5311-0.4234i} & \text{0.5311-0.4234i} & 1 \\ \text{-(0.5311+0.4234i)}e & \text{(0.5311-0.4234i)}e & \text{-}e \\ 1 & 1 & 0 \end{pmatrix} \tag{4.94}$$

Substituting $P_{12} = e$ and eq. (4.40) into eq. (4.83) leads to eq. (4.90). Substituting $P_{12} = -e$ and eq. (4.39) into eq. (4.83) results in

$$\mathbf{A} = \begin{pmatrix} \text{-0.5311-0.4234i} & \text{0.5311-0.4234i} & 1 \\ \text{(0.5311+0.4234i)}e & \text{(-0.5311+0.4234i)}e & e \\ 1 & 1 & 0 \end{pmatrix} \tag{4.95}$$

Note that the second row of $\mathbf{A}$ in eq. (4.89) is multiplied by e and $-e$ to obtain eqs. (4.94) and (4.95), respectively. Substituting $P_{12} = -e$ and eq. (4.40) into eq. (4.83) leads to eq. (4.90).

Substituting $P_{12} = i$ and eqs. (4.44) and (4.45) into eq. (4.83) results in

$$\mathbf{A} = \begin{pmatrix} 0 & \text{-0.5092} & \text{-0.1768}i \\ 0 & \text{0.1768}i & \text{-0.5092} \\ 1 & 1 & 1 \end{pmatrix} \tag{4.96}$$

and

$$\tilde{\mathbf{A}} = \begin{pmatrix} 0 & \text{0.5092} & \text{0.1768}i \\ 0 & \text{-0.1768}i & \text{0.5092} \\ 1 & 1 & 1 \end{pmatrix} \tag{4.97}$$

respectively. In this case, $\tilde{\mathbf{A}} \neq \bar{\mathbf{A}}$. Substituting $P_{12} = -i$, and eqs. (4.44) and (4.45) into eq. (4.83) results in

$$\mathbf{A} = \begin{pmatrix} 0 & \text{-0.5092} & \text{-0.1768}i \\ 0 & \text{-0.1768}i & \text{0.5092} \\ 1 & 1 & 1 \end{pmatrix} \tag{4.98}$$

and

$$\tilde{\mathbf{A}} = \begin{pmatrix} 0 & 0.5092 & 0.1768i \\ 0 & 0.1768i & -0.5092 \\ 1 & 1 & 1 \end{pmatrix} \tag{4.99}$$

respectively. Substituting $P_{12} = ie$ and eqs. (4.44) and (4.45) into eqs. (4.83) results in

$$\mathbf{A} = \begin{pmatrix} 0 & -0.5092 & -0.1768i \\ 0 & 0.1768ie & -0.5092e \\ 1 & 1 & 1 \end{pmatrix} \tag{4.100}$$

and

$$\tilde{\mathbf{A}} = \begin{pmatrix} 0 & 0.5092 & 0.1768i \\ 0 & -0.1768ie & 0.5092e \\ 1 & 1 & 1 \end{pmatrix} \tag{4.101}$$

respectively. Substituting $P_{12} = -ie$ and eqs. (4.44) and (4.45) into eqs. (4.83) results in

$$\mathbf{A} = \begin{pmatrix} 0 & -0.5092 & -0.1768i \\ 0 & -0.1768ie & 0.5092e \\ 1 & 1 & 1 \end{pmatrix} \tag{4.102}$$

and

$$\tilde{\mathbf{A}} = \begin{pmatrix} 0 & 0.5092 & 0.1768i \\ 0 & 0.1768ie & -0.5092e \\ 1 & 1 & 1 \end{pmatrix} \tag{4.103}$$

respectively.

Substituting $P_{13} = 1$ and eq. (4.50) into eq. (4.83) results in three eigenvectors

$$\mathbf{A} = \begin{pmatrix} 1 & 1 & -1 \\ -1.1512+0.9178i & 1.1512+0.9178i & 0 \\ 1 & 1 & 1 \end{pmatrix}. \tag{4.104}$$

For $P_{13} = 1$ and the complex conjugate eigenvalues given in eq. (4.51), eq. (4.90) holds.

Next, the eigenvectors are calculated for the transversely isotropic material presented in Section 4.1.2. Substituting $P_{12} = 1$ and eq. (4.56) into eq. (4.83) results in three complex eigenvectors given by

$$\mathbf{A} = \begin{pmatrix} -0.0298i & 0 & -5.7041i \\ -0.8484i & -1.6246i & -0.2001 \\ 1 & 1 & 1 \end{pmatrix}. \tag{4.105}$$

For $P_{12} = 1$ and eqs. (4.57) and (4.83), eq. (4.90) holds. Next, $P_{12} = -1$ and eq. (4.56) are substituted into eq. (4.83) resulting in three complex eigenvectors given by

$$\mathbf{A} = \begin{pmatrix} \text{-}0.0298i & 0 & \text{-}5.7041i \\ 0.8484i & 1.6246i & 0.2001i \\ 1 & 1 & 1 \end{pmatrix} . \tag{4.106}$$

For $P_{12} = -1$ and eqs. (4.57) and (4.83), eq. (4.90) holds. Substituting $P_{12} = e$ and eq. (4.56) into eq. (4.83) results in

$$\mathbf{A} = \begin{pmatrix} \text{-}0.0298i & 0 & \text{-}5.7041i \\ \text{-}0.8484ie & \text{-}1.6246ie & \text{-}0.2001e \\ 1 & 1 & 1 \end{pmatrix} . \tag{4.107}$$

For $P_{12} = e$ and eqs. (4.57) and (4.83), eq. (4.90) holds. Substituting $P_{12} = -e$ and eq. (4.56) into eq. (4.83) results in

$$\mathbf{A} = \begin{pmatrix} \text{-}0.0298i & 0 & \text{-}5.7041i \\ 0.8484ie & 1.6246ie & 0.2001e \\ 1 & 1 & 1 \end{pmatrix} . \tag{4.108}$$

For $P_{12} = -e$ and eqs. (4.57) and (4.83), eq. (4.90) holds.

Substituting $P_{12} = i$ and eqs. (4.60) and (4.61) into eq. (4.83) results in

$$\mathbf{A} = \begin{pmatrix} 0.0449 & 0 & \text{-}5.9472i \\ 1.2796i & \text{-}0.7996 & 0.2086 \\ 1 & 1 & 1 \end{pmatrix} \tag{4.109}$$

and

$$\tilde{\mathbf{A}} = \begin{pmatrix} \text{-}0.0449 & 0 & 5.9472i \\ \text{-}1.2796i & 0.7996 & \text{-}0.2086 \\ 1 & 1 & 1 \end{pmatrix} \tag{4.110}$$

respectively. Substituting $P_{12} = -i$, and eqs. (4.60) and (4.61) into eq. (4.83) results in

$$\mathbf{A} = \begin{pmatrix} 0.0449 & 0 & \text{-}5.9472i \\ \text{-}1.2796i & 0.7996 & \text{-}0.2086 \\ 1 & 1 & 1 \end{pmatrix} \tag{4.111}$$

and

$$\tilde{\mathbf{A}} = \begin{pmatrix} \text{-}0.0449 & 0 & 5.9472i \\ 1.2796i & \text{-}0.7996 & 0.2086 \\ 1 & 1 & 1 \end{pmatrix} \tag{4.112}$$

respectively. Substituting $P_{12} = ie$ and eqs. (4.60) and (4.61) into eqs. (4.83) results in

$$\mathbf{A} = \begin{pmatrix} 0.0449 & 0 & \text{-}5.9472i \\ 1.2796ie & \text{-}0.7996e & 0.2086\text{e} \\ 1 & 1 & 1 \end{pmatrix} \tag{4.113}$$

and

$$\tilde{\mathbf{A}} = \begin{pmatrix} \text{-}0.0449 & 0 & 5.9472i \\ \text{-}1.2796ie & 0.7996e & \text{-}0.2086e \\ 1 & 1 & 1 \end{pmatrix} \tag{4.114}$$

respectively. Substituting $P_{12} = -ie$ and eqs. (4.60) and (4.61) into eqs. (4.83) results in

$$\mathbf{A} = \begin{pmatrix} 0.0449 & 0 & \text{-}5.9472i \\ \text{-}1.2796ie & 0.7996e & \text{-}0.2086\text{e} \\ 1 & 1 & 1 \end{pmatrix} \tag{4.115}$$

and

$$\tilde{\mathbf{A}} = \begin{pmatrix} \text{-}0.0449 & 0 & 5.9472i \\ 1.2796ie & \text{-}0.7996e & 0.2086e \\ 1 & 1 & 1 \end{pmatrix} \tag{4.116}$$

respectively.

Next, the eigenvectors are calculated for the plain weave presented in Table 4.2. Substituting $P_{12} = 1$ and eq. (4.66) into eq. (4.83) results in three complex eigenvectors given by

$$\mathbf{A} = \begin{pmatrix} \text{-}0.0206i & 2.2451i & \text{-}31.9929i \\ \text{-}0.1808i & \text{-}22.5638i & \text{-}4.6441i \\ 1 & 1 & 1 \end{pmatrix} . \tag{4.117}$$

For $P_{12} = 1$ and eqs. (4.67) and (4.83), eq. (4.90) holds. Substituting $P_{12} = -1$ and eq. (4.66) into eq. (4.83) results in three complex eigenvectors given by

$$\mathbf{A} = \begin{pmatrix} \text{-}0.0206i & 2.2451i & \text{-}31.9929i \\ 0.1808i & 22.5638i & 4.6441i \\ 1 & 1 & 1 \end{pmatrix} . \tag{4.118}$$

For $P_{12} = -1$ and eqs. (4.67) and (4.83), eq. (4.90) holds. Substituting $P_{12} = e$ and eq. (4.66) into eq. (4.83) results in

$$\mathbf{A} = \begin{pmatrix} \text{-}0.0206i & 2.2451i & \text{-}31.9929i \\ \text{-}0.1808ie & \text{-}22.5638ie & \text{-}4.6441ie \\ 1 & 1 & 1 \end{pmatrix} . \tag{4.119}$$

For $P_{12} = e$ and eqs. (4.67) and (4.83), eq. (4.90) holds. Substituting $P_{12} = -e$ and eq. (4.66) into eq. (4.83) results in

$$\mathbf{A} = \begin{pmatrix} \text{-}0.0206i & 2.2451i & \text{-}31.9929i \\ 0.1808ie & 22.5638ie & 4.6441ie \\ 1 & 1 & 1 \end{pmatrix} \tag{4.120}$$

For $P_{12} = -e$ and eqs. (4.67) and (4.83), eq. (4.90) holds.

Substituting $P_{12} = i$ and eqs. (4.70) and (4.71) into eq. (4.83) results in

$$\mathbf{A} = \begin{pmatrix} 1.2008 & \text{-}0.0016i & \text{-}37.4083i \\ 15.2499i & \text{-}0.1648 & 4.2786 \\ 1 & 1 & 1 \end{pmatrix} \tag{4.121}$$

and

$$\tilde{\mathbf{A}} = \begin{pmatrix} \text{-}1.2008 & 0.0016i & 37.4083i \\ \text{-}15.2499i & 0.1648 & \text{-}4.2786 \\ 1 & 1 & 1 \end{pmatrix} \tag{4.122}$$

respectively. Substituting $P_{12} = -i$, and eqs. (4.70) and (4.71) into eq. (4.83) results in

$$\mathbf{A} = \begin{pmatrix} 1.2008 & \text{-}0.0016i & \text{-}37.4083i \\ \text{-}15.2499i & 0.1648 & \text{-}4.2786 \\ 1 & 1 & 1 \end{pmatrix} \tag{4.123}$$

and

$$\tilde{\mathbf{A}} = \begin{pmatrix} \text{-}1.2008 & 0.0016i & 37.4083i \\ 15.2499i & \text{-}0.1648 & 4.2786 \\ 1 & 1 & 1 \end{pmatrix} \tag{4.124}$$

respectively. Substituting $P_{12} = ie$ and eqs. (4.70) and (4.71) into eqs. (4.83) results in

$$\mathbf{A} = \begin{pmatrix} 1.2008 & \text{-}0.0016i & \text{-}37.4083i \\ 15.2499ie & \text{-}0.1648e & 4.2786e \\ 1 & 1 & 1 \end{pmatrix} \tag{4.125}$$

and

$$\tilde{\mathbf{A}} = \begin{pmatrix} \text{-}1.2008 & 0.0016i & 37.4083i \\ \text{-}15.2499ie & 0.1648e & \text{-}4.2786e \\ 1 & 1 & 1 \end{pmatrix} . \tag{4.126}$$

respectively. Substituting $P_{12} = -ie$ and eqs. (4.70) and (4.71) into eqs. (4.83) results in

$$\mathbf{A} = \begin{pmatrix} 1.2008 & \text{-}0.0016i & \text{-}37.4083i \\ \text{-}15.2499ie & 0.1648e & \text{-}4.2786e \\ 1 & 1 & 1 \end{pmatrix} \tag{4.127}$$

and

$$\tilde{\mathbf{A}} = \begin{pmatrix} \text{-1.2008} & 0.0016i & 37.4083i \\ 15.2499ie & \text{-0.1648}e & 4.2786e \\ 1 & 1 & 1 \end{pmatrix} \tag{4.128}$$

respectively.

Next, the eigenvectors are calculated for the Single-Crystal Forsterite presented in Section 4.1.2. The stiffness components are presented in Table 4.3. Substituting $P_{12} = 1$ and eq. (4.75) into eq. (4.83) results in three complex eigenvectors given by

$$\mathbf{A} = \begin{pmatrix} \text{-0.2478}i & 0.9209i & \text{-1.7682}i \\ \text{-0.5522}i & \text{-2.9193}i & \text{-0.9238}i \\ 1 & 1 & 1 \end{pmatrix} . \tag{4.129}$$

For $P_{12} = 1$ and eqs. (4.76) and (4.83), eq. (4.90) holds. Substituting $P_{12} = -1$ and eq. (4.75) into eq. (4.83) results in

$$\mathbf{A} = \begin{pmatrix} \text{-0.2478}i & 0.9209i & \text{-1.7682}i \\ 0.5522i & 2.9193i & 0.9238i \\ 1 & 1 & 1 \end{pmatrix} \tag{4.130}$$

For $P_{12} = -1$ and eqs. (4.76) and (4.83), eq. (4.90) holds. Substituting $P_{12} = e$ and eq. (4.75) into eq. (4.83) results in

$$\mathbf{A} = \begin{pmatrix} \text{-0.2478}i & 0.9209i & \text{-1.7682}i \\ \text{-0.5522}ie & \text{-2.9193}ie & \text{-0.9238}ie \\ 1 & 1 & 1 \end{pmatrix} . \tag{4.131}$$

For $P_{12} = e$ and eqs. (4.76) and (4.83), eq. (4.90) holds. Substituting $P_{12} = -e$ and eq. (4.75) into eq. (4.83) results in three complex eigenvectors given by

$$\mathbf{A} = \begin{pmatrix} \text{-0.2478}i & 0.9209i & \text{-1.7682}i \\ 0.5522ie & 2.9193ie & 0.9238ie \\ 1 & 1 & 1 \end{pmatrix} . \tag{4.132}$$

For $P_{12} = -e$ and eqs. (4.76) and (4.83), eq. (4.90) holds.

Substituting $P_{12} = i$ and eqs. (4.79) and (4.80) into eq. (4.83) results in

$$\mathbf{A} = \begin{pmatrix} 0.7137 & 0.0505i & \text{-3.0355}i \\ 1.9188i & \text{-0.4952} & 1.2156 \\ 1 & 1 & 1 \end{pmatrix} \tag{4.133}$$

and

$$\tilde{\mathbf{A}} = \begin{pmatrix} \text{-}0.7137 & \text{-}0.0505i & 3.0355i \\ \text{-}1.9188i & 0.4952 & \text{-}1.2156 \\ 1 & 1 & 1 \end{pmatrix} \tag{4.134}$$

respectively. Substituting $P_{12} = -i$, and eqs. (4.79) and (4.80) into eq. (4.83) results in

$$\mathbf{A} = \begin{pmatrix} 0.7137 & 0.0505i & \text{-}3.0355i \\ \text{-}1.9188i & 0.4952 & \text{-}1.2156 \\ 1 & 1 & 1 \end{pmatrix} \tag{4.135}$$

and

$$\tilde{\mathbf{A}} = \begin{pmatrix} \text{-}0.7137 & \text{-}0.0505i & 3.0355i \\ 1.9188i & \text{-}0.4952 & 1.2156 \\ 1 & 1 & 1 \end{pmatrix} \tag{4.136}$$

respectively. Substituting $P_{12} = ie$ and eqs. (4.79) and (4.80) into eqs. (4.83) results in

$$\mathbf{A} = \begin{pmatrix} 0.7137 & 0.0505i & \text{-}3.0355i \\ 1.9188ie & \text{-}0.4952e & 1.2156e \\ 1 & 1 & 1 \end{pmatrix} \tag{4.137}$$

and

$$\tilde{\mathbf{A}} = \begin{pmatrix} \text{-}0.7137 & \text{-}0.0505i & 3.0355i \\ \text{-}1.9188ie & 0.4952e & \text{-}1.2156e \\ 1 & 1 & 1 \end{pmatrix} . \tag{4.138}$$

respectively. Substituting $P_{12} = -ie$ and eqs. (4.79) and (4.80) into eqs. (4.83) results in

$$\mathbf{A} = \begin{pmatrix} 0.7137 & 0.0505i & \text{-}3.0355i \\ \text{-}1.9188ie & 0.4952e & \text{-}1.2156e \\ 1 & 1 & 1 \end{pmatrix} \tag{4.139}$$

and

$$\tilde{\mathbf{A}} = \begin{pmatrix} \text{-}0.7137 & \text{-}0.0505i & 3.0355i \\ 1.9188ie & \text{-}0.4952e & 1.2156e \\ 1 & 1 & 1 \end{pmatrix} . \tag{4.140}$$

respectively.

4.3 A three-dimensional Clifford formalism

In this section, a three-dimensional Clifford formalism is derived based on the two-dimensional Stroh formalism and Liu and Hong (2015) where a Clifford formalism was also explored. The stress-strain law for an anisotropic material is given in eq. (1.83) as

$$\sigma_{ij} = C_{ijkl}\epsilon_{kl} , \tag{4.141}$$

where $i, j, k, l = 1, 2, 3$ and repeated indices obey the summation convention. Recall that the stiffness tensor $\mathbf{C}$ satisfies the symmetry conditions in eq. (1.86). The strain-displacement relations are given in eq. (1.84) as

$$\epsilon_{ij} = \frac{1}{2}\left(u_{i,j} + u_{j,i}\right) \tag{4.142}$$

where a comma indicates differentiation. Using the equilibrium equations in eq. (1.87), the governing equations for the displacement components are given by

$$C_{ijkl} u_{k,jl} = 0 \ . \tag{4.143}$$

For a specific eigenvalue and eigenvector pair, the displacement vector is defined as a function of the coordinates x_1, x_2 and x_3 as

$$\mathbf{u} = \mathbf{a} f(y) \tag{4.144}$$

where $f(y)$ is an arbitrary function and

$$y = x_1 + P_{12} x_2 + P_{13} x_3 \ . \tag{4.145}$$

Using three eigenvalue and eigenvector pairs as found in Section 4.2, a general expression for the displacement vector may be written for a general solution as

$$\mathbf{u} = \sum_{\gamma=1}^{3} \left[\mathbf{a}^{(\gamma)} f_\gamma(y_\gamma) + \mathbf{a}^{(\gamma+3)} f_{\gamma+3}(y_{\gamma+3})\right] \tag{4.146}$$

and in matrix form as

$$\mathbf{u} = \mathbf{A}[\mathbf{f}(y)] + \tilde{\mathbf{A}}[\tilde{\mathbf{f}}(y)] \ . \tag{4.147}$$

In eq. (4.147), $\mathbf{A}$ is defined in eq. (4.87) and $\tilde{\mathbf{A}}$ is defined in eq. (4.91). The vectors $[\mathbf{f}(y)]$ and $[\tilde{\mathbf{f}}(y)]$ are defined as

$$[\mathbf{f}(y)] = \begin{pmatrix} f_1(y_1) \\ f_2(y_2) \\ f_3(y_3) \end{pmatrix} \tag{4.148}$$

and

$$[\tilde{\mathbf{f}}(y)] = \begin{pmatrix} f_4(y_4) \\ f_5(y_5) \\ f_6(y_6) \end{pmatrix} \tag{4.149}$$

respectively. In eqs. (4.148) and (4.149),

$$y_\gamma = x_1 + P_{12} x_2 + P_{13}^{(\gamma)} x_3 \tag{4.150}$$

where $\gamma = 1, ..., 6$ accounting for the six eigenvalues $P_{13}^{(\gamma)}$ and $f_\gamma(y_\gamma)$, are arbitrary functions. Recall that $P_{11} = 1$ and P_{12} has a chosen value.

For the special case where $\tilde{\mathbf{A}} = \bar{\mathbf{A}}$ and following Section 5.3 in Ting (1996), assume that the arbitrary functions $f_\gamma(y_\gamma)$ have the form

$$f_\gamma(y_\gamma) = f(y_\gamma)q_\gamma \quad f_{\gamma+3}(y_{\gamma+3}) = f(\bar{y}_\gamma)\bar{q}_\gamma \tag{4.151}$$

for $\gamma = 1, 2, 3$ without summation, and q_γ are arbitrary complex constants, the displacement vector may then be written as

$$\mathbf{u} = 2\ \Re\left[\mathbf{A}\left\langle f(y_*)\right\rangle \mathbf{q}\right]\ . \tag{4.152}$$

In eq. (4.152), $\langle f(y_*)\rangle$ is a diagonal matrix given as

$$\langle f(y_*)\rangle = \mathrm{diag}[f(y_1), f(y_2), f(y_3)] \tag{4.153}$$

and $\mathbf{q}$ is a vector composed of constant complex numbers.

Next, stress functions are found for the Clifford formalism using a specific eigenvalue and eigenvector. Substituting eqs. (4.142) and (4.144) into eq. (4.141) results in

$$\sigma_{ij} = C_{ijkl}P_{1l}a_k f'(y)\ , \tag{4.154}$$

summation is used on repeated indices, and the prime denotes differentiation with respect to the argument y. It is noted that eq. (4.154) is for one eigenvalue and one eigenvector. Using eq. (4.154), the stress components σ_{i1} are found as

$$\sigma_{i1} = \ C_{i1kl}P_{1l}a_k f'(y) \tag{4.155}$$

or

$$\begin{pmatrix} \sigma_{11} \\ \sigma_{21} \\ \sigma_{31} \end{pmatrix} = \begin{bmatrix} C_{11} & C_{16} & C_{15} \\ C_{61} & C_{66} & C_{65} \\ C_{51} & C_{56} & C_{55} \end{bmatrix} \begin{pmatrix} a_1 \\ a_2 \\ a_3 \end{pmatrix} f'(y) + \begin{bmatrix} C_{16} & C_{12} & C_{14} \\ C_{66} & C_{62} & C_{64} \\ C_{56} & C_{52} & C_{54} \end{bmatrix} \begin{pmatrix} a_1 \\ a_2 \\ a_3 \end{pmatrix} P_{12}f'(y) + \\ + \begin{bmatrix} C_{15} & C_{14} & C_{13} \\ C_{65} & C_{64} & C_{63} \\ C_{55} & C_{54} & C_{53} \end{bmatrix} \begin{pmatrix} a_1 \\ a_2 \\ a_3 \end{pmatrix} P_{13}f'(y) \tag{4.156}$$

where contracted notation is used. Next, stress vector components related to the stress components are defined as

$$(\mathbf{t}_1)_i = \sigma_{i1}\ ,\ \ (\mathbf{t}_2)_i = \sigma_{i2}\ ,\ \ (\mathbf{t}_3)_i = \sigma_{i3}\ . \tag{4.157}$$

Use of eq. (4.154) leads to

$$\mathbf{t}_1 = (\mathbf{C}_{11} + P_{12}\mathbf{C}_{12} + P_{13}\mathbf{C}_{13})\,\mathbf{a}f'(y) \tag{4.158}$$

$$\mathbf{t}_2 = (\mathbf{C}_{21} + P_{12}\mathbf{C}_{22} + P_{13}\mathbf{C}_{23})\,\mathbf{a}f'(y) \tag{4.159}$$

$$\mathbf{t}_3 = (\mathbf{C}_{31} + P_{12}\mathbf{C}_{32} + P_{13}\mathbf{C}_{33})\,\mathbf{a}f'(y). \tag{4.160}$$

For an orthotropic material, eqs. (4.158) to (4.160) become

$$\mathbf{t}_1 = \begin{bmatrix} C_{11} & C_{12}P_{12} & C_{13}P_{13} \\ C_{66}P_{12} & C_{66} & 0 \\ C_{55}P_{13} & 0 & C_{55} \end{bmatrix} \mathbf{a}f'(y) \tag{4.161}$$

$$\mathbf{t}_2 = \begin{bmatrix} C_{66}P_{12} & C_{66} & 0 \\ C_{21} & C_{22}P_{12} & C_{23}P_{13} \\ 0 & C_{44}P_{13} & C_{44}P_{12} \end{bmatrix} \mathbf{a}f'(y) \tag{4.162}$$

and

$$\mathbf{t}_3 = \begin{bmatrix} C_{55}P_{13} & 0 & C_{55} \\ 0 & C_{44}P_{13} & C_{44}P_{12} \\ C_{31} & C_{32}P_{12} & C_{33}P_{13} \end{bmatrix} \mathbf{a}f'(y)\ . \tag{4.163}$$

It should be noted that C_{ij} in eqs. (4.161) to (4.163) are compliance components and not matrices. Noting eqs. (4.161) to (4.163), it is possible to write

$$\begin{bmatrix} \sigma_1 \\ \sigma_2 \\ \sigma_3 \\ \sigma_4 \\ \sigma_5 \\ \sigma_6 \end{bmatrix} = \begin{bmatrix} C_{11} & C_{12}P_{12} & C_{13}P_{13} \\ C_{21} & C_{22}P_{12} & C_{23}P_{13} \\ C_{31} & C_{32}P_{12} & C_{33}P_{13} \\ 0 & C_{44}P_{13} & C_{44}P_{12} \\ C_{55}P_{13} & 0 & C_{55} \\ C_{66}P_{12} & C_{66} & 0 \end{bmatrix} \mathbf{a}f'(y)\ . \tag{4.164}$$

Using eqs. (4.161) to (4.164), the stress vectors, when using the three eigenvalue and eigenvector pairs, are given as

$$\mathbf{t}_1 = \begin{bmatrix} C_{11} & C_{12}P_{12} & C_{13}P_{13} \\ C_{66}P_{12} & C_{66} & 0 \\ C_{55}P_{13} & 0 & C_{55} \end{bmatrix} \Big(\mathbf{A}[\mathbf{f}\,'(y)] + \tilde{\mathbf{A}}[\tilde{\mathbf{f}}\,'(y)]\Big) \tag{4.165}$$

$$\mathbf{t}_2 = \begin{bmatrix} C_{66}P_{12} & C_{66} & 0 \\ C_{21} & C_{22}P_{12} & C_{23}P_{13} \\ 0 & C_{44}P_{13} & C_{44}P_{12} \end{bmatrix} \Big(\mathbf{A}[\mathbf{f}\,'(y)] + \tilde{\mathbf{A}}[\tilde{\mathbf{f}}\,'(y)]\Big) \tag{4.166}$$

$$\mathbf{t}_3 = \begin{bmatrix} C_{55}P_{13} & 0 & C_{55} \\ 0 & C_{44}P_{13} & C_{44}P_{12} \\ C_{31} & C_{32}P_{12} & C_{33}P_{13} \end{bmatrix} \Big(\mathbf{A}[\mathbf{f}\,'(y)] + \tilde{\mathbf{A}}[\tilde{\mathbf{f}}\,'(y)]\Big) \tag{4.167}$$

and

$$\begin{bmatrix} \sigma_1 \\ \sigma_2 \\ \sigma_3 \\ \sigma_4 \\ \sigma_5 \\ \sigma_6 \end{bmatrix} = \begin{bmatrix} C_{11} & C_{12}P_{12} & C_{13}P_{13} \\ C_{21} & C_{22}P_{12} & C_{23}P_{13} \\ C_{31} & C_{32}P_{12} & C_{33}P_{13} \\ 0 & C_{44}P_{13} & C_{44}P_{12} \\ C_{55}P_{13} & 0 & C_{55} \\ C_{66}P_{12} & C_{66} & 0 \end{bmatrix} \Big(\mathbf{A}[\mathbf{f}\,'(y)] + \tilde{\mathbf{A}}[\tilde{\mathbf{f}}\,'(y)] \Big) \ . \tag{4.168}$$

In eqs. (4.165) to (4.168), the general solution is again considered, so that

$$[\mathbf{f}\,'(y)] = \begin{pmatrix} f_1'(y_1) \\ f_2'(y_2) \\ f_3'(y_3) \end{pmatrix} \tag{4.169}$$

$$[\tilde{\mathbf{f}}\,'(y)] = \begin{pmatrix} f_4'(y_4) \\ f_5'(y_5) \\ f_6'(y_6) \end{pmatrix} \tag{4.170}$$

where the derivative is with respect to the argument.

Next, two stress function vectors are derived as

$$\boldsymbol{\phi}^{\mathbf{b}} = \mathbf{b} f(y) \quad , \quad \boldsymbol{\phi}^{\mathbf{g}} = \mathbf{g} f(y) \tag{4.171}$$

where

$$\mathbf{b} = (\mathbf{C}_{21} + P_{12}\mathbf{C}_{22} + P_{13}\mathbf{C}_{23})\,\mathbf{a} \tag{4.172}$$

$$\mathbf{g} = (\mathbf{C}_{31} + P_{12}\mathbf{C}_{32} + P_{13}\mathbf{C}_{33})\,\mathbf{a} \ . \tag{4.173}$$

It may be noted that

$$\frac{\partial f(y)}{\partial x_1} = P_{11} f'(y) \ , \quad \frac{\partial f(y)}{\partial x_2} = P_{12} f'(y) \ , \quad \frac{\partial f(y)}{\partial x_x} = P_{13} f'(y) \tag{4.174}$$

and $P_{11} = 1$. Then, the required derivatives of $\boldsymbol{\phi}^{\mathbf{b}}$ and $\boldsymbol{\phi}^{\mathbf{g}}$ are given by

$$\begin{aligned} \boldsymbol{\phi}^{\mathbf{b}}_{,1} &= (\mathbf{C}_{21} + P_{12}\mathbf{C}_{22} + P_{13}\mathbf{C}_{23})\,\mathbf{a} f'(y) \\ \boldsymbol{\phi}^{\mathbf{g}}_{,1} &= (\mathbf{C}_{31} + P_{12}\mathbf{C}_{32} + P_{13}\mathbf{C}_{33})\,\mathbf{a} f'(y) \\ \boldsymbol{\phi}^{\mathbf{b}}_{,2} &= (P_{12}\mathbf{C}_{21} + P_{12}^2\mathbf{C}_{22} + P_{12}P_{13}\mathbf{C}_{23})\,\mathbf{a} f'(y) \\ \boldsymbol{\phi}^{\mathbf{g}}_{,3} &= (P_{13}\mathbf{C}_{31} + P_{12}P_{13}\mathbf{C}_{32} + P_{13}^2\mathbf{C}_{33})\,\mathbf{a} f'(y) \ . \end{aligned} \tag{4.175}$$

Substituting eqs. $(4.175)_1$ and $(4.175)_2$ into eqs. (4.159) and (4.160), respectively, results in

$$\mathbf{t}_2 = \boldsymbol{\phi}^{\mathbf{b}}_{,1} \quad , \quad \mathbf{t}_3 = \boldsymbol{\phi}^{\mathbf{g}}_{,1} \ . \tag{4.176}$$

Rearranging eq. (4.81), and multiplying by $f'(y)$, one may obtain the relation

$$\begin{aligned}&(\mathbf{C}_{11} + P_{12}\mathbf{C}_{12} + P_{13}\mathbf{C}_{13})\,\mathbf{a}f'(y) = \\ &-(P_{12}\mathbf{C}_{21} + P_{12}^2\mathbf{C}_{22} + P_{12}P_{13}\mathbf{C}_{23})\,\mathbf{a}f'(y) - (P_{13}\mathbf{C}_{31} + P_{13}P_{12}\mathbf{C}_{32} + P_{13}^2\mathbf{C}_{33})\,\mathbf{a}f'(y)\ .\end{aligned} \tag{4.177}$$

Noting eqs. (4.158), $(4.175)_3$, $(4.175)_4$ and (4.177),

$$\mathbf{t}_1 = -(\boldsymbol{\phi}^{\mathbf{b}}_{,2} + \boldsymbol{\phi}^{\mathbf{g}}_{,3})\ . \tag{4.178}$$

General solutions with three eigenvalue and eigenvector pairs for the stress function vectors may be written as

$$\boldsymbol{\phi}^{\mathbf{b}} = \sum_{\gamma=1}^{3}\left[\mathbf{b}^{(\gamma)}f_\gamma(y_\gamma) + \mathbf{b}^{(\gamma+3)}f_{\gamma+3}(y_{\gamma+3})\right] \tag{4.179}$$

$$\boldsymbol{\phi}^{\mathbf{g}} = \sum_{\gamma=1}^{3}\left[\mathbf{g}^{(\gamma)}f_\gamma(y_\gamma) + \mathbf{g}^{(\gamma+3)}f_{\gamma+3}(y_{\gamma+3})\right] \tag{4.180}$$

where

$$\mathbf{b}^{(\gamma)} = \left(\mathbf{C}_{21} + P_{12}\mathbf{C}_{22} + P_{13}^{(\gamma)}\mathbf{C}_{23}\right)\mathbf{a}^{(\gamma)} \tag{4.181}$$

$$\mathbf{g}^{(\gamma)} = \left(\mathbf{C}_{31} + P_{12}\mathbf{C}_{32} + P_{13}^{(\gamma)}\mathbf{C}_{33}\right)\mathbf{a}^{(\gamma)}\ . \tag{4.182}$$

It was assumed here that P_{12} has six identical eigenvalues. The general solutions in matrix form may be written as

$$\boldsymbol{\phi}^{\mathbf{b}} = \mathbf{B}[\mathbf{f}(y)] + \tilde{\mathbf{B}}[\tilde{\mathbf{f}}(y)] \tag{4.183}$$

$$\boldsymbol{\phi}^{\mathbf{g}} = \mathbf{G}[\mathbf{f}(y)] + \tilde{\mathbf{G}}[\tilde{\mathbf{f}}(y)] \tag{4.184}$$

where

$$\mathbf{B} = [\mathbf{b}^{(1)}, \mathbf{b}^{(2)}, \mathbf{b}^{(3)}],\ \tilde{\mathbf{B}} = [\mathbf{b}^{(4)}, \mathbf{b}^{(5)}, \mathbf{b}^{(6)}],\ \mathbf{G} = [\mathbf{g}^{(1)}, \mathbf{g}^{(2)}, \mathbf{g}^{(3)}]\ \tilde{\mathbf{G}} = [\mathbf{g}^{(4)}, \mathbf{g}^{(5)}, \mathbf{g}^{(6)}] \tag{4.185}$$

$[\mathbf{f}(y)]$ and $[\tilde{\mathbf{f}}(y)]$ are given in eqs. (4.148) and (4.149). Following Section 5.3 in Ting (1996), for the special case where

$$\tilde{\mathbf{B}} = \bar{\mathbf{B}}\ , \tag{4.186}$$

$$\tilde{\mathbf{G}} = \bar{\mathbf{G}}\ , \tag{4.187}$$

and eqs. (4.90) and (4.151) hold

$$\boldsymbol{\phi}^{\mathbf{b}} = 2\ \Re\left[\mathbf{B}\left\langle f(y_*)\right\rangle \mathbf{q}\right] \tag{4.188}$$

$$\boldsymbol{\phi}^{\mathbf{g}} = 2\ \Re\left[\mathbf{G}\left\langle f(y_*)\right\rangle \mathbf{q}\right] \tag{4.189}$$

where $\langle f(y_*)\rangle$ is a diagonal matrix given in eq. (4.153). Using eqs. (4.147), (4.183) and (4.184) with three eigenvalue and eigenvector pairs as found in Section 4.2, a general

expression for the displacement and stress function vectors may be written in matrix form as

$$\begin{pmatrix} \mathbf{u} \\ \boldsymbol{\phi}^{\mathbf{b}} \\ \boldsymbol{\phi}^{\mathbf{g}} \end{pmatrix} = \begin{bmatrix} \mathbf{A} & \tilde{\mathbf{A}} \\ \mathbf{B} & \tilde{\mathbf{B}} \\ \mathbf{G} & \tilde{\mathbf{G}} \end{bmatrix} \begin{pmatrix} [\mathbf{f}(y)] \\ [\tilde{\mathbf{f}}(y)] \end{pmatrix} . \tag{4.190}$$

It may be noted that eq. (4.190) is more general than eqs. (4.188) and (4.189).

Next, the orthogonality and closure relations, presented in Ting (1996, pp. 144-146), are developed. To develop these relations, one may present an eigenrelation for P_{13}. Using eq. (1.97) as

$$-\mathbf{N}_3^{-1}(\mathbf{N}_1 + P_{12}\mathbf{N}_2)\mathbf{d} = P_{13}\mathbf{d} \tag{4.191}$$

where $\mathbf{N}_1$, $\mathbf{N}_2$ and $\mathbf{N}_3$ are given in eqs. (1.98). However, the matrix $\mathbf{N}_3$ is singular so that is not possible to determine its inverse. On the other hand, to develop an eigenrelation for P_{12}, one may write eq. (1.97) as

$$-\mathbf{N}_2^{-1}(\mathbf{N}_1 + P_{13}\mathbf{N}_3)\mathbf{d} = P_{12}\mathbf{d} \tag{4.192}$$

The matrix $\mathbf{N}_2$ is also singular and cannot be inverted. Hence, the eigenrelation for P_{12} may not be developed. Thus, to develop the eigenrelations for P_{12} and P_{13}, another step is required.

Since eqs. (4.191) and (4.192) could not be used to determine the orthogonality and closure relations, a different approach is taken. These relations are developed separately for both the matrices $\mathbf{A}$ and $\mathbf{G}$ and then for $\mathbf{A}$ and $\mathbf{B}$. To this end, equation (1.98) is used to expand eq. (1.97) to obtain three equations. These equations are given as

$$\begin{aligned} (\mathbf{C}_{11} + P_{12}\mathbf{C}_{12})\mathbf{a} + P_{12}\mathbf{b} + P_{13}\mathbf{C}_{13}\mathbf{a} + P_{13}\mathbf{g} = \mathbf{0} \\ \mathbf{C}_{21}\mathbf{a} - \mathbf{b} + P_{12}\mathbf{C}_{22}\mathbf{a} + P_{13}\mathbf{C}_{23}\mathbf{a} = \mathbf{0} \\ \mathbf{C}_{31}\mathbf{a} - \mathbf{g} + P_{12}\mathbf{C}_{32}\mathbf{a} + P_{13}\mathbf{C}_{33}\mathbf{a} = \mathbf{0} \, . \end{aligned} \tag{4.193}$$

For the case where P_{12} has six identical constant values, eq. $(4.193)_2$ is substituted into eq. $(4.193)_1$ results as

$$\begin{aligned} [\mathbf{C}_{11} + P_{12}(\mathbf{C}_{12} + \mathbf{C}_{21}) + P_{12}^2\mathbf{C}_{22}]\mathbf{a} + P_{13}(\mathbf{C}_{13} + P_{12}\mathbf{C}_{23})\mathbf{a} + P_{13}\mathbf{g} = \mathbf{0} \\ (\mathbf{C}_{31} + P_{12}\mathbf{C}_{32})\mathbf{a} - \mathbf{g} + P_{13}\mathbf{C}_{33}\mathbf{a} = \mathbf{0} \end{aligned} \, . \tag{4.194}$$

Equations (4.194) may be rewritten as

$$(\mathbf{N}_1^* + P_{13}\mathbf{N}_3^*)\mathbf{d}^* = \mathbf{0} \, , \tag{4.195}$$

where,

$$\mathbf{N}_1^* = \begin{bmatrix} \mathbf{C}_{11} + P_{12}(\mathbf{C}_{12} + \mathbf{C}_{21}) + P_{12}^2\mathbf{C}_{22} & \mathbf{0} \\ \mathbf{C}_{31} + P_{12}\mathbf{C}_{32} & -\mathbf{I} \end{bmatrix} , \mathbf{N}_3^* = \begin{bmatrix} \mathbf{C}_{13} + P_{12}\mathbf{C}_{23} & \mathbf{I} \\ \mathbf{C}_{33} & \mathbf{0} \end{bmatrix} . \tag{4.196}$$

In eq. (4.195), the vector $\mathbf{d}^*_{6\times 1}$ is defined as

$$\mathbf{d}^* = \begin{bmatrix} \mathbf{a} \\ \\ \mathbf{g} \end{bmatrix} , \tag{4.197}$$

where $\mathbf{a}$ is the eigenvector related to P_{13} and $\mathbf{g}$ is given in eq. (4.173). Noting that $\mathbf{N}_3^{*-1}$ is given as

$$\mathbf{N}_3^{*-1} = \begin{bmatrix} \mathbf{0} & \mathbf{C}_{33}^{-1} \\ \\ \mathbf{I} & -(\mathbf{C}_{13} + P_{12}\mathbf{C}_{23})\mathbf{C}_{33}^{-1} \end{bmatrix} , \tag{4.198}$$

eq. (4.195) may be rewritten as a standard eigenrelation

$$\mathbf{N}\boldsymbol{\xi} = P_{13}\boldsymbol{\xi} \tag{4.199}$$

where

$$\mathbf{N} = -\mathbf{N}_3^{*-1}\mathbf{N}_1^* \quad , \quad \boldsymbol{\xi} = \begin{bmatrix} \mathbf{a} \\ \\ \mathbf{g} \end{bmatrix} . \tag{4.200}$$

Following equations (5.5-6) to (5.5-16) in Ting (1996, pp. 144-146), the orthogonality and closure relations are developed. Noting that $\mathbf{N}$ is not symmetric, $\boldsymbol{\xi}$ is a right eigenvector. The left eigenvector $\boldsymbol{\eta}$, is given as

$$\mathbf{N}^T\boldsymbol{\eta} = P_{13}\boldsymbol{\eta} \, . \tag{4.201}$$

Presenting a new 6×6 matrix as

$$\hat{\mathbf{I}} = \begin{bmatrix} \mathbf{0} & \mathbf{I} \\ \\ \mathbf{I} & \mathbf{0} \end{bmatrix} , \hat{\mathbf{I}} = \hat{\mathbf{I}}^T = \hat{\mathbf{I}}^{-1} , \tag{4.202}$$

it may be shown that

$$\hat{\mathbf{I}}\mathbf{N} = \mathbf{N}^T\hat{\mathbf{I}}. \tag{4.203}$$

Multiplying eq. (4.199) by $\hat{\mathbf{I}}$ results in

$$\hat{\mathbf{I}}\mathbf{N}\boldsymbol{\xi} = P_{13}\hat{\mathbf{I}}\boldsymbol{\xi} \tag{4.204}$$

and using eq. (4.203)

$$\mathbf{N}^T(\hat{\mathbf{I}}\boldsymbol{\xi}) = P_{13}(\hat{\mathbf{I}}\boldsymbol{\xi}). \tag{4.205}$$

Noting eqs. (4.201) and (4.205)

$$\boldsymbol{\eta} = \hat{\mathbf{I}}\boldsymbol{\xi} = \begin{bmatrix} \mathbf{g} \\ \\ \mathbf{a} \end{bmatrix} . \tag{4.206}$$

Thus, eq. (4.206) results in the left eigenvector as shown in eq. (4.201). The right and left eigenvectors for different eigenvalues $P_{13}^{(\gamma)}$, for $\gamma = 1, .., 6$, are orthogonal. The distinct

eigenvalues $\boldsymbol{\xi}$ and $\boldsymbol{\eta}$ are unique up to an arbitrary multiplier. For distinct eigenvalues, the eigenvectors are normalized by

$$\boldsymbol{\eta}_\alpha^T \cdot \boldsymbol{\xi}_\beta = \delta_{\alpha\beta} \text{ , for } \alpha, \beta = 1, .., 6 \tag{4.207}$$

where $\delta_{\alpha\beta}$ is the Kronecker delta. Using eqs. $(4.200)_2$, (4.206) and (4.207)

$$\mathbf{g}_\alpha^T \mathbf{a}_\beta + \mathbf{a}_\alpha^T \mathbf{g}_\beta = \delta_{\alpha\beta} \ . \tag{4.208}$$

For the case where eqs. (4.90) and (4.187) hold and noting eqs. (4.87) and $(4.185)_3$, eq. (4.208) may be rewritten as

$$\begin{bmatrix} \mathbf{G}^T & \mathbf{A}^T \\ \bar{\mathbf{G}}^T & \bar{\mathbf{A}}^T \end{bmatrix} \begin{bmatrix} \mathbf{A} & \bar{\mathbf{A}} \\ \mathbf{G} & \bar{\mathbf{G}} \end{bmatrix} = \begin{bmatrix} \mathbf{I} & \mathbf{0} \\ \mathbf{0} & \mathbf{I} \end{bmatrix} . \tag{4.209}$$

or

$$\begin{aligned} \mathbf{G}^T\mathbf{A} + \mathbf{A}^T\mathbf{G} = \mathbf{I} = \bar{\mathbf{G}}^T\bar{\mathbf{A}} + \bar{\mathbf{A}}^T\bar{\mathbf{G}} \\ \mathbf{G}^T\bar{\mathbf{A}} + \mathbf{A}^T\bar{\mathbf{G}} = \mathbf{0} = \bar{\mathbf{G}}^T\mathbf{A} + \bar{\mathbf{A}}^T\mathbf{G} \end{aligned} . \tag{4.210}$$

These are the orthogonality relations. It may be noted that the complex conjugate of eq. (4.208) was used. The matrix on the left side of eq. (4.209) is the inverse of the matrix on the right side, and hence their product commutes resulting in the closure relations

$$\begin{bmatrix} \mathbf{A} & \bar{\mathbf{A}} \\ \mathbf{G} & \bar{\mathbf{G}} \end{bmatrix} \begin{bmatrix} \mathbf{G}^T & \mathbf{A}^T \\ \bar{\mathbf{G}}^T & \bar{\mathbf{A}}^T \end{bmatrix} = \begin{bmatrix} \mathbf{I} & \mathbf{0} \\ \mathbf{0} & \mathbf{I} \end{bmatrix} . \tag{4.211}$$

or

$$\begin{aligned} \mathbf{A}\mathbf{G}^T + \bar{\mathbf{A}}\bar{\mathbf{G}}^T = \mathbf{I} = \mathbf{G}\mathbf{A}^T + \bar{\mathbf{G}}\bar{\mathbf{A}}^T \\ \mathbf{A}\mathbf{A}^T + \bar{\mathbf{A}}\bar{\mathbf{A}}^T = \mathbf{0} = \mathbf{G}\mathbf{G}^T + \bar{\mathbf{G}}\bar{\mathbf{G}}^T. \end{aligned} . \tag{4.212}$$

Noting eqs. $(4.212)_1$ and $(4.212)_2$, the real part of $\mathbf{A}\mathbf{G}^T$ is $\frac{1}{2}\mathbf{I}$ and $\mathbf{A}\mathbf{A}^T$ and $\mathbf{G}\mathbf{G}^T$ are purely imaginary, respectively. Hence, following Ting (1996), three real matrices may be defined as

$$\mathbf{S}_1 = i(2\mathbf{A}\mathbf{G}^T - \mathbf{I}) \ , \ \mathbf{H}_1 = 2i\mathbf{A}\mathbf{A}^T \ , \ \mathbf{L}_1 = -2i\mathbf{G}\mathbf{G}^T. \tag{4.213}$$

In Ting (1996), similar matrices were found to be very useful for final solutions of two-dimensional anisotropic elasticity problems. These matrices may be used to develop real solutions for three-dimensional anisotropic elasticity problems. This will not be pursued here.

Next, an explicit expression for $[\mathbf{f}(y)]$ from eq. (4.148) is found for the case where eqs. (4.90) and (4.187) hold. Equation (4.190) may be used as

$$\begin{pmatrix} \mathbf{u} \\ \boldsymbol{\phi}^{\mathbf{g}} \end{pmatrix} = \begin{bmatrix} \mathbf{A} & \bar{\mathbf{A}} \\ \mathbf{G} & \bar{\mathbf{G}} \end{bmatrix} \begin{pmatrix} [\mathbf{f}(y)] \\ [\bar{\mathbf{f}}(\bar{y})] \end{pmatrix} \tag{4.214}$$

where

$$[\bar{\mathbf{f}}(\bar{y})] = \begin{pmatrix} \bar{f}_1(\bar{y}_1) \\ \bar{f}_2(\bar{y}_2) \\ \bar{f}_3(\bar{y}_3) \end{pmatrix} . \tag{4.215}$$

Using eq. (4.209),

$$\begin{bmatrix} \mathbf{G}^T & \mathbf{A}^T \\ \bar{\mathbf{G}}^T & \bar{\mathbf{A}}^T \end{bmatrix} \begin{pmatrix} \mathbf{u} \\ \boldsymbol{\phi}^{\mathbf{g}} \end{pmatrix} = \begin{pmatrix} [\mathbf{f}(y)] \\ [\bar{\mathbf{f}}(\bar{y})] \end{pmatrix} \tag{4.216}$$

and

$$[\mathbf{f}(y)] = \mathbf{G}^T\mathbf{u} + \mathbf{A}^T\boldsymbol{\phi}^{\mathbf{g}}. \tag{4.217}$$

Next, the orthogonality and closure relations, presented in Ting (1996, pp. 144-146), are developed for the case where P_{13} has six identical constant values and P_{12} has six independent values. Substituting eq. $(4.193)_3$ into eq. $(4.193)_1$ leads to

$$\begin{gathered} [\mathbf{C}_{11} + P_{13}(\mathbf{C}_{13} + \mathbf{C}_{31}) + P_{13}^2\mathbf{C}_{33}]\mathbf{a} + P_{12}(\mathbf{C}_{12} + P_{13}\mathbf{C}_{32})\mathbf{a} + P_{12}\mathbf{b} = \mathbf{0} \\ (\mathbf{C}_{21} + P_{13}\mathbf{C}_{23})\mathbf{a} - \mathbf{b} + P_{12}\mathbf{C}_{22}\mathbf{a} = \mathbf{0} \end{gathered} \tag{4.218}$$

Equations (4.218) may be rewritten as

$$(\mathbf{N}_1^{**} + P_{12}\mathbf{N}_2^{*})\mathbf{d}^{**} = \mathbf{0} \, , \tag{4.219}$$

where,

$$\mathbf{N}_1^{**} = \begin{bmatrix} \mathbf{C}_{11} + P_{13}(\mathbf{C}_{13} + \mathbf{C}_{31}) + P_{13}^2\mathbf{C}_{33} & \mathbf{0} \\ \mathbf{C}_{21} + P_{13}\mathbf{C}_{23} & -\mathbf{I} \end{bmatrix} , \mathbf{N}_2^{*} = \begin{bmatrix} \mathbf{C}_{12} + P_{13}\mathbf{C}_{32} & \mathbf{I} \\ \mathbf{C}_{22} & \mathbf{0} \end{bmatrix} . \tag{4.220}$$

In eq. (4.219), the vector $\mathbf{d}_{6\times1}^{**}$ is defined as

$$\mathbf{d}^{**} = \begin{bmatrix} \mathbf{a} \\ \\ \mathbf{b} \end{bmatrix} , \tag{4.221}$$

where $\mathbf{a}$ is the eigenvector related to P_{12} and $\mathbf{b}$ is given in eq. (4.172). Noting that $\mathbf{N}_2^{*-1}$ is given as

$$\mathbf{N}_2^{*-1} = \begin{bmatrix} \mathbf{0} & \mathbf{C}_{22}^{-1} \\ \\ \mathbf{I} & -(\mathbf{C}_{12} + P_{13}\mathbf{C}_{32})\mathbf{C}_{22}^{-1} \end{bmatrix} , \tag{4.222}$$

eq. (4.219) may be rewritten as a standard eigenrelation

$$\mathbf{N}\boldsymbol{\xi} = P_{12}\boldsymbol{\xi} \tag{4.223}$$

where

$$\mathbf{N} = -\mathbf{N}_2^{*-1}\mathbf{N}_1^{**} \quad , \quad \boldsymbol{\xi} = \begin{bmatrix} \mathbf{a} \\ \\ \mathbf{b} \end{bmatrix} . \tag{4.224}$$

Following equations (4.201) to (4.208), for the case where eqs. (4.90) and (4.186) hold and noting eqs. (4.87) and $(4.185)_1$,

$$\begin{bmatrix} \mathbf{B}^T & \mathbf{A}^T \\ \bar{\mathbf{B}}^T & \bar{\mathbf{A}}^T \end{bmatrix} \begin{bmatrix} \mathbf{A} & \bar{\mathbf{A}} \\ \mathbf{B} & \bar{\mathbf{B}} \end{bmatrix} = \begin{bmatrix} \mathbf{I} & \mathbf{0} \\ \mathbf{0} & \mathbf{I} \end{bmatrix} . \tag{4.225}$$

or

$$\begin{aligned} \mathbf{B}^T\mathbf{A} + \mathbf{A}^T\mathbf{B} = \mathbf{I} = \bar{\mathbf{B}}^T\bar{\mathbf{A}} + \bar{\mathbf{A}}^T\bar{\mathbf{B}} \\ \mathbf{B}^T\bar{\mathbf{A}} + \mathbf{A}^T\bar{\mathbf{B}} = \mathbf{0} = \bar{\mathbf{B}}^T\mathbf{A} + \bar{\mathbf{A}}^T\mathbf{B} \end{aligned} . \tag{4.226}$$

These are the orthogonality relations. The matrix on the left side of eq. (4.225) is the inverse of the matrix on the right side, and hence their product commutes resulting in the closure relations

$$\begin{bmatrix} \mathbf{A} & \bar{\mathbf{A}} \\ \mathbf{B} & \bar{\mathbf{B}} \end{bmatrix} \begin{bmatrix} \mathbf{B}^T & \mathbf{A}^T \\ \bar{\mathbf{B}}^T & \bar{\mathbf{A}}^T \end{bmatrix} = \begin{bmatrix} \mathbf{I} & \mathbf{0} \\ \mathbf{0} & \mathbf{I} \end{bmatrix} . \tag{4.227}$$

or

$$\begin{aligned} \mathbf{A}\mathbf{B}^T + \bar{\mathbf{A}}\bar{\mathbf{B}}^T = \mathbf{I} = \mathbf{B}\mathbf{A}^T + \bar{\mathbf{B}}\bar{\mathbf{A}}^T \\ \mathbf{A}\mathbf{A}^T + \bar{\mathbf{A}}\bar{\mathbf{A}}^T = \mathbf{0} = \mathbf{B}\mathbf{B}^T + \bar{\mathbf{B}}\bar{\mathbf{B}}^T. \end{aligned} . \tag{4.228}$$

Noting eqs. $(4.228)_1$ and $(4.228)_2$, the real part of $\mathbf{A}\mathbf{B}^T$ is $\frac{1}{2}\mathbf{I}$ and $\mathbf{A}\mathbf{A}^T$ and $\mathbf{B}\mathbf{B}^T$ are purely imaginary, respectively. Hence, following Ting (1996), three real matrices may be defined as

$$\mathbf{S}_2 = i(2\mathbf{A}\mathbf{B}^T - \mathbf{I}) \ , \ \mathbf{H}_2 = 2i\mathbf{A}\mathbf{A}^T \ , \ \mathbf{L}_2 = -2i\mathbf{B}\mathbf{B}^T. \tag{4.229}$$

An explicit expression for $[\mathbf{f}(y)]$ from eq. (4.148) is found for the case where eqs. (4.90) and (4.186) hold. Equation (4.190) may be used as

$$\begin{pmatrix} \mathbf{u} \\ \boldsymbol{\phi}^{\mathbf{b}} \end{pmatrix} = \begin{bmatrix} \mathbf{A} & \bar{\mathbf{A}} \\ \mathbf{B} & \bar{\mathbf{B}} \end{bmatrix} \begin{pmatrix} [\mathbf{f}(y)] \\ [\bar{\mathbf{f}}(\bar{y})] \end{pmatrix} . \tag{4.230}$$

Using eq. (4.225),

$$\begin{bmatrix} \mathbf{B}^T & \mathbf{A}^T \\ \bar{\mathbf{B}}^T & \bar{\mathbf{A}}^T \end{bmatrix} \begin{pmatrix} \mathbf{u} \\ \boldsymbol{\phi}^{\mathbf{b}} \end{pmatrix} = \begin{pmatrix} [\mathbf{f}(y)] \\ [\bar{\mathbf{f}}(\bar{y})] \end{pmatrix} \tag{4.231}$$

and

$$[\mathbf{f}(y)] = \mathbf{B}^T\mathbf{u} + \mathbf{A}^T\boldsymbol{\phi}^{\mathbf{b}}. \tag{4.232}$$

4.4 Analytical and numerical results of the three-dimensional Clifford formalisms

In this section, solutions for four different problems are presented. A solution for a pure shear problem using a $0°/90°$ weave, is presented in Section 4.4.1. Recall that this material

is tetragonal and described by six independent mechanical properties. In Section 4.4.2, a general solution for a uniform stress field is developed for all materials where P_{12} is a real constant. In Section 4.4.3, solutions for mixed problems of tension and shear stresses and tension-compression stresses are presented using the general solution. In this section, a cubic material is used which is described by three independent mechanical properties. A solution for a uniform tension problem is presented in Section 4.4.4, using the same material as in Section 4.4.1.

4.4.1 A solution for a pure shear problem

In this section, a 0°/90° weave is used. The mechanical properties are taken from Table S8 of Mega and Banks-Sills (2019), and are given in Table 4.2. For the assumption that $P_{12} = 1$, the eigenvalues are presented in eq. (4.66); the eigenvectors are presented in eqs. (4.117) and eq. (4.90) holds. In order to obtain the displacement and stress functions in eq. (4.190), the arbitrary functions $f_\gamma(y_\gamma)$ require definition. From eq. (4.145)

$$y_\gamma = x_1 + x_2 + P_{13}^{(\gamma)} x_3. \tag{4.233}$$

Assuming that

$$f_\gamma(y_\gamma) = 0.0001 y_\gamma \tag{4.234}$$

then

$$f_\gamma(y) = 0.0001\big(x_1 + x_2 + P_{13}^{(\gamma)} x_3\big) \tag{4.235}$$

and

$$f_{\gamma+3}(y) = 0.0001\big(x_1 + x_2 + \bar{P}_{13}^{(\gamma)} x_3\big). \tag{4.236}$$

Note that $f_\gamma(y)$ and $f_{\gamma+3}(y)$ have units of length, namely mm; and value 0.0001 was chosen to make the final units realistic. Thus,

$$f_{\gamma+3}(y) = f_\gamma(\bar{y}). \tag{4.237}$$

Substituting eqs. (4.235), (4.236) and the eigenvectors from eqs. (4.117) and (4.90) into eq. (4.190) leads to

$$\mathbf{u} = \begin{bmatrix} 2.5968 \cdot 10^{-2}\, x_3 \\ 1.2380 \cdot 10^{-2}\, x_3 \\ 0.0600 \cdot 10^{-2}(x_1 + x_2) \end{bmatrix} \tag{4.238}$$

where $\mathbf{u}$ and x_i are measured in mm. The stress functions are

$$\boldsymbol{\phi}^{\mathbf{b}} = \begin{bmatrix} 84.3648\, x_3 \\ 141.05574\, x_3 \\ 28.5545(x_1 + x_2) \end{bmatrix} \tag{4.239}$$

and

$$\boldsymbol{\phi}^{\mathbf{g}} = \begin{bmatrix} 85.0186(x_1 + x_2) \\ 28.5545(x_1 + x_2) \\ -113.5731x_3 \end{bmatrix} . \tag{4.240}$$

It may be noted that $\boldsymbol{\phi}^{\mathbf{b}}$ and $\boldsymbol{\phi}^{\mathbf{g}}$ have units of MPa·mm. The stiffness components were measured in MPa. Using eqs. (4.176) and (4.178),

$$\mathbf{t}_1 = \begin{pmatrix} 0 \\ 0 \\ 85.0186 \end{pmatrix}, \mathbf{t}_2 = \begin{pmatrix} 0 \\ 0 \\ 28.5545 \end{pmatrix}, \mathbf{t}_3 = \begin{pmatrix} 85.0186 \\ 28.5545 \\ 0 \end{pmatrix} \tag{4.241}$$

Using eq. (4.157), the stress vector is found as

$$\sigma = \begin{bmatrix} 0 \\ 0 \\ 0 \\ 28.5545 \\ 85.0186 \\ 0 \end{bmatrix} \text{ MPa} \tag{4.242}$$

Equation. (4.168) leads to the same stress vector. Note that as expected $\mathbf{u}$ and σ are real and a pure shear problem is obtained.

Clearly, eq. (4.242) satisfies the equilibrium equations. The strain components may be calculated from

$$\varepsilon_\alpha = S_{\alpha\beta}\sigma_\beta \tag{4.243}$$

where $\alpha, \beta = 1, ..., 6$ and $S_{\alpha\beta}$ is given in eq. (4.63) with Table 4.2. Use of eq. (4.243) leads to the values of

$$\begin{pmatrix} \varepsilon_1 \\ \varepsilon_2 \\ \varepsilon_3 \\ \varepsilon_4 \\ \varepsilon_5 \\ \varepsilon_6 \end{pmatrix} = \begin{pmatrix} 0 \\ 0 \\ 0 \\ 1.2979 \cdot 10^{-2} \\ 2.6568 \cdot 10^{-2} \\ 0 \end{pmatrix} . \tag{4.244}$$

Note that $\varepsilon_1 = \varepsilon_{11}$, $\varepsilon_2 = \varepsilon_{22}$, $\varepsilon_3 = \varepsilon_{33}$, $\varepsilon_4 = 2\varepsilon_{23}$, $\varepsilon_5 = 2\varepsilon_{13}$ and $\varepsilon_6 = 2\varepsilon_{12}$. Using eq. (4.238) in the strain-displacement equations in eq. (4.142), eq. (4.244) is confirmed. A finite element model was also used to validate the solution. The displacement components in eq. (4.238) were applied to the outer boundaries of a cube of $100 \times 100 \times 100$ mm^3.

The cube was meshed with 1000 brick elements $10 \times 10 \times 10$ mm^3. The displacement and stress fields obtained at each point within the body are given by eqs. (4.238) and (4.242), respectively.

In Liu and Hong (2015), it was suggested to use $P_{12} = const \cdot e$ where *const* is a real constant that is chosen by the boundary conditions of the problem. For the assumption that $P_{12} = e$, the eigenvalues are the same as for $P_{12} = 1$; the eigenvectors are presented in eqs. (4.119) and (4.90). By repeating the same process as for $P_{12} = 1$, where

$$f_\gamma(y) = 0.0001\big(x_1 + ex_2 + P_{13}^{(\gamma)} x_3\big) \tag{4.245}$$

and

$$f_{\gamma+3}(y) = 0.0001\big(x_1 + ex_2 + \bar{P}_{13}^{(\gamma)} x_3\big) \tag{4.246}$$

the displacement and stress vectors are given as

$$\mathbf{u} = \begin{bmatrix} 2.5968 \cdot 10^{-2}\, x_3 \\ 1.2380 \cdot 10^{-2}\, x_3 \\ 0.0600 \cdot 10^{-2}(x_1 + x_2 e) \end{bmatrix} \tag{4.247}$$

$$\sigma = \begin{bmatrix} 0 \\ 0 \\ 0 \\ (27.2344 + 0.1320e) \\ 85.0186 \\ 0 \end{bmatrix} \text{ MPa} \tag{4.248}$$

The displacement and stress vectors are not real. Thus, the assumption that $P_{12} = e$ is not valid.

For the assumption that $P_{12} = i$, the eigenvalues are given in eqs. (4.70) and (4.71); the eigenvectors are presented in eqs. (4.121) and (4.122). By repeating the same process as for $P_{12} = e$, the displacement and stress vectors are given as

$$\mathbf{u} = \begin{bmatrix} 3.0063 \cdot 10^{-2}\, x_3 \\ 0.7229 \cdot 10^{-2}\, x_3 \\ 0.0600 \cdot 10^{-4}(x_1 + x_2 i) \end{bmatrix} \tag{4.249}$$

$$\sigma = \begin{bmatrix} 0 \\ 0 \\ 0 \\ 17.2240i \\ 98.1233 \\ 0 \end{bmatrix} \text{ MPa} \tag{4.250}$$

The displacement and stress vectors are not real. Thus, the assumption that $P_{12} = i$ is also not valid.

4.4.2 A general solution for a uniform stress field

In Section 4.4.1, a judicious choice of $f(y)$ in eq. (4.234) allowed determination of a particular uniform stress field. In this section, a general solution for a uniform stress field is developed. The displacement field and stress functions may be written as

$$\begin{aligned} \mathbf{u} &= x_1\boldsymbol{\varepsilon}_1 + x_2\boldsymbol{\varepsilon}_2 + x_3\boldsymbol{\varepsilon}_3 \\ \boldsymbol{\phi}^{\mathbf{b}} &= x_1\mathbf{t}_2 + x_2\mathbf{t}_1^b + x_3\mathbf{t}^* \\ \boldsymbol{\phi}^{\mathbf{g}} &= x_1\mathbf{t}_3 + x_2\mathbf{t}^{**} + x_3\mathbf{t}_1^g \end{aligned} \tag{4.251}$$

where

$$\boldsymbol{\varepsilon}_1 = \begin{pmatrix} \varepsilon_{11} \\ 2\varepsilon_{12} \\ 2\varepsilon_{13} \end{pmatrix} \ , \ \boldsymbol{\varepsilon}_2 = \begin{pmatrix} 0 \\ \varepsilon_{22} \\ \varepsilon_{23}^{(1)} \end{pmatrix} \ , \ \boldsymbol{\varepsilon}_3 = \begin{pmatrix} 0 \\ \varepsilon_{23}^{(2)} \\ \varepsilon_{33} \end{pmatrix} \ , \tag{4.252}$$

$$2\varepsilon_{23} = \varepsilon_{23}^{(1)} + \varepsilon_{23}^{(2)} \tag{4.253}$$

and

$$\mathbf{t}_1 = -(\mathbf{t}_1^b + \mathbf{t}_1^g) \ . \tag{4.254}$$

The vectors $\mathbf{t}_1$, $\mathbf{t}_2$ and $\mathbf{t}_3$ are defined in eqs. (4.157), and given explicitly as

$$\mathbf{t}_1 = \begin{pmatrix} \sigma_{11} \\ \sigma_{21} \\ \sigma_{31} \end{pmatrix} \ , \ \mathbf{t}_2 = \begin{pmatrix} \sigma_{12} \\ \sigma_{22} \\ \sigma_{32} \end{pmatrix} \ , \ \mathbf{t}_1 = \begin{pmatrix} \sigma_{13} \\ \sigma_{23} \\ \sigma_{33} \end{pmatrix} \tag{4.255}$$

and $\mathbf{t}^*$ and $\mathbf{t}^{**}$ are arbitrary vectors which exist, are not necessary for the solution and are not found. Equations $(4.251)_1$, (4.252) and (4.253) satisfy the strain-displacement equations given in eq. (4.142). Equations $(4.251)_2$, $(4.251)_3$ and (4.254), satisfy eqs. (4.176) and (4.178), the relations between the stress vectors and the stress functions. For the

cases where eqs. (4.90), (4.186), (4.187) and (4.151) hold, the arbitrary functions $f_\gamma(y_\gamma)$ is assumed to have the form

$$f_\gamma(y_\gamma) = y_\gamma q_\gamma \quad f_{\gamma+3}(\bar{y}_\gamma) = \bar{y}_\gamma \bar{q}_\gamma \tag{4.256}$$

for $\gamma = 1, 2, 3$ without summation, and q_γ are arbitrary complex constants. Recalling from eq. (4.174) that

$$\frac{\partial f(y_\gamma)}{\partial x_1} = f'(y_\gamma) \tag{4.257}$$

for $P_{11} = 1$ and noting eqs. $(4.251)_1$, $(4.251)_3$ and (4.256), the derivative of eq. (4.217) with respect to x_1 is given by

$$\mathbf{q} = \mathbf{G}^T \boldsymbol{\varepsilon}_1 + \mathbf{A}^T \mathbf{t}_3 \tag{4.258}$$

where

$$\mathbf{q} = \begin{pmatrix} q_1 \\ q_2 \\ q_3 \end{pmatrix} . \tag{4.259}$$

For the case where P_{13} has six constant values and P_{12} has six independent values and noting eqs. $(4.251)_1$, $(4.251)_3$ and (4.256), the derivative of eq. (4.232) with respect to x_1 is given by

$$\mathbf{q} = \mathbf{B}^T \boldsymbol{\varepsilon}_1 + \mathbf{A}^T \mathbf{t}_2 . \tag{4.260}$$

These solutions may be used to solve the problem of an elliptic hole or rigid inclusion subjected to a uniform loading at infinity for a three-dimensional body as presented in Ting (1996, pp. 380-386), for the two-dimensional plane deformation case. This will not be pursued here. In Sections 4.4.3 and 4.4.4, the solution presented in this section will be used for solving different uniform stress problems.

4.4.3 Combined tensile stress problem for $P_{12} = 1$

In this section, a combined tensile stress problem is solved for a cubic material and $P_{12} = 1$. The mechanical properties are given in Table 4.1. For the assumption that $P_{12} = 1$, the eigenvalues are presented in eqs. (4.39) and (4.40); the eigenvectors are presented in eqs. (4.89) and (4.90). In order to use the uniform stress solution from Section 4.4.2, the matrices $\mathbf{A}$ and $\mathbf{G}$ should be normalized to satisfy eq. $(4.210)_1$. Recall that the columns of $\mathbf{A}$ are eigenvectors which are calculated using eq. (4.83); the columns of $\mathbf{G}$ are related to $\mathbf{A}$ through eq. (4.182) and are given as

$$\mathbf{G} = \begin{bmatrix} (9.8780 - 7.6960i) \cdot 10^4 & (9.8780 + 7.6960i) \cdot 10^4 & -9.0934i \cdot 10^4 \\ (9.8780 - 7.6960i) \cdot 10^4 & (9.8780 + 7.6960i) \cdot 10^4 & 9.0934i \cdot 10^4 \\ (3.9748 + 16.5398i) \cdot 10^4 & (-3.9748 + 16.5398i) \cdot 10^4 & 0 \end{bmatrix} . \tag{4.261}$$

The matrices $\mathbf{A}$ and $\mathbf{G}$ may be redefined as

$$\mathbf{A} = \left[k_1\mathbf{a}^{(1)}\ k_2\mathbf{a}^{(2)}\ k_3\mathbf{a}^{(3)}\right]\ ,\ \mathbf{G} = \left[k_1\mathbf{g}^{(1)}\ k_2\mathbf{g}^{(2)}\ k_3\mathbf{g}^{(3)}\right] \tag{4.262}$$

where k_i for $i = 1, 2, 3$ are normalized factors determined using eq. $(4.210)_1$. The normalization factors are found as

$$\begin{aligned} k_1 &= (6.7103 - 13.9319i) \cdot 10^{-4} \\ k_2 &= (13.9319 - 6.7103i) \cdot 10^{-4} \\ k_3 &= 11.7244(1 - i) \cdot 10^{-4}\ . \end{aligned} \tag{4.263}$$

Using eqs. (4.89), and (4.261) to (4.263) to satisfy eq. $(4.210)_1$, normalized matrices $\mathbf{A}$ and $\mathbf{G}$ are found as

$$\mathbf{A} = \begin{bmatrix} (-9.4630 + 4.5578i) \cdot 10^{-4} & (4.5578 - 9.4630i) \cdot 10^{-4} & -11.7244(1 - i) \cdot 10^{-4} \\ (-9.4630 + 4.5578i) \cdot 10^{-4} & (4.5578 - 9.4630i) \cdot 10^{-4} & 11.7244(1 - i) \cdot 10^{-4} \\ (6.7103 - 13.9319i) \cdot 10^{-4} & (13.9319 - 6.7103i) \cdot 10^{-4} & 0 \end{bmatrix} \tag{4.264}$$

$$\mathbf{G} = \begin{bmatrix} -40.9359 - 189.2613i & 189.2613 + 40.9359i & -106.6153(1 + i) \\ -40.9359 - 189.2613i & 189.2613 + 40.9359i & 106.6153(1 + i) \\ 257.1041 + 55.6099i & 257.1041 + 55.6099i & 0 \end{bmatrix}\ . \tag{4.265}$$

Next, the general uniform solution is used for the case where

$$\mathbf{t}_3 = \begin{pmatrix} 0 \\ 0 \\ 100 \end{pmatrix}\ ,\ \boldsymbol{\varepsilon}_1 = \begin{pmatrix} 0 \\ 0 \\ 0 \end{pmatrix}\ . \tag{4.266}$$

Substituting eq. (4.266) into eq. (4.258) leads to

$$\mathbf{q} = \begin{pmatrix} 0.0671\text{-}0.1393\text{i} \\ 0.1393\text{-}0.0671\text{i} \\ 0 \end{pmatrix}\ . \tag{4.267}$$

Substituting eq. (4.267) into eq. (4.256) and using eq. (4.190) leads to

$$\mathbf{u} = \begin{bmatrix} 0 \\ 0 \\ 0.0640 \cdot 10^{-2} x_3 \end{bmatrix} \tag{4.268}$$

$$\boldsymbol{\phi}^{\mathbf{b}} = \begin{bmatrix} 0 \\ 33.3333(x_1 + x_2) \\ -33.3333\, x_3 \end{bmatrix} \tag{4.269}$$

and

$$\boldsymbol{\phi}^{\mathbf{g}} = \begin{bmatrix} -33.3333\, x_3 \\ -33.3333\, x_3 \\ 100.0000(x_1 + x_2) \end{bmatrix} . \tag{4.270}$$

where $\mathbf{u}$ and x_3 are measured in mm and $\boldsymbol{\phi}^{\mathbf{b}}$ and $\boldsymbol{\phi}^{\mathbf{g}}$ have units of MPa·mm. Using eqs. (4.176) and (4.178),

$$\mathbf{t}_1 = \begin{pmatrix} 33.3333 \\ 0 \\ 0 \end{pmatrix}, \mathbf{t}_2 = \begin{pmatrix} 0 \\ 33.3333 \\ 0 \end{pmatrix}, \mathbf{t}_3 = \begin{pmatrix} 0 \\ 0 \\ 100 \end{pmatrix} . \tag{4.271}$$

Using eq. (4.255), the stress vector is found as

$$\sigma = \begin{bmatrix} 33.3333 \\ 33.3333 \\ 100.0000 \\ 0 \\ 0 \\ 0 \end{bmatrix} \text{ MPa} \tag{4.272}$$

Use of eq. (4.243) leads to the values of

$$\begin{pmatrix} \varepsilon_1 \\ \varepsilon_2 \\ \varepsilon_3 \\ \varepsilon_4 \\ \varepsilon_5 \\ \varepsilon_6 \end{pmatrix} = \begin{pmatrix} 0 \\ 0 \\ 0.0640 \cdot 10^{-2} \\ 0 \\ 0 \\ 0 \end{pmatrix} . \tag{4.273}$$

Note that eq. (4.266) is satisfied. The strain-displacement relations in eq. (4.142) are satisfied by differentiation of eq. (4.268) appropriately; and eq. (4.273) is achieved. A finite element model was also used to validate the solution. The displacement components in eq. (4.268) were applied to the outer boundaries of a cube of $100 \times 100 \times 100$ mm^3. The cube was meshed as explained in Section 4.4.1. The displacement and stress fields obtained at each point within the body are given by eqs. (4.268) and (4.272), respectively.

4.4.4 Combined tensile stress problem for $P_{13} = 1$

In this section, a combined tensile stress problem is solved for a cubic material and $P_{13} = 1$. The mechanical properties are given in Table 4.1. For the assumption that $P_{13} = 1$, the

eigenvalues are presented in eqs. (4.50) and (4.51); the eigenvectors are presented in eqs. (4.104) and (4.90). In order to use the uniform stress solution from Section 4.4.2, the matrices $\mathbf{A}$ and $\mathbf{B}$ should be normalized to satisfy eq. $(4.226)_1$. Recall that the columns of $\mathbf{A}$ are eigenvectors which are calculated using eq. (4.83). To obtain the columns of $\mathbf{B}$, eq. (4.181) is rewritten as

$$\mathbf{b}^{(\gamma)} = \left(\mathbf{C}_{21} + P_{12}^{(\gamma)}\mathbf{C}_{22} + P_{13}\mathbf{C}_{23}\right)\mathbf{a}^{(\gamma)} \tag{4.274}$$

and $\mathbf{B}$ is found as

$$\mathbf{B} = \begin{bmatrix} (-4.3078 + 17.9253i)\cdot 10^4 & (4.3078 + 17.9253i)\cdot 10^4 & -9.0934i\cdot 10^4 \\ (-19.7559 - 15.3920i)\cdot 10^4 & (-19.7559 + 15.3920i)\cdot 10^4 & 0 \\ (-4.3078 + 17.9253i)\cdot 10^4 & (4.3078 + 17.9253i)\cdot 10^4 & 9.0934i\cdot 10^4 \end{bmatrix}. \tag{4.275}$$

The matrices $\mathbf{A}$ and $\mathbf{B}$ may be redefined as

$$\mathbf{A} = \left[k_1\mathbf{a}^{(1)}\ k_2\mathbf{a}^{(2)}\ k_3\mathbf{a}^{(3)}\right]\ ,\ \mathbf{B} = \left[k_1\mathbf{b}^{(1)}\ k_2\mathbf{b}^{(2)}\ k_3\mathbf{b}^{(3)}\right] \tag{4.276}$$

where k_i for $i = 1, 2, 3$ are normalized factors determined using eq. $(4.226)_1$. The normalization factors are found as

$$\begin{aligned} k_1 &= (9.4630 - 4.5578i)\cdot 10^{-4} \\ k_2 &= (4.5578 - 9.4630i)\cdot 10^{-4} \\ k_3 &= 11.7244(1 - i)\cdot 10^{-4}\ . \end{aligned} \tag{4.277}$$

Using eqs. (4.104), and (4.275) to (4.277) to satisfy eq. $(4.226)_1$, normalized matrices $\mathbf{A}$ and $\mathbf{B}$ are found as

$$\mathbf{A} = \begin{bmatrix} (9.4630 - 4.5578i)\cdot 10^{-4} & (4.5578 - 9.4630i)\cdot 10^{-4} & -11.7244(1 - i)\cdot 10^{-4} \\ (-6.7103 + 13.9319i)\cdot 10^{-4} & (13.9319 - 6.7103i)\cdot 10^{-4} & 0 \\ (9.4630 - 4.5578i)\cdot 10^{-4} & (4.5578 - 9.4630i)\cdot 10^{-4} & 11.7244(1 - i)\cdot 10^{-4} \end{bmatrix} \tag{4.278}$$

$$\mathbf{B} = \begin{bmatrix} 40.9359 + 189.2613i & 189.2613 + 40.9359i & -106.6153(1 + i) \\ -257.1041 - 55.6099i & 257.1041 + 55.6099i & 0 \\ 40.9359 + 189.2613i & 189.2613 + 40.9359i & 106.6153(1 + i) \end{bmatrix}. \tag{4.279}$$

Next, the general uniform solution is used for the case where

$$\mathbf{t}_2 = \begin{pmatrix} 0 \\ 100 \\ 0 \end{pmatrix}\ ,\ \boldsymbol{\varepsilon}_1 = \begin{pmatrix} 0 \\ 0 \\ 0 \end{pmatrix}\ ; \tag{4.280}$$

$\mathbf{t}_2$ and $\boldsymbol{\varepsilon}_1$ are defined in eqs. $(4.255)_2$ and $(4.252)_1$, respectively. Substituting eq. (4.280) into eq. (4.260) leads to

$$\mathbf{q} = \begin{pmatrix} \text{-0.0671+0.1393i} \\ \text{0.1393-0.0671i} \\ 0 \end{pmatrix} . \tag{4.281}$$

Substituting eq. (4.281) into eq. (4.256) and using eq. (4.190) leads to

$$\mathbf{u} = \begin{bmatrix} 0 \\ 0.0640 \cdot 10^{-2} x_2 \\ 0 \end{bmatrix} \tag{4.282}$$

$$\boldsymbol{\phi}^{\mathbf{b}} = \begin{bmatrix} -33.3333\, x_2 \\ 100(x_1 + x_3) \\ -33.3333\, x_2 \end{bmatrix} \tag{4.283}$$

and

$$\boldsymbol{\phi}^{\mathbf{g}} = \begin{bmatrix} 0 \\ -33.3333\, x_2 \\ 33.3333(x_1 + x_3) \end{bmatrix} \tag{4.284}$$

where $\mathbf{u}$ and x_i for $i = 1, 2, 3$ are measured in mm and $\boldsymbol{\phi}^{\mathbf{b}}$ and $\boldsymbol{\phi}^{\mathbf{g}}$ have units of MPa·mm. Using eqs. (4.176) and (4.178),

$$\mathbf{t}_1 = \begin{pmatrix} 33.3333 \\ 0 \\ 0 \end{pmatrix}, \mathbf{t}_2 = \begin{pmatrix} 0 \\ 100.000 \\ 0 \end{pmatrix}, \mathbf{t}_3 = \begin{pmatrix} 0 \\ 0 \\ 33.3333 \end{pmatrix} . \tag{4.285}$$

Using eq. (4.255), the stress vector is found as

$$\sigma = \begin{bmatrix} 33.3333 \\ 100.0000 \\ 33.3333 \\ 0 \\ 0 \\ 0 \end{bmatrix} \text{ MPa} \tag{4.286}$$

Use of eq. (4.243) leads to the strain values as

$$\begin{pmatrix} \varepsilon_1 \\ \varepsilon_2 \\ \varepsilon_3 \\ \varepsilon_4 \\ \varepsilon_5 \\ \varepsilon_6 \end{pmatrix} = \begin{pmatrix} 0 \\ 0.0640 \cdot 10^{-2} \\ 0 \\ 0 \\ 0 \\ 0 \end{pmatrix} . \tag{4.287}$$

Note that eq. (4.280) is satisfied. The strain-displacement relations in eq. (4.142) are satisfied by differentiation of eq. (4.282) appropriately; and eq. (4.287) is achieved. A finite element model was also used to validate the solution. The displacement components in eq. (4.282) were applied to the outer boundaries of a cube of $100 \times 100 \times 100$ mm^3. The cube was meshed as explained in Section 4.4.1. The displacement and stress fields obtained at each point within the body are given by eqs. (4.282) and (4.286), respectively.

Chapter 5

Summary and conclusions

This investigation focused on the Virtual Crack Closure Technique (VCCT) and Clifford algebra. The two-dimensional VCCT method was extended for an interface crack between two transversely isotropic materials. It was found in two dimensions that quarter-point (QP) elements are inappropriate for the VCCT. In addition, the VCCT was extended to three-dimensional problems. A three-dimensional Clifford formalism was presented and a general solution for a uniform three-dimensional stress field was found.

In Chapter 1, a literature overview on the VCCT and the Clifford algebra was presented. The basic equations related to a crack in a linear elastic, homogeneous and isotropic material and an interface crack between two different linear elastic, homogeneous and isotropic materials are discussed in Sections 1.1 and 1.2, respectively. In Section 1.3, an overview of the J and M-integrals is presented. The Stroh (1958) and Lekhnitskii (1950, 1963) formalisms are presented in Section 1.4. In Section 1.5, a Clifford algebra is presented. The VCCT, based on the Irwin (1958) crack closure integral, is presented in Section 1.6. In Section 1.7, the research goals are discussed.

In Chapter 2, the VCCT for two-dimensional problems is considered. In Section 2.1, the appropriate element type for obtaining accurate values of the energy release rates and stress intensity factors with VCCT was considered. For this method, the work done in closing the virtual crack extension (VCE) requires corresponding nodes to be opposite each other in the calculation, as shown for QP-elements in Fig. 1.16. It was shown that each pair of nodes m, for the nodal point forces, and m', for the nodal point crack face displacement jumps, should be located at the same relative distance from the origin of the coordinate systems x_1, x_2 and x_1', x_2' in Fig. 2.2c, respectively. For QP-elements, the quarter-point nodes are not located at the proper distances, as shown in Figs. 1.16 and 2.2a. To use a QP-element ahead of the crack tip, a new element, called an inverse quarter-point (IQP) element, was suggested. For this element, as shown in Fig. 2.2c, the node along the element edge on the crack face is moved to the three-quarter distance from the crack tip instead of the quarter-point distance as in a QP-element. In this way, the proper position is obtained, as shown in Fig. 2.2c, although the singular behavior is

incorrect. For regular eight-noded elements, each pair of nodes is located in the proper position for calculating the work done in closing the VCE or the energy release rates.

Five different approaches were presented for solution of a crack in a two-dimensional isotropic and homogeneous material. The first approach used regular eight-noded elements. Approaches 2a, 2b and 3 used a pair of QP-elements. Approach 2a used QP-elements with global nodal point forces taken from elements (1), (2) and (3) in Fig. 1.14 for the calculation; approach 2b used nodal point forces only from elements (1) and (2). The third approach, presented in Nairn (2011), used nodal edge forces. Approach 4 used one IQP-element before the crack tip and one QP-element ahead of the crack tip as shown in Fig. 2.2c. Three problems were solved in Section 2.2 using the different approaches. The problems included a center cracked tension (CCT), a double cantilever beam (DCB) and a pure mode II beam specimen. The most consistent and accurate results were found by means of the first approach using only eight-noded regular elements. The other approaches do not converge to and sometimes diverge from the comparison solution. Indeed in Nairn (2011), it was also seen that eight-noded elements produce the most accurate results. In order to improve the results with VCCT, mesh refinement should be carried out. For errors of about 1%, coarse meshes may be used. Only eight-noded regular elements should be used. Part of Sections 2.1 and 2.2 was published in Farkash and Banks-Sills (2020).

In Section 2.3, the problem of an interface crack between two dissimilar isotropic, homogeneous materials was considered. In the analysis, the phase angle of the stress intensity factors ψ in eq. (1.40) is required. To this end, the phase angle ψ_D, defined in eq. $(2.50)_1$, is calculated. A new equation for ψ_D, was presented. In Banks-Sills and Farkash (2016), ψ_D was found using the inverse trigonometric function $\cos^{-1}(\cdot)$. The value of ψ_D was between 0 and π, the range of $\cos^{-1}(\cdot)$. Hence, there was no difficulty in the calculation. Here, new equations were derived such that ψ_D may be found by using the inverse trigonometric functions $\sin^{-1}(\cdot)$ and $\tan^{-1}(\cdot)$. These are found in eqs. (2.57) and (2.58). The functions $\cos^{-1}(\cdot)$ and $\sin^{-1}(\cdot)$ produce the correct angle ψ_D only for $0 \leq \psi_D \leq \pi$ and $-\pi/2 \leq \psi_D \leq \pi/2$, respectively. But, the inverse trigonometric function $\tan^{-1}(\cdot)$ produces the correct value of ψ_D for all its values and is recommended.

The use of more than one element for the VCE was first suggested in Bueth (1996). In Banks-Sills and Farksh (2016), a criterion for the optimal number of elements for the VCE was presented for an interface crack between two dissimilar isotropic, homogeneous materials. Dual energy release rates, $\mathcal{I}_I$ and $\mathcal{I}_{II}$, given in eqs. (1.176) and (1.177), were found to be analytically equal. When carrying of finite element analyses (FEAs), they are not equal. It was suggested to choose the number of elements for the VCE for which the lowest difference between $\mathcal{I}_I$ and $\mathcal{I}_{II}$ is obtained. The difference between $\mathcal{I}_I$ and $\mathcal{I}_{II}$ was considered in Section 2.4. To understand this subject, a specific problem with an analytical solution was presented. The nodal point forces ahead of the crack tip were

determined analytically; the analytical crack face displacement jumps were taken from the first term of the asymptotic expansion for the in-plane displacement field in eqs. (1.4) and (1.10); and, the analytical values of the dual energy release rate were found. As a result of the stress singularity, large errors in the nodal point forces and the displacement jumps were found in the elements adjacent to the crack tip when calculated by the finite element method. These errors caused the difference between the dual energy release rates, where the numerical value of $\mathcal{I}_I$ underestimates and that of $\mathcal{I}_{II}$ overestimates their analytical values as seen in Table 2.7. For a VCE consisting of many eight-noded elements, the errors in $\mathcal{I}_I$ and $\mathcal{I}_{II}$ resulting from the stress singularity were minimized and their values converged to the analytical values. Thus, it is recommended to use a VCE length which produces the lowest difference between $\mathcal{I}_I$ and $\mathcal{I}_{II}$.

In Section 2.5, the VCCT has been extended to an interface crack between two dissimilar transversely isotropic materials. Equations for calculating the stress intensity factors K_1 and K_2 have been developed for this interface crack. Two pairs of solutions were produced. An analytic condition based on $\mathcal{I}_T$ in eq. (2.90) to determine the valid solution is presented. A low value of $\mathcal{I}_T$, indicates an optimal number of elements to be used for Δa. In all of the load cases considered with fine meshes, $\mathcal{I}_T$ converged towards zero as the number of elements in the virtual crack extension increased. For the coarse mesh, values of $\mathcal{I}_T$ decreased as the number of elements used in the virtual crack extension increased; but then increased. In this study, it was suggested to choose the number of elements for Δa for which the lowest value of $\mathcal{I}_T$ was obtained. According to this suggestion, the errors for the stress intensity factors ranged in absolute value from 0.02% to 0.27%. It may be noted that for an interface crack between two dissimilar isotropic materials the errors ranged in absolute value from 0.02% to 0.22%. It was shown that the same results are achieved when using coarser meshes. A focused mesh that contains fewer elements may be used if $\mathcal{I}_T$ converged towards zero. In this way, the VCCT may be extended for three-dimensional problems with meshes with a reasonable number of elements.

Continuing with the same interface in Section 2.5, an expression for the size of the interpenetration zone was presented. In previous papers (Toya, 1992; Sun and Qian, 1997), use of elements larger than the interpenetration zone was recommended. For cases where the VCE contains the number of elements for which the lowest value of $\mathcal{I}_T$ is obtained, excellent results are achieved even if the elements are smaller than the interpenetration zone. Lastly, new numerical results were presented for a CCT and a DCB specimens with an interface crack between two transversely isotropic materials, as shown in Figs. 2.18a and 2.18b, respectively. It was found that even when the stress intensity factors are the same order of magnitude, a virtual crack extension containing many elements should be used. Most of Section 2.5 was published in Farkash and Banks-Sills (2017).

In Chapter 3, the VCCT was extended to three-dimensional problems. In Section 3.1, equations for calculation of the energy release rates for a straight through crack and a

penny-shaped crack were presented. Note that those equations are applicable for a crack in an isotropic, homogeneous material and an interface crack. Numerical results for a straight through finite length crack and a penny-shaped crack in an infinite body of isotropic, homogeneous material were presented in Section 3.2. For the straight through finite length crack, the results were compared to the J-integral. For a thickness $2b = 15$ mm in Fig. 3.3, the difference between the results obtained by the VCCT and the J-integral is less than 0.02% for $0 \leq x_3/b < 0.96$ where the x_3-axis is shown in Fig. 3.3. For this relatively thick body, the mid-plane results converged to the two-dimensional plane strain analytical solution. For the penny-shaped crack, results were compared to an analytical solution. The analytical stress intensity factors are constant along the crack front. A convergence study was made with two-dimensional axisymmetric meshes. For the finest mesh, the greatest percentage error of K_I was -0.12%. Due to symmetry, the finest mesh was swept through one-quarter of the body. For the three-dimensional mesh, the greatest percentage error of K_I was -0.11%.

In Section 3.3, numerical results for a straight through finite length interface crack and a penny-shaped interface crack in an infinite body were presented. The interface crack in this section is between two dissimilar linear elastic, homogeneous and isotropic materials. For the straight through finite length interface crack, numerical results were compared to those obtained by means of the M-integral. The number of elements for Δa was taken for which the lowest value of $\mathcal{I}_T$ was obtained. For a thickness $2b = 15$ mm, the largest difference between the values obtained for the interface energy release rate $\mathcal{G}_i$ with VCCT and the M-integral is less than 0.06% for $0 \leq x_3/b < 0.96$. The mid-plane results converged to the two-dimensional plane strain solution. As was shown in the two-dimensional cases, if one element is used as the VCE, the percentage error between the M-integral and VCCT is more than 5%. Many elements should be used as the VCE in order to obtain accurate results. For the penny-shaped interface crack, the same three-dimensional mesh from Section 3.1 was used. Numerical results were compared to an analytical solution. For the lowest value of $\mathcal{I}_T$, the errors for K_1 and K_2 were -0.11% and -0.21%, respectively. If only one element is used as the VCE, the error for K_2 is more than 4%.

A new problem consisting of a penny-shaped interface crack between two dissimilar transversely isotropic materials is presented in Section 3.4. The material that was used in this problem is a fiber reinforced composite made of graphite/epoxy AS4/3501-6. For the upper material, the fibers are in the x_1- direction, and for the lower material, they are in the x_3- direction. For $\theta = 0°$, where θ is shown in Fig. 3.2, the interface crack is between $0°//90°$-directions. The double slash denotes interface. For $\theta = 45°$ and $\theta = 90°$, the interface crack is between $+45°//-45°$-directions and $90°//0°$-directions, respectively. In order to use the VCCT for $\theta = 45°$, new equations were derived. The number of elements that should be used as the VCE is determined by the lowest value of $\mathcal{I}_E$ which is defined in eq. (3.56). For $\theta = 0°$ and $\theta = 90°$, the lowest value of $\mathcal{I}_T$ was found for $M = 2$,

Table 5.1: A comparison between the two-dimensional Stroh and Lekhnitskii formalism and the three-dimensional Clifford formalism.

	2D-Stroh	3D-Clifford
Coordinate transformation	$z = p_{11}x_1 + p_{12}x_2$	$y = P_{11}x_1 + P_{12}x_2 + P_{13}x_3$
Eigenvalue problem	$(\mathbf{N}_1 + p_{12}\mathbf{N}_2)\mathbf{d} = \mathbf{0}$	$(\mathbf{N}_1 + P_{12}\mathbf{N}_2 + P_{13}\mathbf{N}_3)\mathbf{d} = \mathbf{0}$
Eigenvector	$\mathbf{d}_{6\times1}$	$\mathbf{d}_{9\times1}$
Eigenvalues	$p_{11} = 1, p_{12}$	$P_{11} = 1, P_{12}, P_{13}$
Stress functions	$\boldsymbol{\phi}^{\mathbf{b}} = \mathbf{b}f(z)$	$\boldsymbol{\phi}^{\mathbf{b}} = \mathbf{b}f(y)$, $\boldsymbol{\phi}^{\mathbf{g}} = \mathbf{g}f(y)$
Stress vectors	$\mathbf{t}_1 = -\boldsymbol{\phi}^{\mathbf{b}}_{,2}$, $\mathbf{t}_2 = \boldsymbol{\phi}^{\mathbf{b}}_{,1}$	$\mathbf{t}_1 = -(\boldsymbol{\phi}^{\mathbf{b}}_{,2} + \boldsymbol{\phi}^{\mathbf{g}}_{,3}), \mathbf{t}_2 = \boldsymbol{\phi}^{\mathbf{b}}_{,1}, \mathbf{t}_3 = \boldsymbol{\phi}^{\mathbf{g}}_{,1}$

where M is the number of elements used for the VCE. The values obtained for $\theta = 0°$ and $\theta = 90°$ are the same. For $\theta = 45°$, the lowest value of $\mathcal{I}_E$ was found for $M = 3$. The values obtained for $\mathcal{G}_i$ with $M = 2$ and 3 are the same up to three significant figures. Hence, the energy release rates obtained along the interface crack front were presented for $M = 2$. The stress intensity factors were calculated for $\theta = 0°$ with $M = 2$ and $\theta = 45°$ with $M = 3$.

In Chapter 4, a Clifford algebra is considered. In Section 4.1, the eigenvalue problem is solved for various anisotropic materials. For isotropic materials, a general solution is found. For anisotropic materials, solutions for specific materials are presented. The eigenvectors for the materials considered in Section 4.1 are found in Section 4.2. Again, only for isotropic material, a general solution is found. A three-dimensional Clifford formalism is derived in Section 4.3. In Table 5.1, a comparison is made between the two-dimensional Stroh and Lekhnitskii (SL) formalisms and the three-dimensional Clifford formalism. For the SL formalisms, the coordinate transformation is two-dimensional and two 6×6 matrices $\mathbf{N}_1$ and $\mathbf{N}_2$ are used for the eigenvalue problem. The parameter p_{11} is taken to be unity so that there is only one unknown eigenvalue p_{12}. For the Clifford formalism, the coordinate transformation is three-dimensional and three 9×9 matrices $\mathbf{N}_1$, $\mathbf{N}_2$ and $\mathbf{N}_3$ are used for the eigenvalue problem. The parameter P_{11} is taken to be unity so that there are two unknowns eigenvalues P_{12} and P_{13}. For the SL formalisms, one stress function $\boldsymbol{\phi}^{\mathbf{b}}$ is used to determine the two stress vectors $\mathbf{t}_1$ and $\mathbf{t}_2$. For the Clifford formalism, two stress functions $\boldsymbol{\phi}^{\mathbf{b}}$ and $\boldsymbol{\phi}^{\mathbf{g}}$ are used to determine the three stress vectors $\mathbf{t}_1$, $\mathbf{t}_2$ and $\mathbf{t}_3$. In Section 4.4, analytical and numerical results of the three-dimensional Clifford formalism are presented. A general solution for a uniform stress field is presented. Problems of applied tensile and shear tractions were solved. Numerical results were identical to the analytical solutions.

The VCCT method has been extended for two-dimensional interface crack problems; namely, for interface cracks between the $0°//90°$-directions (Farksh and Banks-Sills, 2017) and the $+45°//-45°$-directions. The VCCT is much simpler to derive for a new interface than the M-integral. In order to use the M-integral for a new interface, the stress and

displacement fields in the vicinity of the crack tip must be obtained. These developments require great effort. For the VCCT, only the stresses on the interface ahead of the crack tip and the crack face displacement jumps are required. These derivations are much simpler. After the stresses ahead of the crack tip and the crack face displacement jumps are found, two integrals similar to A and D in eqs. (1.169) and (1.170) are required. One may follow the steps and the integral solutions presented here for developing the equations for obtaining the stress intensity factors easily. For example, all the equations and the derivations needed for the interface crack between the $+45°//-45°$-directions appear here in two and a half pages.

The QP-elements are used extensively with the VCCT in recent papers (Jimenez and Miravete, 2004; Chen et al., 2005; Chiu et al., 2008; Chen et al., 2008; Chiu and Lin, 2009; Wahab, 2015; Peixoto and de Castro, 2016; Khaldi et al., 2016; Burlayenko et al., 2016; Salem et al., 2018 and Di Stasio and Ayadi, 2019). It was found that QP-elements produces inaccurate results. Only eight-noded regular elements should be used (Farksh and Banks-Sills, 2020).

In Banks-Sills and Farksh (2016), an equation was presented to obtain the phase angle ψ using the inverse cosine of the phase angle ψ_D. Note that in Banks-Sills and Farksh (2016), ψ_D was denote as χ. This equation was found to produce inaccurate results if $\psi_D < 0$ or $\pi < \psi_D$. Here, a new equation for ψ was derived using the inverse tangent of ψ_D. With this equation, the correct value of the phase angle ψ is always obtained. The relation between ψ and ψ_D is now well established and is illustrated in Fig. 2.10.

The dual energy release rates, $\mathcal{I}_I$ and $\mathcal{I}_{II}$, were found to be analytically equal. But, numerically, they differ. Note that for each interface, the definition of the dual energy release rates vary slightly. For a crack in an isotropic homogeneous material and for an interface crack between two dissimilar isotropic materials, the dual energy release rates, $\mathcal{I}_I$ and $\mathcal{I}_{II}$, are defined in eqs. (1.176) and (1.177), respectively. For an interface crack between the $0°//90°$-directions, the dual energy release rates are $\mathcal{I}_I^{(T)}$ and $\mathcal{I}_{II}^{(T)}$ and defined in eqs. (2.87) and (2.88), respectively. For an interface crack between the $+45°//-45°$-directions, the dual energy release rates are $\mathcal{I}_I^{(E)}$ and $\mathcal{I}_{III}^{(E)}$ and defined in eqs. (3.50) and (3.51), respectively. The numerical difference between $\mathcal{I}_I$ and $\mathcal{I}_{II}$ was considered. It was found that the stress singularity at the crack tip is the reason for the numerical difference. A VCE length that produces the lowest difference between them is recommended for use in calculating the energy release rates. This criterion was found to produce excellent results for the problems considered throughout this investigation.

For an interface crack between the $0°//90°$-directions, two different methods for meshing were presented. In the first mesh, transition elements were used in order to achieve small elements in the vicinity of the crack tip, as shown in Fig. 2.15. For the second and third meshes, a focused zone was used with a square of very small elements in the vicinity of the crack tip, as shown in Fig. 2.16. The main difference between the latter two meshes is

the size and number of elements in the square in the vicinity of the crack tip. It was found that using a focused zone with a small number of elements produces excellent results. In this way, the number of degrees of freedom is relatively small and two-dimensional meshes may be extruded for carrying out three-dimensional FEAs.

The VCCT has been extended for three-dimensional problems of a straight through crack and a penny-shaped crack. Numerical results for cracks in an isotropic homogeneous material and for interface cracks were presented. Excellent results were found compared to two and three-dimensional analytical solutions, as well as with comparison to results obtained with conservative integrals. Many elements should be used as the VCE, for two-dimensional, as well as three-dimensional problems, in order to obtain accurate results. For a penny-shaped interface crack between two dissimilar transversely isotropic materials, the stress intensity factors were found only for $\theta = 0^\circ$ and 45°. However, the modes I, II and III energy release rates and the total interface energy release rate were found along the entire delamination front. It may be noted that the modes I, II and III energy release rates oscillate depending on the length of the VCE, Δa, and were presented here for a specific value of Δa.

It may be pointed out that here results with errors of less than 0.5% were sought. For fatigue crack propagation calculations in metals, Paris' relationship is used where

$$\frac{da}{dN} = C(\Delta K)^n \tag{5.1}$$

a is crack length, N is the cycle number, K is the stress intensity factor and C and n are constants determined from tests. Typically, $3 \leq n \leq 5$. Using eq. (5.1) magnifies the errors. Hence, for practical problems in the aerospace industry that use fracture mechanics calculations, small errors are sought. In Fawaz and Andersson (2004), for some cases, results with errors of less than 0.5% were considered. For other cases, results with errors of less than 1% were found. For these cases, it was suggested to improve the errors to be less than 1%. It may be noted that Fawaz and Andersson are working in industry. Consultation with people who work with Boeing (Wawrzynek, 2006) suggest achieving errors of less than 0.5%.

Progress has been made with the Clifford formalism for solving problems involving anisotropic material. An early aim of this investigation was to use the Clifford formalism to solve problems involving cracks in anisotropic material. The definition of the variable y in eq. (1.90) appears to preclude such a solution. Nonetheless, the eigenvalue problem was solved for specific anisotropic materials. The stress vectors and stress functions for three-dimensional problems were found. In addition, a general solution for a uniform stress field was presented. It seems that the x_1, x_2 and x_3-directions are coupled so that it does not allow solutions of three-dimensional crack problems. Other three-dimensional problems may be solved using this formalism.

Future work on the VCCT may include an extension of this method for elliptical crack problems. New derivations of the Stroh and Lekhnitskii formalisms and the VCCT are required in order to determine the stress intensity factors for more positions along the crack front of the penny-shaped interface crack problem between a cross-ply solved in Chapter 3. For example, for $\theta = 30°$, equations for an interface crack between the $+30°//-60°$-directions are required. These are presented in Rogel and Banks-Sills (2010). In addition, the VCCT may be extended for other interfaces. The steps for these further extensions are presented in this study.

In this investigation, the element thickness, ℓ_3, was assumed to be constant, as shown in Fig. 3.1. For this case, the nodal point forces were distributed equally between the rows. Sometimes, a need arises to change the thickness of the elements throughout the thickness of the body. For these cases, the correct way to apportion the nodal point forces should be considered.

The initial hope was to use the Clifford algebra for solving crack problems. This does not appear to be possible. The Clifford formalism presented here may be extended to solve other problems of anisotropic materials. In Ting (1996), the relations found for the two-dimensional uniform stress solution from the Stroh and Lekhnitskii formalisms were used for solution of an elliptical hole in an infinite body subjected to a uniform loading. Hence, it may be possible to extend the three-dimensional uniform stress solution obtained here with the Clifford algebra to solve the problem of an ellipsoidal cavity subjected to the uniform loading.

Bibliography

[1] ABAQUS. Version 6.4. Hibbitt, Karlsson and Sorensen, Inc. Providence, RI, USA, 2003.

[2] Abaqus/CAE. Version 6.14. Dassault Systèmes Simulia Corp. Providence, RI, USA, 2014.

[3] Abaqus/CAE 2016. Dassault Systèmes Simulia Corp. Johnston, RI, USA, 2015.

[4] Abaqus/CAE 2017. Dassault Systèmes Simulia Corp. Johnston, RI, USA, 2016.

[5] Aboudi, J. The generalized method of cells and the high-fidelity generalized method of cells micromechanical models–a review. Mech. Adv. Mater. Struct. 11:329-366, 2004.

[6] Agrawal A. and Karlsson A.M. Obtaining mode mixity for a bimaterial interface crack using the virtual crack closure technique. Int. J. Fract., 141: 75–98, 2006.

[7] Banks-Sills, L. Use of three-dimensional finite elements in linear elastic fracture mechanics. In: Analytical, Numerical and Experimental Aspects of Fracture Processes, ASME-AMD 91: 89–97, 1988.

[8] Banks-Sills, L. Application of the finite element method to linear elastic fracture mechanics. Appl. Mech. Rev., 44: 447-461, 1991.

[9] Banks-Sills, L. Update: application of the finite element method to linear elastic fracture mechanics. Appl. Mech. Rev., 63: 020803-1 020803-17, 2010.

[10] Banks-Sills, L. and Bortman, Y. Reappraisal of the quarter-point quadrilateral element in linear elastic fracture mechanics. Int. J. Fract., 25: 169–180, 1984.

[11] Banks-Sills L., Travitzky N., Ashkenazi D. and Eliasy R. A methodology for measuring interface fracture properties of composite materials. Int. J. Fract., 99: 143–160, 1999.

[12] Banks-Sills, L. and Boniface, V. Fracture mechanics for an interface crack between a special pair of transversely isotropic materials. In: Multiscale Deformation and Fracture in Materials and Structures-the James R. Rice 60th Anniversary Volume. Eds. Chuang, T.J. and Rudnicki, J.W., Kluwer Academic Publishers, The Netherlands, pp. 183-204, 2000.

[13] Banks-Sills, L., Freed, Y. and Arkady, A. Behavior of a flat internal delamination within a fiber reinforced cross-ply composite. Int. J. Fract., 155: 127-142, 2009.

[14] Banks-Sills, L., Ishbir, C., Fourman, V., Rogel, L. and Eliasi, R. Interface fracture toughness of a multi-directional woven composite. Int. J. Fract., 182: 187-207, 2013.

[15] Banks-Sills, L. and Farkash E. A note on the Virtual Crack Closure Technique for a bimaterial interface crack. Int. J. Fract., 201: 171–180, 2016.

[16] Banks-Sills, L. and Dolev O. Mixed mode testing of a multi-directional woven laminate. Int. J. Fract., 224: 1–13, 2020.

[17] Barnett, D.M. and Lothe, J. Synthesis of the sextic and the integral formalism for dislocations, Greens functions and surface waves in anisotropic elastic solids. Phys. Nor., 7: 13–19, 1973.

[18] Barsoum, R.S. Application of quadratic isoparametric finite elements in linear fracture. mechanics. Int. J. Fract., 10: 603–605, 1974.

[19] Bittencourt, T.N., Ahmabou, B. and Ingraffea, A.R. Comparison of mixed–mode stress–intensity factors obtained through displacement correlation, J–integral formulation, and modified crack-closure integral. In: Fracture Mechanics: Twenty-Second Symposium, ASTM STP 1131, Vol. II, Eds. Atluri S.N., Newman J.C., Raju I.S. and Epstein J.S., West Conshohocken, PA, pp. 69–82, 1992.

[20] Beuth, J.L. Separation of crack extension modes in orthotropic delamination models. Int. J. Fract., 77: 305–321, 1996.

[21] Boniface, V. and Banks-Sills, L. Stress intensity factors for finite interface cracks between a special pair of transversely isotropic materials. J. Appl. Mech., 69:230–239, 2002.

[22] Burlayenko, V.N., Altenbach, H., Sadowski, T. and Dimitrova, S.D. Computational simulations of thermal shock cracking by the virtual crack closure technique in a functionally graded plate. Comp. Mater. Sci., 116:11-21, 2016.

[23] Chan, S.K., Tuba, I.S. and Wilson, W.K. On the finite element method in linear fracture mechanics. Eng. Frac. Mech., 2: 1–17, 1970.

[24] Chen, F.H.K. and Shield, R.T. Conservation laws in elasticity of the J-integral type. Z. Angew. Math. Phys., 28: 1–22, 1977.

[25] Chen, X., Lin, Y.C., Liu, X. and Lu, G. Fracture mechanics analysis of the effect of substrate flexibility on solder joint reliability. Eng. Fract. Mech., 72: 2628–2646, 2005.

[26] Chen, Y.R., Shen, G.S., Yang, H.C., Lin, H.C. and Chiu, T.C. Three dimensional corner delamination analysis for fan-out chip scale package. In: 2008 International Conference on Electronic Packaging Technology & High Density Packaging, Eds. Keyun, B. and Fei, X., Shanghai, China, 2008.

[27] Chiu, T.C., Lin, H.C. and Yang, H.C. Analysis of flip-chip corner delamination using 3-D virtual crack closure technique. In: 2008 International Conference on Electronic Materials and Packaging, Ed. Shen-Li, F., Taipei, Taiwan, 2008.

[28] Chiu, T.C. and Lin, H.C. Analysis of stress intensity factors for three-dimensional interface crack problems in electronic packages using the virtual crack closure technique. Int. J. Fract., 156: 75–96, 2009.

[29] Chow, W.T. and Atluri, S.N. Calculation of stress intensity factors for interfacial crack using virtual crack closure integral. Comput. Mech. 16: 417–425, 1995.

[30] Comninou, M. The interface crack. J. Appl. Mech., 44: 631–636, 1977.

[31] Comninou, M. The interface crack in shear field. J. Appl. Mech., 45: 287–290, 1978.

[32] Comninou, M. and Schmueser, D. The interface crack in a combined tension-compression and shear field. J. Appl. Mech., 46: 345–348, 1979.

[33] Deng, X. General crack-tip fields for stationary and steadily growing interface cracks in anisotropic bimaterials. J. Appl. Mech., 60: 183–189, 1993.

[34] Di Stasio, L. and Ayadi, Z. Finite element solution of the fiber/matrix interface crack problem: convergence properties and mode mixity of the Virtual Crack Closure Technique. Finite Elem. Anal. Des., 167: 103332(1-18), 2019.

[35] England, A.H. A crack between dissimilar media. J. Appl. Mech., 32: 400–402, 1965.

[36] Erdogan, F. Stress distribution in bonded dissimilar materials with cracks. J. Appl. Mech., 32: 403–410, 1965.

[37] Farkash E. Validation of the virtual crack closure technique for accurately calculating stress intensity factors in mixed modes. M.Sc. Thesis, Tel Aviv Universiy, Tel Aviv, 2016.

[38] Farkash E. and Banks-Sills, L. Virtual crack closure technique for an interface crack between two transversely isotropic materials. Int. J. Fract., 205: 189–202, 2017.

[39] Farkash E. and Banks-Sills, L. Quarter-point elements are unnecessary for the VCCT. J. Appl. Mech., 87: 081009-1–7, 2020.

[40] Fawaz, S.A. and Andersson, B. Accurate stress intensity factor solutions for corner cracks at a hole. Eng. Fract. Mech. 71: 1235–1254, 2004.

[41] Freed, Y. and Banks-Sills, L. A through interface crack between a $\pm 45^\circ$ transversely isotropic pair of materials. Int. J. Fract., 133: 1-41, 2005.

[42] Gradshteyn, I.S. and Ryzhik, I.M. Table of integrals, series and products. Eighth Edition, Translated by Scripta Technica, Inc. Academic Press, N.Y., 2015.

[43] Green A.E. and Sneddon I.N. The distribution of stress in the neighbourhood of a flat elliptical crack in an elastic solid. Proc. Cambridge Phil. Soc., 46: 159–163, 1950.

[44] Griffith, A.A. The phenomena of fracture and flow in solids. Philos. Trans. Roy. Soc. A, A221: 163–198, 1920.

[45] Hemanth, D., Shivakumar Aradhya K.S., Rama Murthy T.S. and Govinda R.N. Strain energy release rates for an interface crack in orthotropic media – a finite element investigation. Eng. Fract. Mech. 72: 759–772, 2005.

[46] Henshell, R.D. and Shaw, K.G. Crack tip finite elements are unnecessary. Int. J. Numer. Methods Eng., 9: 495–507, 1975.

[47] Hughes, T.J.R. The finite element method: linear static and dynamic finite element analysis. First Edition, Prentice-Hall, Inc., New Jersey, 1987.

[48] Irwin, G.R. Analysis of stresses and strains near the end of a crack traversing a plate. J. Appl. Mech., 24: 361-364, 1957.

[49] Irwin, G.R. Fracture. In: Handbuch Der Physik, Vol. 6. Ed. Flügge, S., Springer, Berlin, pp. 551-590, 1958.

[50] Isaak, D.G., Orson L.A., Takayasu G. and Isao S. Elasticity of Single-Crystal Forsterite measured to 1700 K. J. Geophys. Res., 94(B5): 5895–5906, 1989.

[51] Isida, M. Effect of width and length on stress intensity factors of internally cracked plates under various boundary conditions. Int. J. Fract. Mech., 7: 301–316, 1971.

[52] Jimenez, M.A. and Miravete, A. Application of the finite-element method to predict the onset of delamination growth. J. Compos. Mater., 38: 1309–1335, 2004.

[53] Kassir, M.K., and Bregman, A.M. The stress-intensity factor for a penny-shaped crack between two dissimilar materials. J. Appl. Mech., 39: 308–310, 1972.

[54] Khaldi, M., Vivet, A., Bourmaud, A., Sereir, Z. and Kada, B. Damage analysis of composites reinforced with Alfa fibers: viscoelastic behavior and debonding at the fiber/matrix interface. J. Appl. Polym. Sci., 133: 43760 (1–10), 2016.

[55] Krueger, R. Virtual crack closure technique: history, approach, and applications. Appl. Mech. Rev., 57: 109–143, 2004.

[56] Lekhnitskii, S.G. Theory of elasticity of an anisotropic body. Holden-Day, San Francisco, 1950, in Russian; translated by P. Fern, 1963, in English.

[57] Li, F.Z., Shih, C.F. and Needleman, A. A comparison of methods for calculating energy release rates. Eng. Frac. Mech., 21: 405-421, 1985.

[58] Liu, L.W. and Hong, H.K. New method for three-dimensional problems of anisotropic elasticity. In: The 39^{th} National Conference on Theoretical and Applied Mechanics, Taipei, Taiwan, November 20-21, 2015.

[59] Malyshev, B.M. and Salganik, R.L. The strength of adhesive joints using the theory of cracks. Int. J. Fract. Mech., 1: 114-128, 1965.

[60] Matos, P.P.L., McMeeking, R.M., Charalambides, P.G. and Drory, M.D. A method for calculating stress intensities in bimaterial fracture. Int. J. Fract. 40: 235–254, 1989.

[61] Mega, M. and Banks-Sills, L. Mixed mode interface fracture toughness of a multi-directional composite UD/woven pair. Theor. Appl. Fract. Mech. 104: 102323, 2019.

[62] Nairn, J.A. Generalized crack closure analysis for elements with arbitrarily-placed side nodes and consistent nodal forces. Int. J. Fract., 171: 11-22, 2011.

[63] Nakamura, T. and Parks, D.M. Antisymmetrical 3-D stress field near the crack front of a thin elastic plate. Int. J. Solids Struct., 25: 1411-1426, 1989.

[64] Narayana, K.B., Dattaguru B., Ramamurthy, T.S. and Vijayakumar, K. Modified crack closure integral using six-noded isoparametric quadrilateral singular elements. Eng. Fract. Mech., 36: 945–955, 1990.

[65] Narayana, K.B. and Dattaguru B. Certain aspects related to computation by modified crack closure integral (MCCI). Eng. Fract. Mech., 55: 335–339, 1996.

[66] Newman, J.C. and Raju I.S. Analysis of surface cracks in finite plates under tension and bending loads. Technical Paper NASA 1578, NASA Langley Research Center, Hampton, VA, 1979.

[67] Okada, H., Higashi, M., Kikuchi, M., Fukui, Y. and Kumazawa, N. Three dimensional virtual crack closure-integral method (VCCM) with skewed and non-symmetric mesh arrangement at the crack front. Eng. Fract. Mech., 72: 1717–1737, 2005.

[68] Oneida, E.K., van der Meulen, M.C.H. and Ingraffea, A.R. Method for calculating G, G_I, and G_{II} to simulate crack growth in 2D, multiple-material structures. Eng. Fract. Mech., 140:106-126, 2015.

[69] Pang, H.L.J., Leggatt, R.H. and Hellen, T.K. Development of linear elastic fracture mechanics benchmarks tests. In: Proceedings of the 5th International Confference on Numerical Methods in Fracture Mechanics, Eds. Luxmore, J.R. and Owen, D.R.J., Pineridge Press, Swansea, pp. 153–168, 1990.

[70] Peixoto, D.F.C. and de Castro, P.M.S.T. Mixed mode fatigue crack propagation in a railway wheel steel. Procedia Struct. Integrity, 1:150–157, 2016.

[71] Raju, I.S. Calculation of strain energy release rates with higher order and singular finite elements. Eng. Fract. Mech., 28: 251–274, 1987.

[72] Raju, I.S. and Newman Jr., J.C. Three dimensional finite-element analysis of finite-thickness fracture specimens. Technical Report NASA TND-8414, NASA Langley Research Center, Hampton, VA, 1977.

[73] Raju, I.S., Shivakumar, K.N. and Crews, J.H. Three-dimensional elastic analysis of a composite double cantilever beam specimen. AIAA J., 26: 1493–1498, 1988.

[74] Raju, I.S., Crews, J.H. and Aminpour, M.A. Convergence of strain energy release rate components for edge-delaminated composite laminates. Eng. Fract. Mech., 30: 383–396, 1988.

[75] Raju, I.S., Shivakumar, K.N. and Crews, .J.H. Three-dimensional elastic analysis of a composite double cantilever beam specimen. AIAA J., 26: 1493–1498, 1988.

[76] Raju, I.S., Sistla, R. and Krishnamurthy, T. Fracture mechanics analyses for skin–stiffener debonding. Eng. Fract. Mech., 54: 371–385, 1996.

[77] Ramamurthy, T.S., Krishnamurthy, T., Narayana, K.B., Vijayakumar, K. and Dattaguru, B. Modified crack closure integral method with quarter point elements. Mech. Res. Commun., 13: 179–186, 1986.

[78] Rice, J.R. A path independent integral and the approximate analysis of strain concentration by notches and cracks. J. Appl. Mech., 35: 379–386, 1968a.

[79] Rice, J.R. Mathematical analysis in the mechanics of fracture. Fracture, Vol. II, H. Liebowitz (ed.), Academic Press, New York, pp. 229-230, 1968b.

[80] Rice, J.R. Elastic fracture mechanics concepts for interfacial cracks. J. Appl. Mech., 55: 98–103, 1988.

[81] Rice, J.R. and Sih, G.C. Plane problems of cracks in dissimilar media. J. Appl. Mech., 32: 418–423, 1965.

[82] Rice, J.R., Suo, Z. and Wang, J.S. Mechanics and thermodynamics of brittle interfacial failure in bimaterial systems. In: Metal Ceramic Interfaces. Eds. Rühle, M., Evans, A.G., Ashby, M.F. and Hirth, J.P., Pergamon Press, Oxford, pp. 269-294, 1990.

[83] Rogel, L. and Banks-Sills, L. A through interface crack between a transversely isotropic pair of materials $(+30°/-60°, -30°/+60°)$. Eng. Fract. Mech., 77: 3261–3291, 2010.

[84] Rybicki E.F. and Kanninen M.F. A finite element calculation of stress intensity factors by a modified crack closure integral. Eng. Fract. Mech., 9:931–938, 1977.

[85] Salem, M., Mohamed, B., Belaïd, M. and Belabbes, B.B. Effect of the angles of the cracks of corroded plate in bonded composite repair. Frattura ed Integrità Strutturale, 12:113-123, 2018.

[86] Sethuraman, R. and Maiti, S.K. Finite element based computation of strain energy release rate by modified crack closure integral. Eng. Fract. Mech., 30: 227–231, 1988.

[87] Shivakumar, K.N., Tan, P.W. and Newman, J.C. A virtual crack-closure technique for calculating stress intensity factors for cracked three dimensional bodies. Int. J. Fract., 36: R43–R50, 1988.

[88] Smelser, R.E. Evaluation of stress intensity factors for bimaterial bodies using numerical crack flank displacement data. Int. J. Frac., 15: 135–143, 1979.

[89] Smith, S.A. and Raju, I.S. Evaluation of stress-intensity factors using general finite element models. In: Fatigue and Fracture Mechanics, ASTM STP 1332, Vol. 29, Eds. Panontin S.N. and Sheppard S.D., West Conshohocken, PA, pp. 176–200, 1999.

[90] Sneddon, I.N. The distribution of stress in the neighbourhood of a crack in an elastic solid. Proc. Royal Soc. London A, 187: 229–260, 1946.

[91] Stroh, A.N. Dislocations and cracks in anisotropic elasticity. Philos. Mag., 3: 625–646, 1958.

[92] Sun, C.T. and Manoharan, M.G. Strain energy release rates of an interfacial crack between two orthotropic solids. J. Compos. Mater. 23: 460-478, 1989.

[93] Sun, C.T. and Qian, W. The use of finite extension strain energy release rates in fracture of interfacial cracks. Int. J. Solids. Struct. 34: 2595–2609, 1997.

[94] Ting, T.C.T. Anisotropic elasticity-theory and applications. Oxford University Press, Oxford, 1996.

[95] Toya, M. On mode I and mode II energy release rates of an interface crack. Int. J. Fract., 56: 345-352, 1992.

[96] Wahab, M.M.A. Simulating mode I fatigue crack propagation in adhesively-bonded composite joints. In: Fatigue and Fracture of Adhesively-Bonded Composite Joints. Ed. Vassilopoulos, A.P., Woodhead Publishing, Cambridge, pp. 323–344, 2015.

[97] Wang, Y. and Williams, J.G. Corrections for mode II fracture toughness specimens of composites materials. Comp. Sci. Tech., 43: 251–256, 1992.

[98] Wawrzynek, P.A. Personal communication, Cornell Fracture Group, 2006.

[99] Whitcomb, J.D. Instability–related delamination growth of embedded and edge delaminations. Ph.D. Thesis, Virginia Polytechnic Institute and State University, Virginia, 1988.

[100] Williams, M.L. On the stress distribution at the base of a stationary crack. J. Appl. Mech., 24: 109-114, 1957.

[101] Williams, M.L. The stresses around a fault or crack in dissimilar media. Bull. Seismol. Soc. Am., 49: 199-204, 1959.

[102] Williams, J.G. End corrections for orthotropic DCB specimens. Comp. Sci. Tech., 35: 367–376, 1989.

[103] Wortman J. and Evans R. Young's modulus, shear modulus, and Poisson's ratio in silicon and germanium. J. Appl. Phys., 36: 153-156, 1965.

[104] Yau, J.F., Wang, S.S., Corten, H.T. A mixed-mode crack analysis of isotropic solids using conservation laws of elasticity. J. Appl. Mech., 47: 335-341, 1980.

[105] Yau, J.F. and Wang, S.S. An analysis of interface cracks between dissimilar isotropic materials using conservation integrals in elasticity. Eng. Fract. Mech., 20: 423-432, 1984.

Appendix A

Maintaining displacement continuity across the interface of a penny-shaped interface crack

In this appendix, the equations for the remote tractions applied to a body with a penny-shaped interface crack between two transversely isotropic materials are developed. These tractions are required to maintain displacement continuity across the interface far from the crack. For the upper material, the fibers are in the x_1- direction, and for the lower material, they are in the x_3- direction. The directions are shown in Fig. 3.9. The effective mechanical properties of graphite/epoxy AS4/3501-6 are used. The compliance matrices of the upper and lower materials are given as

$$\mathbf{S}^{(1)} = \begin{bmatrix} \frac{1}{E_A} & -\frac{\nu_A}{E_A} & -\frac{\nu_A}{E_A} & 0 & 0 & 0 \\ & \frac{1}{E_T} & -\frac{\nu_T}{E_T} & 0 & 0 & 0 \\ & & \frac{1}{E_T} & 0 & 0 & 0 \\ & \text{sym} & & \frac{2(1+\nu_T)}{E_T} & 0 & 0 \\ & & & & \frac{1}{G_A} & 0 \\ & & & & & \frac{1}{G_A} \end{bmatrix}. \tag{A.1}$$

and

$$\mathbf{S}^{(2)} = \begin{bmatrix} \frac{1}{E_T} & -\frac{\nu_T}{E_T} & -\frac{\nu_A}{E_A} & 0 & 0 & 0 \\ & \frac{1}{E_T} & -\frac{\nu_A}{E_A} & 0 & 0 & 0 \\ & & \frac{1}{E_A} & 0 & 0 & 0 \\ & \text{sym} & & \frac{1}{G_A} & 0 & 0 \\ & & & & \frac{1}{G_A} & 0 \\ & & & & & \frac{2(1+\nu_T)}{E_T} \end{bmatrix}, \tag{A.2}$$

respectively. For the upper and lower materials, remote tensile tractions σ_{22} are applied, as shown in Fig. 3.13. Using Hooke's law far from the origin, the strains are found as

$$\varepsilon_{11}^{(1)} = \frac{1}{E_A}\left[\sigma_{11}^{(1)} - \nu_A(\sigma_{22} + \sigma_{33}^{(1)})\right] \tag{A.3}$$

$$\varepsilon_{22}^{(1)} = -\frac{\nu_A}{E_A}\sigma_{11}^{(1)} + \frac{1}{E_T}\left(\sigma_{22} - \nu_T\sigma_{33}^{(1)}\right) \tag{A.4}$$

$$\varepsilon_{33}^{(1)} = -\frac{\nu_A}{E_A}\sigma_{11}^{(1)} - \frac{1}{E_T}\left(\nu_T\sigma_{22} - \sigma_{33}^{(1)}\right) \tag{A.5}$$

$$\varepsilon_{11}^{(2)} = \frac{1}{E_T}\left(\sigma_{11}^{(2)} - \nu_T\sigma_{22}\right) - \frac{\nu_A}{E_A}\sigma_{33}^{(2)} \tag{A.6}$$

$$\varepsilon_{22}^{(2)} = -\frac{1}{E_T}\left(\nu_T\sigma_{11}^{(2)} - \sigma_{22}\right) - \frac{\nu_A}{E_A}\sigma_{33}^{(2)} \tag{A.7}$$

$$\varepsilon_{33}^{(2)} = \frac{1}{E_A}\left[\sigma_{33}^{(2)} - \nu_A(\sigma_{11}^{(2)} + \sigma_{22})\right] \tag{A.8}$$

In order to maintain displacement continuity along the interface,

$$\varepsilon_{11}^{(1)} = \varepsilon_{11}^{(2)} \quad , \quad \varepsilon_{33}^{(1)} = \varepsilon_{33}^{(2)}. \tag{A.9}$$

Since the upper and lower materials are, in fact, the same material rotated by 90° degrees, the strains along the fibers are the same for the upper and lower materials. Hence,

$$\varepsilon_{11}^{(1)} = \varepsilon_{33}^{(2)}. \tag{A.10}$$

In addition, the strains perpendicular to the fibers are the same for the upper and lower materials, such that

$$\varepsilon_{33}^{(1)} = \varepsilon_{11}^{(2)}. \tag{A.11}$$

Substituting eqs. (A.9) to (A.11) into eqs. (A.3) to (A.8), results in

$$\sigma_{11}^{(2)} = \sigma_{33}^{(1)} = \frac{E_A\nu_T - E_T\nu_A}{E_A + E_T\nu_A}\sigma_{22} + \frac{E_T(1+\nu_A)}{E_A + E_T\nu_A}\sigma_{33}^{(2)}. \tag{A.12}$$

The effective mechanical properties of graphite/epoxy AS4/3501-6 are shown in Table 1.1. Choosing $\sigma_{22} = \sigma_{11}^{(1)} = \sigma_{33}^{(2)} = 1$ MPa, results as $\sigma_{11}^{(2)} = \sigma_{33}^{(1)} = 0.6114$ MPa. Using transformation equations, at $r = R$ the body is subjected in the FEA to

$$\sigma_{rr}^{(1)} = \sigma_{11}^{(1)} \cos^2\theta + \sigma_{33}^{(1)} \sin^2\theta \quad , \quad \sigma_{r\theta}^{(1)} = (\sigma_{11}^{(1)} - \sigma_{33}^{(1)}) \sin\theta \cos\theta \tag{A.13}$$

$$\sigma_{rr}^{(2)} = \sigma_{11}^{(2)} \cos^2\theta + \sigma_{33}^{(2)} \sin^2\theta \quad , \quad \sigma_{r\theta}^{(2)} = (\sigma_{11}^{(2)} - \sigma_{33}^{(2)}) \sin\theta \cos\theta \tag{A.14}$$

Note that far from the crack

$$\sigma_{12}^{(k)} = \sigma_{13}^{(k)} = \sigma_{23}^{(k)} = 0 \tag{A.15}$$

where $k = 1, 2$.

Appendix B

Equations of parameters for a $+45° // -45°$ interface

in Section 3.4, a penny-shaped interface crack between two unidirectional composites is considered. The fibers in the upper material are in the 0°-direction and in the 90°-direction in the lower one, as shown in Fig.B.1a. In this appendix, the interface for $\theta = 45°$ is considered, as shown in Fig.B.1b. For this case, the upper material in the delamination front coordinate system is a unidirectional composite with fibers in the +45°- direction in the $x_2 = 0$ plane, with respect to the x_1- direction, as shown in Fig.B.1b. The lower material is the same material as the upper one, rotated about the x_2-axis by 90°. The double slash denotes interface. The materials are tetragonal in the delamination front coordinate system.

Explicit expressions for the parameters E_{11}, E_{22}, E_{33}, E_{23}, E_{32} and ε used in Section 3.4

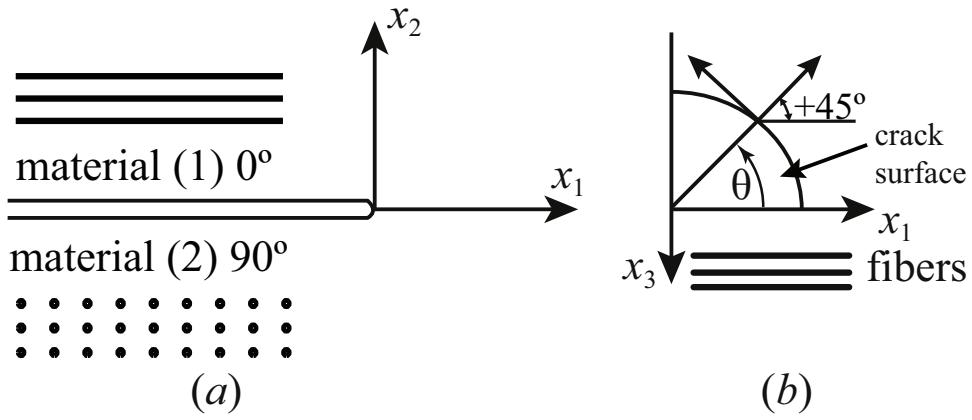

Figure B.1: (a) An interface crack between two unidirectional composites and (b) an upper view of the crack.

are given. The parameters E_{11}, E_{22}, E_{33}, E_{23}, E_{32} are given as

$$\begin{aligned} E_{11} = E_{11}^{(1)} = E_{11}^{(2)} =& \frac{is'_{11}}{\Delta}\left\{\beta_1+\beta_2+\frac{\beta_1\beta_2}{\beta_3(\beta_1+\beta_2)}\left[\frac{\beta_2 Q(\beta_1)-\beta_1 Q(\beta_2)}{Q(\beta_3)}\right]\right. \\ & \left.-\frac{\beta_3}{\beta_1-\beta_2}\left[\frac{\beta_1 Q(\beta_1)-\beta_2 Q(\beta_2)}{Q(\beta_3)}\right]\right\} \\ & +\frac{i(s_{15}^{2\prime})}{\Delta}\left\{\frac{\beta_2^2 Q(\beta_2)-\beta_1^2 Q(\beta_1)}{\beta_1-\beta_2}+\frac{\beta_1\beta_2}{\beta_3}\frac{Q(\beta_1)Q(\beta_2)}{Q(\beta_3)}\right. \\ & \left.+\frac{\beta_3}{\beta_1-\beta_3}\left[\beta_1 Q(\beta_1)-\beta_2 Q(\beta_2)\right]\right\} \end{aligned} \tag{B.1}$$

$$\begin{aligned} E_{22} = E_{22}^{(1)} = E_{22}^{(2)} =& \frac{is'_{22}}{\Delta}\left\{\frac{\beta_1+\beta_2}{\beta_1\beta_2}+\frac{\beta_1\beta_2}{\beta_3^2(\beta_1-\beta_2)}\left[\frac{Q(\beta_1)-Q(\beta_2)}{Q(\beta_3)}\right]\right. \\ & \left.-\frac{1}{\beta_1\beta_2(\beta_1-\beta_2)}\left[\frac{\beta_1^2 Q(\beta_1)-\beta_2^2 Q(\beta_2)}{Q(\beta_3)}\right]\right\} \end{aligned} \tag{B.2}$$

$$\begin{aligned} E_{33} = E_{33}^{(1)} = E_{33}^{(2)} =& \frac{is'_{44}}{\Delta}\left\{\frac{1}{\beta_3}-\frac{1}{\beta_1-\beta_2}\left[\frac{Q(\beta_1)-Q(\beta_2)}{Q(\beta_3)}\right]\right. \\ & \left.+\frac{1}{\beta_3(\beta_1-\beta_2)}\left[\frac{\beta_2 Q(\beta_1)-\beta_1 Q(\beta_2)}{Q(\beta_3)}\right]\right\} \end{aligned} \tag{B.3}$$

$$E_{23} = E_{23}^{(1)} = -E_{23}^{(2)} = s_{25}^{\prime(1)} + \frac{s'_{22}}{s_{15}^{\prime(1)}\Delta}\frac{1}{\beta_3 Q(\beta_3)}\left\{\frac{1}{\beta_3}+\frac{\beta_3-\beta_1-\beta_2}{\beta_1\beta_2}\right\} \tag{B.4}$$

$$E_{32} = E_{32}^{(1)} = -E_{32}^{(2)} = -E_{23}^{(1)} \ . \tag{B.5}$$

In eqs. (B.1) to (B.4), β_i for $i = 1, 2, 3$ are the eigenvalues of the compatibility equations. They are the same for the upper and lower materials. The reduced compliance coefficients, $s'_{\alpha\beta}$, are given as

$$s'_{\alpha\beta} = s_{\alpha\beta} - \frac{s_{\alpha 3}s_{3\beta}}{s_{33}} \tag{B.6}$$

for $\alpha, \beta = 1, .., 6$. Note that $s_{\alpha\beta}^{\prime(1)} = s_{\alpha\beta}^{\prime(2)}$ except for

$$s_{15}^{\prime(1)} = -s_{15}^{\prime(2)} \quad , \quad s_{25}^{\prime(1)} = -s_{25}^{\prime(2)} \quad , \quad s_{46}^{\prime(1)} = -s_{46}^{\prime(2)} \ . \tag{B.7}$$

In eqs. (B.1) to (B.4), $Q(\beta_i)$ for $i = 1, 2, 3$ are given as

$$Q(\beta_i) = \frac{\beta_i^2 - (s'_{25}+s'_{46})/s'_{15}}{s'_{55}\beta_i^2 - s'_{44}} \ , \tag{B.8}$$

and Δ is given as

$$\Delta = 1 + \frac{1}{\beta_3(\beta_1-\beta_2)Q(\beta_3)}\left\{\beta_1\beta_2\left[Q(\beta_1)-Q(\beta_2)\right]-\beta_3\left[\beta_1 Q(\beta_1)-\beta_2 Q(\beta_2)\right]\right\} \ . \tag{B.9}$$

The parameter β is given explicitly as

$$\beta = \frac{E_{23}}{\sqrt{-E_{22}E_{33}}} \tag{B.10}$$

where the sign of β is taken as the sign of E_{23}. The oscillatory parameter, ε, is found by substituting β into equation (1.67).